Plantar Soft Tissue Multiscale Structure and Mechanics with Emphasis on Diabetes-related Changes

Lynda M Brady

A dissertation

submitted in partial fulfillment of the

requirements for the degree of

Doctor of Philosophy

University of Washington

2023

Reading committee:

William R. Ledoux, Chair

Michael R. Bailey

Lucas R. Meza

Program Authorized to Offer Degree:

Department of Mechanical Engineering

University of Washington

Abstract

Plantar Soft Tissue Multiscale Structure and Mechanics with Emphasis on Diabetes-related Changes

Lynda M Brady

Chair of the Supervisory Committee:

William R. Ledoux

Department of Mechanical Engineering

Diabetes mellitus is a significant chronic disease affecting over 37 million Americans. Complications of the lower extremity related to diabetes can be severe, including deformity, ulceration, and amputation. Developing improved prevention and treatment of pedal complications necessitates a better fundamental understanding of the diabetes-related changes to plantar soft tissue microstructure and mechanics. Despite growing agreement that aberrant pressures are associated with ulceration, long-standing hypotheses about shear stresses initiating ulcer injury, and observational assessments of microstructural and biochemical disruptions, microstructural study has not assessed the characteristics of the unique adipose septal chambers of the plantar fat pad, and there has been little *in vivo* measurement of internal multidimensional strains. This gap in knowledge can be related to the difficulty of measuring these important parameters, as

microstructural assessment requires substantial time from a highly trained histologist, and *in vivo* measurements must prioritize human safety and comfort. In order to address these lingering questions, this work develops physical and computational tools to make previously unexplored microstructural, macrostructural, and mechanical measurements of the plantar soft tissue.

First, an automated method for assessing morphology of plantar soft tissue histological samples is reported and applied to quantify changes in the plantar adipose chambers related to tissue depth and diabetes. Adipose chambers were found to be quantitatively smaller in the superficial adipose layer than in the deep adipose layer, and with diabetes the size of the superficial chambers increased and the deep chambers decreased, leading to more similar chamber sizes between the two layers. Then, a volumetric load-bearing ultrasound scanner is constructed to acquire high-resolution, three-dimensional structural scans of the plantar soft tissues in unloaded and naturally loaded conditions. This scanner consists of an elevated platform, a two-axis mechanical translation system for the transducer, and a load-bearing plate capable of transmitting B-mode and shear wave elastography ultrasound modalities. In order to more safely couple the foot and transducer to the load bearing plate, custom polyacrylamide coupling gels were developed to meet application demands for strength and toughness. Finally, the volumetric scanner was integrated into a data collection protocol including computed tomography and plantar pressure, and scans were acquired for four subjects. Analytical methods for acquiring internal axial and shear strains across all three anatomical axes and planes, regional stiffness maps, and plantar pressure based on underlying bony geometry are reported. These methods are applied to the data from several subjects to demonstrate their feasibility.

Table of Contents

Table of Figures

Table of Tables

Dedication

to everyone with a thirst for knowledge

the foundation builders

the shoulder standers

the prize winners

the Great Conversers

those who dared to dream

those who failed courageously

may we all find what we seek

Acknowledgements

This body of work would not be as lengthy, aspirational, or complete without the guidance, support, and care of dozens of friends, colleagues, mentors, and, of course, family members.

First, as they say, girls just want to have fun-ding for scientific research, so thank you to all the organizations that have supported me and my work: The VA Puget Sound graduate fellowship, the Center for Limb Loss and MoBility center grant (VA RR&D A9243C), and the NIDDK Diabetic Complications Consortium (DiaComp, www.diacomp.org) pilot and feasibility program (grant DK076169 and DK115255 subaward 32307-94). I also want to thank the veterans who have participated in our research.

Next, a huge thanks to the grads, undergrads, and engineers in the Center for Limb Loss and MoBility who provided daily support and camaraderie. I'd like to specifically thank Stina Stender for mentoring me, teaching me how to navigate an academic lab, and for endless encouragement in my first few years of graduate school, Corey Wukelic, for his contributions to the last four chapters of this thesis, Will, Aerie, and Nick for making the last year such a fun and collaborative lab atmosphere, and Alyssa Rickettts, Brian Cook, Tony Huynh, Eric Thorhauer, and Alex Bearardo-Cates for being great student lab mates. I couldn't have done this without you.

To my teachers and advisors, particularly William Ledoux and Eric Rombokas, and my committee, Yak-Nam Wang, Michael Bailey, Lucas Meza, and Marco Salviato, thank you for your mentorship, guidance, and support of my research ideas. Even when my research vision wasn't so clear, you let me explore, draw inspiration from the literature, and aim for tackling a hard problem. To the teachers I had in courses at UW and before, who are too numerous to mention by name, thank you for fostering my strong curiosity and deep desire to learn. I'm forever grateful for the opportunities I have had to learn how the physical world works (and doesn't!). To my academic advisor, Wanwisa, thank you for always being a source of joy in our department. Your smile, enthusiasm, and of course, excellent academic guidance have been a grounding and centering force for me and so many. They don't say you're the heart of the department for nothing.

To my lifelong friends, Maya, Linda, Mary, Lauren, Kelsey, Sylvie, Luke, you've seen me through all sorts of successes, celebrations, challenges, and mistakes and supported me in growing into someone who would pursue and complete a PhD. I'm forever grateful for your kindness, phone and zoom calls, wine nights, vent sessions, and most of all your friendship. (Your body MOVES!?!) To my new friends from the department, especially my friends from my first year, the members of the mechanical engineering graduate student association and my grad school big, Soyoung Kang. A graduate experience is so deeply influenced by the peers who share it with you. You were a huge part of my decision to come to UW, and remain one of the best parts of my time here.

Finally, to my very first and best support system: my family. Thank you to my parents for teaching me that my only limitations are my dreams, and encouraging me beyond the world's boxes. To my sister, thank you for being my first and biggest role model and for inspiring me to be more confident, gracious, and ambitious. I'll always be trying to be as cool as you. To my brother, thank you for being my best friend since birth, inspiring me to do a PhD, and supporting me through your own doctoral experience. I wouldn't be who I am today without you.

1 Introduction

1.1 Prevalence and Complications of Diabetes

Over 34 million, or 13%, of U.S. adults live with diabetes mellitus (DM) as of 2018[1], an increase of nearly 50% from 8.7% of U.S. adults in 2000, making it not only one of the most prevalent chronic diseases in the U.S.[2], but suggesting that it will continue to be a significant chronic disease in years to come. DM is a systemic disease, in which the body makes insufficient insulin (Type I) or becomes resistant to insulin (Type II). Insulin promotes absorption of glucose into liver, fat, and skeletal muscle cells. When insulin is unable to sufficiently promote glucose uptake, the level of glucose remains elevated in the blood. This elevated blood-glucose is carried to all tissues in the body through the circulatory system, and can disrupt normal biochemical processes such as advancing glycation of proteins. As a systemic disease, DM is associated with a large number of co-morbid complications such as retinopathy, nephropathy, cardiovascular disease, hypertension, neuropathy, and skin infections. Foot complications of DM encompass a range of pathologies including structural deformities, to loss of sensation, reduced vascular function, and ulceration.

1.1.1 Plantar Ulceration

Ulcers are open wounds of unclear origin that appear on the foot. These wounds can be slow to heal, in part due to the effects of diabetes on peripheral vascularization, and may not be immediately noticed in cases of neuropathy. This combination of factors makes ulcers difficult and expensive to treat[3], and also gives them a high risk of infection. Infection in ulcers can be severe, and if it reaches the bone, it may require amputation of the affected limb up to the level of that bone. In 2016, 130,000 adults with diabetes underwent a lower extremity amputation[1].

An estimated 19% of people diagnosed with DM will develop a foot ulcer during their lifetime[4], meaning of the 34 million adults with diabetes in the U.S., 6.5 million will develop at least one ulcer. Ulcers affect quality of life and are difficult to treat, often doubling healthcare costs[3] and, in severe cases, requiring amputation. Despite the seriousness of this condition, and the recurrence rate of 40% at one year and 65% at 5 years[4], ulcer risk assessment is still largely based on systemic metrics like HbA1c, or comorbidities like peripheral neuropathy and peripheral arterial disease, rather than local factors specific to the foot. Similarly, ulcer prevention consists of controlling blood glucose levels (systemic), non-constrictive footwear (general), and foot self-checks (early identification)[5].

There are a variety of hypothesis for the mechanism of ulceration, with some focusing on risk factors like insensate feet due to peripheral neuropathy and the possibility of unnoticed injury, poor wound healing due to peripheral vascular disease, skeletal deformities like Charcot foot or claw toes, or dry skin. Other hypotheses are mechanically-driven, suggesting that there is a change in plantar loading to generate high plantar pressures that injure tissue with normal motion or a change in shear forces at the plantar surface or in internal soft tissues that causes a tissue injury[6]. The true mechanism of injury is likely to be a combination of these factors, but the change in plantar mechanics is the least understood due to difficulties in measuring the mechanical properties of the plantar soft tissue *in vivo*.

1.1.2 Treatments, Guidelines, and Gaps

Despite a long history of foot ulcers in diabetes and an established connection between ulceration and increased cost, morbidity, and mortality, the prevention and treatment options for complications of DM in the foot, particularly ulceration, have undergone minor changes since the combination of debridement and offloading for plantar ulcer treatment was established before the turn of the century. The International Working Group on the Diabetic Foot (IWGDF) guidelines for prevention of persons with foot ulcers from 2019 lists sixteen recommendations[5]. These recommendations can be broadly summarized as:

- screening patients for risk factors such as history of prior ulceration, foot deformity, neuropathy, vascular disease, or signs of foot injury (recommendations 1 & 2)
- instructing patients to practice good self-care (do not walk barefoot, inspect plantar surface of both feet daily, monitor foot temperature, wear appropriate footwear; recommendations 3-6)
- prescribing therapeutic footwear or custom orthoses (recommendations 7-9)
- treating pre-ulcerative signs such as ingrown toenails or calluses (recommendation 10)
- considering tendon surgeries when conservative treatments fail (recommendations 11 & 12), but not nerve decompression (recommendation 13)
- prescribe light walking and mobility-related exercise (recommendations 14 & 15)
- prescribe integrated foot care (recommendation 16)

These recommendations for prevention of ulcers focus on external signs, however, the pathomechanics of ulceration have been hypothesized to initiate in the deep tissue and propagate outward[6]. Other areas of emphasis include systemic metrics of diabetes severity (peripheral nerve and vascular complications, other comorbities), general self-care, and therapeutic footwear, which is typically only able to target offloading after the first incidence of ulceration.

Treatment of ulcers consists of two components: wound care and offloading. The IWGDF guidelines for wound care contain thirteen recommendations, primarily concerned with techniques for debridement of the wound and considerations of the type of wound dressing that aids wound healing and patient comfort, such as topical treatments, oxygen therapy, and negative pressure. However, the quality of evidence for the majority of these recommendations is low. While debridement and wound dressing are essential to avoid infection and poorer outcomes, it is difficult to heal an ulcer once formed.

After debridement and dressing, the wound must be protected from additional injury through offloading. The IWGDF lists nine recommendations for offloading of an ulcer[7], which can be broadly summarized (Figure 0-1), with the primary interventions being a non-removable off-loading device, a removable off-loading device, or tendon surgery, and with most recommendations being directed at forefoot and midfoot ulcers rather than ulcers at the heel. The recommendations note that heel ulcers are less common but little research on the best way to offload and heal them.

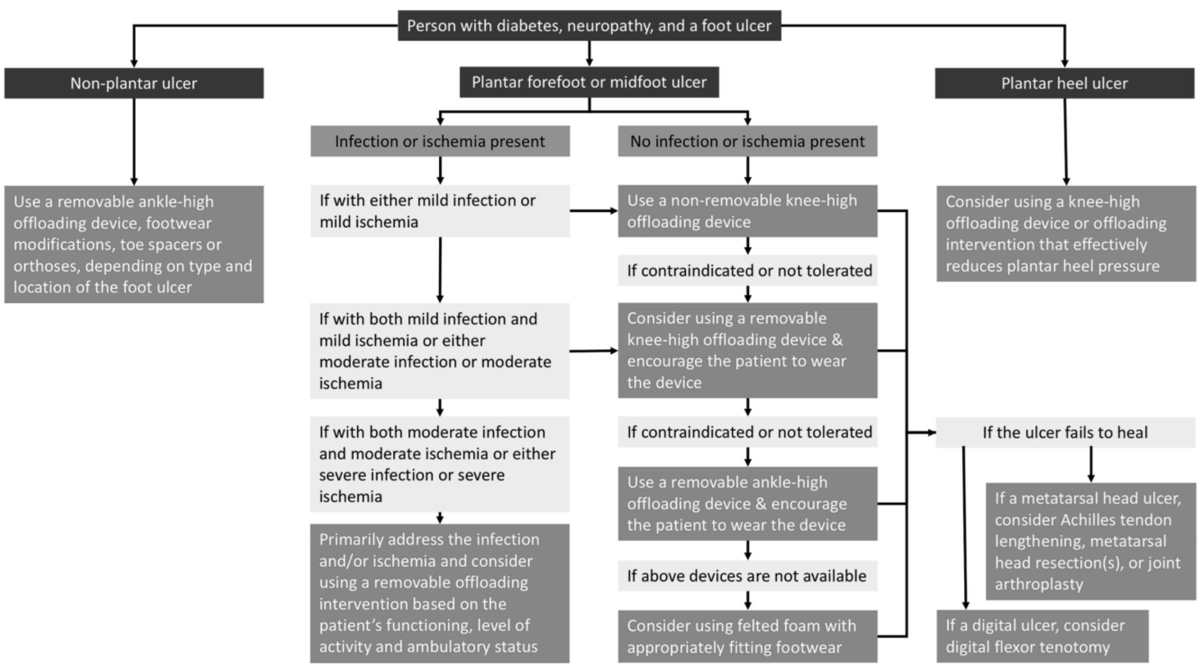

Figure 0-1: Flowchart of plantar ulcer treatment from the IWGDF guidelines for plantar offloading[7], reproduced with permission.

Given the high cost of treating an ulcer, the high rate of recurrence, the difficulty in healing an ulcer, and the low quality of evidence for many of the treatment recommendations, prevention of the initial ulcer is critical. However, preventative care for ulcers lacks clarity and specificity due to a persistent lack of information about the process of ulcer development. There is little information on how to predict when or where an ulcer might occur prior to its occurrence. Plantar pressure has been correlated with ulceration, but with low specificity[8–10], and plantar pressure measurement systems are rarely available in clinics. An improved understanding of how ulcers form, with a focus on diagnostic imaging and targetable early interventions could drastically improve diabetes care.

1.2 Objective

This thesis aims to expand understanding of the plantar soft tissue structure at a microscale, macroscale, and mechanical level in order to provide a basis for improved prevention and treatment of diabetes-related plantar ulceration.

There are several specific hypotheses related to each level:

Microstructure

μH1) The adipose chambers will be larger in the deep layer than in the superficial.

μH2) The adipose chambers will be smaller in the diabetic specimens than the non-diabetic.

μH2) A deep neural network with attention will be able to highlight areas of importance in the plantar soft tissue and guide development of new measurements.

Macrostructure and mechanics

mmH1) All tissues will have increased stiffness in diabetic patients, leading to an overall increase in diabetic plantar soft tissue stiffness, but the magnitude of this change will vary by tissue and location.

mmH2) Shear strain (from rest to standing) between different plantar soft tissues will be increased in diabetic subjects

mmH3) A deep neural network with attention will be able to highlight areas of importance in the plantar soft tissue and guide development of new measurements.

To address these hypotheses, this work will have these specific aims:

Microstructure

μSA1) Develop a method for automated segmentation of different plantar soft tissues from microscopy slides.

μSA2) Investigate attention mechanisms in order to guide selection of areas and morphological parameters of interest with relation to diabetes.

μSA3) Use automated processing to quantify morphological changes to the microstructure of plantar soft tissue.

Macrostructure and mechanics

mmSA1) Develop a mechanical system and the necessary software to generate a three-dimensional scan of the entire plantar soft tissue, using B-mode ultrasound for structural information and shear wave elastography for tissue properties.

mmSA2) Collect plantar soft tissue scans for 7 diabetic non-neuropathic subjects and 7 non-diabetic subjects.

mmSA3) Analyze these scans using segmentation and strain information calculated with digital volume correlation as well as an interpretable classification neural network.

2 Background

2.1 Anatomy of the foot

The foot is the initial load bearing structure in the kinematic chain and is uniquely designed to dissipate high loads encountered during bipedal activities. The foot can be considered in three sections: the dorsal aspect of the foot, which is the superior surface and consists of the soft tissues superior to the bones of the foot; the skeletal aspect, which includes the bones of the foot, the ligaments and tendons that connect bones, provide support to the joints, and maintain the overall structure of the foot; and the plantar aspect, which includes all the soft tissues inferior to the bones of the foot. As the focus of this work is the plantar soft tissues, this discussion of the foot anatomy with begin with a brief overview of the foot skeleton before a detailed description of the soft tissues.

2.1.1 Skeletal Structure

The skeletal aspect of the foot consists of 28 bones connected by primarily plane and condyloid synovial joints. These bones are arranged in a structure that allows significant tri-planar motion and flexibility. This structure is reinforced with numerous ligaments that provide stability and prevent excessive motion at any of the joints. Some tendons as well provide necessary tension that maintains the skeletal structure of the foot. Finally, intrinsic muscles also serve essential function in supporting foot structure.

The skeletal structure is often split into three sections: the hindfoot, which consists of the calcaneus and talus; the midfoot, which consists of the navicular, cuboid, and three cuneiforms; and the forefoot, which consists of the five metatarsals and phalanges.

2.1.2 Plantar Soft Tissue

The plantar soft tissue broadly describes all soft (non-osseous) tissue beneath the bones of the foot. This includes skin, adipose, muscle, ligament, tendon, nerve, blood vessel, and other connective tissue[11]. Starting from the skeletal structure (Figure 2-1A), the first soft tissues encountered (Figure 2-1B) are the ligaments of the arch and the interosseous muscles. These ligaments stretch between the calcaneus or the talus and the cuboids or metatarsals, spanning the hindfoot and midfoot to support the arch structure. These ligaments are generally strong and fibrous.

The next layer moving superficially (Figure 2-1C) consists of three small muscles in the forefoot, which mainly serve as toe flexors. The muscle bodies of these muscles lie just beneath the metatarsals. The deep branches of the lateral and medial plantar nerves are also seen at this level in the forefoot.

The following layer (Figure 2-1D) includes the tendons of the long flexor muscles whose muscle bodies originate in the leg, as well as the muscle bodies and tendons of the lumbricals and quadratus plantae, which assist in toe flexion. Additionally, in this middle layer, the tibial nerve and posterior tibial artery branch into the medial and lateral plantar nerves and plantar arteries and travel along the arch of the foot, branching again into smaller deep and superficial nerves and vessels. While the dorsal foot has several large superficial vessels, the plantar surface undergoes such high stress that large superficial vessels would be unable to adequately function, so plantar blood supply is routed deep and superficial offshoots are small.

The most superficial layer of the plantar muscles (Figure 2-1E) includes the three short abductor-flexor muscles, which flex and abduct the toes. The muscular bodies lie within the arch while the tendons run along the tendon sheaths to the most distal phalanges.

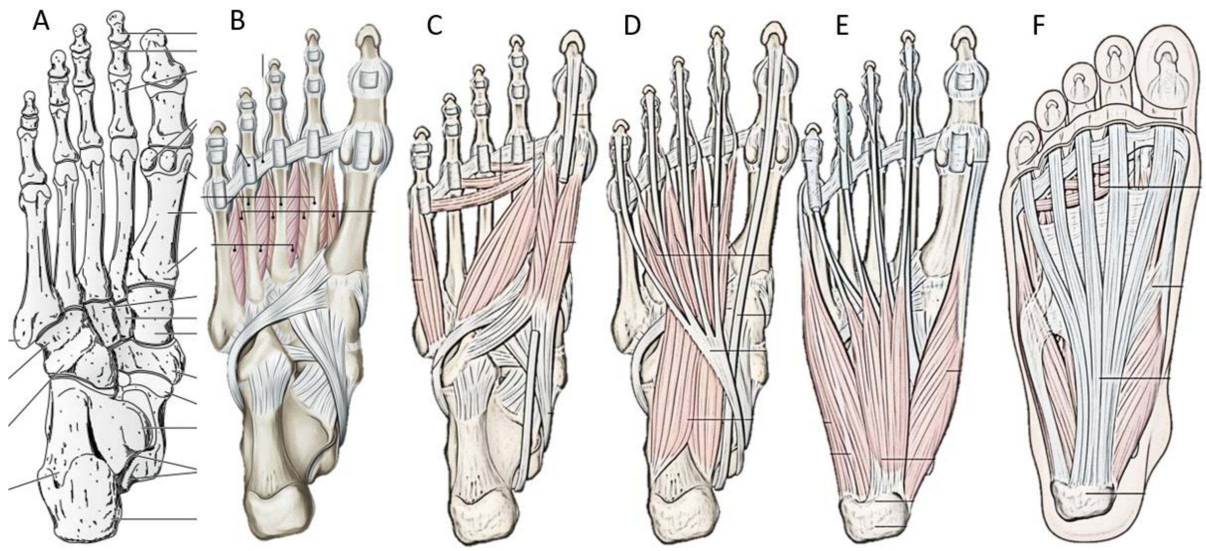

Figure 2-1: From left to right: A) the bones of the foot viewed from the plantar surface, B) the deep layer of interosseous muscles, ligaments, and fibrous capsules, C) the deep plantar intrinsic muscles, D) the mid layer of intrinsic plantar muscles and tendons, E) the superficial layer of intrinsic muscles, and G) the superficial plantar fascia and aponeuroses. Adapted from Hollinshead's Functional Anatomy of the Limbs and Back [11] and Earth's Lab (https://www.earthslab.com/category/anatomy/lower-limb/).

Superficial to the plantar muscles and tendons is the plantar aponeurosis (Figure 2-1F), a strong ligamentous structure that connects the calcaneus to the phalanges. It also extends to help form synovial sheaths for the tendons of the toes and forms a central compartment (medial-laterally) of the foot that includes the flexor digitorum tendons and lumbrical muscles. The foot has separate medial and lateral compartments that house the hallux and fifth digit tendons and muscles. Superficial to this aponeurosis is a layer of adipose tissue which acts as a shock absorber and load dissipater. Finally, the plantar skin is the most superficial layer of plantar soft tissue.

2.1.3 Functional anatomy of the foot

In a typical healthy foot, load is carried through contact of the forefoot, calcaneus, and lateral midfoot. Ligaments and tendons sustain tension between the other bones of the foot such that load is transmitted between skeletal and soft tissues and the other areas of the foot do not make direct contact with the ground. In order for this to happen, the longitudinal and transverse arches run the length and width of the skeletal foot. These two arches function to sustain the complex three dimensional load carrying skeletal geometry of the foot, and the stress at any particular point is proportional to its height on the curve of the arch, similar to the pattern of stress placed on an engineering arch.

2.1.4 Microstructure

Much of the focus of microstructural investigations into the plantar soft tissue focus on the skin and plantar adipose, in part due to the thick layer of plantar adipose at the calcaneus (also called the heel pad) which is the primary soft tissue superficial to that significant load-carrying bone. In one of the earliest investigations into the plantar adipose, Blechschmidt described qualitatively but in great detail the structure of the plantar adipose using formalin-fixed samples stained with fuchsin, carmine, methyl blue, or Hart's elastin stain as well as selective dissolution of thicker tissue sections to photograph relief images of the tissue in solution[12]. Blechschmidt described a complex organization of larger chambers whose walls are thick and fibrous subdivided by more delicate elastic and collagenous divisions which create an irregular yet ordered structure full of asymmetric curves (

Figure 2-2, Left, Middle). He supported the mechanical explanation that this structure of fibrous yet elastic chambers of adipocytes ensures that the total deformation of the plantar fat is the sum of numerous small deformations, despite the stress likely being unequal throughout the plantar adipose and causing uneven deformation across the calcaneal fat pad. He further hypothesized that these septa are structured to provide the greatest padding to the point of highest load—under the calcaneus—and are uniquely oriented to resist vertical loading.

Similarly, Jahss noted the interconnected collagen-elastin septal networks creating isolated adipose chambers as well as medio-lateral and anterior-posterior differences in chamber size[13]. He similarly concluded that “the organization of this structure is what confers upon its unique role as a shock absorber”.

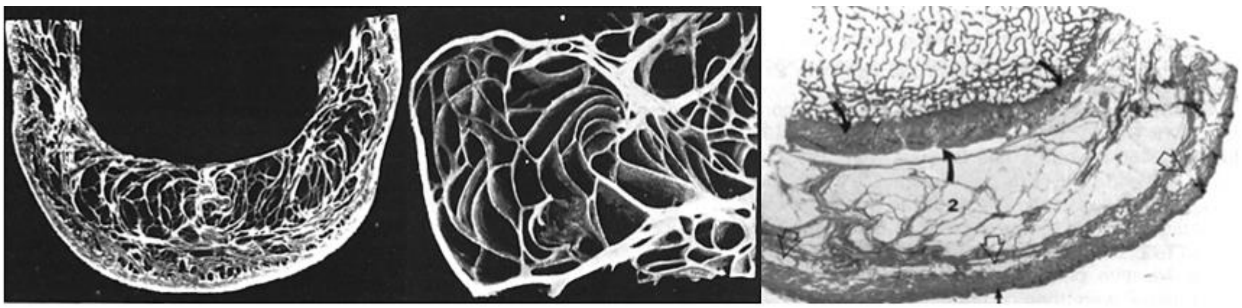

Figure 2-2: Left. Frontal section of subcalcaneal padding showing complex septal structure and skin (adapted from Blechschmidt, 1982, Foot&Ankle, 2:5, 274). Middle. Close-up of thinner and thicker septal divisions (adapted from Blechschmidt, 1982, Foot&Ankle, 2:5, 278.). Right. Section of calcaneus and subcalcaneal tissue showing skin, superficial and deep layers of adipose tissue, fibrous connection of tissue to bone (adapted from Buschmann, 1995, Foot & Ankle International, 16:5, 265).

Buschmann further described the subcalcaneal tissue as consisting of a “very thick dermis” followed by a papillary dermis and a larger reticular dermis with substantial (40-50%) elastic tissue. He then described two ‘subcutaneous’ layers, which are the superficial and deep adipose layers described by Bleschdmidt and Jahss. Finally, he described the anchoring of the subcalcanceal tissue to the calcaneus by varied sized retinacula. These different layers can be seen in

Figure 2-2, Right. Colloquially, the chambers of the deep layer have been called ‘macrochambers’ and the chambers of the superficial layer have been called ‘microchambers’[14–17]. However, while the chambers have been observed qualitatively as larger in the deep layer, the chamber size has not been quantified.

2.1.5 Structure-function Relationship

The effect of microstructure on material properties is well-established in classical mechanics. Microstructural features such as grain size significantly affect the properties of metals, particularly alloys, and form a strong basis for manufacturing techniques like heat treatment. Microstructure can be used to change the strength, ductility, and toughness of materials to best fit the intended use of the material.

Biological materials are often required to sustain large and dynamic loading, and their microstructures are complex, with variability in order, orientation, composition, and shape. The hierarchical structure of biological materials and intricate lattice patterns allow for complex combinations of material properties difficult to replicate in synthetic materials. These unique material property combinations make biological materials and their complex hierarchical structures of particular interest to material scientists.

While the microstructures of some individual tissues have been defined through histomorphological analysis, the microstructure of multiple tissues interactions, particularly the plantar soft tissue, lacks mechanical investigation.

2.1.5.1 Plantar soft tissue

There have been a few investigations into the effect of microarchitecture on plantar soft tissue mechanics. Using *ex vivo* methods, Miller-Young et. al. found no significant difference between specimens of the plantar adipose cut perpendicular and parallel to the skin, suggesting isotropy in the plantar fat[18]. However, the specimens were cut into 8mm diameter, 10mm height samples, which may be smaller than the size of some of the larger septal chambers, introducing the possibility that these tests were not able to effectively test the anisotropy of the plantar adipose structure.

Micromechanical computational models suggest that the extracellular matrix of the plantar adipose tissue may be 2-3 times stiffer than the whole tissue[19], and that the septal walls and adipose chambers may have similar volumetric stiffness but that septal walls have higher shear stiffness[20]. Recently, Johnson et. al. attempted to recreate the properties of the plantar soft tissue using only a 3D printed lattice[21], and found that by modulating only the cross-sectional area and spacing of struts in a lattice, a relatively hard but compliant material (Tango, Stratasys, Eden Prairie, MN, USA, E=2500) could mimic the properties of plantar soft tissue. These works emphasize the importance of the microstructure on the function of the material.

A comprehensive analysis of the interaction of specific tissue types, the effect of relative tissue composition, and geometric and morphological tissue structure, and changes therein on the functional properties of the plantar soft tissue would be a useful resource for applications in tissue damage prevention, tissue replacement, and artificial limbs.

2.1.5.2 Challenges in Plantar Soft Tissue Mechanical Testing

Soft tissue presents specific challenges to describing its behavior. Soft tissues tend to display both nonlinearity and viscoelasticity. Soft tissues are also hydrated and often pre-stressed *in vivo* in addition to being at body temperature, and often temperature-sensitive. This combination of environmental factors makes *ex vivo* testing particularly difficult both to perform and to apply to the *in vivo* state. However, *in vivo* testing presents challenges as well. It is difficult to visualize the tissues and measure strain in real-time as there ate tissue visualization limitations inherent to noninvasive imaging modalities. Additionally, parameters like radiation exposure, subject pain and comfort, and human elements like blood flow and movement must be considered as well. While *ex vivo* testing is more controllable, it is difficult to translate to clinical intervention. While *in vivo* testing is easier to translate to clinical intervention, the test parameters are difficult to control.

2.2 Ulcer-related Diabetes Pathophysiology

DM is a systemic disease characterized by elevated levels of glucose in the blood. DM can have wide-ranging complications due to its systemic nature. Two primary areas of investigation have emerged with regards to diabetes and plantar soft tissue—mechanical changes that may predispose the plantar soft tissue to injury, and biochemical and histological changes that may form the basis for mechanical changes or targets for therapeutic intervention.

2.2.1 Mechanical and macrostructure changes

Given that ulceration presents as a tissue injury, and tissue injuries are often a result of mechanical damage, aberrant mechanics are a common hypothesis for ulcer etiology. As a result, there have been many approaches to quantifying changes in mechanical properties of plantar and other soft tissues in diabetes. These approaches can be grouped as involving *ex vivo* mechanical tests on biopsied or dissected tissue, *in vivo* imaging tests using ultrasound, MRI, or X-ray radiography, and computational finite element models.

2.2.1.1 Ex vivo tests

Ex vivo tests are a critical component of understanding tissue mechanics and the function and dysfunction of the plantar soft tissue. In order to fully understand a multi-material structure, it is important to understand the properties of each material in the structure as well as parameters like the strength of connection between materials. The plantar adipose and the plantar skin have been characterized as materials, and changes to those material properties with diabetes have also been quantified. In the most thorough characterization to date, our laboratory characterized the compressive[22] and shear[23] properties of the plantar adipose at six locations and also separately tested the skin[24] of the same specimens, allowing some comparison between changes of two different tissues. Similar to other soft tissues, the plantar adipose and skin are both nonlinear and viscoelastic (Figure 2-3). However, the plantar adipose has a longer toe region, remaining in the initial low-modulus phase of the compression stress-strain curve for nearly 40% strain before increasing sharply (Figure 2-3A). In contrast, the toe region for the plantar skin lasts only 20-30% strain (Figure 2-3, c), dependent on location. As may be expected from the rule of mixtures, a structural test of similar set up using specimens with both plantar adipose and skin had a toe region of between 30 and 40% strain[25].

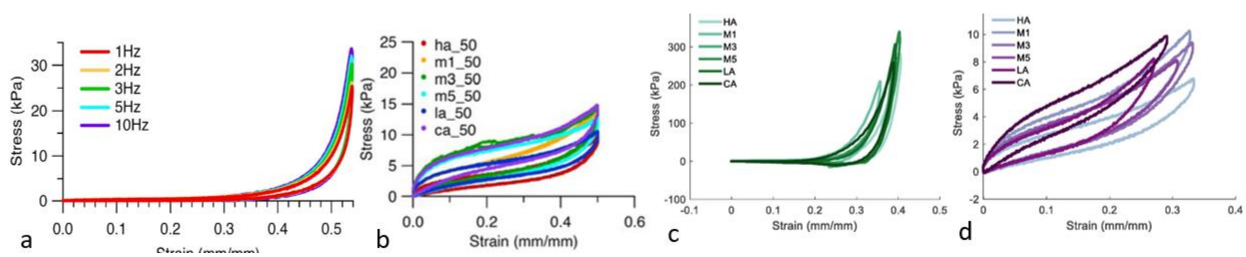

Figure 2-3: Example stress-strain curve for A) adipose in compression, showing frequency-dependence (from Pai 2010, reproduced with permission), B) adipose in shear showing location dependence (from Pai 2012, reproduced from with permission) , C) skin in compression, showing location dependence (from Brady 2021, reproduced with author rights), D) skin in shear, showing location dependence (from Brady 2021, reproduced with author rights).

In compression, the elastic modulus, calculated from the second half of the stress-strain curve, from the diabetic specimens was nearly twice the elastic modulus of the non-diabetic specimens in adipose and 1.25 times the elastic modulus of non-diabetic specimens in skin. In shear, the final modulus was 47% higher in diabetic adipose tissue but only 27% higher in diabetic skin. These studies show that the magnitude of the increase of stiffness in the plantar adipose is considerably larger than that of the skin. Such a difference could cause dramatic shifts in the local stress concentrations under loading, particularly with the irregular bony surfaces. However, as these studies performed physiologically realistic loading based on a normal gait cycle, there is no information about changes in the fatigue or fracture characteristics of the tissue.

In a structural test, Chen[26] showed that the plantar skin-adipose interface was 27% stronger with diabetes, but that the plantar skin was 12% stiffer and less extensible with diabetes. This supports a modest change in skin mechanics, but that there are additional shifts in other parts of the plantar soft tissue to accommodate the irregularity.

While *ex* vivo testing has contributed significantly to our understanding of plantar soft tissue mechanics and the changes of specific plantar soft tissues with diabetes, these tests are often limited to material-level tests and steps must be taken to alleviate differences in moisture, temperature, and other conditions that are different from *in vivo.* Fixative and dissection processes can alter the natural structure of the whole plantar soft tissue, limiting utility of cadaveric models for structural investigations and clinical translation.

2.2.1.2 In vivo imaging

MRI is a popular choice for studying the plantar soft tissue. MRI produces a three-dimensional volume and has excellent soft tissue resolution. Studies using MRI have shown that the effective shear[27] and elastic[27–29] moduli of the plantar soft tissue are higher in diabetic feet compared to non-diabetic, and that muscle fiber atrophy and fibrosis of the adipose tissue occurs in the metatarsal head of the diabetic foot[30]. However, MRI is expensive, requires lengthy acquisition and highly specialized technicians, and cannot resolve dynamic motion. Therefore, its use in studying the mechanics of the plantar soft tissue is limited.

Another 3D modality, computed tomography (CT), has similar limitations. While it has been used to demonstrate changes in plantar mechanics due to bony structures and soft tissue thickness in diabetic and non-diabetic ambulators[31], and reduced muscle density and increased arthropathy at the forefoot with diabetes and prior ulcer[32], CT is an uncommon choice, due to the higher doses of radiation and poor soft tissue resolution. Similarly, while fluoroscopy can resolve dynamic motion, soft tissue resolution is poor, and as such, fluoroscopy is often used to track bone motion and infer properties of the soft tissue by using the foot bones and the ground as a reference[33]. This method has been used to demonstrate that the heel pad operates close to its pain threshold in barefoot walking[33].

A real-time, safe, relatively inexpensive, imaging modality with good soft tissue resolution, ultrasound is a common choice for studying the plantar soft tissue. One of the most common methods of interrogating the plantar soft tissue using ultrasound involves attaching an ultrasound transducer to a mechanical actuator and applying a pressure to the plantar soft tissue while imaging its deformation, thus allowing the calculation of a force-deformation relationship. Using this method, several groups have shown an increase in stiffness with diabetes[34–36]. Additionally, ultrasound has been used to measure plantar soft tissue thickness, showing no difference in thickness between diabetic peripheral neuropathic subjects and controls[34,36], increased overall plantar soft tissue thickness[35], and progressively decreased epidermal thickness with diabetes, comorbid peripheral neuropathy, and history of or present ulcer[35]. Separating the plantar soft tissue into a superficial and deep layer, Hsu et. al used ultrasound indentation to describe a decrease in strain but increase in stiffness of the deep layer with diabetes and a decrease in stiffness of the superficial layer with diabetes[16]. However, ultrasound indentation is limited by the small area of action as well as the discomfort threshold of the device (~500kPa at the heel)[37], which is somewhat lower than the final modulus of the plantar soft tissue at maximum physiological compression[22].

2.2.1.3 Plantar pressure

Plantar pressure is an external measurement that describes the distribution of bodyweight over the plantar surface during either static standing or a dynamic motion such as walking. As an easily measureable non-invasive mechanical quantity, plantar pressure is an intuitive and desirable measurement for assessing ulcer risk due to changes in mechanics. Plantar pressure has been correlated with ulcer incidence[8], and is often used as an indicator of ulcer risk in research as well as a metric of effectiveness of strategies to prevent ulceration[38–40] and a method of validating computational models for answering diabetes and ulcer-related questions[41]. Plantar pressure is often higher at the site of a previous ulceration[42]. However, while some have measured ulcer incidence occurring in only those patients with abnormally high general plantar pressure[8], incidence of ulcers at *locations* of high or peak plantar pressure has been measured at 38%[8] and 57%[10]. Ledoux et al. demonstrated that for the metatarsals, higher peak plantar pressure was associated prospectively with ulceration; the same was not true elsewhere in the foot[9]. Additionally, there seems to be differences in the distribution of plantar pressure, as Abriu et al found a significant inverse relationship between midfoot peak plantar pressure and severity of neuropathy, suggesting that increase in plantar pressure in one location may be accompanied by a decrease in plantar pressure at another location. One group found that peak plantar pressure and peak plantar shear occurred at the same location in 20% of patients with diabetes and 0% of subjects without diabetes, suggesting that the combination of peak plantar compression and shear may contribute to injury[43].

Clearly, plantar pressure, while sometimes indicative of future ulceration, is not comprehensively predictive, suggesting there is a need for additional metrics to provide comprehensive preventative care. Additionally, plantar pressure measurements require specialized equipment and is highly variable with shod conditions. Plantar pressure measurements are not often available clinically, making them difficult to integrate into preventative care.

2.2.1.4 Computational experiments

Given the difficult of measuring internal stresses and strains *in vivo* due to patient comfort and ethics, and *ex vivo* due to difficulty maintaining structure, computational models have long been used to estimate internal stresses and strains for plantar soft tissue conditions. Finite element models have been used to evaluate the change in plantar stress given a change in material properties of the plantar soft tissue with diabetes[44], demonstrate that internal strains near pedal bones are ten times higher than plantar surface strains[45], demonstrate increased maximum principal stress and decreased minimum principal stress (increased magnitude compressive stress) in diabetic plantar adipose tissue[46], and show that nonlinearity of the plantar soft tissue material properties leads to uneven stress distribution[47].

However, finite element models are limited by simplifications in anatomical geometry, material models, meshing, assumed boundary conditions, and lack of validation. One study found that addition of sliding contact between tissues in a finite element foot model improved the fidelity of the plantar pressure distribution[48], though many models assume fixed connections between tissue layers, when multiple tissues are present. In a review of 96 finite element models of the foot, Behforootan et. al. noted that ligaments and cartilage were only modeled in just over half, and rarely nonlinear or viscoelastic when present, 77% of studies modeled the distinct layers of skin, fat, and muscle together as a single bulk 'plantar soft tissue' despite significant differences in the material properties of each, 44% of reviewed studies did not offer any validation of the model, and only five studies listed the number of elements in the mesh[49]. Of the reviewed studies, 79% modeled healthy feet, and just 13% were focused on the diabetic foot. Inclusion of anatomically realistic geometry, distinct material models, and nonlinear, viscoelastic models all increase the computational time required to run a model. However, the assumptions used to simplify the models, combined with a striking lack of validation, makes many finite element models difficult to rely on or conclude from.

A computational micromechanical model used a lattice structure of septa and adipose chambers, showing that the volumetric stiffness of connective septa and adipose chambers may be four and two times higher, respectively in diabetic adipose tissue, but that the shear stiffness may remain unchanged[20].

2.2.1.5 Effect of Location

Not all plantar locations are equally susceptible to ulceration[31,50]. In an analysis of 212 patients, 32.3% of ulcers occurred on the second to fifth toes, 31.6% on the hallux, 9.5% beneath the metatarsals, and 9.5% at the heel, suggesting that the forefoot is the primary location of ulceration[50]. In a study of 230 patients, 22.2% of ulcers occurred at the hallux, 14.7% at the metatarsals, 12.6% at the heel, 8.7% at the other toes, and 3.1% at the midfoot[51]. While these results again suggest the forefoot as the location of the majority of ulcers, there are a large share at the heel. *Ex vivo* compression and shear testing of plantar adipose and skin found significant variation in mechanical properties by location, though there was no interaction assessment between location and diabetes status[22–24]. Finally, while skeletal deformity of the foot is a known risk factor for ulceration, and ulcers are clearly location-dependent, attempts to link deformity and location of ulceration are mixed, with some finding a correlation[31] and others finding no correlation[51]. Ultimately, there are clear differences in both material properties of plantar soft tissues and ulcer risk by plantar location, making location an important consideration in analysis of ulcer etiology and diabetic plantar soft tissue mechanics.

2.2.2 Biochemical and Histological changes

Biochemical and histological investigations are often targeted toward non-plantar tissues or non-specific tissue components like collagen fibrils, but systemic changes to biochemistry and cellular histology can be presumed to occur in similar ways throughout the body.

Early work experimentally induced diabetes in the skin and aorta of a rat model using streptozotocin[52], finding that collagen fibers were lower in quantity but increased in strength. Additional work showed thicker capillary basement membrane, increased endocardial interstitial fibrosis, and decreased myocyte size with diabetes[53]. Reihsner et al[54] showed that the exponential coefficients fit to the stress-strain curve of skin taken from the plantar and dorsal aspect of the hand of persons with diabetes are higher than those coefficients for unaffected skin. They further showed that similar changes occur when artificially glycation unaffected skin specimens *in vitro*, and that the fluorescence of artificially glycated and diabetic specimens have similar luminance and peak wavelength, suggesting that the stiffening mechanism may be a direct result of increased glycation.

Of those studies focused specifically on the plantar soft tissue, Brash et. al reported fibrosis of the subcutis, which caused thicker and more fibrous septal separations as well as compressed adipocytes within the adipose chambers[30]. In a combined study of the biochemical and histological properties of the plantar adipose[55] and skin[24], there was no change in total collagen content, collagen: elastin ratio, collagen I:III ratio, size of adipocytes, total adipose area, skin thickness, or adipose/seta area fraction with diabetes, but the septal wall separating adipose chambers were 75% thicker and total elastin content was 25% higher in diabetic plantar adipose specimens. Additionally, of these parameters, only the total collagen content and septal thickness (adjusted for location) were correlated with mechanical parameters (energy loss and modulus, respectively)[56].

Supporting the idea of a change in the adipose structure, Johnson et. al. found that a lattice with increased spacing and increase diameter of struts produced material properties similar to diabetic plantar soft tissue and a lattice with smaller strut spacing and diameter produced material properties similar to non-diabetic plantar soft tissue for the same base material, strut orientation, and strut organizational pattern[21]. This suggests that increased septal thickness even if combined with larger adipose chambers could account for the increase in stiffness seen in diabetic tissue.

While there is evidence that collagen glycation may change the mechanical properties of the plantar soft tissue, there is little structural evidence of changes to the microstructure of plantar soft tissue being associated with the macroscale functional differences seen in diabetes[56]. Therefore, there are still unanswered questions about how the microstructure influences the functional ability in diabetes.

2.3 Mechanical Testing and Models

2.3.1 Mechanical testing methods and considerations

Mechanical analysis is often performed using a series of tests defined by engineering standards. These test are designed to mimic real-word use cases but in an idealized environment to reduce errors in measurements. These tests include tension, compression, bi-axial, impact, and drop tests, among others. In normal activities such as gait, the plantar soft tissue experiences complex loading that includes motion in all three anatomical planes due to the numerous joints and bones of the foot. However, the majority of plantar soft tissue testing is performed using compression testing methods as the primary axis of loading is normal to the plantar surface.

Much *ex vivo* testing of the plantar adipose is performed in compression on cylindrical specimens[18,22,25], while *in vivo* testing of the whole plantar soft tissue is often performed using impact or indentation techniques[27,36,37,57]. *Ex vivo* compression tests struggle with the boundary conditions of friction between the sample and the platens, opting for securing with glue, sandpaper, or assuming frictionless testing. Another issue with these tests is the high rate of slipping when specimens are not secured. Finally, in compression testing of elastic materials of high recoverability, identifying failure can be difficult, as there is unlikely to be a brittle fracture. In an inhomogeneous material like plantar adipose, it may be difficult to identify small cracks that signify plasticity in barrel deformation.

In order to fully understand the mechanics of the plantar soft tissue in relevance to injury during activities of daily living, the ideal mechanical test mimics the loading pattern and allows visualization of the entire structure's response to loading in a controlled way. Given the multi-axial loading in the foot, the aforementioned difficulty imaging the diverse tissues of the foot, and the numerous variables that arise with both *in vivo* and *ex vivo* testing, many methods are able to achieve one or more but not all of these conditions.

2.3.2 Mechanical models of soft tissues and composites

Soft tissues are classically nonlinear and viscoelastic, meaning that the change in load resisting an applied deformation is not linearly related to the applied deformation over a range of deformation (nonlinear), and also that the force-deformation behavior is time-dependent (viscoelastic), exhibiting a change in either force or deformation for a constant application of the other (creep or relaxation), and a change in the force-deformation relationship depending on the rate of applied deformation (rate-dependence). These properties are in contrast with most engineering materials, which are linear and elastic; exhibiting the same linear force-deformation relationship irrespective of total applied deformation or the rate of applied deformation up to the point of yielding.

Linear elastic behavior can be described with a simple linear equation, but nonlinearity and viscoelasticity are described by more complex models. Nonlinear materials are represented by hyperplastic models like Mooney-Rivlin[58], Ogden[59], neo-Hookean, and Arruda-Boyce[60] models, while viscoelastic materials are classically taught using simple combinations of springs and dashpots such as the Maxwell and Kelvin models. A common model for both nonlinear and viscoelastic biological soft tissues is the quasilinear viscoelastic model[61], which assumes the elastic ($F^{(e)}(\varepsilon)$) and temporal $G(t)$ components of material behavior are separable:

$$F(t) = \int_0^t G(t-\tau') \frac{\partial F^{(e)}[\varepsilon(\tau')]}{\partial \varepsilon} \frac{\partial \varepsilon(\tau')}{\partial \tau'} d\tau'.$$

Equation 2.3-1

Soft tissues can also be thought of as composite structures, composed of fibers and filling media with drastically different properties. As a result of this inhomogeneous constitution, composite materials have properties that are in between the properties of the two components. This combination of properties can be predicted by the rule of mixtures, which states that for a material made of multiple components, the material's property is a weighted sum of the component materials, where the weight is a volume fraction.

Finally, these are material and microstructural models, but there many structural considerations as well. Boundary conditions between different materials, morphology and orientation of different components, and direction and type of applied loads all affect the way that materials behave in a structure.

2.4 Medical image analysis

Medical images include modalities like MRI, CT, X-ray, ultrasound, and histology or pathology microscopy images. Given their importance in the diagnosis, monitoring, and treatment of disease, there are a wealth of methods to analyze such images in order to improve the consistency and quality of care.

2.4.1 Classic image analysis

Classically, image analysis methods derived from attempting to describe qualitative and quantitative human observations in digital terms or from attempting to extract information that may be obscured through some processing of the image. Such image descriptors and enhancers draw from qualities like edges between objects; changes in illumination, contrast, or color; texture; morphology; connected components; distance between objects; arithmetic combinations of images; or abstractions like frequency decomposition or principal components.

These classic image analysis methods have been used to successfully aid tasks in medical imaging, particularly in histological and bone analysis, such as measuring and counting adipocytes in histology[62–64], evaluating cortical geometry and trabecular microarchitecture in CT[65], quantifying axonal myelination in fluorescent microscopy[66], describe elastin fiber alignment in the cerebral artery in histology[67], measuring nuclei to detect cervical carcinoma pathology[68], counting and quantifying features of nuclei in retinal histology[69].

However, manual or semi-manual image processing techniques can be costly, requiring both large quantities of time and highly skilled personnel. These requirements often cause bottleneck in analyses, particularly in cancer biopsy review. Alleviating this burden on pathologists as well as incentive to reduce human bias and error has led to a drive for automated recognition of tissue types in digital histology images. Solutions aim to automatically detect areas of cancerous growth in large images composed of entire tissue slides at micron or nanometer resolution, correlating to pixel-level labeling in gigabyte sized images.

2.4.2 Machine Learning and Deep neural networks

Two of the most common tasks in medical image analysis are classification, typically attempting to classify images or regions of images as disease or health tissue, and segmentation, typically attempting to label each pixel in an image as one of multiple tissue types. These tasks tend to be difficult in medical imaging because the difference in appearance between tissues—particularly at tissue boundaries or mildly pathological tissue—is relatively small compared to other image analysis tasks. Therefore, more robust learning algorithms often outperform classic image analysis techniques, though with a tradeoff of increased complexity. Learning algorithms, often referred to as machine learning, optimize high-dimensional models to model complex relationships between instances of high-dimensional data. In order to model these relationships, the optimization is 'trained' on a large dataset and then 'tested' or 'validated' on a smaller, unseen subset.

Statistical machine learning techniques usually take image information abstracted via some classic image descriptors, and develop a model of the relationship between that image information and the desired output, often a classification. There are many different statistical machine learning algorithms, including nearest neighbor, regression, support vector machines, graphical models, random forests, decision tress, and Bayesian decision making. Supervised machine learning refers to the class of machine learning algorithms that are given a label as well as a feature or feature vector in the training data, while unsupervised machine learning is given only the feature vector in the training data, and is allowed to find its own pattern via clustering or pattern recognition techniques. Statistical machine learning algorithms have been used with classic image descriptors to successfully classify images by disease state[70] or severity[71] as well as perform segmentation[72] or clustering[73]. However, these methods are limited by the human choice of feature descriptors and require experienced engineers to choose and supervise the process.

Deep neural networks are composed of multiple linear and nonlinear differentiable transformation functions that, when ‘layered’ sequentially create a complex nonlinear functional relationship. These networks are optimized by evaluating a target function and propagating the gradients of each layer backwards to the input layer to update the weights of the function in each layer. The most common neural network in medical image analysis uses the convolution function for the bulk of its image transformations, earning it the name ‘convolutional neural network’, or CNN. CNNs have been used to classify large image datasets into thousands of classes[74,75], identify instances of objects in images[76], segment images[77], and more. One of the most common and successful variations of the CNN, the UNet[77], employs a down sampling chain of convolutions and nonlinear rectified linear units (ReLUs), and an equivalent up sampling chain of deconvolutions and ReLUs to directly convert an input image into a same-size segmentation image. Variations of the UNet have been applied to segment nearly all medical image types.

Deep neural networks are less developed for three-dimension inputs due to the difficulty of the increased input size. However, some groups have applied CNNs to volumetric MRI or CT inputs by using slices of the volume as inputs[78–80], breaking the inputs into smaller volumes[80,81], or downsampling the volumes using some interpolation algorithm[82]. As computational power continues to improve, and deep neural networks become more efficient, there may be more advances in leveraging the predictive power of the deep neural network for volumetric medical images.

2.5 Ultrasound Elastography

Ultrasound has been used to image the plantar soft tissue and calculate deformation with applied stress in order to measure changes in mechanics with diabetes. However, newer techniques alleviate the issues inherent in *in vivo* testing such as patient discomfort by directly measuring the tissue stiffness. Measurement of stiffness through imaging has been coined ‘elastography’. Elastography techniques exist for both MRI and ultrasound, and there are various methods of accomplishing this measurement.

Initial elastography techniques involved an external mechanical actuator which would induce a mechanical deformation or the body’s own mechanical deformation, such as from heartbeats or breaths, and produced a color-coded relative stiffness image of the tissues in frame based on their deformation by assuming uniform applied stress. This method of estimating stiffness based solely on deformation to get relative stiffness value within an image is called strain elastography. The use of an external mechanical actuator was useful for imaging superficial tissues, such as in investigating breast lumps, but imaging deeper tissues was more difficult. Such externally-actuated elastography was qualitative and subject to considerable error due to difficulty measuring probe displacement, location of the ultrasound probe in space, difficulty obtaining sequential images in the same plane due to user variability, and difficulty measuring accurate force.

Eventually, a high-powered ultrasonic pulse, called an acoustic radiation force impulse or ARFI, was developed in order to create a targeted applied force at a specific depth to provide improved control over applied stress and remove the need for an additional external mechanical actuator. The ARFI was used in some commercial strain elastography systems.

2.5.1 Shear Wave Elastography

The next breakthrough in ultrasound elastography was shear wave elastography, which allows quantitative measurements of stiffness rather than the qualitative strain measurements. Shear wave methods use the ARFI to create an internal tissue stress, which then creates a perpendicularly propagating shear wave. A method called point shear wave elastography induces a single ARFI at a single focal point, but a more common method is to induce multiple ARFI's along the axis of the transducer in rapid succession to create a 'mach cone' which then propagates a quasi-plane shear wave.

One of the most popular and first commercially available techniques to use shear wave elastography for quantitative modulus measurement is the supersonic shear imaging method (SSI) developed in 2004 by Bercoff et al[83] as an answer to the problems addressed above. In SSI, the ARFI, generates a Mach cone and a subsequent quasi-plane shear wave, which then propagates as two plane shear pressure waves roughly perpendicular to the initial pulse. This shear wave creates low intensity, lower frequency displacements that can be measured using ultrafast B-mode ultrasound imaging at speeds around 1000fps. The displacements are measured over time and used to compute the shear wave speed, which is then related to the elastic modulus assuming homogeneity, isotropy, infinite extent, and incompressibility using the equation:

$$E \approx 3\mu \approx 3\rho c_s^2$$

Equation 2.5-1

where μ is the shear modulus, ρ is the material density, and c_s is the shear wave speed of sound.

2.5.1.1 Validation

This approach to measuring soft tissue stiffness *in vivo* has been widely adopted in several fields, particularly where pathological tissue has been found to have different mechanical properties than healthy tissue. The primary application of SWE has been in diagnosis of soft tissue tumors, particularly breast[8485] and prostate[84] tumors and identifying liver fibrosis[84]. Many validations and studies of error sources have been performed for shear wave elastography due to the complexity of the method and the assumptions involved.

Many external and internal factors can also influence the ability of SWE to obtain quantitative, objective measurements of internal tissue mechanics, including the incident angle of the transducer on the skin, striations and anisotropy in soft tissue, thin layers of tissue acting as acoustic wave guides, pre-stress, and more. The plantar soft tissue encompasses areas of primarily adipose tissue, which can be generally assumed isotropic, muscle, which is strongly anisotropic, thin layers of skin, tendons, and the thick aponeurosis. Additionally, the plantar surface is non-planar, with the curved geometry of the heel, arch, and cushions at the metatarsal heads and distal phalanges, making a consistent isonification angle difficult, and the plantar soft tissue undergoes cycles of extreme stress and deformation. Therefore, all of these considerations are applicable to study of the plantar soft tissue.

The effect of pre-stress on shear wave speed has been studied and a theoretical model described to calculate the change in shear wave speed with applied stress in soft solids. Building on prior work establishing a general energy density equation[86] and separating the compressible and shear components thereof[87,88], Gennison et. al developed the acoustoelasticity equation for shear propagation perpendicular to the axis of applied force:

$$\rho {c_{sw}}^2 = \mu - \sigma \frac{A}{12\mu}$$

Equation 2.5-2

where ρ is the density of the material at zero stress, μ is the initial shear modulus at zero stress, σ is the applied stress, and A is a nonlinear constant from the third order elastic strain energy density equation developed by Landau[89].

2.5.2 Measurements in plantar soft tissue

Recently, ultrasound elastography gained popularity in biomechanical analysis of muscle, tendon, and soft tissues. However, soft tissues have demonstrated viscoelasticity and strain rate dependence. Therefore, correlations and validations of low strain, low strain rate mechanical testing of soft tissues and shear wave elastography may not translate to high strain, high strain rate soft tissue applications such as muscle contraction, tendon tension, and plantar soft tissue deformation during gait.

Both strain elastography and shear wave elastography have been used to measure the relative and quantitative stiffness of the plantar soft tissues in various pathologies. One study showed that introducing strain elastography stiffness standardized relative to a gel standoff pad into a model of ulcer prediction based on systemic parameters and comorbidities improved the model's sensitivity, specificity, prediction accuracy, and strength[90]. The same group later showed using the acoustoelasticity relationship that the elastic modulus and nonlinear parameters calculated using SWE in the subcalcaneal tissue are linearly related to those determined with finite element analysis, though they are not the same[91]. A different group showed that stiffness decreased with depth in the subcalcaneal tissue, though this result may be confounded by attenuation of signal[92]. SWE has also been used to evaluate age-related changes in stiffness and estimate material properties for finite element modeling of subcalcaneal tissue strain[93]. While SWE is becoming more popular for measuring stiffness of musculoskeletal tissues, including the plantar soft tissue, there are still questions about its accuracy and utility for predicting and preventing diabetic ulcers.

2.6 Three-dimensional ultrasonography

One drawback of prior work using ultrasound is its planar nature. Ultrasound systems typically use linear or sector transducers which are composed on one line of piezoelectric elements that produce mechanical vibrations at ultrasonic frequencies. Transducers are limited to one line of piezo elements in part due to the complexity of controlling a large number of elements electronically and the high volume of data that must be processed for each element, and in part due to the difficulty of controlling for the complex interference patterns of a matrix of elements. While matrix array transducers to exist to image three dimensional ultrasound in real time, they are limited to a small (1cm x 1cm) window. An alternative way to obtain a three-dimensional ultrasound is to mechanically sweep a linear array across a volume, either along a prescribed path or with some motion tracking system to re-align the planar images into a volume[94]. This technique is more widely available in commercial volumetric probes, though these probes also have a relatively small volume. In research, the swept volume three-dimensional ultrasound has been investigated for breast diagnostics as an alternative to mammography and freehand planar ultrasound, with high success[95,96]. In musculoskeletal applications, there has been some work to use ultrasound translated radially around the residual limb of amputees for prosthetic design[97,98], and freehand tracked ultrasound to study changes in muscle volume with age[99,100] and cerebral palsy[94,101].

However, while some have constructed ultrasound loading platforms[102–104] for plantar soft tissue, none have yet attempted to create an ultrasound-based tomographic map of the plantar soft tissue. Additionally, no known studies have looked at three-dimensional shear wave elastography in the plantar soft tissue.

2.7 Conclusion

While there have been numerous investigations into the basis of ulceration in the foot affected by diabetes, there is no consensus on how ulcers form nor how best to prevent them. The mechanical properties of the plantar soft tissue have been shown to change with diabetes and to differ by location in *ex vivo* materials tests as well as *in vivo* structural tests. Additionally, the microstructure of the plantar and other soft tissues has demonstrated minor changes with diabetes. Based on hypotheses of mechanical initiation, a thorough mechanical analysis of the plantar soft tissue is needed, but difficult to perform due to the inherent difficulty of *in vivo* measurements and limitations of imaging methods.

Shear wave elastography presents an attractive method to measure the plantar soft tissue stiffness of the intact foot *in vivo* and allow comprehensive analysis. Though it is limited to a single plantar image while the foot is a complex three dimensional structure. A method to measure the three-dimensional structure and stiffness of the plantar soft tissue and identify abnormalities within that image may improve clinical ability to identify and prevent an ulcer.

Since there have been few microstructural investigations of the plantar soft tissue specifically and changes therein with diabetes, there are still gaps in knowledge about the microstructure of the plantar soft tissue. In particular, the size of adipose chambers have yet to be quantified despite being considered the primary load-dissipating structure of the plantar soft tissue.

3 Comparison of texture-based classification and deep learning for plantar soft tissue histology segmentation

Published, Computers in Biology and Medicine, Volume 134, July 2021. Reproduced under Elsevier authors rights permissions.

3.1 Abstract

Histomorphological measurements can be used to identify microstructural changes related to disease pathomechanics, in particular, plantar soft tissue changes with diabetes. However, these measurements are time-consuming and susceptible to sampling and human measurement error. We investigated two approaches to automate segmentation of plantar soft tissue stained with modified Hart's stain for elastin with the eventual goal of subsequent morphological analysis. The first approach used multiple texture- and color-based features with tile-wise classification. The second approach used a convolutional neural network modified from the U-Net architecture with fewer channel dimensions and additional downsampling steps. A hybrid color and texture feature, Fourier reduced histogram of uniform improved opponent color local binary patterns (f-IOCLBP), yielded the best feature-based segmentation, but still performed 3.6% worse on average than the modified U-Net. The texture-based method was sensitive to changes in illumination and stain intensity, and segmentation errors were often in large regions of single tissues or at tissue boundaries. The U-Net was able to segment small, few-pixel tissue boundaries, and errors were often trivial to clean up with post-processing. A U-Net approach outperforms hand-crafted features for segmentation of plantar soft tissue stained with modified Hart's stain for elastin.

3.2 Introduction

Diabetes remains a pervasive problem, affecting an estimated 10.5% of the US population in 2018[1]. Diabetes is associated with several comorbid complications including vasculopathy, retinopathy, peripheral neuropathy, and pedal ulcers. These ulcers precede 84% of lower extremity amputations in patients with diabetes [105], and lower extremity amputation rates have been increasing in recent years [106].

Many diabetic ulcers occur on the plantar aspect of the foot, in the plantar soft tissue, which serves a complex biomechanical role. The plantar soft tissue dissipates large compressive loads during locomotion, a function likely either enhanced or enabled by the tissue's microstructure[12,107]. Increased shear loads have been correlated to disease-independent pressure ulcers[108] but remain an unproven hypothesis in the initiation of diabetes-related plantar ulcers[109], in part due to the difficulty measuring shear loads *in vivo* and at rates comparable to activities of daily living.

Changes in the plantar soft tissue microstructure could indicate changes in resistance to shear loads. Histological sectioning, staining, and analysis are used to identify microstructural changes related to disease. Previously, histomorphological analysis has been used to identify changes in tissue microstructure and tissue fiber content related to diabetes[55,110]. However, these studies are limited by a small sample size. Due to the scale and expertise involved, histomorphological analyses can be time-consuming and require careful attention to sampling and sectioning to avoid bias in measurements, often leading to small sample sizes. Analogous constraints have led to an increase in research on computational aids for pathology, including hand-crafted image processing and deep neural network approaches to aid pathologists with tasks such as locating cancerous cells in breast tissue [111] and segmenting glands in colon histology slides [112]. Similar techniques could also aid biomechanics research efforts by allowing higher-throughput analyses and enabling whole slide analyses.

Our work aims to address this gap between computer-aided pathology methods and microstructural analysis to address biomechanical questions. Biomechanical analyses have been slower to take up automated processing methods, and as in many other biomedical fields, human-interpretable methods like feature-based classification are often preferred due to the potential impact on clinical care. Therefore, we explore both popular feature-based machine learning methods as well as deep learning in order to provide a baseline for future work in this area. We expand and apply the texture-based classification framework of [113] and modify the popular medical image segmentation U-Net[77] deep neural network to the novel task of segmenting the plantar soft tissue stained with modified Hart's stain for elastin for subsequent morphological analysis. Our work contributes a baseline of common automated machine learning methods for a tissue, pathology, stain, and future application where these methods have yet to be explored.

3.3 Prior work

The automation of histology and pathology processes has unique challenges, such as the large size of images, difficulty manually labelling training images leading to a small training pool, dense images with information at multiple magnification levels, texture-like appearance with various rotations and organizations, and random variations in color and tissue appearance[114]. These challenges have been addressed in a variety of ways, including both hand-crafted classification frameworks and deep learning approaches.

3.3.1 Texture and color features in histology classification and segmentation

Texture features have been used in a variety of histological tasks, including prognostic prediction in urothelial carcinoma [115], breast cancer identification [116,117], and Gleason grading of prostate cancer [118,119]. An 8-class colorectal cancer tissue classification of histology images used a framework of multiple texture descriptors and classifiers, and performance improved when features were combined into a multi-feature set[113]. This study further segmented larger images using patch-wise classification, though the segmentation was not assessed quantitatively. While this framework achieved promising results, the texture features used gray-scale images, discarding valuable tissue discriminability provided by targeted histology staining. Additionally, while combined feature sets were investigated, the size of the feature sets was not addressed.

Some studies attempt to control for color by using deconvolution, which separates out the main colors associated with a histological stain, or normalization, which attempts to normalize the coloring throughout a dataset. However, Binaconi et. al found such preprocessing to have little effect on classification for histology images[120]. Several works attempt to address the issue of color by incorporating color into texture descriptors directly, either by adding color to existing texture descriptors[117,121] or designing novel texture descriptors with color in mind[118,122]. Local binary patterns have been a common target for color incorporation, including soft quantized color LBP[123], Hue-LBP[122], and multi-color space LBP[121]. An Improved Opponent Color LBP (IOCLBP) uses point-to-average rather than point-to-point thresholding, to compare both within-channel and between channel local neighborhoods[120]. IOCLBP was evaluated over both generic and histological image datasets, and performed on-par with or better than CNN-extracted features for classifying histological images.

Color space transformations are another approach for leveraging color information. Digital whole slide images are typically stored the red, green, and blue primary color space, but transformation to Luminance-chrominance spaces like YIQ (luma, in-phase, quadrature), YCbCr (luma, blue-difference, red-difference), and CIE L*a*b (brightness, green-red, blue-yellow), or to perceptual spaces like HSV (hue, saturation, value) may transform the image information into a more separable form for classification. DiRuberto et. al. adapted gray level run-length and difference matrices to color images in five color spaces and used these features to classify multiple histology databases[124]. The most performant color space transformation was HSV. In looking at non-histological texture images, Porebski et. al. suggested from a review of color spaces used with texture descriptors that the best color space for texture descriptor depends on the application, and further investigated combinations of features from different color spaces with a feature selection scheme[121]. The result of this investigation suggested that combining features from different color spaces was beneficial, and that reducing the feature set size by selection further improved performance.

This improvement by feature selection may indicate that some color feature sets become too large for the training data. Bolstering the case for feature selection, Bouatmane et. al. used sequential wrapper methods to reduce gray-scale texture features and significantly improve classification of tissues in prostate biopsy images using a k-nearest neighbors classifier[125].

There are a large number of possible frameworks that use texture and color for histology patch classification. Due to the relatively large number of features and classifiers in the Kather et. al framework, their popularity, and their interpretability, we chose this framework for a first investigation into segmenting plantar soft tissue histology images stained with modified Hart's stain for elastin. We additionally chose to incorporate simple color information, feature selection, and additional classifiers in order to investigate the importance of color and feature set size for the task.

3.3.2 Deep Neural Networks

Despite advances in hand-crafted feature sets and machine learning methods for the specific tasks of histology classification, deep learning approaches often outperform hand tuned approaches[119,126,127].

Deep neural networks have also been designed directly for the task of segmentation, removing the time consuming intermediate step of applying the classification to small, often rectangular patches of the image. In particular, the U-Net encoder-decoder architecture with skip connections[77] is commonly used for medical image segmentation and has been adapted for many tasks. The original U-Net takes a 512 x 512 input through four convolution-max pool blocks and symmetric up-convolution-convolution blocks with skip connections, starting with 64 channels after the first convolution and doubling the channel dimension after each max pooling operation. This channel dimension increases the network capacity, but can lead to large networks based on the doubling convention. Several groups have found segmentation success while reducing the number of output channels. Oskal et. al. adapted this U-Net to have fewer convolution channels at each down-sampling layer by starting with 32 rather than 64 channels to reduce network size in an epidermis segmentation task[128]. Similarly, Xiao et. al. reduced the initial channels to 16 on an epidermal segmentation task[129]. Reducing the channel size of the network allows more flexibility to increase the depth of the network or add additional connections while maintaining a reasonable size, training time, and inference time.

Increased depth and additional convolutions can increase the receptive field and include more contextual information in pixel-level class decisions. Additional connections between layers improves information sharing and alleviates issues of vanishing gradients or loss of information. Several of these architecture adaptations have been applied to U-Nets for histology tasks. Mavuduru used larger convolution kernels and additional convolutional layers to increase the effective receptive field and increase the number of trainable parameters[130]. Kalapahar included residual blocks to improve flow of information and promote complex relationship modeling for modest to significant performance improvements in a Gleason grading segmentation task[131]. Zeng replaced convolutions with residual and inception layers and added channel attention blocks to the down-sampling branch and an additional instance segmentation upsampling branch for moderate improvements[132]. Finally, Zhang2018 adapted the U-Net to incorporate more feature re-use and multi-scale information sharing by adding dense connections to the encoder and decoder as well as additional skip connections between them for an increase of 0.02 in the Dice coefficient[133].

Other recent efforts in biomedical image segmentation have incorporated newer deep learning techniques into the U-Net architecture such as deep supervision[134], residual attention gates[135], and spatial and channel attention [81]. Some have also moved away from the U-Net, for example, Bayesian deep learning[136] and multiscale networks based on classification networks backbones[137]. In contrast, Isensee automated selection of basic U-Net parameters like depth, channel size, batch size, and number of convolutions based on relationships with characteristics of the dataset, like image size[80]. These optimized U-Nets were able to achieve performance on par with the more complex state of the art for a variety of segmentation tasks across multiple 3-D imaging modalities. This success suggests that a basic U-Net structure, if correctly designed, can perform as well as more complex methods.

Considering the prior work increasing contextual and multi-resolution information and decreasing U-Net size, we increased the input image size, total number of convolutions, and number of down-sampling and up-sampling steps in the U-Net and decreased the channel dimension to balance the network size.

3.4 Methods

3.4.1 Texture and color features for histology multi-class tissue classification

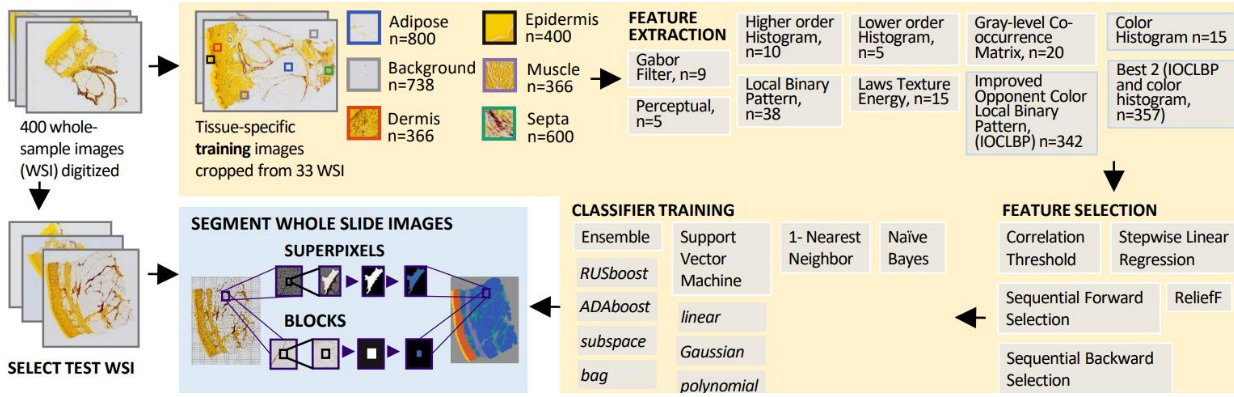

Figure 3-1: Texture-based framework. The yellow box outlines the training framework where single tissue patches are passed through texture- and color-based feature extractors, these features are reduced, and then used to train classifiers. Trained classifiers are then applied to selected test whole slide images (WSI) using either superpixels or square blocks to create a whole slide segmentation.

A texture- and color-based feature detection and classification framework was adapted from [113] (Figure 3-1). One additional texture feature, Laws' texture energy, was added to the six grayscale features previously included (Gabor filters, perceptual features, higher and lower order histograms, LBP, and gray level co-occurrence matrices (GLCM)), and two performant The specificity of Laws' texture energy measures[138] in identifying ripples, levels, edges, spots, and waves, compared to the more broad gray level co-occurrence matrices or LBP, is attractive for processing tissue structures both because these features are present in the tissues of interest (for example, septa are often wavy), and because they are easily interpretable. Vectors designed to identify the above mentioned features were convolved to form 5x5 pixel convolution kernels. These kernels were used to filter a mean-subtracted image, and the average intensity over all 5x5 neighborhoods of the filtered image for each of the 15 combinations of filters was used as a feature vector.

The LBP had the lowest classification rate in[113], followed by the lower-order histogram features. These two feature sets represent a range of texture description: the histogram features are global (within the image patch) and simple to compute, while the LBP is local, and more complex. Based on the prior accuracy on a multiclass histological task and the difference between these two features, they were selected for color adaptation. The lower-order histogram adaptation consisted of calculating mean, variance, skewness, kurtosis, and fifth central moment for each color channel, then concatenating into a single 15-feature vector. In addition to the native RGB color format, HSV, YIQ, YCbCr, and CIE L*a*b color spaces were investigated.

The LBP used in [113] is rotation invariant due to Fourier processing of binned uniform local binary patterns[139]. This feature was adapted to three color channels using the methods of the improved opponent color local binary pattern (IOCLBP) algorithm from [120], except all nine opponent-channel pairs were used. While similar pairs such as B-G and G-B are likely to be redundant, there is no way to assure that the best pair is chosen [121]. After computing the IOCLBP, the discrete Fourier transform of the histograms of uniform local binary patterns was then applied to each color channel combination to yield 342 rotation-invariant ’f-IOCLBP’ features.

Kather et. al. found the six grayscale texture features investigated to be unique and uncorrelated[113], prompting further investigation of the predictive power of combinations of features. Following that precedent, our two best features as assessed by training accuracy, the RGB f-IOCLBP and the YCbCr lower order histogram were combined into the 'best2' feature. This combination feature was subjected to the same additional feature selection as the individual features and an additional feature scaling as a single feature set.

Addition of color and combinations of features may introduce redundancy, and all extraction methods may yield nondescriptive features. In order to remove poorly-descriptive or repetitive features, a step was added to the architecture to allow investigation of five feature selection methods: correlation threshold, stepwise multilinear regression, ReliefF, sequential forward selection, and sequential backward selection. For the correlation threshold, the correlation of feature vectors and class labels was calculated for each feature vector and those features with an absolute correlation less than 0.5 were removed. This threshold was empirically set so that feature selection did not remove entire feature sets from consideration. For the stepwise multilinear regression, the tolerance for entering the model was set at the default $p<0.05$, the tolerance for removing features was set at $p=0.10$, and the number of model updates was limited to 50. The implementation of ReliefF [140] used 8 neighbors, all training examples for each update, and empirical prior probabilities. For both sequential forward selection methods, features were selected until the Cohen's Kappa coefficient no longer improved by more than 0.001 using a 10-fold cross validation.

Five classifiers were added to the four (1-nearest neighbor, linear and Gaussian kernel support vector machines (SVM), and RUSBoost-aggregated tree learners) investigated in Kather et. al[113]. First, polynomial kernels allow SVMs to model increasingly complex nonlinear functions. However, higher order polynomials may be prone to overfitting data. Therefore, a second order polynomial kernel was added to the SVM investigation in addition to the linear and Gaussian kernels previously investigated.

Second, ensembles of weak learners can be formed using many different aggregation algorithms. The RUSBoost used with tree learners in[113] alleviates issues of unequal class representation by sampling from larger classes the number of examples in the smallest class. However, removing training data from more variable classes may negatively impact the classification. ADABoost does not perform this subsampling. Boost algorithms create wide ensembles of shallow learners, while bagging methods create narrow ensembles of deep learners. ADABoost and bagging were investigated for alternate tree aggregation. Subspace aggregation uses random sampling without replacement. Because some of the feature detection methods output a large number of features and because there were a large number of training samples, the subspace method with quadratic discriminant weak learners was also investigated. All of these ensemble classification algorithms were implemented using options of built-in MATLAB functions.

Finally, the naïve Bayes classifier's linear temporal cost and scalability with number of features make it an attractive option for large problems. While the conditional independence assumption is often broken in real problems, the classifier generally still achieves good performance. A naïve Bayes classifier was implemented using built-in MATLAB functions assuming normal probability distributions for each class.

3.4.2 Modified U-Net

We made three main adaptations to the U-Net [77] architecture: increased input image height and width, increased downsampling layers, and decreased output channel size (Figure 3-2). The input image was increased from 512 x 512 to 576 x 576 to increase the amount of contextual information included in each input image. The size was chosen with sufficient factors of 2 to allow concatenation between skip connected layers without cropping, and padding on each convolutional layer was set so that only max pool operations changed height and width dimensions. The original four downsampling steps were increased to six steps to increase the effective receptive field for

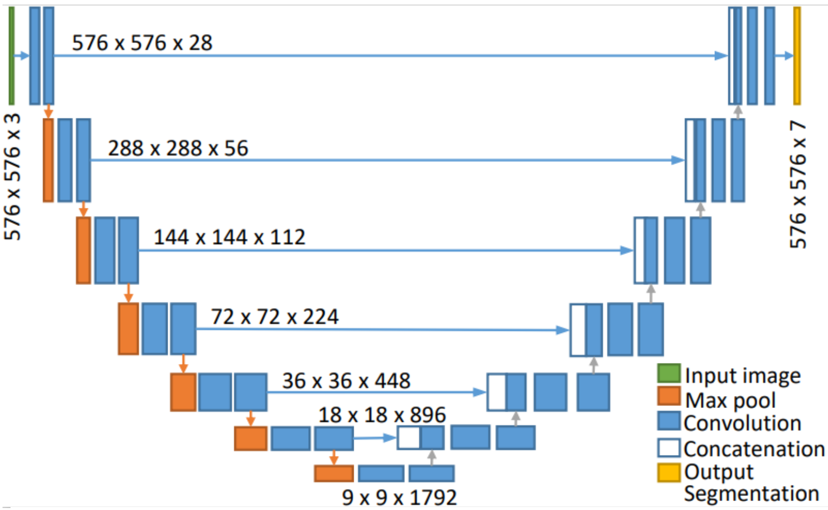

Figure 3-2: The modified U-Net takes color images of size 576 x 576 as input and follows the same convolution-max pool and upconvolution-convolution pattern as the original U-Net. The modified U-Net has six downsampling and upsampling steps, increased from four, to provide more contextual information to pixel level decisions.

each pixel decision. Skip connections were maintained between all symmetric downsampling and upsampling layers. Finally, the original 64 channels in the first convolutional layer were reduced in order to reduce the total size of the network to reduce computational time and memory use. The final channel dimension was selected empirically by testing increasing multiples of the number of classes (7) until the network had sufficient capacity. The final initial output size was 28 channels. Standard doubling of output channels after max pooling was maintained. All other parameters including kernel size and max pool strides were unchanged.

3.4.3 Whole slide segmentation

Whole slide images were too large to be processed in their entirety, so whole slide segmentation was performed on smaller patches. In the texture-based method of Kather et.al, whole slide images were segmented by classifying 15x15 pixel center tiles using information from a 45x45 pixel area, making a 30x30 pixel overlap. However, the septal walls in the plantar soft tissue can be as small as a few pixels in width, requiring a finer segmentation. Therefore, tile (center, overlap) sizes of 23 (2,21), 24 (4,20; 6,18), and 28 (3,25) were investigated. Additionally, many of the tissue boundaries were not rectangular or square, making them less amenable to a tile processing strategy and requiring smaller base tiles for a fine grained segmentation. Superpixels group pixels together based on features like color value and spatial location, allowing feature extraction from a larger group of more similar pixels. Therefore, superpixels [141] with target sizes of 500, 1500, 2500, 3500, and 4500 were also investigated.

Whole slide images were also too large to take as input into the U-Net network. Therefore, validation images were cropped into 576 x 576 tiles for processing and stitched into the final segmentation. Overlaps of 10, 20, 30, 40, and 50% were investigated for stitching. Images were stitched by summing overlapping regions per channel to create a probability map for the whole slide image for each class. Classes were then assigned by softmax scaling the probabilities to the range [0, 1] per pixel along the channel dimension and thresholding each probability map to create a per class segmentation.

The raw output of both the texture-based and U-Net segmentation included some errors that could be filtered by simple rules based on knowledge of the gross tissue structure. Therefore, a simple segmentation cleaning code was written to improve the accuracy based on prior knowledge, including:

1. Removing areas classified as dermis that were infiltrating the adipose chambers and muscle
2. Removing dermis, septa, epidermis, and adipose “speckles” below 300 pixels, an empirically chosen threshold.
3. Ensuring that the epidermis is contiguous
4. Filling holes in the dermis
5. Filling holes created by removing pixels with nearest neighbor approximations.

Each single class segmentation was subjected to morphological cleaning based on known tissue relationships and single class segmentations were merged to create a segmentation. Any pixels not assigned by this process were then assigned the mode of the six nearest neighbors by Euclidean distance.

3.4.4 Evaluation

The texture-based classifiers were evaluated for training accuracy on single tissue classes using basic classification accuracy and the more robust multi-class Mathews correlation coefficient (MMCC) [142]. Final whole slide image segmentations from both methods were evaluated using the Dice coefficient[143], defined as $2|X \cap Y| / (|X| + |Y|)$, as the Dice coefficient is a standard evaluation metric for medical image segmentation.

3.5 Data and Experiments

Plantar soft tissue specimens were obtained from nine fresh cadaveric feet (4 diabetic, 5 non-diabetic, age 61-79 years), sectioned, and prepared for histological analysis with modified Hart's stain for elastin using standard methods[110]. Digital whole-slide images (WSI) were obtained using a Nikon Eclipse i80 (Melville, New York, USA). Twelve WSI (n=4 diabetic, n=8 non-diabetic) were manually segmented using FIJI [144] by an experienced reviewer (Y-NW) into the six tissue classes of background, dermis, epidermis, adipose, muscle, and septa for ground truth labels.

To train the texture-based classifiers, 3372 single-tissue images (adipose = 800, background = 738, dermis = 366, epidermis = 400, muscle = 366, septa = 600) were manually cropped from 33 whole slide images without ground truth segmentations. Representative feature sets were created by applying the feature extraction algorithms on these images. These representative feature sets were then used as the input for feature selection algorithms. Both full and reduced feature sets were then used to train classifiers using 10-fold cross validation with a 90/10 data split. The best performing classifier-feature selection combination for each feature set was then applied to the 12 manually segmented images to determine segmentation accuracy. Training, selection, and segmentation were all performed using 4, 8, or 12 CPU cores.

To train the U-Net, seven of the twelve WSI with ground truth segmentations were augmented by random saturation, illumination, rotation, and elastic deformation and subsequently cropped into 576x576 pixel tiles for a total of 5307 tiles. Underrepresented classes (epidermis, muscle) were over sampled to alleviate class imbalance. Affine transforms introduced black pixels at image borders, which were assigned to a seventh class to avoid confusion with the desired classes. As the network had novel architecture, it was trained from scratch using Xavier initialization. The U-Net was trained for 12000 iterations using Adam optimization [145], an initial learning rate of 0.0002, a step-down multiplier of 0.92 every 300 iterations, and a batch size of 1 with 40-batch accumulation. Training was performed in caffe[146] on an NVIDIA Quadro GP100 (Santa Clara, CA, USA). One of the manually segmented images was sampled into 1113 images for the test pass of the network to test accuracy and generalizability. Training was stopped when the accuracy plateaued and the test loss diverged from the training loss. The remaining four images were used to validate the network and for comparison of whole slide image segmentation between the texture-based and U-Net methods.

3.6 Results

3.6.1 Texture--based Training

The combination feature best 2 achieved higher average classification accuracy and MMCC in the classifier training than any single feature (best 2: 0.949, 0.933). Hybrid color-texture features performed better than grayscale texture-only features (Figure 3-4).

The SVMs and 1-nearest neighbor were most performant, while the naïve Bayes and subspace ensemble classifiers were the least performant. Within SVMs, the Gaussian and polynomial kernels slightly outperformed the linear kernel on average. Within ensemble algorithms, ADABoost and bagging slightly outperformed the RUSBoost (Figure 3-3, Left).

Some feature selection provided modest improvements in the overall accuracy, while others reduced accuracy (Figure 3-3, Right). The correlation method yielded the lowest average MMCC (0.787), followed by ReliefF, while regression and sequential methods yielded the best MMCC (regression: 0.824, sfs: 0.826, sbs: 0.830). Sequential backward selection created the largest final feature sets on average (114 features), while sequential forward selection created the smallest feature sets on average (7 features). The size of feature vectors had no effect on accuracy.

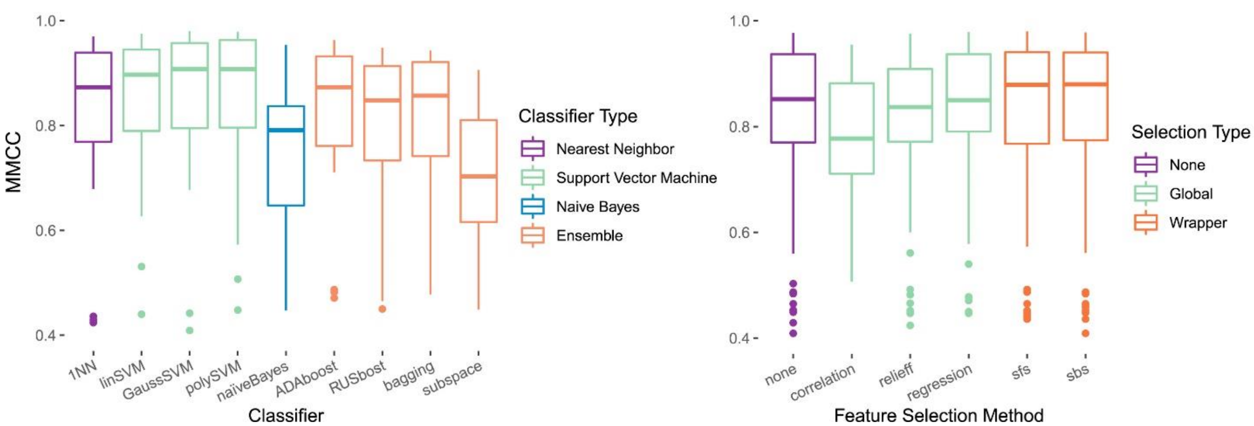

Figure 3-3: Results of classifier training. Visual outliers represent data outside 1.5*Interquartile Range but are included in reported means Left. Multiclass Mathews correlation coefficient by classifier. Regression and sequential methods provided modest improvements while correlation and ReliefF reduced accuracy compared to the non-reduced set. SVMs yield best performance, and of these, the polynomial kernel. ADABoost outperforms all other ensemble methods. Right. Multiclass Mathews correlation coefficient by selection method. Regression and sequential methods provided modest improvements while correlation and ReliefF reduced accuracy

3.6.2 WSI Segmentation

The morphological cleaning improved the texture-based segmentation Dice coefficient by 0.02 on average (0.691 raw vs 0.714 cleaned) and the U-Net segmentation by 0.003 on average (0.921 raw vs 0.924 clean, Figure 3-5). However, this improvement was not equally distributed among classes (Figure 3-6). Morphological cleaning improved segmentation accuracy of background, epidermis, muscle, and septa but decreased accuracy of dermis and adipose for the U-Net, while for the texture-based segmentation, accuracy of background, dermis, epidermis, and adipose increased and muscle and septa performance suffered.

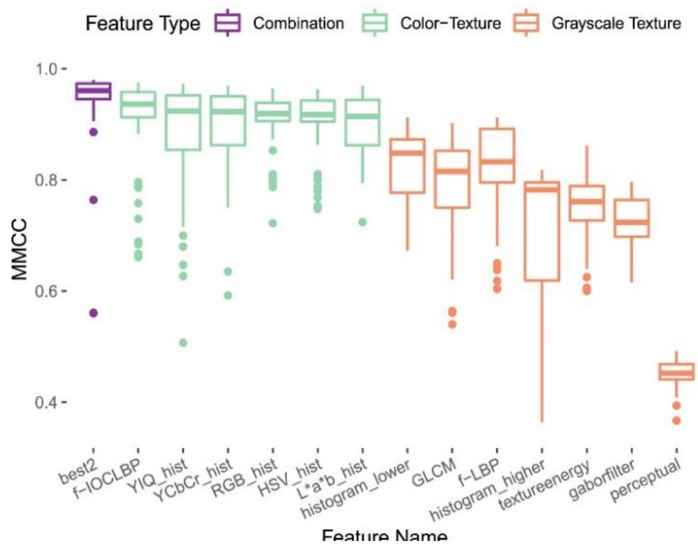

Figure 3-4: Results of classifier training. Combination features perform best, followed by color-texture hybrid features. Grayscale texture

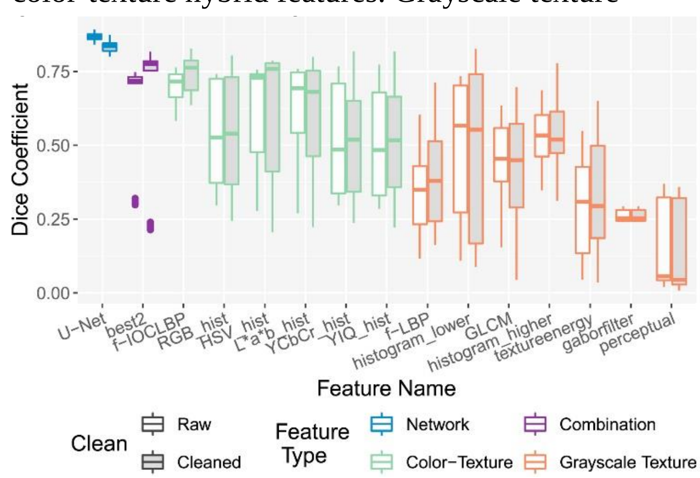

Figure 3-5: Whole Slide Image Segmentation. The U-Net outperforms all of the texture-based methods. Cleaning generally improves performance for all methods. In the whole slide image segmentation, the single-feature f-IOC outperforms the combination feature best 2, in contrast to training results. Visual outliers represent data outside 1.5*Interquartile Range, but are included in reported means.

3.6.2.1 Texture-based

In contrast to training accuracy, the f-IOCLBP performed best for all but one of the images tested, while the combination best 2 feature was the second most accurate.

For the majority of images tested, the block processing approach yielded higher Dice coefficients than the superpixel approach (median: 0.754 block, 0.705 superpixel). This effect was large in some features (perceptual) and small in others (f-IOCLBP). However, the most performant block size was inconsistent. Within the block-processing strategy, only texture energy and grayscale f-lbp accuracy varied with block size. However, the poorer performance of smaller superpixel sizes was consistent across most features.

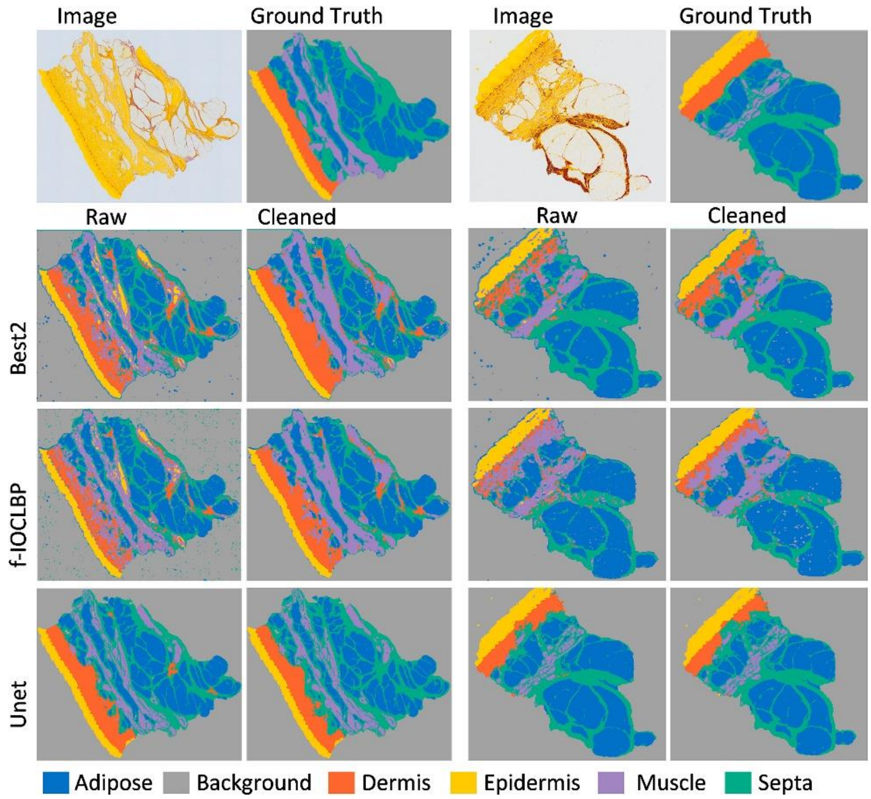

Figure 3-6: Effect of morphological cleaning. Cleaning corrects misclassification of background, dermis, epidermis, and adipose in the texture-based segmentations (best 2 and f-IOCLBP) at the expense of septa and muscle. Cleaning corrects misclassification of background, epidermis, muscle and septa for the U-Net at the expense of dermis and adipose.

Segmentation errors tended to occur in large areas, sometimes with entire sections of tissue misclassified as another tissue. In the cases where errors were small, they were often concentrated at boundaries between tissues. Muscle-epidermis, muscle-dermis, and dermis-septa were common misclassifications. Images with visible illumination differences from the norm had more severe segmentation errors.

3.6.2.2 U-Net

The U-Net segmentation performed well on background, dermis, epidermis, adipose and septa, but performed poorly on muscle. The stitching overlap size did not have a major effect on the dice coefficient. On average, the Dice coefficient for the raw output of the network was 2.1% higher than the raw output of the most accurate texture-based method (0.875 vs 0.857), and the Dice coefficient for the cleaned U-Net output was 3.6% higher than the most accurate cleaned texture-based output (0.912 vs 0.880). However, while the gross accuracy was moderately improved, the types of errors commonly seen in the U-Net output were different than those seen in the texture-based output. The U-Net had fewer gross misclassifications and clearer tissue boundaries. The U-Net was robust to changes in illumination and stain intensity (Figure 3-7).

3.7 Discussion

A modified U-Net segments plantar soft tissue histology whole slide images better than a texture-based feature extraction and classification framework for a secondary morphology task (Figure 3-5). Within a texture-based framework, color-texture hybrid features and combinations of color-texture hybrid features create better segmentations than features without color information (Figure 3-5). SVMs perform better on a classification task with texture-and color-based features than naïve Bayes, 1-NN, or ensembles of learners, and polynomial and Gaussian kernels perform better than linear kernels (Figure 3-3, Left). Intelligent selection of features using wrapper and global methods does not significantly improve patch classification performance (Figure 3-3, Right).

While segmentation is a prerequisite for many image processing tasks, evaluation metrics rarely reflect subjective evaluation of segmentation performance. These evaluation metrics yield single scores that are useful for ranking algorithms but fail to capture segmentation errors that affect secondary morphological analysis, which depends on accurate tissue boundaries. In the case of a secondary quantitative histology task, the types of segmentation errors may be more informative than the overall accuracy as measured by the Dice coefficient. Some metrics attempt to emphasize important tissue boundary information. The boundary F-1[147] calculates the popular F-1 score only for pixels within some distance of the ground truth tissue boundary, while the Berkeley contour matching score [148] calculates the distance between the segmented and ground truth boundaries. However, these metrics may still only be loosely correlated with human perception of segmentation quality[147]. Multiple quantitative scores or task-specific scores, such as difference between measurements made on automated segmentation and ground truth segmentation of the same images, may provide better estimates of segmentation quality.

Of particular interest for a secondary morphology task in the plantar soft tissue, the U-Net segmentation accurately the segments small, few-pixel septal walls separating adipose chambers (Figure 3-7, A zoom and C zoom). These chambers are hypothesized to be the main load-dissipating structure in the plantar soft tissue[12] and thus are of interest when looking for microstructural changes that may contribute to mechanical disparities in the diabetic foot. These septal walls are particularly tedious to segment by hand, making an automated method capable of segmenting these walls particularly useful. These small septal boundaries, being only a few pixels wide, could be mistaken for the boundaries of the adipocytes contained by the chamber, making them difficult to identify with a texture-based method. A different type of hand crafted feature could augment the texture-based features to more effectively segment the chambers. For example, a blob detector like MSER[149150] might be able to better identify the relatively blob-like chambers at a macro-scale and if combined with the micro-scale IOCLBP, might better refine the hand-crafted segmentation.

The U-Net's superior performance at small tissue boundaries can also be seen in the segmentation of muscle. The U-Net often picks up septal separation between muscle bundles that are not explicitly segmented in the ground truth image (Figure 3-7, A zoom). This delineation may be informative if the muscle quality differs between diabetic and non-diabetic specimens, as muscle quality may have an effect on the ability of the foot to exert and respond to loading. However, these additional separation boundaries in muscle may be influenced by tissue sectioning and fixation, so care must be taken to differentiate segmentation results within the context of histological expertise.

The usefulness of these septal boundaries within muscle regions is dampened by the tendency for the U-Net to make classification errors in muscle regions. Despite similar under-representation of muscle and epidermis in the training data due to lower relative native representation of these tissues and their similar color under the modified Hart's stain for elastin, the U-Net consistently performs better on epidermis than on muscle. One reason for this discrepancy may be more reliable structural information and clearer boundaries around the epidermis. The epidermal tissue is always flanked by background, an easy to segment and well-represented class, and the papillary dermal-epidermal junction. In contrast, muscle is often surrounded by variable mixtures of septal walls, adipose tissue, and dermis, and is more integrated into surrounding tissues, without a consistently defined border.

The muscle is most often misclassified as septa or dermis, suggesting that structure or context is the driving force behind the misclassification. Including better contextual information through multi-scale approaches[137,151,152] could reduce this type of error by incorporating more of the regular macro-scale structural patterns, such as muscle typically appearing between two layers of adipose or dermis being contiguous and adjacent to epidermis. Alternatively, a custom loss function that specifically penalizes these errors or a fuzzy classification levels approach like that used in [153] might provide better discrimination at these boundaries. It is also possible that the U-Net

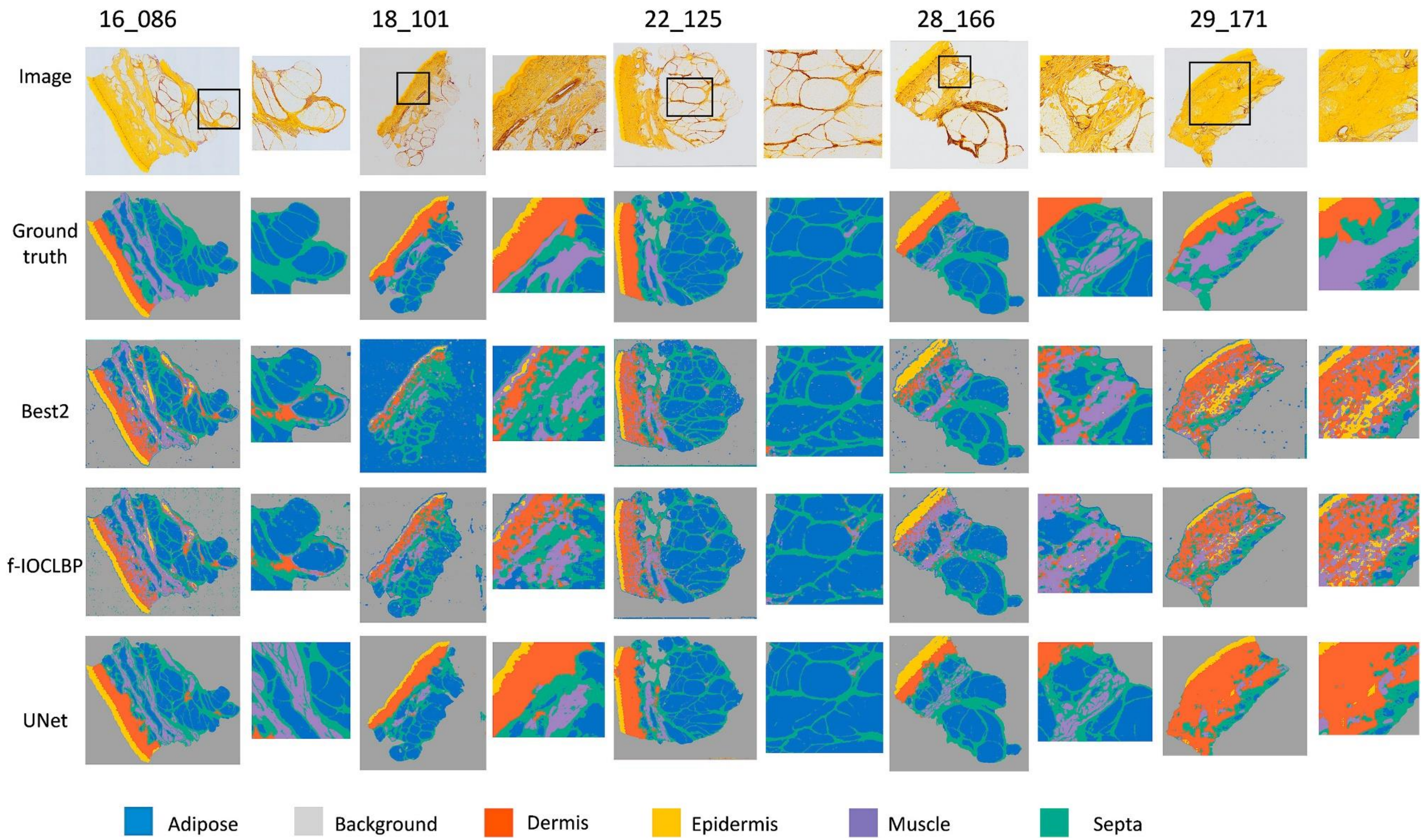

Figure 3-7 Comparison of best feature-based and U-Net segmentations after post-processing cleaning on all test images. Whole slide gross segmentation accuracy is shown in the whole slide images and individual tissue classification discrepancies are shown in the higher magnification extracted patches. A) (zoom) shows variations in muscle, thin septal walls separating adipose chambers, and dermis-muscle misclassification. B) (zoom) shows variations in septal walls and muscle misclassification, C) (zoom) shows variation in presence of thin septal walls, D) (zoom) shows variation in muscle segmentation, and E zoom shows muscle misclassification. Note that B) is darker than the other test images, causing the best 2 classifier to misclassify the background as adipose.

parameters we chose does not have the optimal architectural or training hyperparameters. A semi-automated method of choosing these model parameters such as the nnU-Net [80] may find a basic model that better handles the few misclassifications seen in our U-Net.

In contrast to the U-Net, muscle in the texture-based methods was more often misclassified as epidermis. Both tissues stain a bright yellow, and the epidermis is smooth while the muscle texture can be irregular, making very large or very small scale texture differences the main distinguishing factor between the two tissues. Some of these errors can be corrected using known structural information in post-processing, however, this remains an area for improvement. Inclusion of more grayscale texture features designed to pick up larger or smaller scale textures or a training metric that emphasizes muscle-epidermis differentiation could improve the texture-based performance.

Interestingly, in contrast to [113], combining two different features did not improve the whole slide image segmentation accuracy as measured by the Dice coefficient, nor did it improve the qualitative quality of the segmentation. This non-intuitive result may be due to the relatively higher susceptibility of the lower order histogram features to variations in color, which can be high in histological images due to variations in brightness, sample thickness, stain intensity, and preparation artifacts like folded tissue[154]. An obvious example of this is in Figure 3-7, image B, where the best 2 feature misclassifies most of the background as adipose. However, the f-IOCLBP of the same image does not have the same problem. The lower overall brightness of image B may contribute to this misclassification in the histogram features. Images were not normalized or mean subtracted in this texture analysis, but such a preprocessing step could alleviate this kind of error.

Boosting algorithms like RUSBoost have been designed to improve performance for training data with an uneven class distribution. However, RUSBoost did not perform as well in classifying single tissue images during training as ADABoost, which uses all the data with no uneven class mitigation strategy. This surprising result may indicate that for the tissue classification task tested, additional data are more important than an even class distribution, or that reducing the dataset based on the smallest class simply removed too much data.

During training, we found that the U-Net network performs poorly on diabetic specimens if no diabetic specimens are included in the training set, suggesting that there is some fundamental difference between the two conditions that can be learned by the network. While deep convolutional network decisions are still difficult to interpret, some visualization or attention techniques could provide novel insight into which areas of the tissue differ with diabetes status and could be an avenue of future exploratory research.

While we present an extensive comparison of texture-based classification and deep neural networks for segmentation of plantar soft tissue, several aspects of this study limit broad inference of this work. First, there were a small number of manually segmented ground truth images available. Efforts were made to increase variability in the sample, such as selection of both diabetic and non-diabetic specimens, a visual variety of stain intensities, inclusion of different locations within the foot, and data augmentation including color and light enhancement and affine transforms. However, the network was trained with only 5 whole slide images, creating the potential for unintentional over-learning. Second, all histology slides were prepared and stained by a single researcher, and images were taken from a single digital microscope. Machine learning algorithms that are not exposed to a sufficient variety of staining and imaging conditions could be fooled by changes related to image preparation, leading to poor generalizability[120]. While data augmentation steps such as contrast, white balance, and brightness alterations can combat some of the issues associated with different digital microscopes, there may still be some features of the images that prevent effective segmentation on images prepared on different equipment or by different researchers. In the texture-based framework, images were not pre-processed using mean-subtraction or histogram normalization, which may have contributed to poor segmentation performance on images that had lower overall illumination like image B. Such pre-processing may have changed the relative performance of texture-based features, but it is unlikely to have improved the texture-based framework to be on par with the neural network.

This work presents a foundation for developing an automated segmentation pathway for plantar soft tissue stained with modified Hart's stain for elastin. In expanding the texture-based framework to include color, feature selection, and additional classifiers, we found that color information improves performance in tissue classification tasks in histology and SVM classifiers perform better than naïve Bayes, nearest neighbors, and ensembles of learners, but surprisingly, found no effect of feature selection. These results emphasize the importance of choosing a feature set that includes both color and texture for histology. However, we also add to the growing body of literature suggesting that deep neural networks perform better for segmentation than approaches using hand-crafted features and classification. Our U-Net incorporates a larger input image and more downsampling steps to increase the receptive field and contextual information incorporated into pixel level decisions and uses a reduced output channel size to manage the network size. While the U-Net output still required some cleaning in order to be used as a pre-processing step for subsequent automated histomorphological analysis, this technique can obtain sufficiently accurate segmentations to aid and expand future microstructural and biomechanical investigations.

3.8 Graphical Abstract

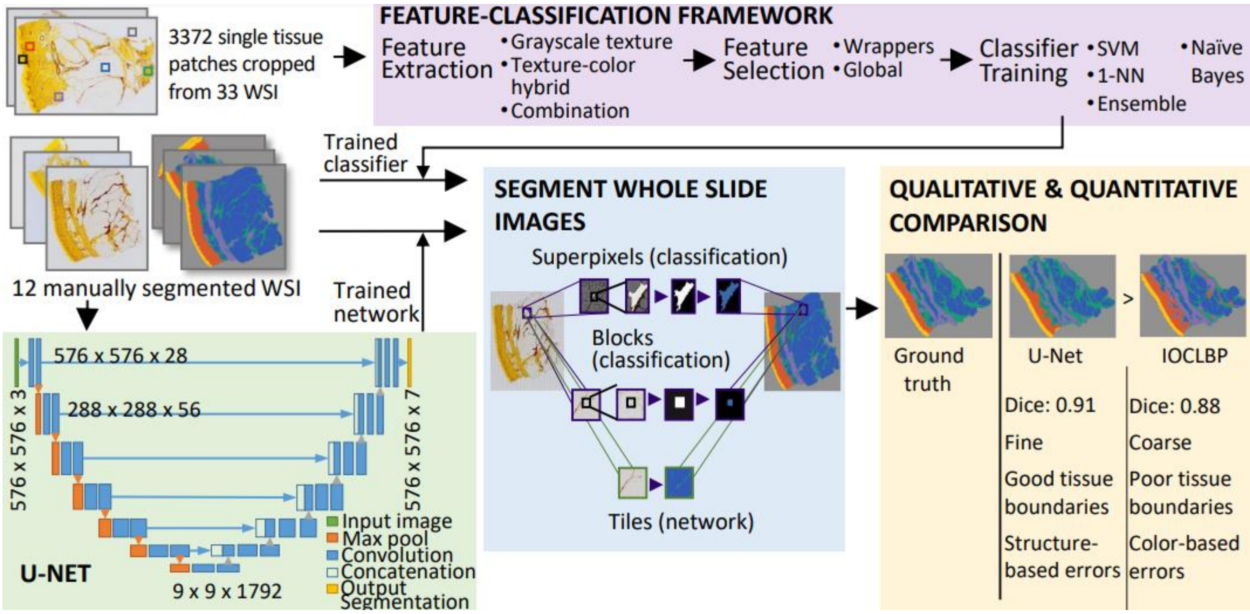

3372 single tissue patches cropped from 33 WSI
FEATURE-CLASSIFICATION FRAMEWORK
Feature Extraction
•Grayscale texture
•Texture-color hybrid
•Combination
Feature Selection
•Wrappers
•Global
Classifier Training
•SVM
•1-NN
•Ensemble
•Naïve Bayes
Trained classifier
12 manually segmented WSI
Trained network
SEGMENT WHOLE SLIDE IMAGES
Superpixels (classification)
Blocks (classification)
Tiles (network)
QUALITATIVE & QUANTITATIVE COMPARISON
Ground truth
U-Net
IOCLBP
Dice: 0.91
Fine
Good tissue boundaries
Structure-based errors
Dice: 0.88
Coarse
Poor tissue boundaries
Color-based errors
576 x 576 x 28
288 x 288 x 56
576 x 576 x 3
576 x 576 x 7
9 x 9 x 1792
Input image
Max pool
Convolution
Concatenation
Output Segmentation
U-NET

4 The effect of diabetes and tissue depth on adipose chamber size and plantar soft tissue features

Published, The Foot, Volume 56, February 2023. Reproduced under authors rights permissions.

4.1 Abstract

Plantar ulceration is a serious complication of diabetes. However, the mechanism of injury in ulceration is still unclear, making preventative treatment difficult. Within the plantar soft tissue, there is a superficial layer of adipose containing ‘microchambers’ of adipocytes, and a deep layer with ‘macrochambers’. While these layers have been a benchmark for ultrasound mechanical studies[14,16,17,155], the chamber size has yet to be quantified in diabetic or non-diabetic tissue. Additionally, recent advances in interpretable computer-aided methods may help generate new hypotheses about differences in microstructure with disease status. Adipose chambers in the superficial and deep layers of diabetic and non-diabetic plantar soft tissue specimens were automatically segmented with a pre-trained UNet and area, perimeter, and minimum and maximum diameter were calculated using morphological techniques. The plantar soft tissue specimens were also classified as diabetic or non-diabetic using the Axial-Deeplab attention network. Adipose chambers were significantly larger in the deep chambers than the superficial, but the difference was significant only for non-diabetic specimens. The attention network was able to achieve 82% accuracy on validation, but the resolution of the attention was too coarse to identify meaningful features of interest for additional measurements. The size of adipose chambers in the plantar soft tissue may be a useful feature with which to contextualize mechanical changes in plantar soft tissue with diabetes. Attention networks are promising tools for classification, but additional care must be taken when designing networks for identifying novel features.

4.2 Introduction

Plantar ulcers are a severe complication of diabetes. These ulcers can be slow to heal and can become infected, sometimes requiring amputation. The mechanism of ulceration is not fully understood, and has been hypothesized to result from some change in mechanics[6,44], which then predisposes the tissue to injury during activities of daily living.

The plantar soft tissue, comprising the epidermis, dermis, a superficial adipose layer, a muscle layer, and a deep adipose layer, is uniquely structured to dissipate the high loads encountered during ambulation[12,107]. *In vivo* ultrasound studies have described the superficial layer of small chambers containing adipocytes and a deep layer of similar adipose chambers as "micro-chambers" and "macro-chambers", respectively, based on prior qualitative histological work[12,14,107]. This micro-chamber and macro-chamber distinction has carried over into additional work in plantar soft tissue mechanics[15,17]. However, the size of adipose chambers and the differences between these two layers have not been quantified in either diabetic or non-diabetic plantar soft tissue, nor has a difference in adipose chamber size been considered as a pathological change in diabetic foot mechanics.

Prior histological and biochemical study demonstrated increased septal wall thickness, increased elastin content, and frayed septal walls in diabetic tissue, and effects differed by plantar location[55,156]. Additionally, the skin has been found to be thicker in people with diabetes[24,110], and skin thickness again differs by location[24,55,157–159]. Attempts to quantify mechanical changes have found higher modulus in plantar soft tissue[22,23,35] and skin[24] affected by diabetes and increased energy loss in plantar soft tissue affected by diabetes[156,160,161]. However, previously measured microstructural changes have only weakly correlated with mechanical changes[24,56]. Adipose chambers may be an essential structural component of the plantar soft tissue, and changes to the size and shape of these chambers may lend insight into abnormal plantar soft tissue mechanics.

Manual techniques are the established standard for taking histological measurements. However, a growing body of literature attempts to automate clinical pathology measurements in order to keep up with growing medical demand, and these techniques may be extended to histomorphological research. Convolutional neural networks have shown promise in tasks of segmentation[81,137], disease classification[162–164], and even grading disease severity[165–167]. However, lack of interpretability is a barrier to clinical adoption of these methods. In response, methods to interpret network decisions have been developed. Class activation mapping (CAM)[168] assigns a weight to each feature map in a given convolutional layer based on class scores, and calculates a weighted sum of feature maps. The result is a single spatial heat map of feature importance for a given class on a given image. Typically, the layer used is the last convolutional layer in a classification network, as this layer has been shown to learn the most complex features[169]. Classic CAM requires a global average pooling layer in the classification network, and uses all activation values, making it less adaptable and susceptible to negative features. ScoreCAM[170] uses the change in class score associated with masking the input with an up sampled feature map instead of the weights from the global average pooling layer to remove dependence on the specific layer type as well as improve localization of objects and features.

Attention methods go beyond just providing interpretability by introducing a learned weight that is used to improve predictions by assigning more importance to discriminative spatial areas. This learned weight can then be used to identify areas the network learned to be important when performing a task. Classically, this attention weighting or mapping occurs between layers. Attention methods have succeeded in a diverse range of tasks including unsupervised[171] and weakly-supervised segmentation[172] and classification[173]. Self-attention allows connections between pixels within a sequence or image, capturing the context of the pixel within the image or sequence in contrast to the between-step transformational mapping of regular attention. Self-attention has been successful in sequence processing, however, the size of images makes self-attention computationally difficult. Histological images are larger still. The vision transformer performs self-attention on smaller image patches, making the attention operation tractable, but sacrificing longer-range connections. Long range connections are likely useful in histological images, where the structure of the whole slide is often essential context for understanding the tissue and microstructure of a specific region. The axial-deeplab network addresses computational issues by applying self-attention to rows and columns sequentially, reducing computation in a single step but allowing full-range attention in two steps. This network is therefore capable of modeling long-range dependencies.

Typically, interpretability methods confirm that the network is learning features known by prior medical research to predict disease. However, for more novel tasks, interpretable networks could rapidly advance knowledge by identifying novel features of interest. In order to better describe plantar soft tissue generally, and changes within the plantar soft tissue between diabetic and non-diabetic specimens, we performed quantitative measurements of the fat chambers. We also trained an attention classification network in order to identify novel network-derived features that may be of interest in quantifying changes with diabetes status.

4.3 Methods

4.3.1 Data

Plantar soft tissue specimens were obtained from nine fresh cadaveric feet (4 diabetic, 5 non-diabetic, age 61-79 years), from six distinct locations: the hallux, first, third, and fifth metatarsal, the lateral midfoot, and the calcaneus. Specimens were obtained using vertical uniform random sampling, fixed in paraffin, sectioned, and stained with Modified Hart's stain for elastin using previously described methods[55]. Samples were imaged using a Nikon Eclipse i80 (Melville, New York, USA) and digitized into whole-sample images (WSI) using a 12.6 megapixel digital camera (DXM-1200C, Nikon, Melville, NY). A total of 920 samples were digitized.

Table 4.3-1: Exclusion criteria

0	No issues
1	No clear muscle layer
2	No visible Dermis
3	Tissue folded over (tissue damage)
4	Glass/plating artifact (bubbles, bad seal, crack, too close to edge, etc)

4.3.2 Hand-crafted morphology

Four exclusion criteria (Table 4.3-1) were developed to ensure that the superficial and deep layers were separable and that measurements would be accurate in each included image. Superficial and deep adipose chambers are separated by a layer of muscle, called the *panniculus carnosus*. Therefore, the absence of a muscle layer was the first identified exclusion criterion. Similarly, the superficial adipose chamber is immediately adjacent to the dermis, while the deep adipose layer is adjacent to the muscle layer and often has no clear deep boundary as it is dissected away from the bone. Therefore, the dermal layer is necessary to identify which layer is superficial and which is deep, and the absence of a dermal layer was identified as a second exclusion criterion. During the sectioning and fixing process, some samples can be damaged, or plating artifacts such as bubbles or cracks can occur. These errors distort the geometry of the specimen and can occlude the specimen, making the measurements unreliable. Therefore, we introduced two additional exclusion criteria, to exclude specimens with obvious tissue damage due to folding over of the specimen on itself and specimens with obstructive plating artifacts. Specimens with tissue damage due to tearing were used, but adipose chambers adjacent to damage were removed, as described below.

Three independent raters rated each sample according to the criteria. A majority vote of 2/3 agree to include was used to determine which samples were appropriate to include in the morphology calculations. In addition to exclusion criteria, two samples taken from adjacent slices were placed on each slide for redundancy. Due to the slices being adjacent, they contained extremely similar information. Therefore, only one of each adjacent slice was used for morphology calculations. If both slices had at least 2/3 inclusion, the slice to be included was chosen at random. After exclusion criteria were applied, 323 images were included for morphological study.

In order to ensure repeatable measurement over the large dataset, we developed an automated segmentation and morphology calculation process. A U-Net [77] was previously trained on 7 manually-segmented images to automatically segment images into one of 5 tissue classes: epidermis, dermis, adipose, muscle, septa, or background (6 classes total; described in [174]). This UNet was used to automatically segment all 323 images included.

A binary mask of adipose chambers was created from the segmented image. These chambers were separated into superficial or deep groups by manual region selection using the muscle layer as the separation boundary. Any adipose chambers with an unclear placement were discarded from measurements. Additionally, any adipose chamber that was immediately adjacent to background was discarded from measurement, as an adipose chamber without a septal wall is likely to have

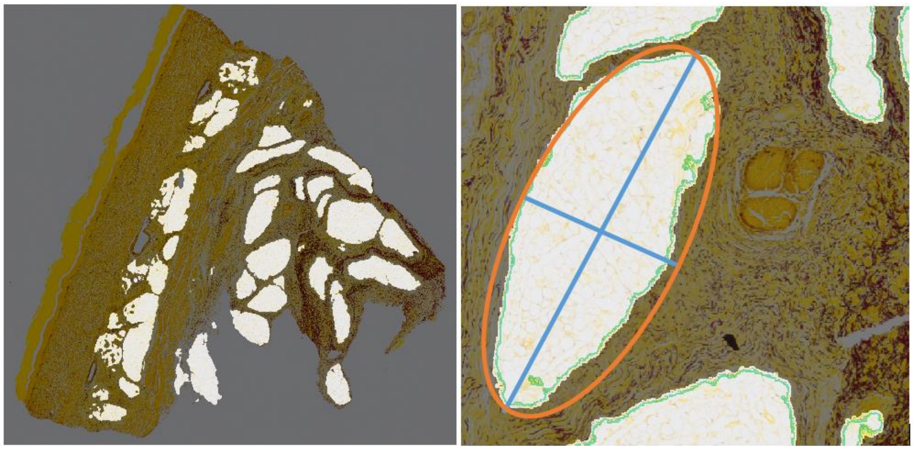

Figure 4-1: Description of morphological parameters. Adipose chambers were segmented with a UNet, then masks of the adipose chambers were created, and the area, minimum and maximum diameter, and perimeter were calculated.

incurred damage. The area, minimum diameter of the best-fit ellipse, maximum diameter of the best-fit ellipse, perimeter, and eccentricity were calculated for each adipose chamber using built-in MATLAB functions (Figure 4-1). As described later, a large number of subhallucal images were excluded for lack of a muscle layer. Due to this location bias, we performed an additional analysis calculating the adipose chamber areas for these samples without the superficial vs deep distinction.

4.3.3 Attention Network

In contrast to a strict morphological calculation, variability in data quality is useful for training a deep neural network. Therefore, only samples excluded by the error criterion of plate artifacts (excl4) were excluded from the dataset used to train the network. Additionally, both adjacent slices were used to train the network. In total, 911 images were used to train the attention network (262 diabetic, 556 non-diabetic, and 134, 128, 134, 102, 106, 226 slides per location, respectively). Full-resolution images were down sampled to 480x480 pixels due to GPU memory limitations.

A ResNet26 image classifier with Axial Deeplab attention was used to classify images as either diabetic or non-diabetic[175]. Briefly, this architecture uses column-wise and row-wise self-attention to identify important pixels for class decisions. The network was trained using Adam optimization[145], an initial learning rate of 0.008, step-down learning rate schedule, and a batch size of 8. The network was trained on a NVIDIA Quadro GP100 for 180 epochs. The snapshot at epoch 80 had the highest validation accuracy and was used for inference and visualization.

The ScoreCAM method[170] was used to visualize the final attention layer of the network. The attention map was upsampled using box resampling to the size of the input image, colorized, and overlaid on the input image to identify regions of interest.

4.3.4 Statistical Analysis

Linear mixed effects regression was used to test for an association between morphological measurement (the dependent variable) and diabetes status, plantar location, and adipose layer (the independent fixed effect covariates, evaluated in a single model). Random effects were modeled for the foot, plantar location, and specimen. Omnibus tests of associations between tissue measurement variable and each independent fixed effect variable were carried out using the likelihood ratio test. Estimated marginal means and standard errors (SE) by fixed effect factor were calculated across category for each fixed effect. To address size variable skewness which produced non-normal errors and variance heterogeneity, models of area, perimeter, maximum and minimum feret diameters (FDs) were carried out using logarithms, with estimated marginal means presented back transformed to the original units (unlogged units). Pairwise comparisons for these variables are presented as ratios. As eccentricity was strongly correlated with size, a second set of models was carried out with log area as an additional independent fixed effect covariate. Furthermore, as the distribution of eccentricity is bimodal, and thus non-normal, deviation in tissue shape from circularity was also assessed by analysis of the maximum/minimum FD ratio. In the mixed effects regression, this difference is modeled as the log(maximum Feret/minimum Feret), equivalent to the log(maximum FD) minus the log(minimum FD), with log(minimum FD) as an additional independent fixed effect covariate. Analyses were carried out using R 4.0.3[176], and packages lme4[177], emmeans[178] and tidyverse.

4.4 Results

4.4.1 Hand-crafted morphology

There was data from 13 feet (4 D and 9 ND), comprising 66 samples across 6 locations; 312 sections, resulting in 23,992 tissue chambers measured (Table 4.4-1). Adipose chambers that were not able to be classified as either superficial or deep due to the absence of a muscle layer were more common in the forefoot and less common in the hindfoot. Specimens from at least two donors per disease state remained for each location after exclusion criteria were applied.

		HA	*M1*	*M3*	*M5*	*LA*	*CA*
Foot	*D (of 4)*	4	4	3	3	2	4
	ND (of 9)	9	8	9	7	7	6
Deep chamber	*D*	128	270	117	156	340	848
	ND	420	539	496	533	1067	2204
Superficial chamber	*D*	162	147	71	113	149	570
	ND	351	772	448	636	977	2315
Unknown chamber (no muscle)	*D*	982	1067	155	152	0	194
	ND	1976	1666	1570	1083	810	508

Table 4.4-1 Counts of samples used (from 4 D and 9 ND donors) and chambers measured at each plantar location for each disease group and adipose layer.

The largest differences in size measures occurred between adipose chambers of the superficial and deep adipose layers, the latter of which were 26-66% larger deep chambers compared to superficial chambers ($p<0.001$). Differences in size measures by diabetes status were small and non-significant ($p\geq0.2$, Table 4.4-2). However, there were significant interaction effects between diabetes status and adipose layer (Table 4.4-3, $p\leq0.04$). When stratified by disease status, the difference in size between superficial and deep chambers was strong for non-diabetic specimens, but weak for diabetic specimens, with a general trend toward decreased size parameters in deep chambers of diabetic compared to non-diabetic specimens (ND 16% to 44% larger, $0.04 \le p \le 0.26$). Size measures varied with location (omnibus $p \le 0.02$), with the largest adipose chambers beneath the lateral midfoot and the smallest beneath the first metatarsal.

	D (n=6)	***N (n=11)***	***ND/D (log outcomes) or ND-D***		
	Mean ± SE	**Mean ± SE**	**Mean ± SE**	**95%CI**	**p**
Area	17182 ± 1916	19538 ± 1462	1.14 ± 0.15	(0.88, 1.48)	0.29
Perimeter	327 ± 19	345 ± 13	1.06 ± 0.07	(0.92, 1.21)	0.38
Max Feret Diameter	214 ± 13	233 ± 9	1.09 ± 0.08	(0.95, 1.25)	0.2
Min Feret Diameter	115 ± 6	121 ± 4	1.05 ± 0.07	(0.93, 1.19)	0.38
Max/Min Feret Diameter	1.86 ± 0.03	1.92 ± 0.02	1.03 ± 0.02	(0.99, 1.08)	0.1

Table 4.4-2 Morphological measurements by disease status. Outcomes back-transformed from logarithms.

		Deep	***Sup***	***Unk***	***Interaction p-value***	***Deep / Sup***	
		Mean ± SE	**Mean ± SE**	**Mean ± SE**		**Mean ± SE**	**95%CI, p**
Area	*D*	18695 ± 2576	16627 ± 2130	15615 ± 2049	0	1.12 ± 0.13	(0.84, 1.5), p=1
	ND	26954 ± 2428	14157 ± 1153	19785 ± 1632		1.9 ± 0.13	(1.61, 2.25), p=0
Perimeter	*D*	341 ± 24	320 ± 21	314 ± 21	0	1.06 ± 0.06	(0.92, 1.23), p=1
	ND	405 ± 19	291 ± 12	349 ± 15		1.39 ± 0.05	(1.28, 1.52), p=0
Max FD	*D*	221 ± 16	210 ± 14	205 ± 14	0	1.06 ± 0.06	(0.91, 1.23), p=1
	ND	277 ± 13	197 ± 8	233 ± 10		1.41 ± 0.05	(1.29, 1.54), p=0
Min FD	*D*	121 ± 8	114 ± 7	109 ± 7	0	1.06 ± 0.06	(0.92, 1.22), p=1
	ND	140 ± 6	104 ± 4	122 ± 5		1.34 ± 0.04	(1.24, 1.46), p=0
Max/Min	*D*	1.84 ± 0.04	1.86 ± 0.04	1.88 ± 0.04	0.004	0.99 ± 0.02	(0.95, 1.03), p=1
FD	*ND*	1.98 ± 0.03	1.9 ± 0.02	1.91 ± 0.02		1.04 ± 0.01	(1.02, 1.07), p=0

Table 4.4-3 Interaction of Adipose layer and diabetes status. D=diabetic, ND=non-diabetic. P-value is for the interaction of the two variables. Deep/Sup mean, SE, CI, p are the mean, standard error, confidence interval and p-value for the difference between deep and superficial chambers within diabetic or non-diabetic samples. Deep chambers are larger than superficial, but the difference is smaller in diabetic specimens; the interaction effect is significant.

4.4.2 Attention Network

The network achieved a peak of 82% accuracy on the validation set after 117 epochs. While the network achieved better than random accuracy, the interpretability methods used were not able to identify regions or features that would inform secondary calculations or lend insight into new areas that might be of interest. The ScoreCAM heatmap was too coarse to identify specific features of interest in the high-resolution images. The attention map from the Axial-Deeplab network showed that the network attended to primarily septal walls when making a classification decision (Figure 4-2). The network typically neglected to attend to the regions of adipocytes within the septal walls and occasionally attended to muscle or skin. Often, misclassified samples were not stained as darkly as correctly classified samples (Figure 4-3), and in many samples the network attended to only a few areas, and fewer areas than the correctly classified samples.

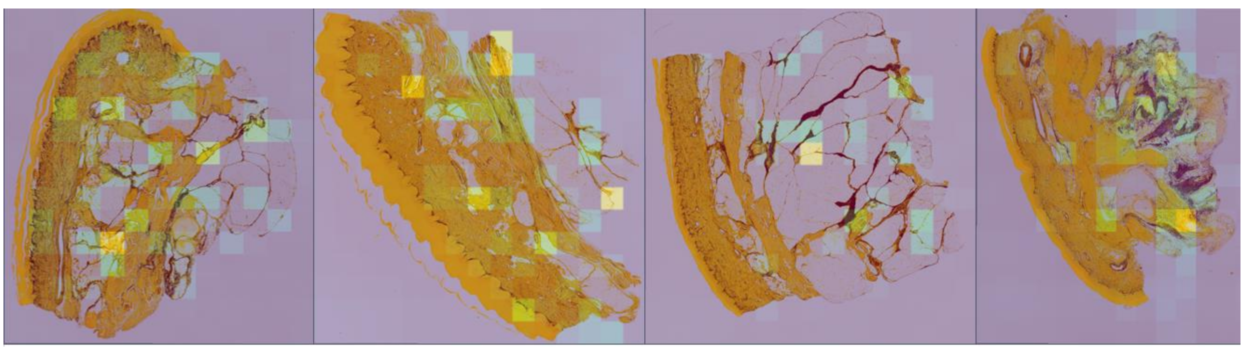

Figure 4-2: *Correctly classified example images with attention outputs overlaid (left to right: non-diabetic, non-diabetic, non-diabetic, diabetic). The network attended to septal walls, and occasionally muscle or skin.*

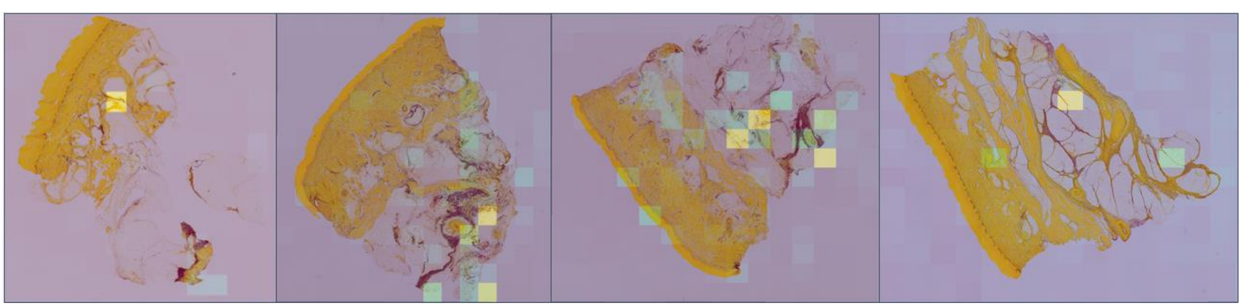

Figure 4-3: *Misclassified example images with attention outputs overlaid (left to right: diabetic, non-diabetic, non-diabetic, diabetic). Compared to correctly classified samples, these samples have less contrast (lighter staining) and the network attends to fewer areas.*

4.5 Discussion

Prior work has used the terms “micro-chambers” and “macro-chambers” to describe the chambers of adipocytes contained in septal walls that make up the bulk of the plantar adipose tissue[14–16] based on qualitative descriptions. We found that the adipose chambers in the deep layer had 66% larger area, 31% and 26% larger maximum and minimum diameter, and 30% larger perimeter than those in the superficial layer on average (Table 4.4-3), confirming the informal naming convention.

However, the difference in chamber size between the superficial and deep chambers was not significant in diabetic specimens when stratified by disease status. Non-diabetic chambers were 34% to 90% larger in the deep adipose layer compared to the superficial across size parameters, while diabetic chambers demonstrated a 6-12% difference (Table 4.4-3). The evidence for smaller deep diabetic chambers was stronger than the evidence for larger superficial diabetic chambers. Smaller adipose chambers in diabetic specimens is also consistent with prior work that found that the septal walls separating adipose chambers are thicker and frayed in diabetic specimens[55]. Smaller adipose chambers in the deep layer of adipose tissue may reduce the ability of the plantar soft tissue to dissipate load. Prior work using a subset of the same specimens found that diabetic plantar soft tissue has a higher elastic modulus in both compression[22] and shear[23], and that diabetic tissue has a higher magnitude relaxation modulus[179]. However, associations between these mechanical results and previously measured histological properties were weak. Adipose chamber size could account for some of these differences.

Adipose chamber morphology also varied by location under the foot. Ulcers are most common at the forefoot but still occur at the hindfoot[50,51]. However, the forefoot and hindfoot have significantly different microstructure. Adipose chambers are significantly larger by area at the hindfoot than the first metatarsal of the forefoot, and non-significantly larger than the third and fifth metatarsals and the hallux. Similar trends can be found across all morphological measurements. Interestingly, the lateral midfoot had the largest adipose chambers by area, despite it being an uncommon area of interest in plantar soft tissue research. This difference by location, along with prior work showing differences in location[22–24,35], suggests that plantar soft tissue mechanics and possibly mechanism of ulceration differ by plantar location.

The eccentricity was borderline significantly higher in non-diabetic plantar soft tissue, indicating that the non-diabetic chambers were less circular. However, the difference was small (0.012), and unlikely to explain the significant changes in mechanics.

The attention network attended strongly to darkly stained (elastin) septal walls and in some specimens also looked at muscle or parts of the skin. In prior work on a subset of the same specimens and in other work on diabetic plantar soft tissue, septal walls affected by diabetes have been characterized as significantly thicker, with frayed fibers[55]. Additionally, diabetic plantar soft tissue was found to have significantly higher total elastin content[56]. In prior work on a reduced subset of the same specimens, there was no difference in the interdigitation index, a measurement of the quality of the dermal-epidermal junction[180], between diabetic and non-diabetic groups[55]. While this junction has been shown to be important in ageing skin[180], and there are similarities between ageing and diabetes, there may be a better method of quantifying this junction that could lend insight into diabetic skin mechanics.

While the focus of this attention network on the tissue area lends credibility to its predictions, network decisions are still difficult to interpret. Additionally, most classification networks downsample the input image size to create multiresolution spatial connections, but most CAMs use the spatially smallest layer as it has the most semantic and complex information[169]. Often, these CAMs are upsampled using a bilinear or other smoothing upsampling technique, since the result for one pixel of the deeper layer is often informed by a much wider input area than the simple square upsample. However, this presentation may suggest finer resolution than exists in the visualization (Figure 4-4). Since histological structures can be very small relative to the whole sample image, this mismatch in image and attention resolution makes identifying features from CAMs difficult.

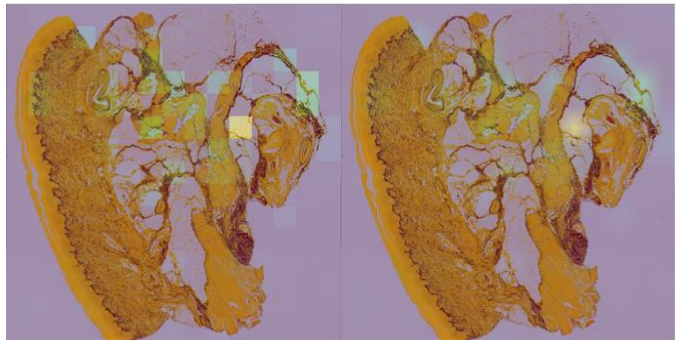

Figure 4-4: *Left. Square upsampled overlay image. Right. Bilinear interpolation upsampled overlay image. Bilinear interpolation suggests smaller attention areas.*

In addition to the difficulty of interpreting CAM methods, there are other limitations of the Axial-Deeplab and CAM method of interpretability. There is potential that a different network or attention structure, or a different loss function or task could provide a better attention map for identifying novel areas of interest for understanding microstructural differences related to diabetes and mechanics in the plantar soft tissue. The current network only classifies tissue images by disease state. To answer questions about how the microstructure changes with diabetes and how those changes affect plantar soft tissue mechanics, a regression network predicting mechanical parameters by image information may provide more informative attention maps. However, this kind of task would require a much larger sample size.

Histomorphological measurements should also be considered in light of their limitations. While efforts were made to ensure that the segmentations from the UNet were accurate compared to an expert, there is still potential that some tissue boundaries were misclassified, leading to errors in the measured parameters for some samples. Additionally, the histology specimens are of unknown depth, meaning there may be additional adipose tissue between where the specimens ended and the original bone. This missing tissue could affect the deep layer adipose chamber measurements, but there were a large number of deep chambers measured (Table 4.3-1), mitigating the risk of insufficient deep chamber measurements. Finally, there is always the risk that the wrong parameters were measured, however the use of an attention net mitigates the likelihood that there was a parameter that was significantly different between diabetic and nondiabetic specimens that was not identified. Finally, adipose chambers are three-dimensional structures. While efforts were made in sample sectioning and image analysis to avoid biasing the measurements, there is still potential that these two-dimensional metrics are insufficient to capture differences in this three-dimensional structure, similar to trabecular connections in bone.

This work presents a novel application of deep learning and automated morphology to improve histology workflows and contributes novel information about plantar soft tissue microstructure, namely the quantitative difference in size between superficial and deep adipose chambers, and the difference in size between diabetic and non-diabetic deep chambers. This difference in size could contribute to the change in mechanics previously seen in diabetic plantar soft tissue, and demonstrates that microstructural changes with diabetes may affect different parts of the plantar soft tissue differently. This information could be used to improve future finite element models. While this preliminary work on using attention-based neural networks to interpret network decisions and inform research hypotheses lacked the necessary resolution for utility, there is likely a network architecture that would provide better information and this work may serve as a foundation for choosing an appropriate model and scale in future work.

5 An ultrasound-based 3D plantar soft tissue scanner

Portions of this work have been submitted in manuscripts titled *Volumetric ultrasound of the plantar soft tissue under body weight loading* and *Anatomically Realistic Foot Models for Biomechanics and Imaging* to IEEE Transactions on Medical imaging and Frontiers in Manufacturing Technology: Additive Manufacturing and its Biomedical Application, respectively.

5.1 Abstract

The plantar soft tissue is a complex three-dimensional structure that experiences complex, multi-dimensional loading. However, measurement of three-dimensional mechanics of this unique structure is difficult. Previous investigations into the plantar soft tissue structure and function have been either *ex vivo*, uniaxial, or computational, or some combination of the three. Measurements using medical imaging methods such as magnetic resonance imaging (MRI) can be expensive and time-consuming, limiting their clinical potential. The goal of this work is to develop an ultrasound-based method to acquire three-dimensional scans of the plantar soft tissue in both unloaded and naturally loaded states and using both imaging B-mode and shear wave elastography (SWE) modes. A mechanical scanning apparatus was constructed using a stiff, acoustically translucent load-bearing plate and an x-y scanning axis. A software system was developed to control the scanner, record subject and scan information, and reconstruct acquired ultrasound images and shear wave speed values into a volume. An anatomically realistic phantom was developed to aid the evaluation and development of the scanning system. The resulting system is capable of producing volumetric plantar soft tissue scans in both B-mode and SWE with resolution on par with existing volumetric medical imaging systems.

5.2 Introduction

The plantar soft tissue is a complex and unique structure capable of withstanding high loads during daily activities. The breakdown of this function, as occurs in a variety of pathologies such as heel pain, plantar fasciitis, or diabetic ulceration, is widely studied in biomechanics. Measurement of plantar soft tissue mechanics presents several challenges, including complex three-dimensional normal motion; a large number of bones, tendons, ligaments, and intrinsic muscles; high loads; and complex three-dimensional structure. Measurement of the plantar soft tissue in the specific case of diabetes-related ulcers presents additional challenges as the pathology is associated with higher risk of severe tissue injury and complications. Prior efforts to quantify pathological changes to the plantar soft tissue related to diabetes largely fall into *ex vivo* material tests, *in vivo* two-dimensional (planar or projection) imaging analyses, magnetic resonance imaging (MRI) analyses, and computational models.

Ex vivo efforts have measured the material properties of isolated plantar fat[18,22,23] and skin[24], the microstructure of the plantar fat[35,56,107,110] and skin[24,35,56,110], and the structural properties of plantar fat and skin[25], and the strength of the skin-fat interface[26]. In these *ex vivo* tests, higher moduli and stiffnesses were reported in tissue affected by diabetes, and the adipose chambers were reported to be smaller and surrounded by thicker, frayed elastic septa, with the effects stratified more severe in superficial tissue. Though these works are particularly useful for designing and validating computational models and understanding mechanical changes, they are difficult to translate into clinical tools.

Plantar and projection imaging analyses are largely ultrasound methods using either single-line acquisitions[34,35,37,181,182], B-mode imaging[104,183], or shear wave elastography (SWE)[184,185], which uses an acoustic radiation force to create shear waves whose speed of propagation is related to material modulus. Works using single-line or B-mode imaging are often accompanied by force measuring instrumentation to calculate localized tissue stiffness, typically in the heel[35,181,182,186], hallux [35,181,182], or metatarsal heads[35,181,182,186] where ulcers are most common[50,51]. Some imaging methods are performed with subjects prone[155,187–189] or supine[35,36,90,181,190,191] while others attempt to load the tissue through plates[103,192–195] or using cutouts for the transducer[37,104,194,196]. A few works also use radiographs to calculate bulk tissue stiffness, tissue thickness, and total deformation[31,197,198]. However, X-ray-based methods suffer from poor soft tissue resolution. While these analyses are useful for understanding *in vivo* stiffness and deformation, they are limited in their ability to assess the complex three-dimensional nature of plantar soft tissue mechanics.

A few groups have pursued volumetric measurements using MRI by applying external load either through indentation[27], vibration for MR elastography [28,199] or applying sustained normal[29,200,201] or combination normal and shear[202] loads to evaluate volumetric changes in the plantar soft tissue. However, these acquisitions must be performed with the subject in the supine position, meaning that intrinsic and extrinsic muscles, tendons, and ligaments are not in typical tension; loads are lower than those seen in typical standing or walking due to subject comfort[29]; and due to limitations of the hardware and imaging volume are analyses of either the forefoot or the hindfoot only, not the entire foot. MRI is also expensive and difficult to schedule, making this tool difficult to translate to clinical measures or outcomes.

Computational models are the gold standard for investigating internal stresses and strains in the plantar soft tissue, and a variety of models with varying degrees of complexity have been reported[44,47,203–206]. However, these analyses are sensitive to constitutive models, geometry, and mesh size, and it is difficult to assess the accuracy of the internal stress and strain estimations without comparable measurements. Additionally, many models simplify the plantar soft tissue geometries or contact mechanics due to limitations of computational power.

Extension of ultrasound acquisition from plantar to volumetric acquisitions could address many of the above limitations as it is fast, safe, relatively inexpensive, and has been used to image through a load bearing plate. Additionally, elastic registration methods could be used to directly measure internal strains from loaded and unloaded volumes[202]. The goal of this work is to develop a volumetric ultrasound scanner capable of withstanding bodyweight loading and acquiring high quality images in both B-mode and shear wave elastography.

5.3 Design

5.3.1 Design requirements

The following criteria were developed for the design of this device, where requirements are listed in main bullets and requests are in sub bullets:

- Capable of taking a weighted and unweighted ultrasound scan
- At least 2-axis motion
    - 3 axis motion preferred
- Imaging volume of 320 x 110mm to accommodate most foot sizes[207]
- 0.3mm resolution to be comparable to CT scanner (Curve Beam, Hafield , PA , USA)
- Able to support weight at or above 300lb without failure
- Flat, acoustically transparent or translucent scanning surface
- Mobile (can move between rooms)
    - Able to fit through a standard sized door
    - Able to move with just 1-2 people

    - Easy to assemble and disassemble
    - Easy to secure
- Safe for subject to sit and stand on
    - No sharp pieces
    - Sufficiently strong
    - No places to trip
    - Hand rails/supports
    - Safeguards to prevent falling
    - Steps of reasonable size
    - Not too tall for the room
    - Electrically safe
- Comfortable for subject to sit and stand on
    - Wide enough for a comfortable chair
    - Opaque load bearing surface (clear surface may be unnerving)
    - Feels stable
    - Low noise
- Easy to operate
    - Easy to adjust & position motors
    - Easy to connect & align platform
    - Easy to set up prior to data collection
    - Easy to store
    - Easy to calibrate

5.3.2 Design and Construction

The final design of the scanner frame is constructed from 1.5” aluminum t-slot rail, and the dimensions of the frame are 4’ x 3’ x 3’ (Figure 5-1).

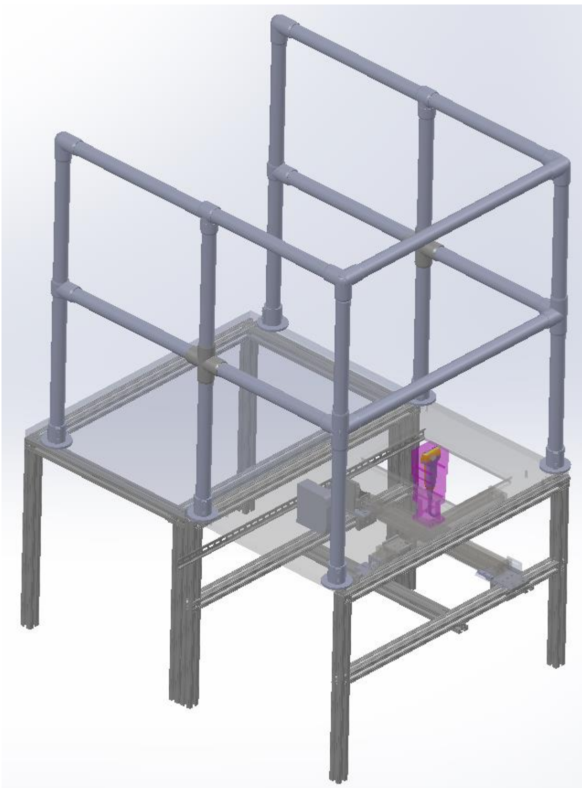

Figure 5-1 *CAD model of final scanner*

5.3.2.1 Finite Element Analysis

Once the design was drafted in Solidworks (Dassault Systèmes, Bellevue, WA, USA), the model was simplified so that finite element analyses could be performed in Ansys (Canonsburg, PA, USA) to ensure that the dimensions and materials were acceptable for the anticipated weights to be supported. In particular, the thickness of the sonolucent plate affects the quality of ultrasound images, therefore, the optimal plate is the thinnest plate capable of withstanding loading. The simplified model consisted of just the 1” high density polyethylene (HDPE) plate supported by 1” square hollow tube supports and supporting 1 7/8” aluminum speed rail railings. The HDPE plate had two rectangular cutouts. Both cutouts had a 0. 5” wide, 0.3” thick lip. In the left cutout was a ¼” HDPE plate which was connected to the thicker HDPE plate with a sliding contact. The right cutout contained a water bath with 0.4” thick bottom and 0.5” thick sides connected to the thicker HDPE plate with a bonded contact. All other contacts were defined as bonded and the four rectangular supports were defined as fixed to the ground. A 1334N (300lb equivalent) force was applied to the left thinner plate, and a 677N (150lb equivalent) force was applied to the right plate.

The maximum von mises stress within the thinner, sliding HDPE plate was 3.7MPa (Figure 5-2, middle), which is 8x lower than the yield strength. The maximum von mises stress within the aluminum was 18MPa, which is 15x lower than the yield stress. The maximum displacement was 4.5mm in the thinner HDPE plate at the location of load application (Figure 5-2, left). However, the maximum principal stress was 0.3%, indicating that the sliding contact is likely related to the displacement. The displacement of the section between the two cutouts was 1.53mm, and the first principal strain was .06% (Figure 5-2, Right). The maximum magnitude of lateral displacement was .0046" (A-P) -0.009" (M-L) in the thinner sliding plate, which is far below the 0.5" wide lip.

The applied load of 1377N at the center of one imaging plate and 667N at the center of the other imaging plate represents a larger load than is expected for the target population. The expected load on the plate is ½ bodyweight, which likely will not be 1334N, but could approach that for some subjects. While the expected load is ½ bodyweight, short-duration loads may approach 100% bodyweight as subjects may naturally shift weight while positioning their foot, during or after the scan is taken, or at some other point while on the scanner. This analysis indicates that this design is safe for the target use case. However, several changes were made during construction to improve the design. First, fasteners were added to the thinner plate to reduce sliding and buckling of the scanning surface. Second, only one cutout was machined to reduce the displacement and strain of the center section of the thicker 1" plate. Third, additional horizontal t-slot aluminum supports were added between the vertical aluminum t-slot supports to add bracing to the perimeter of the HDPE plate, and these were secured to the aluminum rail as well.

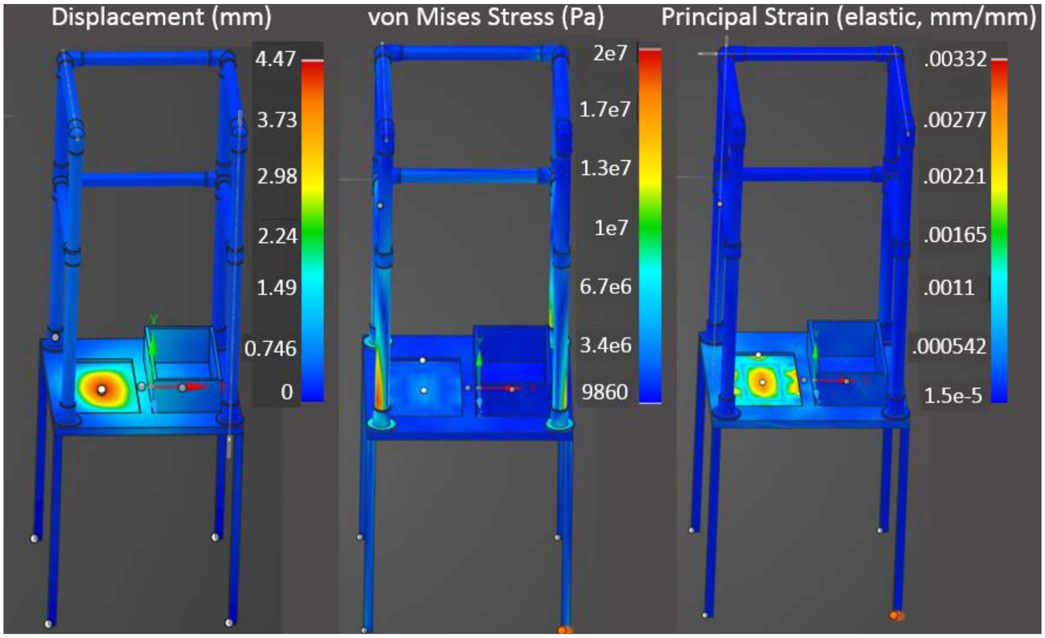

Figure 5-2. Results of simplified finite element analysis to assess whether the high density polyethylene and low density polyethylene could sustain bodyweight loading. Left: Maximum displacement. Middle: von Mises stress. Right: Principal Strain

5.3.2.2 Motor and actuator sizing

When designing a motion application, the choice of motors and linear actuators is governed by parameters like resolution, accuracy, speed, load, and orientation.

Element	**Weight (g)**
SL18-5 transducer	140.5
3D printed housing	321.2
Hardware (screws, springs, etc)	125.5
Total (longitudinal)	587.2
Longitudinal axis	200
Total (transverse)	787.2

Table 5.3-1: Weight of components to be translated by the longitudinal and transverse axes for selection of motion components.

This application involves two perpendicular horizontal axes, with a load that is primarily normal to the direction of motion. The horizontal axes are less complex and require fewer engineering controls than a vertical axis, making this unlikely to be a limiting factor. While a third axis is desirable, it is not essential and was removed from the automated motion control system due to cost.

The load carried by the top axis is composed of the ultrasound transducer, the transducer housing, and the components that connect the transducer to the actuator (Table 5.3-1**)**. The anticipated load for the longitudinal axis of 587g or 1.2lb is relatively small, which means it likely will not be a limiting factor. Similarly, while the addition of the weight of the longitudinal axis increased the anticipated load for the transverse axis to 787.2, this load is still relatively small relative to typical applications.

Typical resolution of other volumetric medical imaging systems is approximately 0.3mm. In order to image a large foot, the total span of the motion needed to be approximately 320mm in the anterior-posterior direction and 230mm in the medial-lateral direction. This combination of resolution and span is a limiting factor in the choice of linear actuators. Additionally, accuracy and precision are of importance for a research medical imaging motion application, as the true anatomy is the primary output of interest. High resolution and accuracy over a long span is a limiting factor.

Finally, the number and type of scans that can be taken are limited by the speed at which the motion control system can be operated. In order to obtain a high quality image and to have confidence in the reconstruction of the volume, the motion should stop while the image is being acquired. Given that an image acquisition via the research interface takes approximately 0.04 s, the minimum scan time for the maximum scan is

$$320\text{mm}/0.3\text{mm} \times 3 \text{ passes} \times 0.04 \text{ s/pass} = 128\text{s} / 60 \text{ min} = 2.1 \text{ min.}$$

This is already longer than a weightbearing cone beam CT acquisition, which can acquire a 0.3mm resolution scan in under 30 seconds, without factoring in data storage, communication between control and motors, and motor motion. As such, minimizing the time required to perform each step was an important consideration.

5.3.2.2.1 Actuator

Due to cost, all-in-one motion control solutions were largely impractical, leading to the choice to purchase separate linear actuators and motors.

Linear actuators transform the common rotational motion of most motors into linear motion, and come in a variety of configurations. Among the most popular configurations are ball screws, lead screws, belts, and pulleys.

In belt-driven actuators, toothed pulleys apply torque to a toothed timing belt which is attached to a carriage. The driveshaft and motor are often perpendicular to the belt and direction of motion. Belt pulleys are typically used in applications that require long strokes, high linear travel speed, high efficiency, and high duty cycles. However, belt driven actuators tend to have lower accuracy and positional reliability, can have issues with belt tensions, and require higher input torque. Lead screw driven actuators tend to have high accuracy and positional repeatability, have agile acceleration and deceleration rates, are self-lubricated, are quiet, can have lightweight polymer nuts to support carriages and loads, are self-locking, and are good for light load, high-duty cycle applications. However, lead screws can have difficulty with high loads, can generate significant heat from friction, and historically have an inverse relationship between length and speed. Ball screw driven actuators attempt to address the friction limitation of lead screws, by incorporating a rotating ball bearing system. This bearing system also reduces the required motor torque by reducing the friction. However, ball screws typically require lubrication and can be noisy.

As a result of the requirements for high precision, accuracy, and repeatability and quick acceleration and deceleration; in combination with the low load, a 1-mm lead, 10mm diameter lead screw was chosen with a constant-force anti-backlash nut. (CSLSM10AHXR1ZF-2LT-0240-0 and CSLSM10AHXR1ZF-2LT-0440-0, PBC Linear, Roscoe, IL,USA) This actuator uses a recirculating ball bearing between the carriage and the rail which has a static coefficient of friction of 0.02-0.025 and a dynamic coefficient of friction of <0.01.

5.3.2.2.2 Motor

The required minimum torque of the motor was calculated using the diameter, length, lead, efficiency, and material of the lead screw, along with the load, acceleration, deceleration, maximum speed, stopping accuracy, and safety factor of 2.

There are two main types of motors typically used in motion control applications: stepper motors and servo motors. Stepper motors consist of a permanent magnet rotor and wound electromagnetic stator. The motor is turned by alternating the current through the magnets, changing the polarity. Stepper motors are generally inexpensive, easy to control, don't require closed loop feedback control, and can easily be operated at low speeds and for short times. However, without the closed loop feedback, steppers can skip steps undetected, and steppers also have an inverse relationship between torque and operating speed, draw the same current at all times, and can't respond to changes in load. Servo motors are composed of a 3-phase stator and a permanent magnet rotor. Given the additional phases, a servo motor requires more sophisticated control signaling to operate, and requires positional feedback. Given the relatively low and anticipated static nature of the load, the regularity of the motion, and the simplicity of control, stepper motors were chosen for this application.

Motors were sized based on anticipated requirements for step resolution, load, friction, resistive forces, required acceleration, and the chosen leadscrew actuators. Updating the values in Table 5.3-1 for the actuators chosen and their carriages, the load for the longitudinal axis is 737.19g and for the transverse axis is 2126.4g. An additional 'worst case' load of 12kg (1/6 body weight) was added to each of these loads for the potential case of severe bending of the plate or force transmission through the plate.

The anti-backlash nut is coated with low friction, 'self-lubricating' polytetrafluoroethylene (PTFE), which has a coefficient of friction between 0.05 and 0.1. The actuator is a PTFE-coated 300 series stainless steel leadscrew, and the combination of the two has 28% efficiency according to the manufacturer. The breakaway torque of the leadscrew can be estimated using the equation

$$T_B = \frac{cNL}{2\pi}$$

Equation 5.3-1

Where c is the static coefficient of friction, N is the normal force, and L is the screw lead. Using c=0.05-0.2 for PTFE on steel, N= 21N for the transverse axis, and L=1mm, T_B =.6637Nmm = 0.09 oz-in.

In order to calculate the speed requirements, the ideal scan time (5 minutes) was divided by the anticipated maximum number of images (320 / 0.3 resolution *3 passes = 3200 images) to give a per-image time of .09375 seconds per image. Assuming half of this time is devoted to image acquisition (see section 7.4.2 for a discussion on image acquisition time), this leaves 0.047 seconds for moving 0.3mm, or a speed of 6.3mm/s. Considering that the motor must ramp up and down to speed, the acceleration and deceleration time was estimated to be 0.01s. For the transverse scan, there is no imaging, so the speed should be maximized as much as possible. Based on this the desired speed range was set to 6-20 mm/s.

For a resolution of 0.3mm, minimum desired stopping accuracy was chosen to be 1% or 0.003mm. For a 1mm lead, this is about 3.6 degrees.

Based on these parameters and a factor of safety of 2, the estimated required torque was 0.26 Nm or 36.7 oz-in. Using this information the NEMA17-16-06PD-AMT112S (CUI devices, Lake Oswego, OR, USA) was selected for both axes. It is rated to 40-25oz-in for speeds from 3000 to 4000 pulses per second with an accuracy of 0.2 degrees.

5.3.2.3 Top Surface

The top surface of the scanner needs to be strong and stiff enough to support the weight of the lower limb alone for the unweighted scans as well as ½ body weight for the weighted scan without buckling to allow for linear translation of the transducer on the bottom surface. The material also needs to allow sufficient transmission of sound waves to allow both B-mode imaging and shear wave elastography.

Few of prior works have attempted to use ultrasound through a stiff material in order to investigate the plantar soft tissue[103,194]. The PVC and polypropylene used in Parker et. al and Bygrave and Betts are not well matched acoustically with high acoustic impedance and high speed of sound, respectively, and the image quality suffers as a result (Figure 5-3). There is also a ringing effect due to the design in Parker et. al. that makes the image difficult to distinguish [103]. Rome et. al and Matteoli et.al used an acrylic sheet, which is again quite different acoustically from soft tissue, though only the latter included an image from their system and neither included plate thickness, the image quality was noticeably degraded[195,208]. All three of these studies use a static transducer and image in a single plane through the plate at a single location. More recently, Matsumoto et.al. used a 5mm thick polymethylpentene plate for a heel-only investigation of the subcalcaneal fat pad[187]. These investigators used a commercial quality assurance phantom to measure reduction in ultrasound signal through the plate, and found a significant reduction in signal intensity and a reduction in lateral resolution through the PMP. However, the quality of images are improved compared to prior work. As a result of the variation in image quality with different materials, and in order to identify materials that will allow acquisition of shear wave elastography, an investigation into both mechanical and acoustic performance of materials was performed.

Sound transmission at a material boundary is governed by the similarity of acoustic impedance between two materials using the equation: $T= Z1 / Z2$, where Z is the acoustic impedance calculated by $Z=\rho c$, where ρ is the density of the material and c is the speed of sound through the material. In order to match sonic properties, the speed of sound and density of a variety of

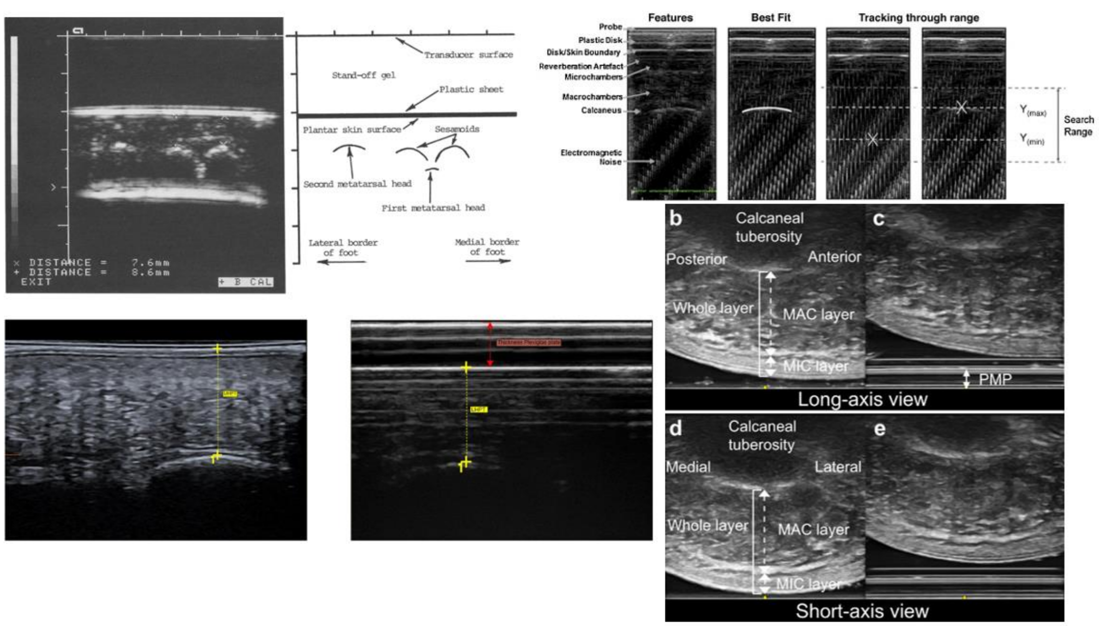

Figure 5-3: Prior work using ultrasound to image through plastic for biomechanically realistic loading. Top left: Bygrave & Betts 1992, *The Foot* 2, 74, reproduced with permission. Top right, Parker et al 2015, Medical Engineering and Physics 37:11,110 , reproduced under CC BY-NC-ND license. Bottom right, Matsumoto. Bottom left: Matteoli.

materials was compared with those of various biological tissues, and 8 materials were selected for testing (Table 5.3-2). All materials were obtained from McMaster Carr (Elmhurst, IL, USA) or Grainger (Lake Forest, IL, USA). Materials were evaluated using an elastography quality assurance phantom (CIRS, Norfolk, VA, USA) and an Aixplorer with a SLH 20-6 high frequency transducer (SuperSonic Imagine, Aix en Provence, France). The experimental set up consisted of a generous amount of ultrasound gel (Aquasonic 100, ParkerLabs, Fairfield, NJ, USA), sufficient to span the vertical distance between the phantom surface and the external walls. The plastic materials were placed on top of the gel so that each side of the plastic material was supported on the external walls of the phantom. Parameters such as speed of sound, acoustic power, focal depth, dynamic range, total gain, and time gain compensation were adjusted top obtain the best image.

Table 5.3-2: Acoustic and material properties of candidate materials tested for load bearing 'sonolucent' plate.

Material	*speed of sound*	*density*	*Acoustic impedance*	*young's modulus (Pa)*	*thickness*	*attenuation (db/cm @5MHz)*
polypropylene	2700	885	2.39	1.86E+09	3/8"	6.65
polystyrene	2390	1040	2.49	1.86E+09	1/4"	2.7
Nylon	2770	1140	3.15	3.45E+09	1/4"	
Polymethylpentene	2153	831	1.79	1.10E+09	1/16"	12.1
Low density polyethylene	1950	920	1.79	8.30E+08	1/8"	2.4
Low density polyethylene	1950	920	1.79	8.30E+08	3/8"	
High density polyethylene	2430	960	2.33	6.23E+09	1/8"	
High density polyethylene	2430	960	2.33	6.23E+09	3/16"	11.1
High density polyethylene	2430	960	2.33	6.23E+09	1/4"	
High density polyethylene	2430	960	2.33	6.23E+09	1"	
ultra high molecular weight polyethylene	2657	941	2.50	3.04E+09	3/16"	
ultra high molecular weight polyethylene	2657	941	2.50	3.04E+09	1/4"	
Bone (ref)	3514	1908	6.7	8.00E+09		
Fat (ref)	1440	911	1.31	1.00E+06		
Skin (ref)	1624	1109	1.8	2.00E+06		

With regards to B-mode imaging, despite relatively similar acoustic impedances, no signal was able to penetrate the polypropylene, very little signal passed through the polystyrene, reasonably good but low intensity (high gain required) signal was obtained through the UHMWPE and marine grade HDPE, and excellent signal was achieved through the basic HDPE (Figure 5-4). No signal was visible in the image taken through the nylon plate, which had the highest expected acoustic impedance. Polymethylpentene yielded the highest signal intensity, but it was also the thinnest material at half the thickness of the next thickest material. In contrast, while it should have a similar acoustic impedance and a low attenuation coefficient, LDPE yielded much lower signal intensity than either regular HDPE or PMP.

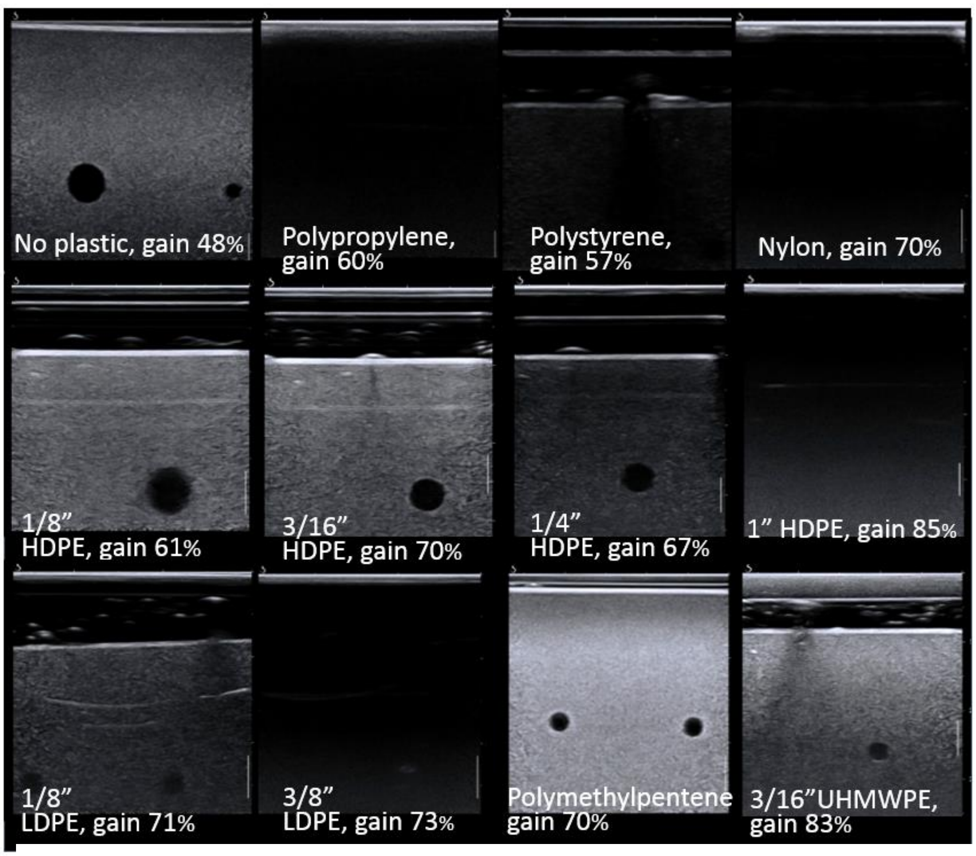

Figure 5-4: B-mode imaging signal through different plastics with similar acoustic impedances to soft tissue. Plastic and total gain are listed for each image. HDPE and PMP are the most performant while polypropylene and nylon are the least performant.

The materials that yielded the best images in B-mode were subjected to SWE imaging. Again, B-mode and SWE parameters were adjusted to obtain the best signal in the phantom area. Of the seven materials tested, only three yielded acceptable signal:

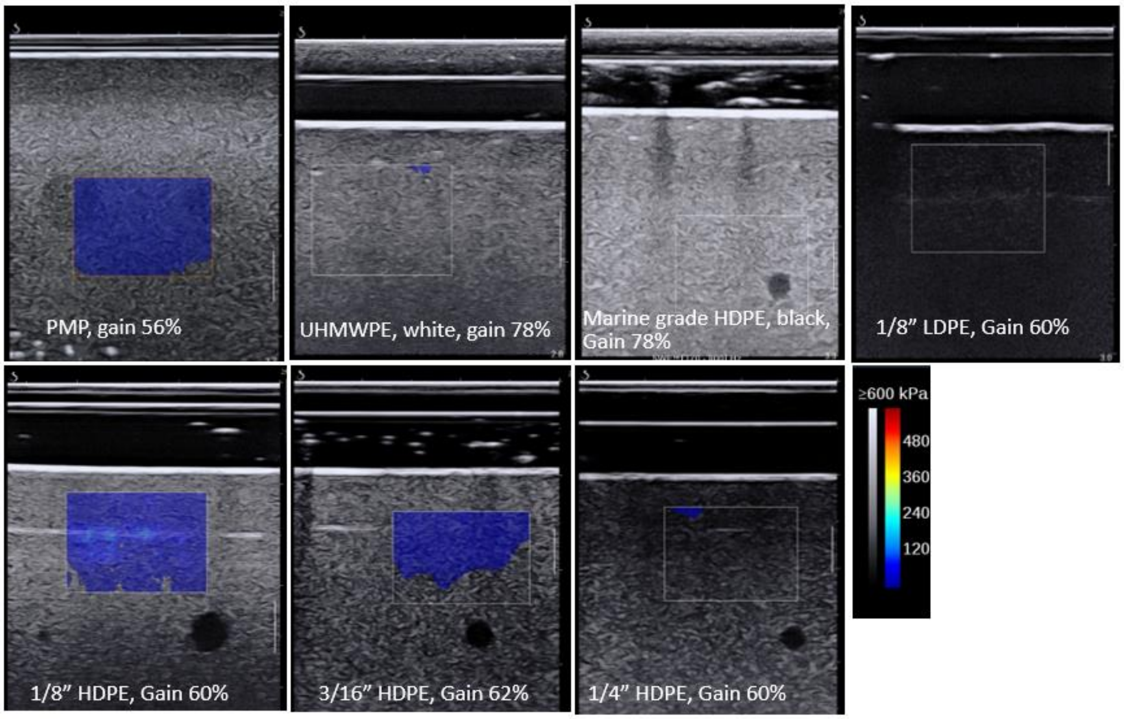

Figure 5-5. SWE signal through materials with visible B-mode signal. Only PMP and HDPE 3/16" and thinner allowed SWE through.

polymethylpentene and the 1/8" and 3/16" HDPE sheets. At ¼" the SWE signal was no longer able to get through the HDPE, and the signal was not able to break through the other types of polyethylene (Figure 5-5).

While both low density and high density polyethylene were both able to acquire good signal in B-mode and SWE, there is a significant difference in attenuation between the two, as observed through the proxy of the gain required to display a clear image. The modulus of HDPE is also higher than that of LDPE. Based on finite element modeling, 1/4" HDPE can support a weight of 300lb single- or double-supported standing weight on the scanning surface. The lower modulus of LDPE would require a thicker plate, and there was no visible signal through the 3/8" LDPE plate. Based on these criteria, a 1/4" HDPE plate was chosen for loaded scanning. However, there was no visible SWE signal through the 1/4" HDPE. Therefore, the decision was made to use a thinner plate for unweighted scans and a thicker plate for weighted scans. The plate chosen for thinner scans was 1/8” HDPE.

While the both SWE and B-mode signal through PMP were clear, it was ½ the thickness of the HDPE plate. Based on the difference in signal between the 1/8” and ¼” HDPE, it was possible that the PMP would not be as performant in a thicker sheet. Additionally, the cost for a 12” x 24” sheet of HDPE was $8.93 while PMP sheets from several suppliers were listed in the thousands of dollars, making them prohibitive for this pilot study.

5.3.2.4 Transducer housing

While the top surface is designed with sufficient stiffness to prevent excessive bending and failure, the plate material best suited to ultrasound imaging and SWE acquisition will likely undergo some bending. This bending may be sufficient to alter the ultrasound signal (via additional compression in areas under more load) or damage the transducer elements. In order to both protect the transducer and ensure that ultrasound signal is as consistent and high-quality as possible, the housing to connect the transducer to the longitudinal linear actuator was designed to respond to increased pressure due to bending. An additional requirement was the need to protect the transducer cord from excessive bending or force.

The final housing is consists of four pieces: The housing, the sheath, the interface part, and the topper (Figure 5-6). The housing is the main component of the design. The housing is molded to fit the body of the transducer and has a track and outlet hole designed to protect the transducer cord from crushing or excessive bending. The top portion of the housing is molded around and flush with the transducer element face to provide additional load support and distribution to protect the transducer elements. A recessed cut surrounding this supportive face ensures that any gel used

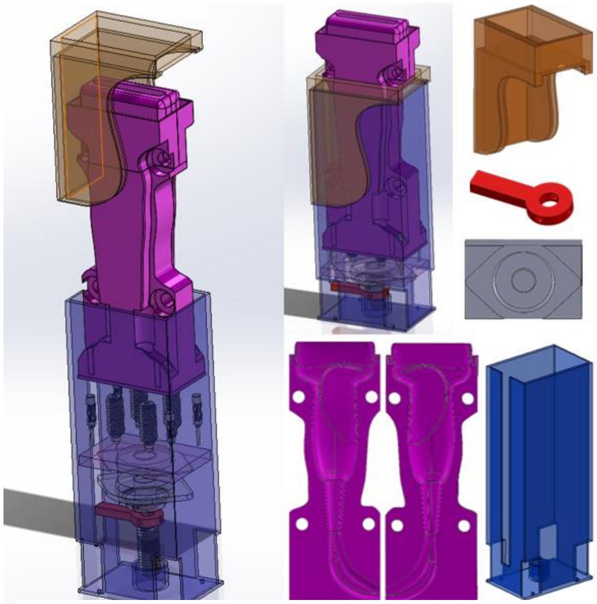

Figure 5-6: CAD of transducer housing. Left: exploded view illustrating how the pieces fit together. Top middle. Non-exploded view of the entire assembly. Top right: 'topper' piece to reinforce weaker areas and constrain transducer motion, semi-transparent. Right middle: custom designed set-screw handle and pillow bearing interface block. Bottom right: Sheath for housing featuring channel for transducer cord and well for threaded rod. Bottom middle: transducer housing featuring transducer and cord cutouts.

for coupling is captured by the reservoir, protecting the actuators from potential damage due to water or increased friction due to stickiness from wet or dried gel. The housing is composed of two halves that are clamped around the transducer body and closed using M10 hex head screws and nuts. On the bottom of the housing are eight holes. The smaller, 0.25" diameter holes at the corners accommodate press-fit spring plungers with a maximum load capacity of 1.1lb each and a maximum deflection capacity of 0.5". The larger, 0.5" diameter holes are situated in the center along each long edge of the housing and accommodate externally threaded spring-plungers with a maximum load capacity of 9.3lb each and a maximum deflection of 0.25". Using the additive property of spring constants, these 8 spring plungers can accommodate a total load of 41.6lb, with an initial deflection of the longer, 0.25" diameter plungers beginning at around 1.2lb of applied force. This spring system will allow the transducer to move and angle in order to maintain contact and coupling with the deformed plate.

Incorporating a spring mechanism into the housing means that it cannot be directly attached to the actuator carriage. Additionally, the spring mechanism chosen is secured only at one end, leaving the housing free to tilt. Therefore, a sheath was designed to keep the housing upright and in place as well as to secure it to the actuator carriage. The sheath consists of four walls with four cutouts to allow access to the four M3 holes that secure the sheath to the carriage. There is a 0.62" diameter well with a 0.1" wall thickness designed for a 5/8" threadded rod in the center of the based of the sheath. The threaded rod is connected to a pillow block bearing and secured with a custom-designed handedled shaft collar to allow fine-grain manual Z-axis adjustment outside of the passive mechanism.

The pillow block bearing is embedded in the interface part, which serves to extend the shape of the bearing to fit the exact dimensions of the rectangular footoprint of the sheath. This interface part provides the surface on which the spring plungers of the housing rest.

In order to allow the ultrasound cord to fit into the sheath, a channel was cut into the side of the sheath where the cord will exit the housing. However, this channel introduces weakness into the sheath. Additionally, for ease of assembly, the sheath is designed 0.05-0.1" larger than the housing on each side. In order to reduce motion in the anterior-posterior direction, reduce the possibility of losing signal due to tilting of the transducer away from the plate, and reinforce the sheath around the cord cut-out, a topper was designed to fit snugly over the top and sides of the sheath. The topper is longer on the side that requires reinforcement as well as thicker on the anterior and posterior sides to limit motion in that direction. The topper is also contoured to reduce stress concentrations that were points of failure in testing. The custom designed parts were printed in PLA on an Ultimaker S5+.

The final component of the transudcer housing was coupling the transducer to the underside of the load-bearing plate. Due to bending in the plate, free-standing ultrasound gel was often scraped off during the inital scan, leaving little to no coupling material behind for the overlapping second pass.

Ultrasound standoff pads, made of hydrogels or fluids or gels encased in thin plastic are used clinically to improve signal quality and reduce the amount of gel required for a scan. In order to avoid this decoupling as well as provide extra cushion to protect the transducer elements, a hydrogel pad was investigated. The initial design uses commercially available hydrogel bandages for treatment of burns, and consists of a hydrogel cut to size and secured to the transducer face and surrounding housing using a transparent adhesive, stretchy, polyurethane bandage. This hydrogel is then coupled to the plate using a small amount of gel. An additional treatment of coupling methods can be found in section 7.6.

5.3.3 Electrical

5.3.3.1 Motor circuits

Each motor requires a driver, which has 10 connections: four motor windings (A+, A-, B+, B-), a pulse connection to control the motor motion (PUL+, PUL-), a direction connection to control whether the motor turns clockwise or counterclockwise (DIR+, DIR-), and an enable signal that controls whether the motor is enabled (can move) or not (ENA+, ENA-). The four motor windings must be connected to the A-, A+, B+, B-. The pulse and direction signals must be connected to either ground or the positive voltage source to the driver (here, 5V), and the Arduino pin that sends high and low signals to indicate motion and direction. The enable for the selected drivers must be connected to a low to enable the motors, so in this case it was connected directly to ground.

5.3.3.2 Encoder

Stepper motors are easy to program and offer precise positioning with relatively fast stop-start speeds. However, when a stepper motor encounters too much torque for its power, it can miss steps, causing mispositioning in the system. Stepper motors typically are not run in closed-loop systems with positioning feedback, meaning that when steps are missed the operator typically doesn’t know until after the fact or until enough steps accumulate that there is significant misalignment or catastrophic failure. Because the steps in this system are sub-millimeter and the motor system is below a standing surface, it would be difficult for the operator to recognize missed steps until a significant delay had been accumulated. Additionally, regular image intervals are required for volume reconstruction from images. Therefore, it is essential to incorporate some monitoring and position recording into the system. Rotary encoders can be attached to dual shaft stepper motors in order to count steps. One CUI AMT112 series encoder was attached to the stepper motor of each axis. quadrature output and programmable resolution between 96 pulses per revolution (PPR) and 8000 PPR. Both encoders were programmatically set to 100 PPR. The encoder positive and negative were connected to the 5V output of the Arduino Uno and the ground of the Arduino, and each of the A, B, and Z signals was connected to one of the digital input pins of the Arduino.

5.3.3.3 *Finalizing the circuit*

In order to create a more permanent circuit that can withstand potential jostling with transferring the scanner between rooms, the breadboard design was transferred to a printed circuit board (PCB). The PCB was designed in Autodesk Eagle (Figure 5-7) and printed using a Voltera-One printer. The design allows external wired connections to the motor drivers and encoders to be soldered directly to the PCB while the PCB is connected to the Arduino using male headers.

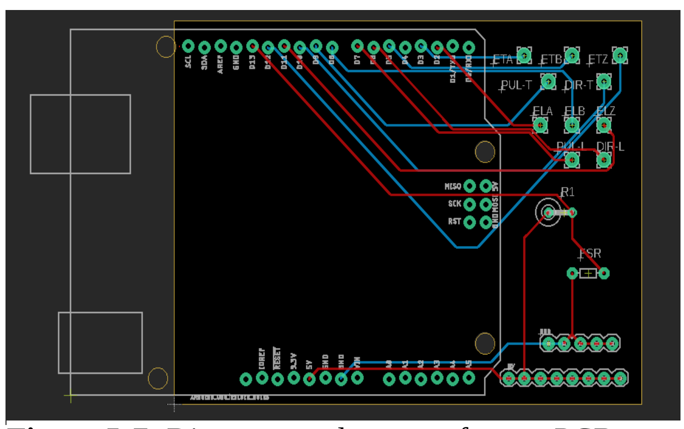

Figure 5-7: Diagram used to manufacture PCB on Voltera One

5.3.3.4 Power supply

A power supply is required to supply sufficient voltage and current to the motors, as the required power cannot be supplied through the Arduino or the computer. Each motor is rated for 1.4A, meaning that the power supply must be capable of supplying at least 2.8A in the event that both motors are required to move at one time. Additionally, the motor drivers are rated for 20-50VDC, so the power supply must be capable of supplying power within that voltage range but not above it. Typical voltage ratings for power supplies are 12V, 24V, and 48V. For this application, a 24V power supply was selected. Based on the rated current and voltage, 24V*2.8A = 67.2W of power are required to run the motors. Typically, a power supply does not run at 100% efficiency, and some power is lost to the internal components required to convert 120V 60Hz AC wall power to the DC power required for running the stepper motors.

Therefore, the power supply selected for this application was rated for 75W which allows for around 89% efficiency for the worst case scenario of both motors drawing power at the same time. Given that movement on the axes is unlikely to occur simultaneously based on the needs of the system, the motors should not draw power at the same time, and the software will be designed to avoid full power to both motors occurring at the same time. However, there could still be some residual power draw depending on the timing between motor pulses and potential overload or backlash if the scanner is misaligned or encounters some resistance.

5.3.3.5 Circuit Breakers

One of the main protections to put in place to protect subjects from electric sock is overcurrent protection. There are two common ways to protect a circuit from current draw: fuses and breakers. Both methods, when the current is too high, will create a short circuit, removing all current flow from the circuit. When fuses short, they must be replaced. However, when breakers short, they can be switched back on. For this convenience in the longevity of the machine, breakers were chosen for this application. Breakers were placed in between the wall power and the power supply, and between the power supply and each motor. The current rating was chosen using the equation P/V =I, where P is the power rating of the power supply and V is the voltage from the wall and from the power supply. Using a 130% overload protection, the estimated current draw was 0.8 A from wall power and 4 A from power supply. Therefore, a 1A type C circuit breaker was inserted between wall power and the power supply and a 4A type C circuit breaker was inserted between each motor driver and the power supply.

5.3.3.6 Final circuit diagram

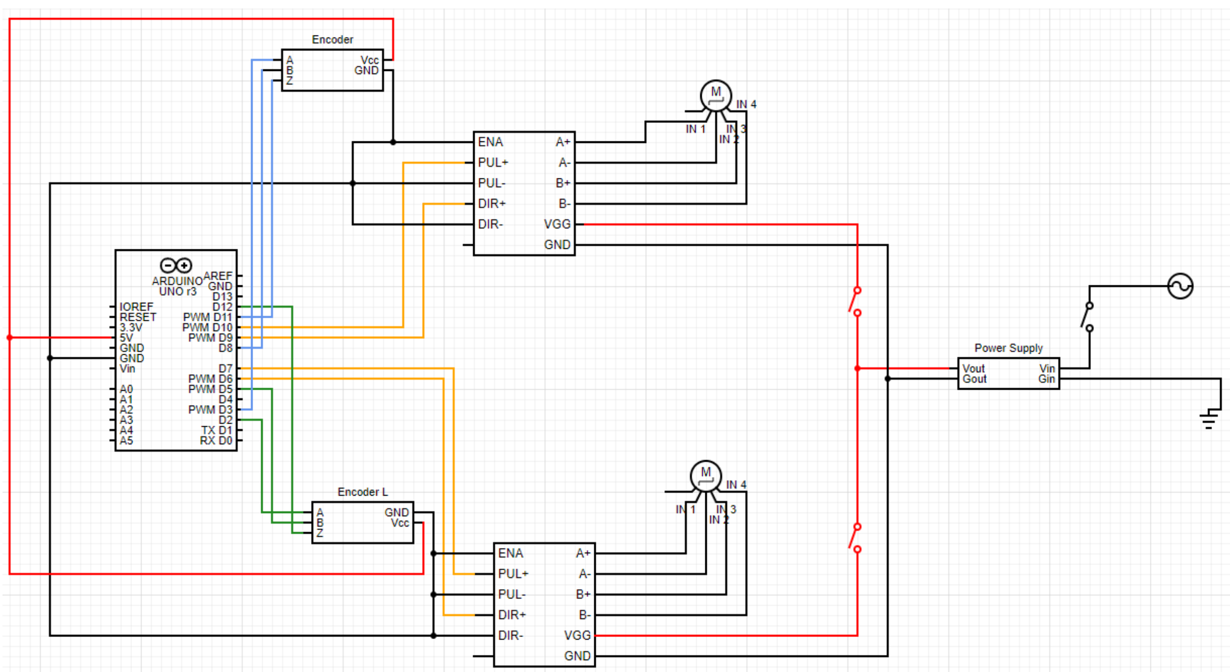

Figure 5-8: Final Circuit Diagram

5.3.4 Constructed scanner

The constructed scanner can be seen in Figure 5-9. The linear motion element consists of two linear actuators (CSLSM10AHXR1ZF-2LT-0240-0 and CSLSM10AHXR1ZF-2LT-0440-0, PBC

Figure 5-9: The final constructed scanner including both mobile halves secured together, a set of stairs with handles, motors, linear actuators, and DIN rail mounted electrical system, HDPE plate and water bath, and a chair for the subject to sit on during unweighted data collections.

Linear, Roscoe, IL,USA) secured perpendicular to each other using a manufacturer-provided mount, each of which is attached to a stepper motor (NEMA17-16-06PD-AMT112S, CUI devices, Lake Oswego, OR, USA) via a 4mm diameter set screw flexible shaft coupling. The actuators are secured to the t-slot frame using custom-designed parts printed on a Stratasys F370 in acrylonitrile styrene acrylate (ASA). This scanning mechanism is mounted on the t-slot frame, using additional custom-designed parts printed in ASA. The surface of the scanner is one inch thick high density polyethylene (HPDE). A 14.5" x 8.75" window with a 0.5" lip was milled into the HDPE at 3.5" from the front and 6" from the right side of the plate to allow attachment of an interchangeable thinner HDPE pane for imaging. Four holes were drilled into the lip, on in each corner such that ¼-20 fasteners could be used to further secure the interchangeable plates. Finally, aluminum safety rail was added around the perimeter of the scanner to create a more secure environment for subject safety and comfort. The safety rail was secured through the HDPE plate and directly into the t-slot frame. The scanner was made from two parts and mounted on locking wheels for improved mobility, as it was designed be used and stored in different areas. The 8 legs of the t-slot frame were fitted with 3" rubber caster wheels which were secured directly to the center hollow of the t-slot rail. The two sides of the scanner lock together using a custom designed locking pin mechanism mounted to the t-slot legs.

A DIN rail system designed to hold the electrical system was mounted to the t-slot rail using custom designed pieces printed in ASA. The DIN rail system was attached to the front half of the scanning platform for proximity to the motors.

5.4 Software design and development

The scanner hardware involves several different components that must be controlled in the appropriate order at regulated time intervals, necessitating custom automation software. In particular, the ultrasound image acquisition and the motor linear translation should be synched to allow image acquisition at regular intervals and allow for easier image reconstruction. The Aixplorer has an available research package that allows direct image acquisition through a MATLAB interface, making MATLAB the ideal choice for a control software despite its lack of real-time processing. Therefore, an image acquisition graphical user interface (GUI) was developed in MATLAB to perform the scanner control.

5.4.1 The user interface

The user interface contains five sections: subject demographics and test information, quality control checks, imaging parameters, a digital motor positioning system, a scan time estimator, and safety features.

5.4.1.1 Subject demographics and test information

Some demographic information is required from each subject to set up the scan. The number of images taken and number of longitudinal scans performed will depend on the length and width of the subject's foot. Additionally, the anonymized subject ID will link the scan to other subject data taken during the clinical scan and plantar pressure testing. Five demographic and test information fields appear on the GUI:

- Scan type.
    - This field is used in the backend to create the correct motion trajectory. Distance between images and motor timing are different depending on whether the scan is take with B-mode or SWE, and whether the scan is taken weightbearing or not. This field also serves the purpose of labeling each scan as weighted, unweighted, SWE, or Bmode, removing the possibility of acquired scans being unlabeled.
- Foot Length
    - The foot length is used to determine the number of images taken and the length of the scan. Scans are customized for each subject to reduce testing time and ultrasound dose.
- Foot Width
    - Similar to foot length, foot width is used to determine the number of overlapping longitudinal scans that must be taken. Scans are customized for each subject to reduce testing time and ultrasound dose.
- Subject ID
    - The subject ID is a unique identifier that is attached to the data to protect the privacy of human subjects. This ID allows correlation of acquired scans with other study data.
- Aixplorer IP
    - This field is used to store the Aixplorer IP address, which is used to communicate with the Aixplorer and enable MATLAB-controlled image acquisition.
- COM port

- This field is used to store the COM port to which Arduino is connected. Arduino creates a virtual serial from the USB port and as such the COM port may change depending on the board connected and the USB port used.

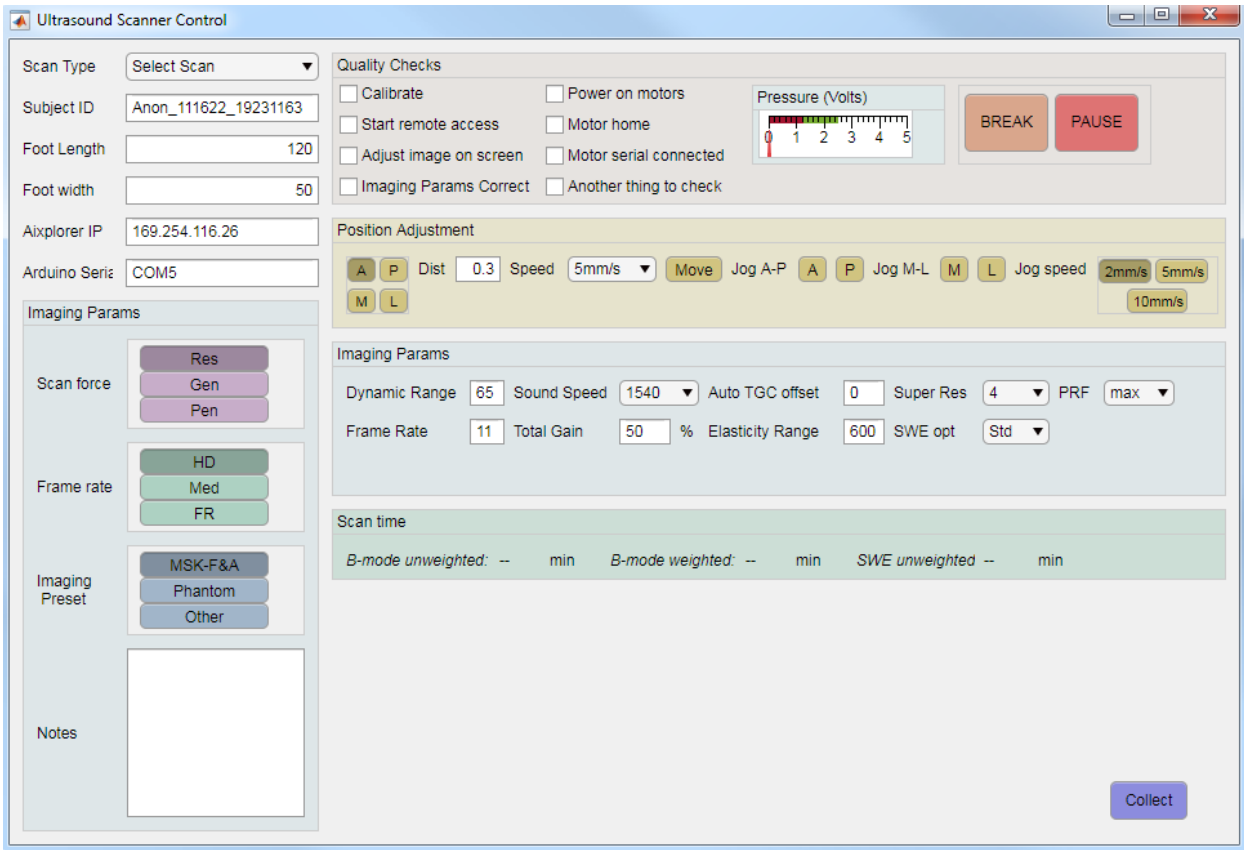

Figure 5-10 The Graphical User Interface through which the operator interacts with the scanning software during collection of a volumetric ultrasound scan.

5.4.1.2 Quality control checks

There are several failure points for both scan acquisition and scan quality. Several checks are implements to avoid these failure points and are displayed on the top of the GUI:

- Calibrate
    - This check reminds the user to perform calibration of the system prior to beginning a scan of a subject. This ensures that the user has checked that the scanning system

is operating as intended and ensures that a reference calibration image is available should issues arise in post-processing.

- Start remote access
    - In order to allow MATLAB acquisition of ultrasound images, the remote access must first be enabled through the Aixplorer user interface. This check ensures that this critical step is completed prior to attempting to acquire a scan.
- Adjust image on screen
    - This check ensures that the user has first adjusted the ultrasound image for clarity for each subject before acquiring a scan. This ensures high quality images are taken in the scan.
- Imaging params correct
    - This check ensures that the user has correctly changed the imaging parameters to reflect those parameters that have been adjusted for the subject.
- Power on motors
    - This check ensures that the motors are powered on and ready to complete the motion trajectory for the scan. This check avoids a potential situation where all images are taken of a single location, both ensuring efficient use of time and prioritizing subject safety as repeated imaging of one location can lead to increase temperature in the tissue.
- Motor home
    - This check ensures that the motors have been set to their home location for the scan.
- Motor serial connect

    - This check ensures that the motors are connected to the serial COM port to allow Arduino communication to control the motors.
- Pressure monitor
    - Excessive pressure on the transducer could harm the transducer. Additionally, changes in pressure can affect the ultrasound reading. This gauge would allow the user to monitor the pressure and stop the test should the pressure become too high.
- Programmatic emergency stop
    - The programmatic emergency stop is designed to allow the user to stop an acquisition in the event of user error or an issue with the scan being acquired. This safety stop should be used for low-stakes issues such as poor image quality, significant subject movement, or incorrect input parameters. The physical breaker is provided for serious equipment issues.
    - There are two stop features due to the limitations of MATLAB.
        - BREAK The break function will break a loop. This function will exit the longitudinal scan and the manual move command loops. However, since the transverse move and jog functions are executed in Arduino, this button will not pause these commands. The hardware Estop is recommended for these situations.
        - PAUSE The pause button will execute the pause command, which halts all MATLAB function until the user enters a keystroke in the command window. The program will continue when a keystroke is entered in the command window, allowing the user to resume the program.

5.4.1.3 Imaging parameters

Imaging parameters such as frequency, frame rate, imaging presets, dynamic range, assumed sound speed, pulse repetition frequency, gain, and averaging can all greatly affect the image quality and speed of image update. These parameters are important to record for each scan in the event that issues with image quality appear in post-processing or to reference issues related to incorrect measurements. Therefore, each of these scan parameters is displayed prominently on the GUI screen to facilitate user input.

On the left hand side of the screen are buttons for the main imaging parameters: ‘Scan Force’ (frequency), frame rate, and imaging preset. These are ‘common sense’ parameters typically displayed on commercial ultrasound systems and select background processing processes within the commercial ultrasound software.

The ‘Scan Force’ (Res/Gen/Pen) setting adjusts the frequency of the ultrasound wave. The resolution setting uses a higher frequency to allow better axial resolution at the expense of penetration depth. The Frame rate setting (HD/Balanced/FR) adjusts scan line density to trade off between spatial and temporal resolution. The imaging preset contains initial parameter values such as gain, color map, filter, or expected tissue speed of sound that have been optimized for a particular tissue. The foot and ankle subset of the musculoskeletal preset is most likely to be used for this application, however, due to the thickness of the plate and other intervening materials, it is possible that this preset may not be optimal for different acquisitions. Therefore, there are additional options for this setting in the software.

On the right hand side of the screen is a second imaging parameters box with the more advanced settings. The dynamic range controls the mapping of returning ultrasound amplitudes to displayed image intensities. A larger dynamic range maps amplitudes to a wider range of intensities.

The sound speed is related to image reconstruction. When reconstructing an image, the software assumes a speed of sound to place reflections at appropriate spatial locations based on the time required to receive the reflection. This time is based on the speed of sound through the material being imaged. Incorrect sound speed can introduce error in distance measurements.

Super resolution is an image processing technique that reduces speckle and enhances borders by combining multiple steered echo lines to create a composite image. Tracking the number of lines combined is important for interpreting image quality issues.

The pulse repetition frequency (PRF) refers to the number of ultrasound pulses emitted by a transducer over a period of time. A lower PRF (longer time between pulses) may reduce some types of artifacts and may allow larger image depths. A higher PRF may allow more send-receive cycles and subsequently more sophisticated signal processing to improve image texture without sacrificing frame rate, or may improve frame rate.

The frame rate is determined automatically by the combination of previously mentioned parameters. However, recording the frame rate is useful for assessing motion artifacts in reconstruction and can be useful for informing changes to the protocol.

The total gain is determined by a total gain parameter, the time gain compensation offsets, and dynamic range. The total gain is useful to record as a well-balanced gain is important for image reconstruction and segmentation.

For SWE acquisitions, the additional parameters of maximum elasticity (elasticity range) and SWE opt should also be recorded. The maximum elasticity gives the anticipated maximum recorded shear wave speed, which is used to process SWE volumes, while the SWE opt, similar to the ‘Scan Force’ determines whether the SWE pulse is optimized for resolution or depth.

5.4.1.4 Position Adjustment

During data acquisition, there could be a need to move the transducer a small amount in each direction to align with the subject's foot or to reposition the motors and the transducer after some change to the configuration. The position adjustment section was added to facilitate these manual movements and includes two methods:

- Move
  - These commands allow the user to select an axis and direction (anterior, posterior, medial, or lateral), a distance between 0.3 and 50mm, and a speed between 2 and 10 mm/s. When the user presses the 'move' button, the selected axis will move the prescribed distance at the selected speed.
- Jog
  - These commands allow extremely fine tuning and are equivalent to the move command with the distance set to 0.3mm. Each of the four buttons will jog a single step in the anterior, posterior, medial, or lateral directions. The motor speed can also be selected – either 2mm/s, 5mm/s, or 10 mm/s

5.4.1.5 Scan Time

The time required for a single scan varies with the length and width of the foot. In order to assist the operator in guiding the subject through the scan, the estimated time to complete each of the three scans is displayed on screen after the operator fills in the subject's foot length and width.

5.4.1.6 Safety features

In addition to the aforementioned break and stop features, the program performs several checks before starting to prevent potentially common errors. If the quality control checkboxes are not checked, the scan type is not selected, or the foot length or width are outside of pre-defined reasonable ranges, the scan will fail to start. Additionally, if the user fails to change the subject ID, foot length, or foot width, the program will create a warning pop-up window.

5.4.2 The control code

Ultrasound imaging and transducer translation were synchronized through use of the advanced research package provided by the ultrasound manufacturer, which uses a MATLAB interface to control the ultrasound acquisition.

Three functions were investigated for image acquisition: getSWE, getEcho, and getLiveImage. getSWE and getEcho return a single shear wave or echo (B-mode) acquisition along with an informational structure that includes the resolution and position of the values within the frame. However, getSWE does not return the underlying B-mode image to orient the stiffness values to the underlying tissue. getLiveImage returns the image as displayed on screen along with a structure containing resolution information.

getLiveImage was selected as the method of image acquisition for B-mode scans, while both getliveImage and getSWE were employed for SWE scans. The time required to acquire a single image is a limiting factor in the length of the full scan as the anterior-posterior resolution must be balanced with the total scan time. The time required to acquire a single image was measured on three different computers to measure the effect of different hardware on image acquisition time. The main limiting factor on image acquisition speed is the speed of the ethernet connection between the ultrasound and the control computer (Table 5.4-1). A 1GB or higher ethernet speed is required for sufficient speed to acquire images. With a 1GB Ethernet speed, acquisition of a single image was returned in ~0.1s on average.

	Processor speed (ghz)	RAM (gb)	GPU	Ethernet	Time per image (s)
Laptop1	2.9	8	-	10MB	1.53
Desktop1	2.13	14	1	1GB	0.04
Desktop2	2.6	96	2	1GB	0.035

Table 5.4-1 Hardware specifications of computers used to test image acquisition time through the Aixplorer MATLAB-based research interface**.**

Both getLiveImage and getSWE contain the option to acquire a loop of images ('all') or a single image ('last'). The loop feature causes MATLAB to hang for live image acquisition. However, the single frame option does not reliably pull the correct SWE data for the live image frame. Therefore, the 'last' option was selected for the B-mode imaging, while raw SWE data was acquired using the 'all' option.

Control of a stepper motor requires rapid, real-time communication with the electronics. However, MATLAB has a communications delay. In order to interface motor control with MATLAB, an Arduino was chosen for its ease of access and usability. While there is a MATLAB add-on that allows control of Arduino read and write using MATLAB commands, these were too slow for this application.

As a result, serial communication was used to trigger a specific motion control and sensor read sequence, and the sensor information was sent back to MATLAB and recorded via serial communication. In this way, high motor speeds could be instructed and high speed encoder data recorded. The Arduino control code can be found in Appendix B. Briefly, the MATLAB program sends a three- to five-character sequence consisting of a number identifying the type of move, the direction to move, speed (for jog and move), distance (for jog and move), and a character signifying the end of the sequence. The key for the digits in each position can be found in Table 5.4-2. Within the Arduino code, the microcontroller waits for data to arrive in the serial stream, then reads it in, stores the initial two characters in an array, and uses these characters to select the hard-coded function with the appropriate motion control and sensor read sequences.

Digit	Scan type	Direction	Speed (jog and move)	Distance (move)
1	longitudinal (A-P) B-move	anterior	2mm/s	0.3mm
2	0.35mm transverse move	posterior	5mm/s	1mm
3	longitudinal SWE move	medial	10mm/s	2mm
4	jog	lateral		5mm
5	move			10 mm
6				20mm
7				50mm

Table 5.4-2: Value associated with digit in the first (Scan Type), second (Direction), third(Speed) and fourth (Distance) position of encoded sequence sent to the Arduino to control motor motion.

While the motor speed, step size, and sensor information is hard-coded at this time, this structure is flexible and these parameters could be incorporated into the GUI for user input control by adding additional input characters to the serial read sequence and updating the appropriate areas of the Arduino code. Such user-control could be advantageous for additional applications of the scanner that may need coarser or finer resolution, or that wish to trade-off resolution for scan speed.

5.4.3 Post-processing, stitching, and volume reconstruction

5.4.3.1 Ultrasound Registration and Stitching

The full-plantar surface scan is created from 2 to 4 longitudinal passes. Each of these passes must be registered to the others and stitched together in order to create a cohesive volume. There are a variety of techniques to register and stitch images to create accurate and cohesive reconstructions. However, investigations into several automated techniques was not satisfactory. Therefore, a manual registration GUI was devised to facilitate manual registration of the images.

The manual registration GUI asks the user to select an ultrasound scan file, reads in the ultrasound image data, and overlays the appropriate scans from each pass based on the parameters selected and the knowledge that the first and third passes start from the posterior extent (heel) and the second pass starts from the anterior extent (toe).

The right hand side parameters section of the GUI consists of an initial section of the current image number, the folder to save the images, and the file format to save the images. The current image number is automatically changed using the “previous’ and ‘Next’ buttons for incremental image adjustments but also allows user input to start at or jump to a desired image. The second sections involves parameters used to register and stitch images from pass1 to pass2. The third section involves parameters to stitch pass2 to pass 1 and 3. These two parameters are simply the amount to crop from the left and right hand sides of the image to facilitate smooth and unobtrusive stitching seams. The fourth section is similar to the second but for the third pass. On the bottom of the parameters section are buttons to increment the image number and allow adjustments of sequential images. When the ‘Next’ button is depressed, it triggers a function that saves the stitched image to the save folder, appends the stitched image to the stitched volume and the transform parameters to a matrix, and changes the current image to the next image. If there are not additional images to stitch, the ‘next’ function will save both the stitched volume and the transform parameters to the save folder. The ‘Previous’ button only changes the current image to the previous image. If the image number is changed manually, it does not trigger a save function.

Future improvements to the GUI might involve automatically calculating and initial horizontal and vertical offset using the saved encoder information. Future improvements to the stitching protocol would involve identifying a method to automatically register and stitch the passes to reduce manual worktime involved in reconstructing scans.

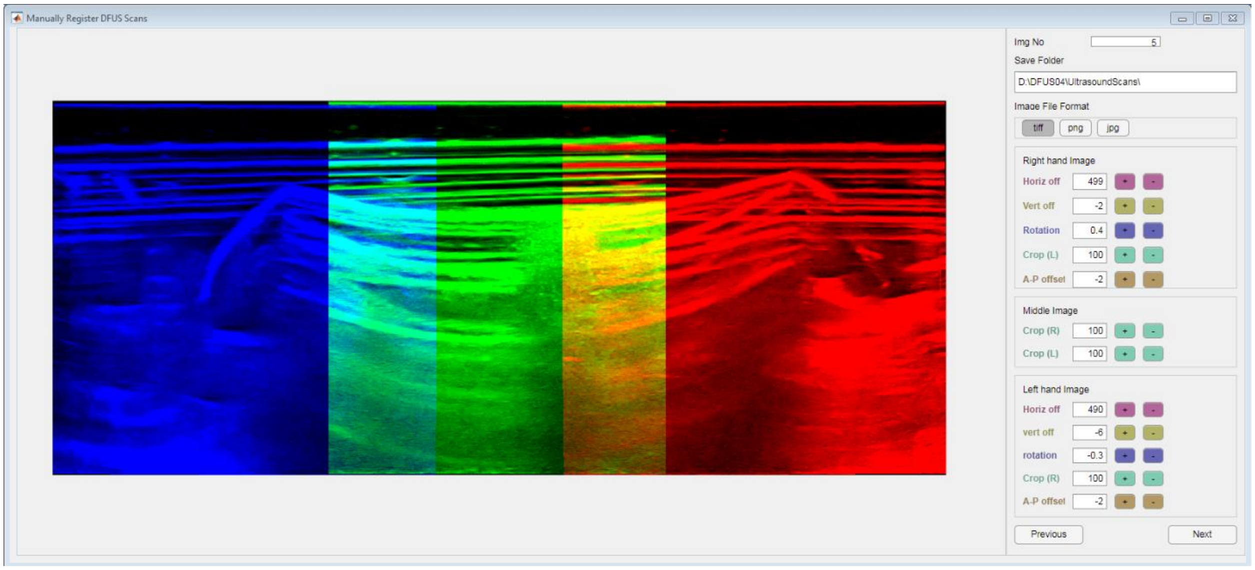

Figure 5-11 Manual registration GUI. Overlapping areas should be teal and yellow for a good registration. Buttons and user input fields allow incremental adjustments or large jumps.

5.5 Validation and Safety testing

Development of a novel imaging scanner requires rigorous testing to establish the validity of volume reconstruction and measurements. A realistic phantom is useful for this repetitive testing. Additionally, a shelf-stable phantom designed for this purpose serves the dual purpose of acting as a validation and calibration for future quality control of the scanning system.

5.5.1 Proof of concept phantom

Commercial block-encased phantoms are difficult to use with the developed scanner. The offset needed between the phantom surface and the surrounding walls increases the required acoustic power, depth, and focus required for adequate visualization, making it difficult to determine appropriate settings. These phantoms are also typically rectangular and have simple, small, regular geometries which may not accurately reflect the challenges in reconstructing volumes from multiple passes. Therefore, a phantom was designed to meet several criteria:

- Visible on X ray and ultrasound to allow co-registration of CT and ultrasound for validation of measurements against a known validated imaging modality
- Multi-layered to visualize different textures, validate out-of-plane resolution in reconstructed volume
- Large, known-dimension inclusions for easy visual assessment of accuracy and interpolation as well as smaller wire inclusions to assess accuracy and resolution.
- Shelf-stable, not prone to desiccation
- Easy to place on the scanner, no or minimal offset between phantom surface and scanner surface

5.5.1.1 Phantom design

The phantom was designed to create a pattern that would only be clearly resolvable in three dimensions (Figure 5-12), making it possible to assess the ability of the scanner to take equidistant steps and to assess the predetermined z-direction resolution on reconstruction. Six copper core, PVC-jacketed wire inclusions were chosen with varying diameters (Table 5.5-1) all larger than the minimum resolution of the ultrasound (0.0512mm/px). In order to improve discrimination of the wires, each wire was cut to a different length so that the length of the wire could be correlated to its diameter on the ultrasound. Wires were cut between 14-26mm long, with the longest also being the thinnest. As PVC may change the wire diameter, all wires were partially stripped to aid discrimination of each wire in the resulting volume.

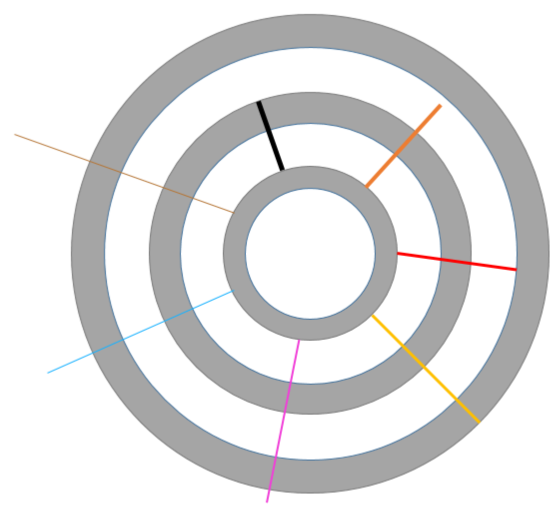

Figure 5-12 Design of proof of concept phantom

Color	Gauge (AWG)	OD (mm)	Wire diameter (mm)	Solid or stranded	Length (mm)
Black	22	1.37	.65	Solid	14
Orange	24	1.32	.51	Solid	16
Red	26	1.21	.48	Stranded	18
Yellow	28	1.13	.31	Solid	20
Pink	30	.78	.26	Stranded	22
Bright blue	30	.5	.24	Solid	24
Brown	30	.63	.21	Solid	26

Table 5.5-1: Sizes and colors of wire inclusions in proof of concept phantom

Additional inclusions were designed in a circular pattern that would show up as a line or block on a single image, but would create a circular observable pattern in the 3D reconstruction. Three rings were printed on a Stratasys F370, each with different outer diameter, width, and thickness. The inclusions were printed out of ASA, which is similar to ABS, a material that has relatively similar properties to soft tissue. The similarity between ABS and soft tissue may enable measurement of the inclusion thickness, however, air inside the part due to imperfect printing may reflect the acoustic signal and create shadow.

5.5.1.2 Casting

The phantom was cast in a 96 mm diameter x 16mm height petri dish in several layers. The first layer was made from Gel #0 (Humimic Medical, Greenville, SC, USA; modulus 0.57Mpa, speed of sound 1449.3m/s) with glitter scatterers, and the medium printed ring was molded into this layer. A layer of no-scatterer Gel#2 (Humimic Medical, Greenville, SC, USA; modulus 0.26Mpa, speed of sound 1457.4m/s) was added on top of the first layer, and the wire and smallest ring were molded into this layer. A final layer of glitter scatterer Gel #0 and

Figure 5-13: Final molded proof of concept phantom

Gel#2 mixed were then poured and the final, largest printed disk was molded into this layer (Figure 5-13).

5.5.1.3 Ultrasound scan of phantom

The phantom was scanned with a variety of settings to choose the final settings for the ultrasound scanner. A representative scan is shown in Figure 5-14. Unfortunately, both the plastic petri dish mold and the circular inclusions caused acoustic shadowing and reflection, which obscured the wire. Additionally, the commercial medical gel is prone to retaining bubbles, adding additional scatter and occlusion, depending on how large the air bubble is. However, the circular inclusions and speckle are still useful for troubleshooting aspects of the scan such as stitching, scan length, and scan time and for assessing the accuracy of the reconstruction. Additionally, this phantom was used to validate the feasibility of obtaining SWE signal through the scanning plate and reconstructed into a volume.

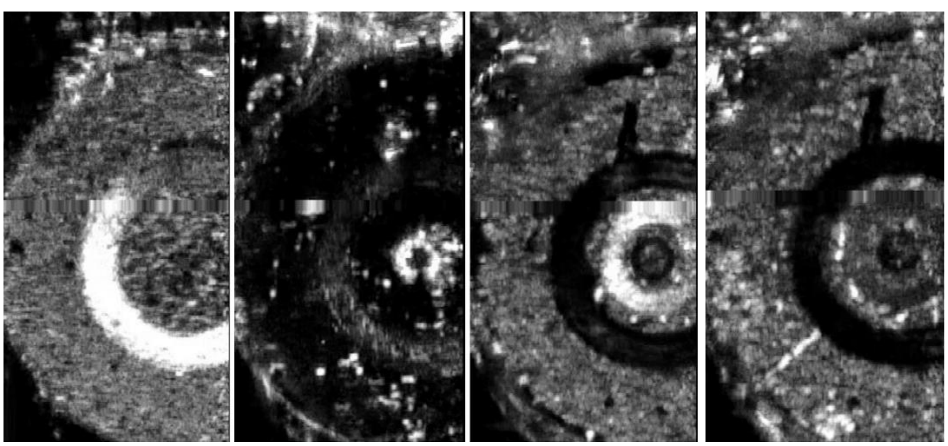

Figure 5-14: Ultrasound of proof of concept phantom reconstructed and displayed in the transverse plane. From left to right: large, small, and medium rings. Right: A wire inclusion is visible on the bottom and an air inclusion is visible on the top.

The rings were segmented and measured in Mimics (Materialise, Leuven, Belgium). The measurements from each scan relative to the expected measurements can be found in Table 5.5-2.

The similarity between the measured and actual ring diameters, widths, and thicknesses lends confidence to the volume reconstruction.

Ring	D_*expected*	D_*meas*	w_*expected*	w_*meas*	t_*expected*	t_*meas*
Outside	48 mm	48.8 mm	16 mm	17.3 mm	5 mm	.84 mm
Middle	24 mm	25.6 mm	8 mm	10.1 mm	3 mm	.93 mm
Inside	10 mm	10.7 mm	4 mm	5.5 mm	1.5 mm	.78 mm

Table 5.5-2. Dimensions of the rings embedded in the proof of concept phantom expected based on stereolithograph file sent to 3D printer and measured from resulting 3D ultrasound image. D = diameter, W = width of the ring, T = thickness of the ring.

5.5.1.4 Computed tomography

The inclusions in the proof of concept phantom are visible on CT, however the metal of the wires does create metal artifacts (Figure 5-15). Future work could improve on this phantom design by selecting materials that will not scatter as much as metal.

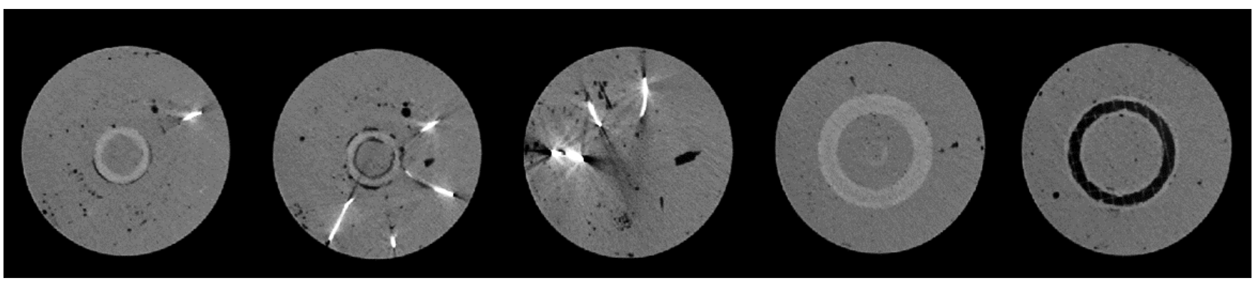

Figure 5-15. Computed tomography scan of the proof of concept phantom. Wires create metal artifacts in the reconstructed phantom.

Ultimately, this phantom design is distinguishable on both ultrasound and CT with minor image processing adjustments and represents a useable standard for development of the ultrasound scanning device. This phantom also enabled validation of the reconstruction process through measurements of the diameter and thickness of inclusions on the volumetric ultrasound scan.

5.5.2 Anatomically Realistic Foot Ultrasound Phantom (ARFUP)

Additional concerns of imaging the foot that are not addressed by the initial phantom include the unique geometry of the plantar surface, the varying depth of the plantar soft tissue, and the size of the foot. A second phantom was designed to meet several criteria:

- Multi-layered to visualize different textures, validate out-of-plane resolution in reconstructed volume.
- Small, anatomically realistic 3D printed inclusions of complex shapes to assess ability to reconstruct and visualize complex geometries.
- Shelf-stable, not prone to desiccation.
- Variable minimal offsets between phantom surface and scanner surface to test coupling methods and arch visibility.

5.5.2.1 Phantom design

The phantom was designed in three parts: the whole foot, the fat pad layer, and the bony inclusions. The manufacturing process was a combination of additive manufacturing and casting.

5.5.2.1.1 Whole foot

First the entire foot volume of a right foot was segmented from an MRI scan of a prior study[29,209] using thresholds of 14 and 324 for the upper and lower gray value. This segmentation was cleaned using hole fill and morphological tools in Mimics. Once a fidelic segmentation was obtained in the mask feature, a part was created from the mask and exported to a stereolithography (STL) file.

5.5.2.1.2 Plantar fat

Next, a second mask was created from the same MRI scan using thresholds for 48 and 313 for the upper and lower gray value, which corresponds to roughly the values present in the layer of plantar fat. However, this large range of gray values also includes many other tissues in the scan.

Therefore, several passes of morphological operators and some manual slice edits followed by minor hole filling was required to isolate the plantar fat. Once a satisfactory plantar fat segmentation was achieved, a part was created from the mask and exported to an STL file.

This STL file was then imported to nTopology. The imported body was converted to an implicit body, which allowed for the software's rapid lattice visualization. A gyroid lattice was applied to the plantar fat volume with a cell size of 15x18x25mm and a wall thickness of 1mm to create an approximation of the whorled plantar adipose septal structure[12]. The lattice was converted into a mesh and exported as an STL file. The mesh size was reduced in MeshLab before printing.

5.5.2.1.3 Pedal bones

The bones of the foot were segmented from a CT scan[210] corresponding to the MRI used. The Mimics bone preset was used to create an initial approximation of the bony structure, which was then finalized using morphological operators and multi-slice edit tools. The bone segmentation was dilated so that all bones were connected for ease of printing. Once a satisfactory segmentation was achieved, a part was created from the mask and exported to a STL file.

5.5.2.1.4 Mold for casting

The mold for casting was designed in SolidWorks. A foot-shaped solid was created with contoured edges to save printing material. Several counter-sunk holes were added to use as a means of clamping the two sides together during casting. The whole foot volume was imported to SolidWorks and a cavity was generated in the solid from the foot volume. Finally, the solid with the cavity was split in such a location that the unmolding process would not damage the final phantom.

5.5.2.2 Printing and Casting

The mold and attached bones were printed using acrylonitrile styrene acrylate (ASA) on a Stratasys F370 filament deposition printer. The latticed plantar adipose septal structure was printed using Tango Grey on a Stratasys Connex 3 polyjet printer.

After support material was removed from the prints, the mold was prayed with a mold release spray and the attached bones were coated in silicon carbide powder to increase reflection at the bone interface since ASA is acoustically similar to soft tissue while bone is not.

Two medical gels (Gel #0 and Gel #2) from Humimic medical were melted according to manufacturer instructions. These shelf stable ballistic gels are designed to mimic the material properties of muscle or skin (Gel #0) and subdermal fat tissue (Gel #2). A small amount of scattering material (craft glitter) was added to Gel #0 to create visual contrast between the two clear gels. To begin, a thin layer of Gel #0 was poured into both sides of the mold to simulate skin. After that layer set, a small amount of Gel #2 was poured into the bottom mold and the plantar fat lattice structure was pushed into the hot gel to encourage perfusion of the gel through the lattice holes. Another layer of Gel #2 was poured on top of the lattice to fill the lattice and create the plantar fat layer. While this layer cooled, a small amount of Gel #0 was poured into a freehand shape resembling

Figure 5-16: ARFUP with gyroid lattice visible through the clear gel.

the plantar muscles for an additional layer of anatomically realistic contrast. This structure was placed on top of the plantar fat structure, the attached bones were placed on top of this structure, and the top half of the mold was secured. Finally, the remaining Gel #2 was poured into the mold, and the mold was tilted in order to make sure the gel flowed into the toe region of the mold. Finally, the remaining Gel #0 was poured on top of the final Gel #2 layer to form a continuous skin layer on the outside of the phantom. The phantom was allowed to cool for 30 minutes before being unmolded. The clarity of the gel allows visualization of the underlying geometry, which aids orientation and comparison of reconstructed scans to the phantom (Figure 5-16).

5.5.2.3 Ultrasound of Phantom

A B-mode volumetric scan of the phantom was taken using the SL18-5 transducer (SuperSonic Imagine, Aix en Provence, France), rigidly registered using built-in MATLAB functions, and reconstructed in Mimics. The phantom appears similar to a foot on ultrasound (Figure 5-17).

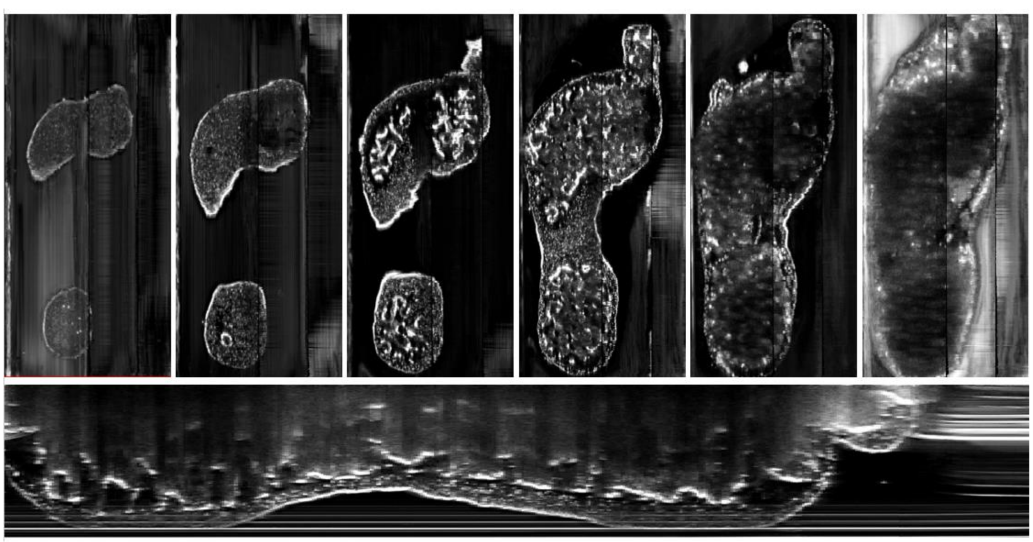

Figure 5-17 Slices through the transverse plane of the reconstructed ultrasound volume of the ARFUP demonstrating capture of the gyroid lattice structure. Bottom: sagittal plane slice of the reconstructed ultrasound volume.

However, there is less contrast at the bony interface and more attenuation through the fat layer than is seen in an *in vivo* scan, and the lattice reflects more strongly than typical soft tissue structures. These issues could likely be mitigated by painting a metallic layer onto the bone, printing the bone out of a different material or casting the bone from a harder material, and printing the lattice structure out of a material that is better acoustically matched to soft tissue and the surrounding gel. It is also possible that using a different gel that attenuates less may allow more acoustic signal to reach deeper into the tissue.

5.5.2.4 Computed tomography

The inclusions in anatomically realistic phantom are visible on CT. However, the materials do not provide as clear of contrast in CT as they do in ultrasound. The density of the ASA and Tango inclusions are close enough to the density of the Gel #0 and Gel #2 to make them difficult to distinguish without contrast enhancement.

Figure 5-18 Computed tomography scan of the ARFUP. Material densities are close to each other, making a low-contrast image. However, inclusions are visible in the scan with minor contrast enhancement.

Future work could improve on this phantom design by selecting materials with increased variation in density to allow better visualization on CT. However, this density variation would need to be accompanied by a variation in sound speed to ensure that the ultrasound image is not significantly affected.

Ultimately, this phantom design is distinguishable on both ultrasound and CT with minor image processing adjustments and represents a useable standard for development of the ultrasound scanning device. Additive manufacturing is valuable for creating an anatomically realistic phantom due to the ease of manufacturing complex structures, and is a valuable method of creating a reusable validation phantom for creating novel scanning systems as the measurements made from the scan can be validated against the known measurements used to create the phantom.

5.5.3 Safety

Relative to other medical imaging modalities, ultrasound is generally considered safe. However, one bioeffect that has potential to be detrimental is the increase in tissue temperature due to the dissipation of ultrasound energy as heat. Shear wave elastography uses more energy than typical B-mode imaging, increasing the potential for adverse biothermal effects. In order to ensure the safety of the prolonged imaging required for this protocol, a temperature testing protocol was employed.

A waterproof DS18B20 temperature sensor was connected to an Arduino as depicted in Figure 5-19. This temperature sensor was used to measure the increase in temperature associated with B-mode and SWE imaging during a large scan, defined as 300mm longitudinally and three overlapping scans, corresponding to a size 12.5 men's shoe. This scan corresponds to across two different phantoms.

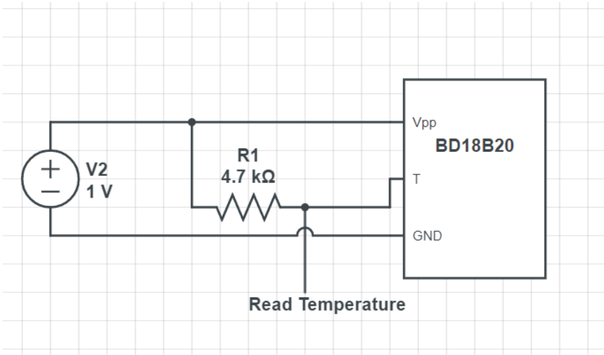

Figure 5-19. Circuit used to read temperature data from the temperature sensor.

The first phantom was a small quantity of Aquasonic 100 gel. Aquasonic gel is thermally similar to biological tissue and is easy to apply, making it an ideal candidate for this testing. However, it is difficult to measure the exact quantity of gel used. The volume of gel used was calculated in ImageJ by manually defining the barrier of the gel in one top-down and one side-view image which were calibrated using in-frame rulers (Figure 5-20, a&b). The quantity of gel was determined to be 36cm^3.

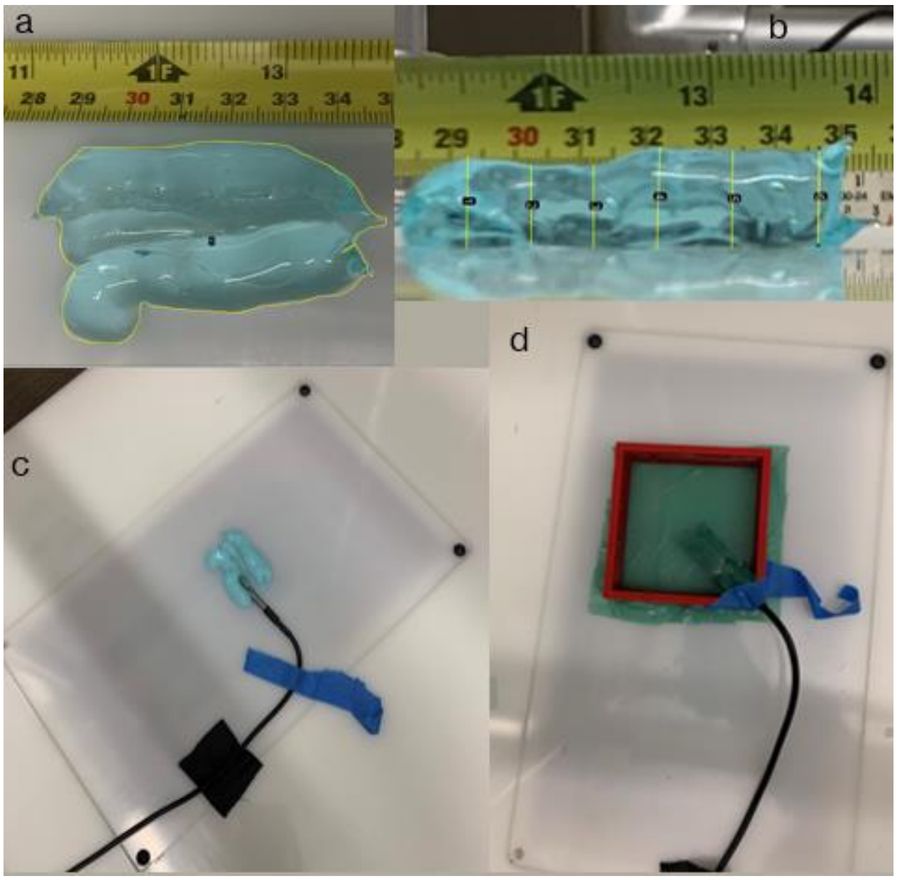

Figure 5-20 Top: measurements in Image J used to estimate the volume of gel tested. Bottom: Set up of temperature experiments for gel (left) and water (right).

However, this quantity of gel is much smaller than a typical human foot. The volume of the plantar fat segmented in section 7.5.1 for the anatomically realistic phantom was measured at 262.25 cm^3. An enclosure was designed based on this volume to hold water for testing. The water bath was 3. 5” x 3.5” x 1.3” (15.9in^3), or 8.89 cm x 8.89 cm x 3.3 cm (260.9cm^3).

The temperature sensor was submerged in either the gel or the water bath on top of the HDPE scanning plate (Figure 5-20, c&d), and the transducer was positioned directly beneath the phantom. Then the scanning protocol was performed without power to the motors so that the entire acoustic dose of the scan was delivered to the phantom area. One B-mode scan and three SWE scans were acquired and the temperature readout from the temperature sensor was read at 2.8s intervals.

5.5.3.1 Results and Conclusions

The number of image acquisitions, total scan length, time between scans, and total temperature increase are displayed in Table 5.5-3. The absolute change in temperature was higher when increasing from a lower ambient temperature (SWE1 gel and water, SWE2 gel). Temperature increases were higher in the lower volume gel than the higher volume water and in the higher energy SWE scans than the lower energy B-mode scan. The temperature decreased over the course of the B-mode scan. The decrease in temperature may also indicate that the rest time between SWE and B-mode acquisition may not have been sufficient to return the gel to ambient temperature before beginning the test. However, as the temperature did not increase or remain steady, the energy from that scan does not substantially increase the temperature of the imaged volume.

	Water			**Gel**			
	SWE1	SWE2	SWE3	SWE1	SWE2	SWE3	B1
number acquisitions	5400	5400	5400	5400	5400	5400	3090
run time (min)	35.90	36.76	35.84	32.34	36.52	39.60	8.63
rest time (min)		3.24	12.16		141.48	5.40	8.37
Temperature Change (°F)	1.58	1.34	0.79	2.47	5.17	3.04	-0.22
(°C)	.88	.74	.44	1.37	2.87	1.69	-0.12

Table 5.5-3: Time, number of images, and temperature change for each temperature experiment performed on the water and gel conditions

The temperature increase in the foot with activities has been widely studied, and increase in temperature with activity has been correlated with diabetes and ulcer risk. Reddy et. al. measured increase in plantar temperature between sitting, standing, and treadmill walking at three different speeds [211]. They found that plantar temperature increases close to 2 °C with standing and a further 3.5-6 °C with walking, with larger increases during walking among participants at higher ages. Beach et. al. found that simply donning a shoe followed by sitting can increase the temperature at the plantar surface by 2 °C [212]. Within the context of typical temperature increase in the foot with activities of daily living, the measured increase of 0.44 – 2.87 °C due to the SWE scan is within normal variation and is not expected to create risk for the subjects.

Additionally, this study was designed to be a worst-case scenario, wherein the entire scan energy was focused on one static tissue area. In practice, the transducer would be moving and the energy would be distributed over a wider area, and in the event that the transducer got stuck or was not moving, the scan would be ended or the SWE frozen prior to completion of the entire protocol. Additionally, in living tissue, there is regular blood flow and cooling mechanism such as vasodilation and sweating which actively cool the foot. While these mechanisms could be less effective in diabetic tissue due to the effects of diabetes on the vascular system, some amount of cooling is likely to happen.

With the context of typical temperature rise with activity, study design, and active biological cooling, the risk to subjects due to heating from acoustic energy dissipation is low. Additionally, B-mode scans did not increase temperature at all. Therefore, a safety strategy could be to alternate B-mode and SWE scans such that the foot has several minutes to reach homeostasis between scans.

5.5.4 Coupling testing

The two most common methods of coupling the ultrasound transducer to the skin are to use a layer of aqueous gel designed for ultrasound applications or to submerge the area of interest in a water bath. Both of these methods were tested to identify if one option was superior in terms of image quality or subject comfort. In order to test the image quality, several scans were taken using the ARFUP. A 1/8” layer of ultrasound gel was applied to the underside of the 3/16” HDPE plate, which was secured to the cutout of the 1” thick HDPE scanner surface. For the gel coupled scan, a generous amount of gel was applied to the top of the 3/16” HDPE plate, and the ARFUP was placed on top of the gel. For the water bath coupled scan, ARFUP was placed inside the bath and room-temperature tap water was poured into the bath until it reached the level of the arch. The scans were equivalent in clarity. However, in areas of low load that required large quantities of gel, there were occasionally air bubbles trapped inside the gel, which created regions of acoustic shadow. Creating the appropriate distribution of gel to couple the arch was also challenging, and would be more difficult with patient motion. The gel is also slippery and becomes sticky as it dries. Therefore, the water was determined to be superior for subject comfort as it is easier to hold a static position in the water bath and easier to clean the foot after imaging. The drawback of the water bath was a bright acoustic reflection at the superior surface where water meets air. This reflection creates bright artifacts in the tissue directly next to the air-water interface. This issue could be alleviated with a deeper water bath that extends beyond the imaging depth. An additional drawback of the water bath is potential increased risk of injury due to skin softening or drying. This is treated in more detail in chapter 6.

5.5.5 Validation of SWE values through HDPE

The addition of an HDPE plate could interfere with acquisition of SWE in several ways:

1) Increase attenuation of and reduce the power of the acoustic radiation force, causing no or fewer shear waves to propagate
2) Interrupt the signal, causing issues with the reconstruction of the SWE

3) Change the assumed speed of sound so that reconstructed signals are noisy, offset, or incorrect

In order to assess the accuracy of SWE values obtained by imaging through the plate, 100cm diameter phantom discs were molded from the materials in Table 5.5-4. The materials had a range of expected moduli based on prior work (Appendix 0) and commercial documentation. The samples were individually imaged by placing them on top of the SL18-5 probe and allowing the SWE signal to stabilize. In this way, the base SWS and SWE modulus for each disc could be measured with no weight on the sample and only ultrasound gel in between the sample and the transducer. These images were saved using the getLiveImage and getSWE functions. The average SWS was calculated from the SWE value map as the average of all values within the acquisition excluding zeros. The SWE modulus was calculated using average density values from prior work.

Material	Agar (%wt)	Gelatin (%wt)	height	density (g/cm3)	expected mechanical modulus (kPa)
10	0.6	9.99	10.8	0.998	118
15	0.7	14.96	9.9	1.013	170
17.5	1.81	17.57	9.9	1.052	368
20	0.91	20.01	10.1	1.033	311
25	0.77	25.06	10.5	1.056	332
Gel #0			12.2	0.880	570
Gel#2			7.7	0.923	260

Table 5.5-4: Components, dimensions, and expected mechanical modulus of tested phantom materials

As the gelatin-containing discs are sensitive to water absorption, the discs were placed on ultrasound gel rather than into a water bath for coupling. A SWE scan was taken through the 1/8" HDPE plate using 0.8775mm longitudinal resolution and a focal depth of the maximum height of the sample. The live image scan was reconstructed using step gradient descent optimization of a mean squares criterion for registration and taking the average value of the overlapping regions.

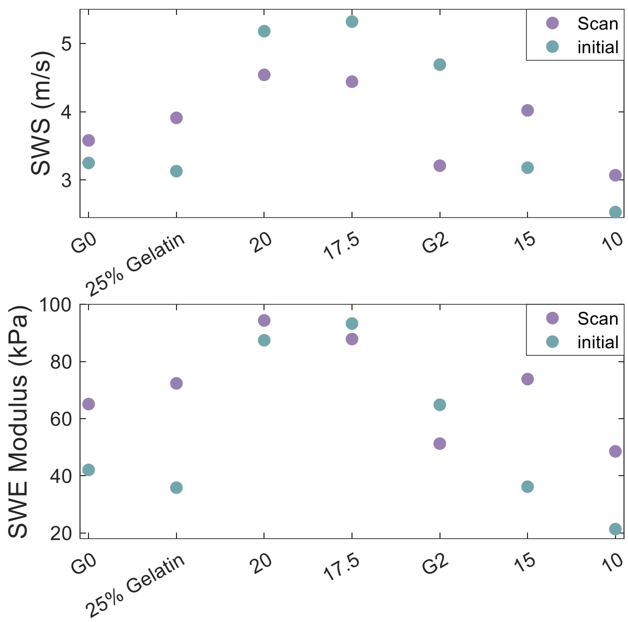

Figure 5-21: Differences in shear wave speed (top) and calculated modulus (bottom) for each of the tested phantom materials.

The shear wave speed value volume was reconstructed by placing the SWE values in an empty array of the image size and applying the calculated offsets to the resulting values matrix to obtain a values-only matrix of the same size as the image volume. The phantom discs were segmented from the SWE scan using 3D slicer[213] and the segmentation was exported in Neuroimaging Informatics Technology Initiative (NifTI) format. The segmentation was imported into MATLAB and used to create binary masks. These masks were applied to the SWE values-only volume and the average shear wave speed was calculated for each phantom disc as the average of all values within the acquisition excluding zeros. The SWE modulus was calculated using average density values from prior work.

On average the absolute difference between measurement with the HDPE plate and without was 0.69 m/s or 16.60 kPa. This difference was not a consistent under or overestimation in the samples measured. In comparison, the difference between measurements of multiple samples made from the same concentration was 0.11 m/s or 0.91 kPa, and the difference between samples of adjacent expected moduli was 1.17 m/s or 31.25 kPa. The difference between expected moduli was 50kPa on average, except for Gel#0, which had an expected modulus 202kPa higher than the next material. 50kPa is a relatively small variation relative to biological tissues which vary in orders of magnitude[214,215]. Additionally, these phantoms vary by much smaller amount than the expected variation in stiffness related to diabetes, which has been reported at 500kPa for both plantar fat and plantar skin[23,24]. The measured SWE moduli were substantially lower than the expected moduli, however, this is expected due to differences in the way the moduli are calculated (Appendix 0). Based on these results, the addition of the 1/8” HDPE plate does interfere with acquisition of SWE signal but in an inconsistent way with an effect size smaller than the difference between phantom materials and is unlikely to affect measurement of general trends in stiffnesses related to diabetes.

5.5.6 Step size testing

In order to achieve spatial resolution on par with other medical imaging systems, a goal of 0.3mm voxel resolution was set to match the resolution of a commercially available weightbearing CT system (Line Up, Curve Beam, Hatfield, PA, USA). The axial and lateral resolution of ultrasound imaging systems are determined by the frequency and beam width of the ultrasound wave emitted by the transducer. These are set within the system depending on the ultrasound parameters discussed in section The user interface. The elevational, or longitudinal, resolution will be determined by the size of the step taken by the motor. Resolution in this direction is inversely related to the length of the scan. Scans were taken at five different longitudinal resolutions in order to assess the tradeoff in clarity and time between different step sizes.

An additional scan was taken with a deeper focal depth to assess the effect of focal depth on image quality, namely the tradeoff between resolution of adipose structures and the discriminability of the intrinsic muscles. While a deeper focus may improve lateral resolution, it may not be sufficient to overcome attenuation and therefore a shallower focus may be more beneficial.

With increasing step size, the adipose chamber walls become less discriminable, and the muscle striations become less clear. There are more registration issues in the 0.5mm step scan, likely due to increased difficulty matching images that may be farther apart and thus less similar between passes. However, the quality of the scan is not seriously reduced with larger steps. Step size could be adjusted on-the-fly based on subject specifics such as diabetes status and foot length to tune the scan time.

Increased image depth resulted in less detail at the most superficial layers of tissue, but resulted in much more detail in deeper layers of tissue, particularly at the midfoot. One of the most limiting factors in terms of deeper tissue discriminability is the reflection of the water level, which obscures the medial and lateral tissue structure. In order to obtain images with sufficient detail to answer questions of interest, structural scans with different focal depths should be acquired if possible.

The same test was performed to assess the difference in measured SWE values with different step sizes. As SWE both has longer single acquisition times (lower frame rate) and requires multiple images for stabilization and averaging due to noisy signal, the SWE images take the longest to acquire and present the highest risk related to skin softening and breakdown due to moisture contact. However, within the axial-lateral plane, the resolution of SWE values is about four times lower than that of the underlying B-mode image. Therefore, a four-fold reduction in longitudinal resolution of the SWE scan relative to the B-mode scan should yield acceptable results. For a B-mode scan with longitudinal steps of 0.3mm – 0.5mm, the corresponding SWE scan should have step sizes of 1.2mm – 2mm. SWE scans were taken of the circular phantom and a smaller anatomically realistic phantom with step lengths of 0.9mm, 1.2mm, 1.8 mm, 2.1 mm, and 2.4 mm to assess the effect of larger steps on SWE signal and acquisition time (Table 5.5-5).

Scan	length	# steps	step size	time (min)	passes	imgs/step	time per img	Plot
1	205	227	0.9	26.23	3	3	0.011	
3	205	227	0.9	25.97	3	3	0.011	x
4	205	170	1.2	17.73	3	3	0.011	x
6	205	113	1.8	12.09	3	3	0.011	x
7	205	97	2.1	12.72	3	3	0.013	
8	205	97	2.1	12.77	3	3	0.013	x
9	205	85	2.4	11.30	3	3	0.013	x
10	195	81	2.4	11.46	3	3	0.013	
11	175	72	2.4	6.62	3	4	0.008	
12	175	72	2.4	9.89	3	4	0.013	

Table 5.5-5: The total full scan time for a single SWE scan at each step length and scan volume tested. Step sizes need to be over 2 mm to achieve scan times under 15 minutes.

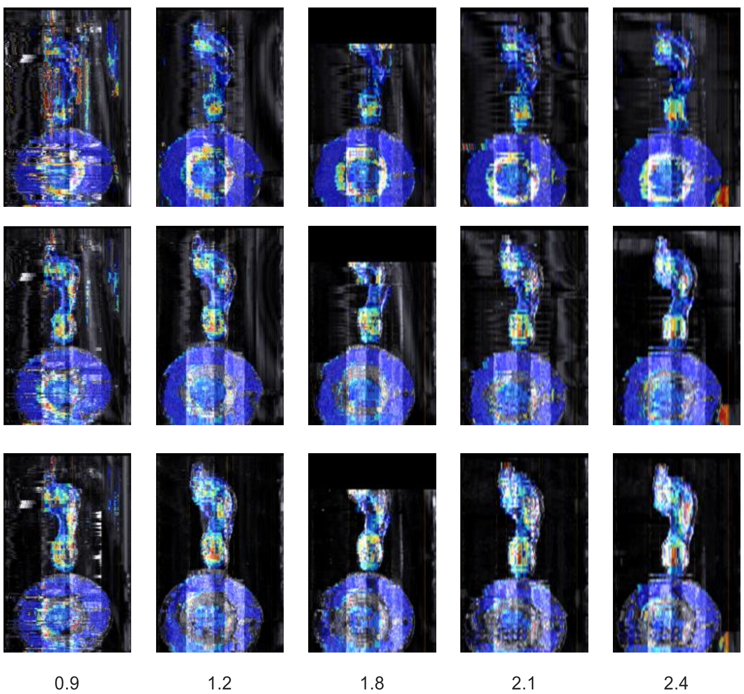

Figure 5-22: Comparison of SWE values obtained from scans with different step sizes. SWE values remain similar despite steps over 2x larger. Steps are labeled in millimeters.

Three slices through the SWE volume with the underlying B-mode images are presented in Figure 5-22. While there is noticeable degradation of B-mode image quality as the step size decreases, the quality of the SWE signal does not appear to degrade. Therefore, a larger step size can be used for SWE scans to reduce the time of exposure to the coupling materials.

5.6 Conclusion

Measurement of the plantar soft tissue biomechanics under typical physiological loading is difficult due to the high degree of complexity in applied load, muscle tension, and subject-specific bone geometry. Prior work has attempted to quantify plantar soft tissue material and structural properties using simplified uniaxial or bi-axial loading[201,216,217], planar imaging measurements[34,103,187,190,193] or finite element estimates[203,218,219]. To address the limitations of simplified loading and planar imaging, this work details the design, manufacture, and evaluation of a device for obtaining volumetric scans of the plantar soft tissue using both in B-mode and shear wave elastography and in unloaded and naturally loaded conditions.

Through design of this device, several materials were evaluated for the load-bearing surface, which requires the difficult combination of strength sufficient to support bodyweight loading and acoustic impedance low enough to allow ultrasound transmission. Prior work attempting to use ultrasound through a load-bearing surface often does not report the acoustic properties of the material used[103,194,195,220], and the materials used are not optimally matched acoustically to soft tissue. Matsumoto et. al. does report a characterization of the material chosen in terms of bending and attenuation. However, they do not compare the plate chosen to other materials[187]. Additionally, the plate selected for that work is expensive and difficult to acquire in the dimensions needed for this work. Based on prior acoustic characterization, the low-density polyethylene was expected to perform better than other materials tested. However, the high density polyethylene variants performed better than other materials tested in similar thicknesses. There may be some variation in density or attenuation due to manufacturing processes that caused this discrepancy, and such manufacturing variabilities reduce the applicability of this testing to future work using similar materials from different manufacturers.

The device was evaluated using custom phantoms, one designed with regular geometries and one with anatomically realistic geometries. The literature on custom ultrasound phantoms is large, encompassing low-cost phantoms for destructive applications as well as more durable phantoms for repeated use. The commercial gels used for the proof of concept and anatomically realistic phantom are marketed with the Young’s modulus, speed of sound, and density specifically to attract ultrasound phantom applications. These gels have previously been used in combination with additive manufacturing to develop anatomically realistic training phantoms for medical education[221,222]. The work presented here adds support to the utility of these materials and methods for stable anatomically realistic ultrasound phantoms.

While the evaluation of structural B-mode imaging through the plate strongly supported the ability to reconstruct useful volumes, the evaluation of SWE values through the plate demonstrated high, inconsistent error. However, the average variation between methods was lower than the expected variation between samples, and the samples tested had smaller variation than those expected between soft tissues. Accurate and repeatable SWE values can be difficult to obtain and are sensitive to parameters like pressure between the transducer and the tissue and focal depth. The plate likely interferes with the ability of the acoustic radiation force to generate strong shear waves, contributing to the reduced number of candidate materials when considering SWE in addition to B-mode imaging. Inconsistent disruption to the SWE initiation could account for some of the variation in through-plate values. While effort was taken to ensure that samples were not compressed in either the initial or scan conditions, it is possible that this was insufficient to ensure pure SWE values for the initial SWE value readings, which could also contribute to the variability. While the results presented in this work suggest that SWE can be used with an intervening plate, future work should investigate this issue further to more rigorously characterize the effect of the plate and ensure the comparability of SWE readings from volumetric scans to prior work using no intervening materials.

This work demonstrates the feasibility of volumetric structural, SWE, and load-bearing ultrasound for the evaluation of biomechanical hypotheses related to plantar soft tissue pathologies. Such a device is capable of acquitting data required to address gaps in knowledge regarding plantar soft tissue structure and mechanics and could improve understanding of plantar soft tissue pathomechanics and improve prevention and clinical management of severe musculoskeletal complications such as pedal ulcers in diabetes.

6 Development of a low-creep load-bearing solid acoustic coupling gel

6.1 Abstract

Three-dimensional ultrasound methods often use a water bath for coupling the ultrasound transducer to the skin. However, extended immersion in water can compromise the integrity of the plantar skin, increasing risk of injury. Increased plantar injury risk and poor wound healing are already complications of diabetes, making the use of a water bath unacceptable for study plantar soft tissue changes with diabetes. Hydrogel couplants can offer a compromise between acoustic and biological considerations by reducing the amount of water in contact with the skin and more tightly controlling its location. However, hydrogels have not been manufactured with the goal of supporting bodyweight loading. Polyacrylamide gels were manufactured in variable concentrations from 10 – 30% weight per volume (w/v) with variable chitosan (0 – 1.8% w/v) added to increase strength and toughness. Gels were molded into 14mm x 10mm discs and subjected to ramp and hold compression tests up to 500 kPa or 90% strain and the creep of the material under load was measured. . Additional gels were molded into rectangular strips and imaged at different sound speeds to estimate material sound speed. Candidate gels were manufactured in bilayer formulations with the stiffer material inferior to the softer material and molded in custom designed molds modeled after the plantar geometry. Gels with at least 23% w/v combined concentrations of acrylamide and chitosan were capable of withstanding bodyweight loading with <1.5% creep strain. Material stress-strain responses were nonlinear. Material sound speeds were highly variable using the estimation method. Bilayer gels provided clear images, maintained effective coupling, and did not demonstrate visible creep or failure over the duration of a weight bearing volumetric ultrasound scan.

6.2 Introduction

Typically, ultrasound transducers are coupled to the skin using ultrasound gel or by submersion in a water bath. Unfortunately, soaking of the feet has previously been linked to increased risk of amputation in patients with diabetes[223]. Soaking the feet can lead to increased elasticity and decreased load resistance[224,225], as well as reduction of protective moisturizing oils in the skin barrierand lasting reduction in skin hydration[226], with the magnitude of these effects generally proportional to time spent in water [227]. Both softened and dry skin are more prone to injury. Since the diabetic foot is already at increased risk of injury, infection, and slow wound healing, it is essential to avoid introducing additional injury potential.

Polymer gels have been investigated extensively as tissue-mimicking phantoms, and several of these polymers have been investigated for the purpose of ultrasound coupling. Acoustically, a good coupling material candidate should have an acoustic impedance close to that of soft tissue, preferably with both speed of sound through the material and material density similar to soft tissue. A matched acoustic impedance will prevent significant reflection at the tissue-couplant interface and the matched speed of sound will allow for effective reconstruction of the acoustic signal since the reconstruction uses a speed of sound estimation. Additionally, a good coupling material will be anechoic so as not to interfere with discriminating skin boundaries. Finally, a good coupling material must also have minimal attenuation to allow acoustic power to reach the tissue of interest. From a biomedical perspective, the coupling material should be biocompatible and hypoallergenic to avoid skin sensitization or allergic reactions. Mechanically, for this application, a coupling material will be solid, toughness, temporally and thermally stable, and sufficiently stiff to hold a predetermined shape under the weight of the lower limb.

The common poylmers used fall into several categories: biologically-derived, synthetic water-based, and synthetic oil-based.

Biologically-derived materials include gelatin, agar, collagen, hyaluronic acid, chitosan, and alginate, which are all derived from plant or animal ceullular structures. The most common of these are gelatin and agar, which have been used extensively in tissue-mimicking phantoms for decades[228–232]. Gelatin and agar phantoms have been used to develop a range of therapeutic and diagnostic ultrasound imaging techniques, including shear wave elastography [89,233–235], high intensity focused ultrasound[236], burst wave lithotripsy[237,238], and microbuble contrast imaging[239]. However, gelatin- and agar-based hydrogels are prone to microbial colonization[228,240,241], water transfer[228,241], and temperature instability[240], making them poor choices for couplants. More recently, chitosan[242], alginate[243–245], hyaluronic acid[246], and gellan gum[247–249] have been used either on their own or as components of ultrasound phantoms to impart additional favorable properties such as increased extensibility or toughness.

Synthetic- and/or oil-based materials include polydimethylsiloxane (PDMS), poly(styrene-ethylene-butylene-styrene) (SEBS), silicones, polyurethanes, and paraffin wax. These materials have similar mechanical properties to soft tissues and acoustically effective gels, however, they typically have sound speeds lower than biological tissues[250–256] and high attenuation coefficients[250–252,254,257–259], making them less effective phantoms and poor couplants.

Synthetic water-based gels include polyvinyl alcohol (PVA), polyacrylamides (PAA), and polyethylene glycol diacrylate (PEGDA). PVA is a common and popular material for tissue-mimicking phantoms due to favorable properties of low toxcicity, easy manufacture, and native speckle[250,260]. PVA phantoms are manufactured by mixing the monomer with water and any other desired additives and then putting the phantom through freeze-thaw cycles to polymerize and modulate the modulus of the resulting material. While this freeze-thaw protocol makes manufacturing PVA technically simple, it is time-intensive, and mechanical and acoustic properties of large phantoms may be varible due to low thermal conductivity of the material[261]. PVA gels also have similar speed of sound, density, and attenuation to soft tissues[250,262]. PVA has been investigated as a couplant for automated whole breast ultrasound and its adaptation to the digits of the hand[263] as well as for low intensity transcranial focused ultrasound[264]. While the method was able to produce viable reconstructions of the breast, the echogenicity of the material makes delineating the skin from the couplant difficult, and the couplant still required some water for coupling between the skin and the PVA.

Polyacrylamide gels were one of the first synthetic gels to be described for use as a solid acoustic couplant[265], and remain a common choice for ultrasound tissue mimicking phantoms[245,248,250] and couplants[230,242,266]. PAA phantoms have been used for varied applications such as high intensity focused ultrasound (HIFU)[245,267,268], shear wave elastorgaphy (SWE)[269,270], segmentation algorithms[271], additive manufacturing[272], Doppler[273], and quality assurance[274,275]. PAA has also been used as a substrate ultrasound- and mechanically-mediated tissue engineering[276,277] and drug delivery[278,279]. PAA gels are generally optically transparent, well-matched acoustically to soft tissues, very low in attenuation, and easily adaptable to create different stiffnesses. Prior work has noted the hazards of the monomer compontents of polyacrylamide as a deterrent for use as a phantom or couplant[254], however the polymerized material has repeatedly been found to be biocompatible[242,266,276,277,280–283]. Recently, Chen et. al. have developed a bilayer PAA couplant that allows for consistent pressure appliction and improves ultrasound quality on difficulty to image geometries such as the elbow[230]. The combination of a stiffer and a more compliant layer allows for better adhesion of the couplant to the skin and reduces decopling around complex geometries. Simialrly, using a combination of PAA and chitosan, Wang et. al. developed a coupling gel to incorporate into a wearable adhesive ultrasound transducer[242]. This study examined the biocompatibility of the material when worn over a period of 48hr and found no adverse effects. Yi et. al 2020 investigated use of a polyacrylamide-alginate couplant for intraoral ultrasound and found good acoustic and biological compatibility[266].

PEGDA has more recently been invesrigated for tissue mimicking phantoms, with partiular application to the additive manufacturing of complex phantom shapes[284–287], though it has been applied in the study of ultrasound-mediated drug delivery[288], contrast agents[289], and nonlinear acoustics[290] as well. Typicaly preparation including photoinitiation likely contributes to its populartiy in addivite manufacturing applications[291]. The monomers used to create PEGDA are less hazardous than those used in PAAm gels, but the manufacturing process for molding these materials is more complex;they are less stable over time; and they have higher reported sound speeds, acoustic impedances, and attenuation coeffcients than polyacarylamide formulations of the same monomer concentration[291].

We chose to investigate PAA hydrogels based on the prior application as a couplant for complex geometries[230] and long skin contact time[242], the large body of prior work evaluating mechanical and acoustic properties, and reported low attenuation. The advantage of this coupling pad would be reduced contact with water, additon of incredients that support the skin barrier, and reduced contact of the coupling medium with the space between the toes, which is particularly vulerable to skin softening and wound formation.

6.3 Methods

Acyrlamide (A8887), *N*,*N′*-Methylenebis(acrylamide) (146072), ammonium persulfate (A3678), *N*,*N*,*N′*,*N′*-Tetramethylethylenediamine (TEMED, T7024), and alginic acid sodium salt (A2033) were purchased from Sigma Aldrich (Burlington, MA, USA) following the protocol of [230]. Additionally, acetic acid (A6238), high-molecular weight chitosan (419419), and α-ketoglutaric acid (75890) were purchased, also from Sigma Aldrich, following the protocol of [242].

An initial test was performed to determine the ideal monomer concentrations to obtain the desired stiffness for phantom coupling. Based previously reported methods [230,242], initial concentrations of monomer, crosslinker, and initiatior (Table 6.3-1) were mixed in 10mL of water. Discs 1-4 use free redical polymerization initiated by TEMED and ammonium persulfate and polymerized at room temperature for 12 hours. Disc 5 uses light-initiated poylmerization and was polymerized under UV light for 1 hour.

Acrylamide (w/w)	N,N'-methylenebis(acrylamide) (w/v)	TEMED (v/v)	Ammonium persulfate (w/v)	Alginate (w/v)	Chitosan (w/w)	α-ketogluartic acid (w/w)	acetic acid (w/w)
10%	0.05%	0.15%	0.05%				
12%	0.07%	0.15%	0.05%				
15%	0.10%	0.15%	0.05%				
12%	0.10%	0.15%	0.05%	2%			
15%					3%	0.30%	1%

Table 6.3-1: Initial concentrations matching those previously reported.

After initial manufacture, the resulting gels were found to be brittle. They were not resistant to localized forces and failed catastrophically when squeezed between fingertips with moderate force. For loadbearing applications, load is distrbuted unevenly, and curvatures are likely to create stress risers. Previously, chitosan[242,245] and alginate[230] have been added to increase toughness in hydrogels. We performed additional experiementation to obtain a gel that was sufficiently stiff to hold a molded insole shape yet also tough enough to resist catastrophic failure under uneven bodyweight loading.

In order to assess the ability of the material to resist fracture under bodyweight loading, creep/stress rupture tests were performed using test discs made from serial additions of acrylamide (monomer), N,N'-mehtylenebis(acrylamide) (crosslinker), and chitosan and its accompanying solvent, acetic acid (strengthener and toughener) (Table 6.3-2).

Acrylamide	N,N'-methylenebis(acrylamide)	Chistosan	Acetic Acid
10	0.01,0.2,0.03,0.04, 0.05		
10	0.02	0.25,0.5,0.75,1, 1.25, 1.5, 1.75	0.03,0.03,0.05,0.08, 0.11, 0.14, 0.14,
8,9.5,11,12.5,14	0.02		
12	0,0.01,0.2,0.03,0.04,0.05		
12		0,0.25,0.5,0.75,1,1.25, 1.5, 1.75	
14,16,18,20,22	0	0	0
14		1,1.1,1.2,1.3,1.4,1.5	0.03,0.03,0.05,0.08,0.11, 0.14
16		0.9,1,1.1,1.2,1.3,1.4	0.03,0.03,0.05,0.08,0.11,0.14
14,16,18,20,22	0.01		

Table 6.3-2: Variations in monomer, crosslinker, and additive concentrations tested**.**

Based on the results of these initial tests, additional test concentrations were developed to narrow down the range of conditions that would work for the different scan conditions (Table 6.3-3). These gels were also subjected to creep/stress rupture testing.

Acryalmide	N,N'-methylenebis(acrylamide)	Chistosan	Acetic Acid
15	0.01	1.25	0.16
16	0.01	1.55,1.8	0.16
18	0.01	1.55,0.5	0.16,0.2
20	0.01	0,0.1,0.25,0.5,1.25	0.03,0.03,0.03,0.2,0.2,0.16
22	0.01	1.25	0.2

25	0.01	0.5,1	0.03,0.25
26	0.01	0.75	0.25
28	0.01	0.75	0.25
29	0.01	0.75	0.25
30	0.01	0.5	0.25

Table 6.3-3 Additional Acrylamide and Chitosan combinations tested after the initial round of mechanical testing to refine the best formulas for each couplant needed**.**

Test solutions were degassed, poured into 14mm diameter x 10mm tall discs for mechanical testing and for speed of sound testing, UV cured for 1 hour at 302 nm, and submerged in a 1M CaCl solution overnight.

6.3.1 Mechanical testing

Stress rupture testing was performed using an Instron E3000 fitted with a 1kN load cell. The desired load resistance was calculated from average peak plantar pressure in people with and without diabetes. Typical static peak plantar pressures range between 250-300kPa. The desired length of the test was based on the maximum scan time for the loaded scan. The loaded scan is anticipated to take no longer than 10 min, and therefore, a 15 min hold time was chosen. Finally, the strain rate was based on a typical sit-to-stand time of 1.7-3 seconds for the anticipated age range of the target population[292]. Using an approximate plantar soft tissue compression of 50% and the sample height of 10mm, the calculated displacement rate was (10mm*0.5)/2.35s = 2.1mm/s Therefore, discs were compressed to either a load equivalent to 250 kPa or the safe lower displacement limit of the test machine, whichever occurred first, at a rate of 2mm/s and the load was held, in force control, for 15 min, or until rupture or the displacement limit was reached. Displacement and force were recorded, and the initial ramp modulus, maximum test time, maximum pressure, hold strain, and creep displacement were calculated for each sample using custom MATLAB code.

6.3.2 Speed of sound testing

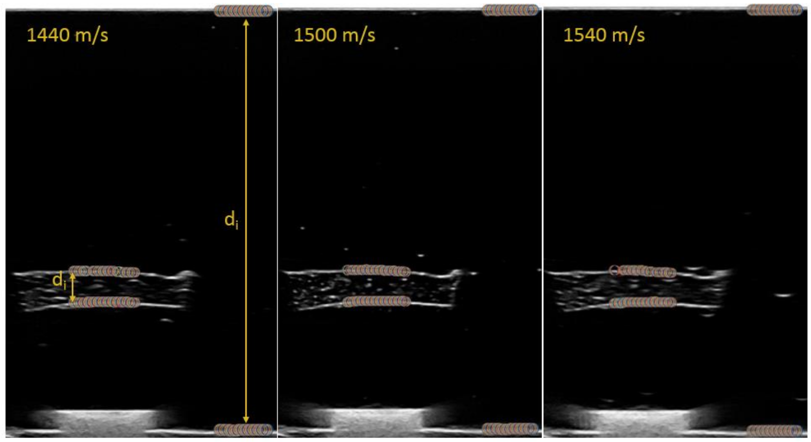

Figure 6-1: Representative example of sound speed distance calculation. Multicolored circles indicate location of top and bottom of sample and water bath measured by the software. L: image taken at 1440 m/s, M: image taken at 1500 m/s, R: image taken at 1540 m/s. Note the difference in the appearance of point scatters at different assumed sound speeds.

In order to ensure the couplant was within reasonable acoustic ranges, an acoustic measurement was derived from the ultrasound image. Using the assumed sound speed set by the ultrasound machine, *c*, and the distance between the reflections in the resulting image, d, the time between surface reflections, Δt, in the sample was calculated using the equation Δt = 2d/c. 36x14x2mm rectangular strips were molded from the same solution and using the same protocol as a subset of the the mechanical testing discs (Table 6.3-3 and the last three rows of Table 6.3-2). Rectangular samples were removed from CaCl2 solution and secured in a custom-designed clamp. The clamp was designed to allow the sample to be submerged in water to allow for accurate sound speed measurements. The thickness of the rectangular sample was measured no less than 4 times using digital calipers immediately before imaging. Images were taken at all twelve available sound speeds using the general preset of the SL18-5 probe of an Aixplorer (SuperSonic Imagine, Aix en Provonce, France). Images were acquired using the MATLAB research interface in order to extract the pixel resolution of the images. Distance measurements were atuomatically calculated using image-specific thresholds via custom MATLAB code. Distances were calculated both between the reflective faces of the sample and between the transducer and the bottom of the water bath. The distance between the transducer and the water bath was measured using digital calipers. The speed of sound through the sample and through the water was calculated as the digital caliper measurement divided by the change in time. Water measurements were compared to known values based on temperature, pressure, and salinity[293–296] in order to validate measurements.

6.3.3 Mold designs

Three different molds were designed to for data collection: one for weightbearing foot coupling, one for non-weight bearing foot coupling, and one for coupling the transducer to the underside of the plate. Due to the higher deformation under bodyweight loading, the weighted gel conforms more to the foot shape, requiring a less detailed mold. Additionally, curves and corners introduced in the mold can make the gel more difficult to stand on and introduce stress concentrations, making it more likely that the gel will fractue. Therefore, the weighted gel mold consisted of a simple, mostly flat rectangle with a gentle vertical slope in the area of the arch.

In contrast, the unweighted gel undergoes minimal deformation, requiring a more sculpted initial shape to allow for conformation to the foot geometry. The unweighted gel mold was designed with deeper indentations for the metatarsal heads and heel, and shallower indentations along the midfoot and toes, raised areas at the mid-toe, where the toe typically naturally curves up at rest and at the arch. This design was chosen to maximize contact between the foot and the gel pad for optimal imaging area while keeping in mind the vulnerability of the regions between toes.

The transducer coupling mold was designed as a rectangular box with the positive of the transducer housing embedded. The resulting gel fit exactly to the top of the transducer housing and had a flat top surface to couple to the flat surface of the plate. The mold had a 5.84mm clearance between the top surface of the positive of the transducer and the top edge of the mold.

Gel molds were printed at 50% (A-P) x 35% (M-L) x 50% (S-I) (weighted), 60% (A-P) x 40% (M-L)x 40% (S-I) (unweighted), and 55% (axial) x 55% (lateral) x 50% (elevation) (probe) of desired dimensions to account for the swelling that the gels underwent during curing, soaking, and storage in CaCl solution. Molds were printed in clear PLA on an Ultimaker S5+. The clear PLA allows for UV light to pass through, which is necessary for UV-induced free radical polymerizaton.

6.3.4 Mold testing

Following mechanical and molding tests, three gels were molded, one for each of the three molds described above. Couplants were demolded and submerged overnight in a 1M CaCl2 solution as escribed above, and then rinsed with tap water and submerged in a 0.9% NaCl solution two hours before use to further reduce risk of contamination with unreacted products and remove potentially drying agents from the gel surface. One subject was recruited as part of an IRB-approved study, and images of the foot were taken through the transducer couplant, the HDPE plate, and the skin gel couplant to assess the quality of the images through the gel.

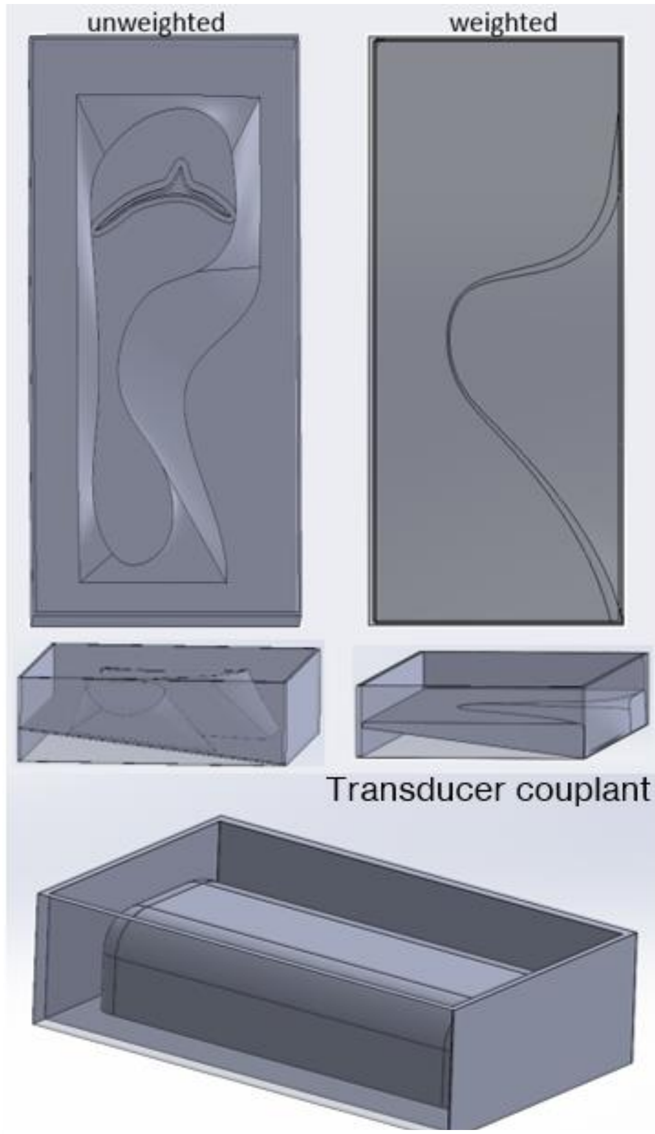

Figure 6-2: Top left: CAD design of 3D printed mold for the coupling gel for the unweighted condition. This mold includes a n elevated foot shape with a curved depression designed to create contact with the irregular geometry of the arch and the curve of the toes. The bottom of the mold is at an angle to allow the required arch height while allowing sufficient UV light through the mold for curing. Top right: CAD design of the mold for the gel for the weighted condition. The mold is mostly flat except for a gentle slope in the arch. Bottom: mold for the transducer couplant gel consisting of a hollow, 5-sided rectangular prism with the positive of the probe geometry inside.

6.4 Results

Due to the limitations of the test (leaving a vertical buffer to avoid damage to the mechanical test system), samples below 12mm in height (after expansion during soaking) were unable to achieve the desired peak force and hold pressure (Figure 6-3). Monomer concentrations below 20% were not capable of reaching and sustaining the desired peak pressure. Among solutions that were capable of reaching and sustaining the target loads, total creep over the duration of the test varied between 0.03 - 0.82mm (Figure 6-4, Left). Restricting these results to

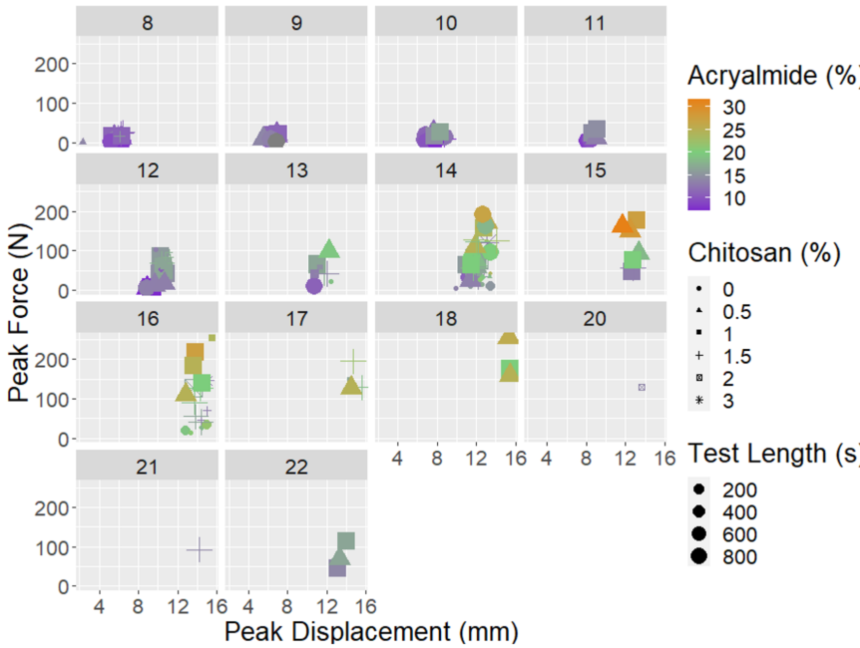

Figure 6-3: The peak force and displacement reached in each sample test. Facets are sample height. Samples below 12 mm in height did not reach the desired loads.

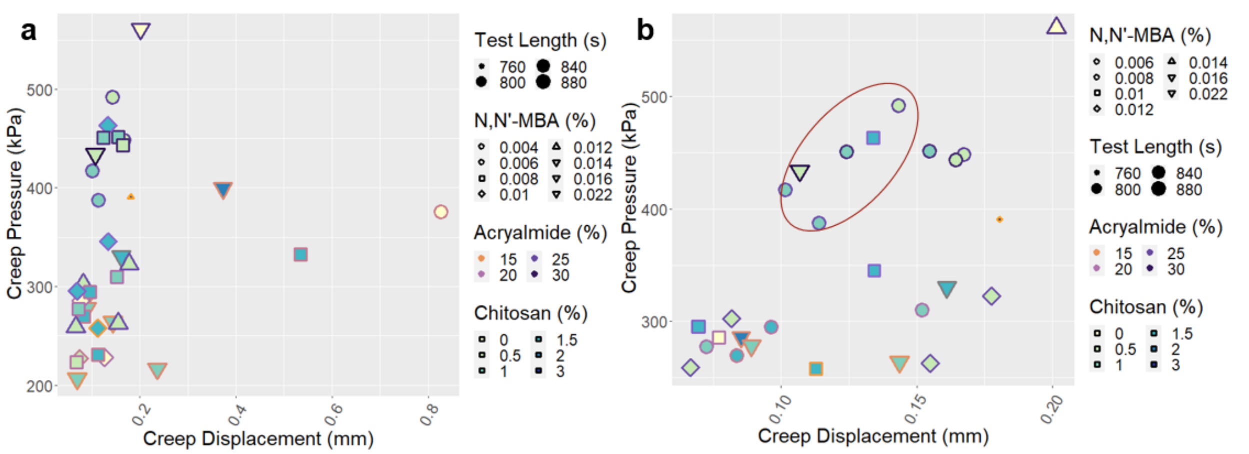

Figure 6-4: Left. Tested materials that meet the criteria of creep pressure greater than 200kPa and test length greater than 750 seconds. Right. Subset of the same figure with samples that meet stricter criteria of creep displacement less than the target resolution of 0.3mm, creep pressure >300kPa, and test length > 850 seconds. The ideal sample is in the top left of the plot. The six samples selected as best meeting the goal of a strong, tough, resilient gel for weight bearing scans are located in the top center of the graph between 375 kPa and 500kPa and 0.1 mm and 0.15 mm. (in circle)

samples where the total creep was lower than the target resolution of the system (0.3mm) left 32 candidate mixtures (Figure 6-4, Right). Among these, the samples with the most desirable combinations of high load tolerance and low creep displacement were composed of combined acrylamide and chitosan content of over 23% by weight.

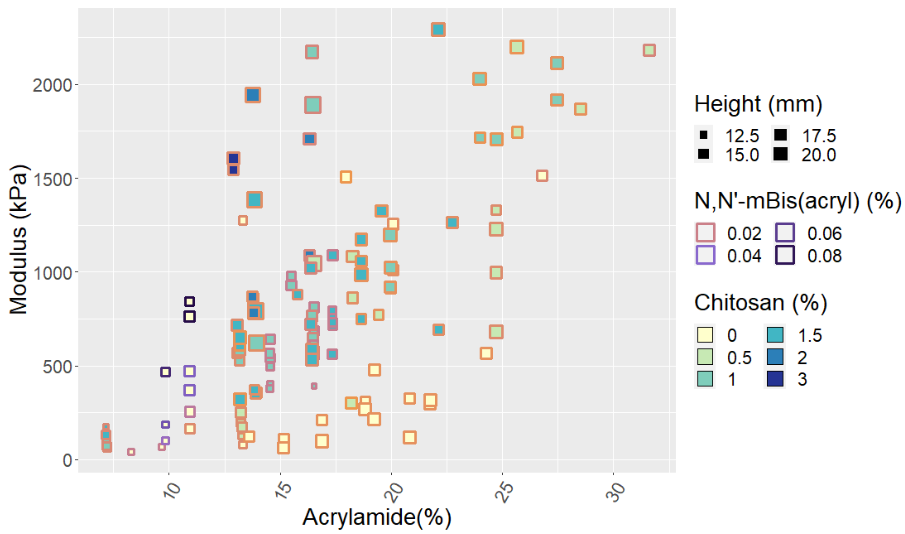

Figure 6-5: The modulus measured during the ramp portion of the mechanical test was positively associated with acrylamide content (x axis) and crosslinker content (border color). Plotted samples exclude those with heights less than 11mm as low height may confound results due to strain limits.

The elastic modulus was positively correlated with acrylamide, chitosan, and N,N'-methylenebis(acrylamide) content (Figure 6-5). The ramp loading curves were nonlinear (Figure 6-7), and the creep curves demonstrated higher initial relaxation moduli before leveling off.

Sound speed was not correlated with acrylamide or N,N'-methylenebis(acrylamide) content (Figure 6-6). However, while the variability within each acquisition was low, the variability between acquisitions was high, which could indicate some error in either the caliper measurements or the image processing. Ultimately, the sound speeds measured both within the gels and within the water, were largely within expected and acceptable ranges despite the low resolution of the measurements.

Based on these results, the final weightbearing couplant gel was molded as a bilayer with the larger layer closest to the skin made from 22% acrylamide, 0.01% N,N'-methylenebis(Acryalmide), 0.85% chitosan, and 0.2% acetic acid and the thinner, layer, in contact with the plate, made from 30%

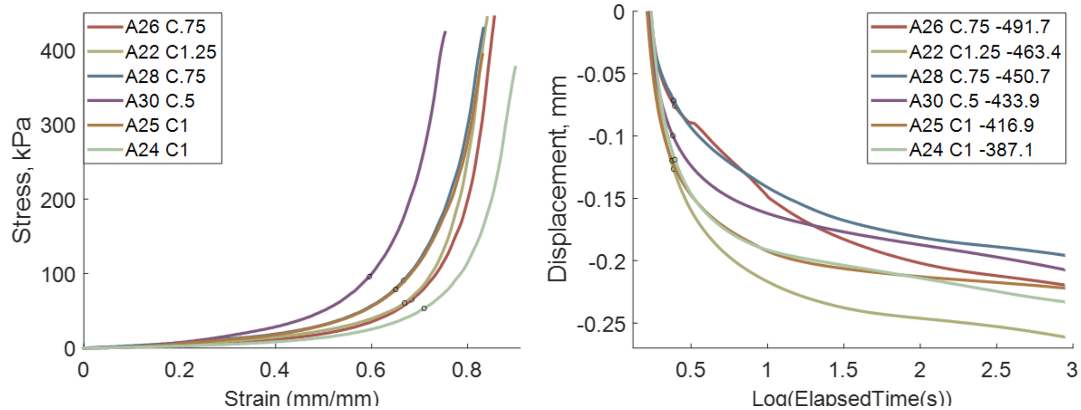

Figure 6-7: Left. Loading stress-strain curve for the six best samples, representative of the shapes of all curves. Stress-strain behavior is nonlinear. Right. Creep displacement for the best six samples illustrating sharp initial displacement followed by slow creep. Curves for other samples varied depending on how much the sample strained and whether it failed.

acrylamide, 0.01% N,N'-methylenebis(Acryalmide), 0.85% chitosan, and 0.2% acetic acid. The non-weightbearing gel was molded also in a bilayer from 9.2% acrylamide, 0.01% N,N'-methylenebis(Acryalmide), 0. 5% chitosan, and 0.25% acetic acid in the layer closest to the skin and 16% acrylamide, 0.01% N,N'-methylenebis(Acryalmide), 0.85% chitosan, and 0.2% acetic

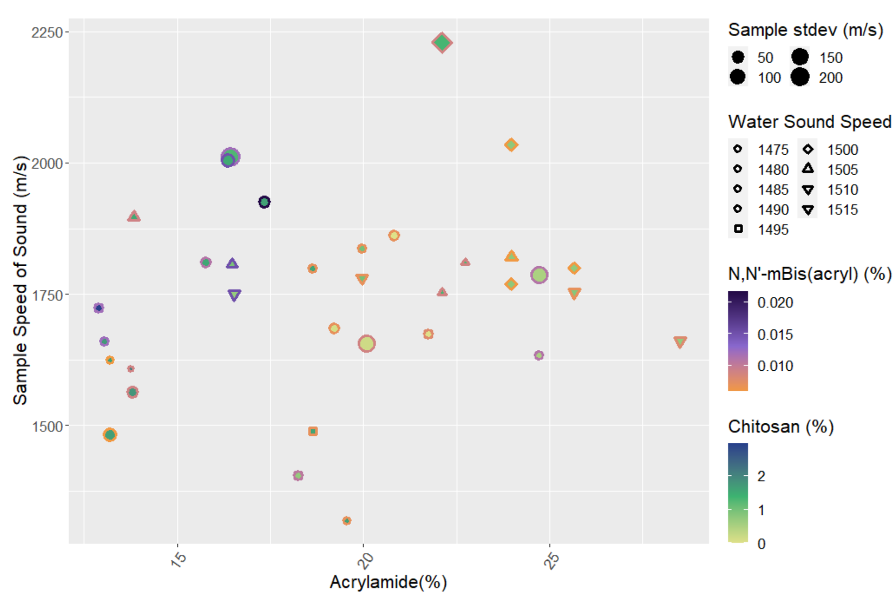

Figure 6-6: Sample speed of sound is not correlated with acrylamide content. Standard deviation of measurements within sample are shown as marker size and marker shape represents measured speed of sound in water for that sample as a rating of confidence in the measurement. Circles are closer to the expected speed of sound in water.

acid in the layer in contact with the plate. This bilayer structure allows for better conformation to the plantar geometry with the softer skin contact layer while retaining the resilience and shape of the stiffer bottom layer. These gels performed well as acoustic couplants. (Figure 6-8)

The transducer coupling gel was molded out of 30% acrylamide, 0.01% N,N'-methylenebis(Acryalmide), 0.85% chitosan, and 0.2% acetic acid, which produced a strong, tough, and elastic gel that effectively coupled and cushioned the transducer while imaging along the curved surface of the load-bearing plate. The images obtained through the plate and two gels were good, with clear skin, fat, and bone boundaries (Figure 6-8).

6.5 Discussion

Hydrogels have long been used as both ultrasound phantoms and acoustic couplants due to their acoustic similarity to soft tissue. Prior work has developed acoustic couplants with varying stiffness, toughness, acoustic impedance, speckle texture, and attenuation for varied acoustic and clinical applications. However, for the novel application of loadbearing ultrasound, the required acoustic couplant capable of retaining its structure over the course of a loadbearing acquisition has not previously been investigated. This work extends prior knowledge to applications with large,

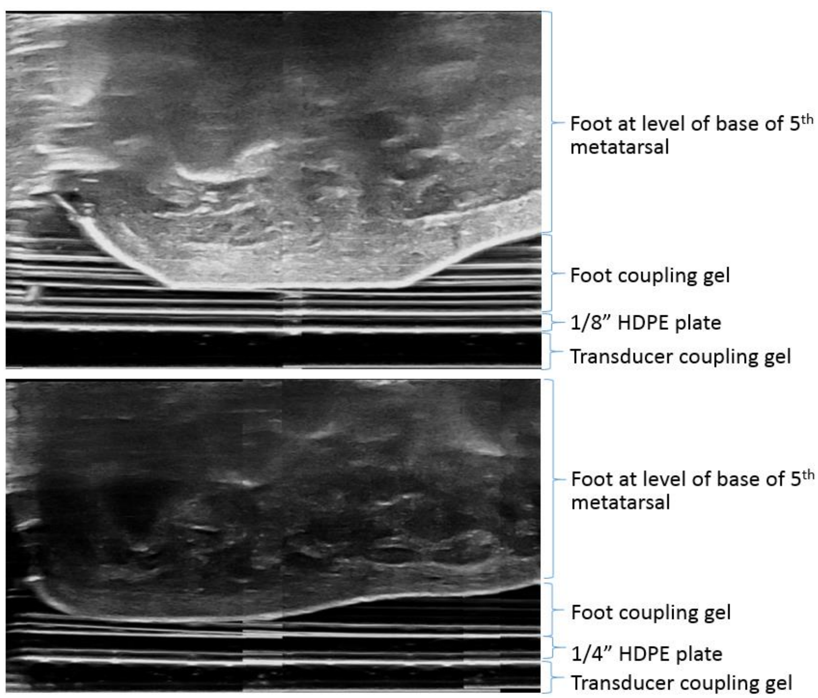

Figure 6-8: Images taken at the midfoot of the unloaded (top) and loaded (bottom) conditions through their respective gel couplants. Skin, fat, and bone are all distinguishable

sustained loads common in musculoskeletal applications, demonstrating that polyacrylamide gels with combined arylamide and chitosan content of at least 23% by weight are capable of withstanding bodyweight equivalent loading for at least 15 minutes. Furthermore, a design for a bilayered gel mold was demonstrated to be effective at coupling the varied plantar topography during seated and weightbearing acquisitions.

Prior work has established a positive correlation between both acrylamide content[269,276,297,298] and modulus and crosslinker content[269,276,297–300] and modulus (Figure 6-9, Left) up to an inflection point of crosslinker content[297] at around 40% of the acrylamide content within a sample. This finding is again replicated in the current results. However, prior work has recorded lower moduli at the ranges of acrylamide tested for the load bearing couplant (Figure 6-9, Left). One large difference in methods between these works and the present work is the peak strain of the mechanical tests. Peak strain in prior compression tests ranged from 8%-35% (Figure 6-9, right), but in this work the peak strain is around 90% for most samples. Given the nonlinear shape of the loading curve, this difference could account for the higher moduli measured. Some of this difference could be attributed to differences in testing methods, as values derived from indentation tests are not always directly comparable to those from macro scale compression tests, particularly for nonlinear or viscous materials. Prior work has used displacement rates of 0.008 mm/s – 0.08mm/s, equivalent to 16-20%/s. While the displacement rate used here is higher (2.1 mm/s) it is similar in strain rate (~21%/s), and is therefore unlikely to contribute to the higher moduli. Interestingly, Troia et. al report rupture of the 10% acrylamide, .5% N’,N-methylenebis(acrylamide) gel at around 40% strain. This aligns with our qualitative observations that lower acrylamide and higher crosslinker combinations are more brittle.

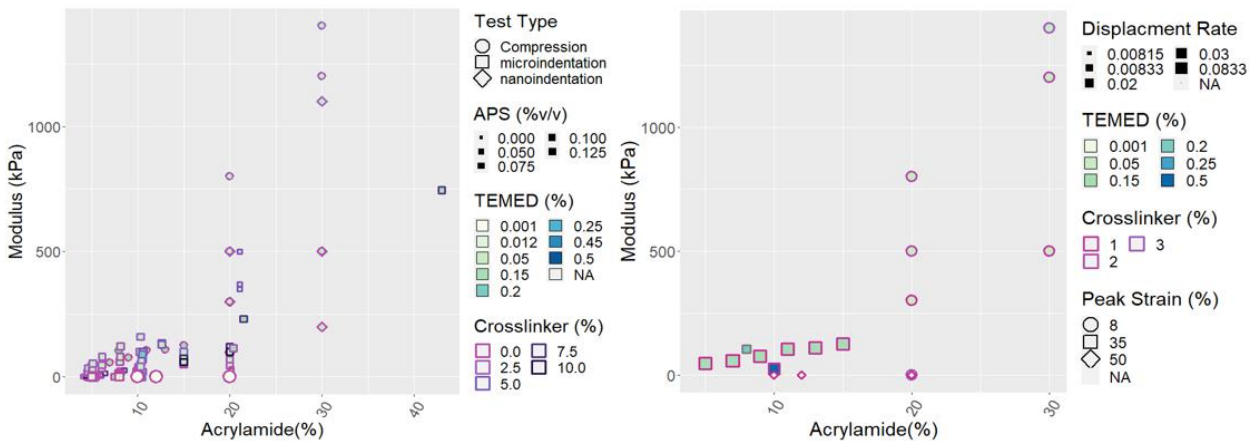

Figure 6-9: Left. Prior work evaluating changes in elastic modulus with acrylamide and crosslinker content demonstrating positive correlations for both. The magnitude of the moduli in prior works is lower than those presented here. This may be due in part to testing methods. Right. Prior work of compression tests only, with size represented by displacement rate and shape represented by peak strain. Peak strains from prior work are 2-10x lower than those in this study.

Previously, both acrylamide content and N’,N-methylenebis(acrylamide) content have been positively correlated with sound speed, density, attenuation, and acoustic impedance (Figure 6-10). In contrast, the measured speed of sound for the present work were not strongly correlated with either acrylamide or N’,N-methylenebis(acrylamide) content, and were larger in magnitude than those previously recorded. While the addition of chitosan in could contribute to the overall larger magnitude, as prior work on chitosan thin films have measured 1500 m/s and 1660 m/s from 0.05 %w/v

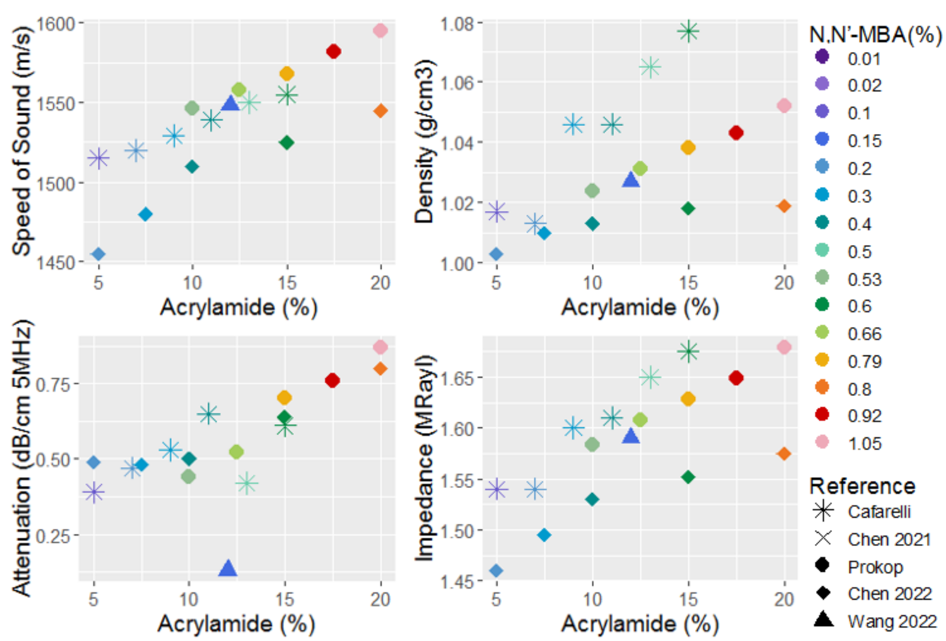

Figure 6-10: Effect of Monomer and crosslinker content on speed of sound, attenuation, density, and acoustic impedance

to 1.4%w/v chitosan formulations[301], the methodology used to estimate speed of sound through the material likely contributes to this discrepancy. This methodology also overestimated the speed of sound through water for many samples and estimated a wider range of sound speeds than expected based on calculations using ambient temperature, pressure, and salinity. The variation in estimated speed of sound through water was about 3.7 times larger than expected and the variation in speed of sound through samples was 6 times larger than expected based on prior work. Modern ultrasound machines perform complex processing of hundreds of send-receive signals to create a clear image. This may include dynamic focusing, dynamic speed of sound adjustment, or harmonic imaging. As a result, this estimation of speed of sound using the on-screen image may not be feasible. Additionally, the image processing uses a simple threshold and edge detection method to identify the gel and bottom surface of the water bath. There may be an error is this distance measurement on the order of a few pixels, which could increase error in the estimation. This method also relies on an accurate measurement of the sample thickness. These gel materials are highly compressible, making accurate measurements using digital calipers difficult. Finally, the images for these measurements are taken in a pure water bath. While the measurements are performed quickly, there is potential that the hydrogel materials swell when submerged in a hypotonic solution, further increasing the error of the thickness measurements. A more rigorous treatment of the speed of sound for each of these materials would help inform choice of material for scan coupling as this information could help tune the reflection due to impedance differences between the skin, gel, and plate, as well as attenuation through the gel to improve image quality.

Few works have attempted to couple irregular geometries for a regularized scan or normal weight bearing ultrasound. Among these, coupling methods for volumetric scans have included water baths[97,98,263,302,303] and combinations of water baths and stiff PVA material[263,303] and have not attempted weight bearing. Among those that have attempted load bearing, coupling methods included ultrasound gel[104,187,192,304], commercial standoff pads[305], or were not reported[306]. A custom-molded load bearing solid couplant gel could improve data acquisition protocols for applications such as residual limb imaging[97,98], whole breast ultrasound[263,307] , and dynamic in vivo measurement of plantar soft tissue properties[305,306] and other biomechanical study. Additionally, the high extensibility and elastic recovery of these materials could be useful for dynamic applications where contact is required throughout a large range of motion such as the in-shoe ultrasound[305,306].

Similarly, many 3D ultrasound applications use a water bath to couple the transducer to the imaging surface[97,98,263,302,308]. Creating water-compatible mechanical and electrical systems and protecting the transducer during submersion poses engineering challenges. Other approaches use ultrasound gel, but this can be similarly difficult as the gel must cover a large area and can become sticky as the aqueous component evaporates. The transducer couplant described in this work is custom molded to the transducer, secured to the transducer, and maintained high quality coupling over the course of several hours, making it more versatile for both mechanically translated and freehand volumetric ultrasound.

There are several areas where this work could be improved. First, there was substantial noise and possibly error in the speed of sound measurements. A more rigorous treatment of the speed of sound of these gel couplants could improve selection of the appropriate concentrations for matching to the transducer, the plate, and the skin and reducing reflections between those layers. Much of the signal lost in imaging through the couplants and the plate is lost to reflection, and tuning the density and speed of sound of the couplants could reduce this loss as well as reduce image artifacts related to strong reflection. Second, these gel couplants do use formulations of toxic monomers. While the safety of the polymerized material has been repeatedly demonstrated, and steps were taken to mitigate risks of unreacted products, it is possible that similar material and acoustic properties could be obtained from less hazardous components. Due to time constraints, the mechanical data do not include repeated measurements over time, and the effect of storage on material properties and image quality were not tested. Polyacrylamide gels have previously demonstrated small changes in properties over time with different storage conditions, though less changes than hydrogels with different base polymers[250]. Future work should consider the effects of storage on the quality of these gels.

6.6 Conclusion

This work demonstrates that acoustic coupling gels with >23%wt combined acrylamide and chitosan are capable of withstanding bodyweight loading with minimal creep, further expanding the known applications and material properties of polyacrylamide, polyacrylamide-chitosan hybrid, and bilayered hydrogels. Furthermore, custom molded gels of single and bilayer formulations can effectively couple irregular geometries under variable loads, increasing the potential applications of volumetric ultrasound, particularly in areas or populations that are vulnerable to skin injury from long-term water submersion.

6.7 Graphical Abstract

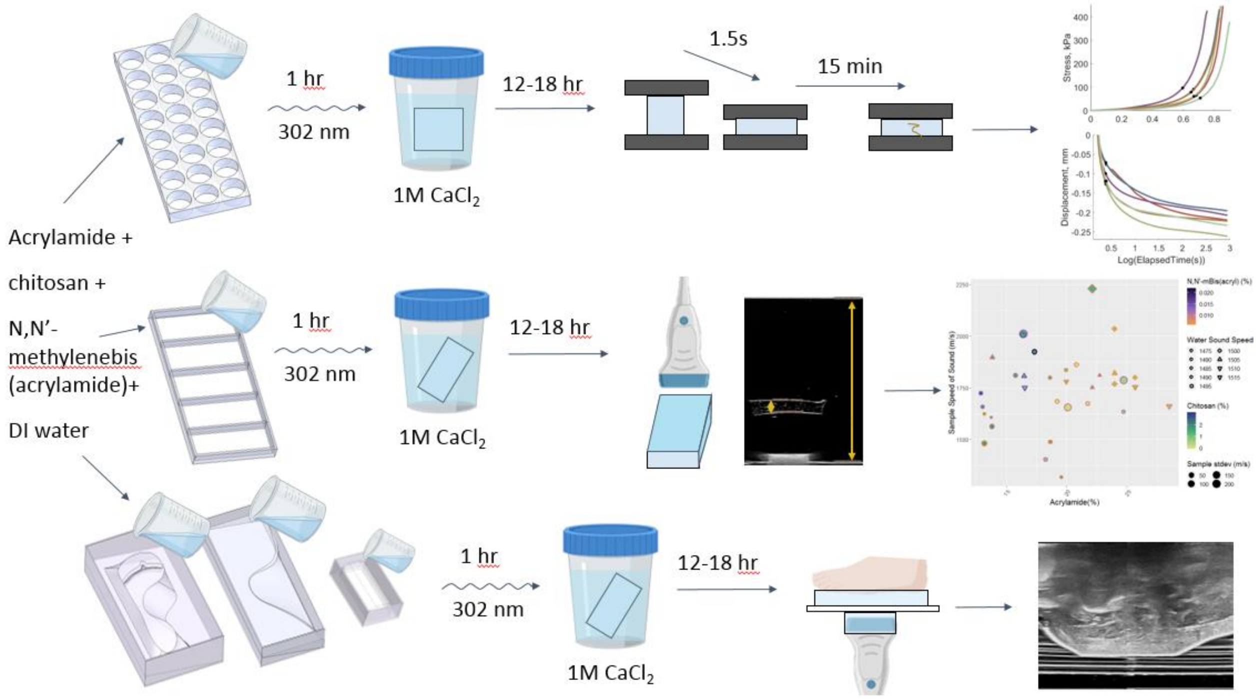
Acrylamide +
chitosan +
N,N'-
methylenebis
(acrylamide)+
DI water
1 hr
302 nm
1M CaCl$_2$
12-18 hr
1.5s
15 min
Stress, kPa
Displacement, mm
Log(ElapsedTime(s))
Sample Speed of Sound (m/s)
Acrylamide(%)
N,N'-mBis(acryl) (%)
Water Sound Speed
Chitosan (%)
Sample stdev (m/s)

7 A method for automated masking and calculation of plantar pressure metrics using segmented computed tomography scans

This work is under review in the journal Gait & Posture.

7.1 Abstract

Plantar pressure, a common gait and foot biomechanics measurement, is typically analyzed using proprietary commercial software packages. Regional plantar pressure analysis is typically reported in terms of underlying bony geometry, and recent advances in image processing have made computed tomography, radiographs, and magnetic resonance imaging more common in biomechanical study. A plantar pressure analysis method was developed based on bony geometry from computed tomography scans to calculate peak pressure, pressure time integral incorporating sub-peak values, force time integral, pressure gradient, and pressure gradient angle. Static and dynamic plantar pressure were acquired for 4 subjects (male, 65 ± 2.4 years). Plantar pressure variables were calculated using commercial and computed tomography-based systems. The difference between peak pressure and force time integral computed using the bone-based software and commercial software was 6% on average. Region masks of the metatarsals and toes differed between commercial and computed tomography-based software due to subject-specific bone geometry and toe shape. Pressure time integral values incorporating sub-peak pressure were higher and demonstrated higher relative hindfoot values compared to those without. Removing step-on frames to static pressure analysis decreased forefoot pressures. Regional maps of peak pressure and maximum pressure gradient demonstrate different peak locations. Computed tomography-based regional masks are comparable to commercial masks. Inclusion of static step-on frames and sub-peak pressures may change regional plantar pressure patterns. Differences in location of

maximum pressure gradient and peak pressure may be useful for assessing subject specific injury risk.

7.2 Introduction

Plantar pressure, a measure of the force exerted through the foot during various activities normalized by the contact area, is a common metric in biomechanical analysis of gait, foot bone deformities, and plantar soft tissue pathology. Changes in peak plantar pressure have been associated with peripheral neuropathy [8,309], diabetes-related ulceration [310,311], and bony deformities [312], and has been suggested as a predictive clinical tool [311]. Additional metrics have also been derived from plantar pressure, such as pressure time integral (PTI), which is used to estimate the cumulative spatial load [313], and plantar pressure gradient (PPG) and pressure gradient angle (PGA), which are used to estimate shear stress or complex loading [314,315], which has been associated with increased risk of ulceration in plantar soft tissue affected by diabetes. Increased PPG and decreased PGA have also been associated with diabetes[315].

Often, plantar pressure metrics are subdivided into plantar regions as foot mechanics are complex and load bearing changes both spatially and temporally over the course of gait and standing. Regional plantar pressure analysis is typically performed using commercial software packages associated with plantar pressure collection systems. However, these packages can be inflexible to developing new metrics, such as PPG and PGA listed above, new masking schemes, or changing the method of calculation for a predefined metric. In particular, the method of calculating PTI for some commercial systems tends to be highly correlated to the peak pressure as it is a summation of peak pressures only [316], and does not take sub-peak pressures into account. The lack of flexibility in these commercial software packages, while reducing risk of user error, increases difficulty when comparing metrics calculated using different systems or attempting to extend plantar pressure evaluations with new measurements.

Regional plantar pressure analysis uses regions largely defined by underlying bone geometry, with common regions including forefoot (distal metatarsals and proximal phalanges), toes (distal phalanges), hindfoot (calcaneus), and medial and lateral midfoot (proximal metatarsals, cuboid, navicular, and cuneiforms). Therefore, for studies that utilize computed tomography (CT) for geometric bone analysis or biplanar fluoroscopy for gait analysis, an automated plantar pressure analysis based on registered CT scans could be useful as the bones are often already segmented for these tasks. This work aims to create a flexible, automated, and platform-independent method of analyzing plantar pressure data based on segmented CT scans.

7.3 Methods

Four subjects (male, age 65 ± 2.4 years) were recruited for an IRB-approved study through the Veteran Affairs Puget Sound Health Care System. A single static plantar pressure trials and at least three dynamic plantar pressure trials at a self-selected speed were taken using the emed X plantar pressure platform (novel, St. Paul, MN, USA).

Plantar pressure regional analysis was performed using both traditional commercial software (novel, St. Paul, MN, USA) and the custom CT-based software. For the traditional commercial analysis, the 11-region novel mask was applied to each static and dynamic trial using the *automask* program. The peak pressure, PTI, and force-time integral (FTI) were calculated for each mask using the *multimask evaluation* program. Regional variables were exported to a text file and an additional variable, PTI_F was calculated as FTI divided by contact area as previously reported[316].

Partial weight-bearing CT scans were acquired using the CurveBeam Line Up (Hatfield, PA,USA). Scans were acquired using the Large patient Large FOV setting (120 kV, 5mA) for optimized bone contrast.

Bone masks (all toes, all metatarsals, all cuneiforms, calcaneus, navicular, and cuboid, n=16 total) were segmented from each CT scan using Mimics (Materialise, NV Leuven, Belgium). Bone masks were exported from Mimics to .bmp file format as opaque colorations overlaid on the original images in the coronal plane. These images were converted into a bone label map using custom MATLAB code. The three-dimensional bounding box and centroid of each bone were calculated from the label map using the built-in function *regionprops3*. The transverse plane coordinates of the bounding boxes and centroids for each bone (Figure 7-1, left) were used to compute 11 regional masks as follows (Figure 7-1, right).

The medial-lateral boundaries of the hallux mask were defined as the midpoint between the hallux and second phalangeal centroids and the medial limit of the hallux bounding box. The anterior-posterior boundaries were defined as the centroid of the hallux and the anterior extent of the hallux and second phalangeal bounding boxes.

The medial-lateral boundaries of the second to fifth toes mask were defined as the midpoint between the hallux and second phalangeal centroids and the lateral limit of the fifth phalangeal bounding box. The anterior-posterior boundaries were defined as the centroids of the second to fifth toes posteriorly and the anterior extent of the second, third, and fifth phalanges.

The medial-lateral boundaries of the first metatarsal head mask were defined as the midpoint between the first metatarsal and second metatarsal centroids and the medial limit of the first metatarsal bounding box. The anterior-posterior boundaries were defined as the midpoint between the first metatarsal and second metatarsal centroids and the midpoint between the hallux and second phalanx centroids.

The boundaries of metatarsal heads two to four were defined as the midpoints between adjacent centroids of metatarsals and phalanges. The boundaries of the fifth metatarsal were mask were defined as the midpoint between the fourth and fifth metatarsals or phalanges, and the lateral extent of the fifth metatarsal and fifth phalanx bounding boxes.

The boundaries of the lateral midfoot mask were defined by the lateral extent of the fifth metatarsal and the midpoint between the lateral extent of the fifth metatarsal lateral extent of the calcaneus bounding box laterally and the centroid of the intermediate cuneiform and the midpoint between the centroids of the second and third metatarsal medially. The anterior-posterior boundaries were defined by the midpoints between centroids of third to fifth metatarsals and the lateral bounding box of the fifth metatarsal anteriorly and the centroid of the intermediate cuneiform and the bounding box of the cuboid posteriorly.

The boundaries of the medial midfoot bounding box were defined by the centroid of the intermediate cuneiform and the midpoint between the centroids of the second and third metatarsal laterally and the bounding box of the first metatarsal and the calcaneus medially. The anterior-posterior boundaries were defined by the midpoints between centroids of second and third metatarsal heads and the anterior bounding box of the navicular anteriorly and the anterior bounding box of the calcaneus posteriorly.

The boundaries of the hindfoot were defined by the bounding box of the calcaneus extended posteriorly, the medial extent and lateral extent of the calcaneus bounding box, the centroid of the intermediate cuneiform, and the posterior extent of the cuboid bounding box.

Some of the bounding boxes were extended by a small margin in order to account for the extension of the soft tissue past the bone. These offsets were determined empirically based on CT scan projections (Figure 7-1).

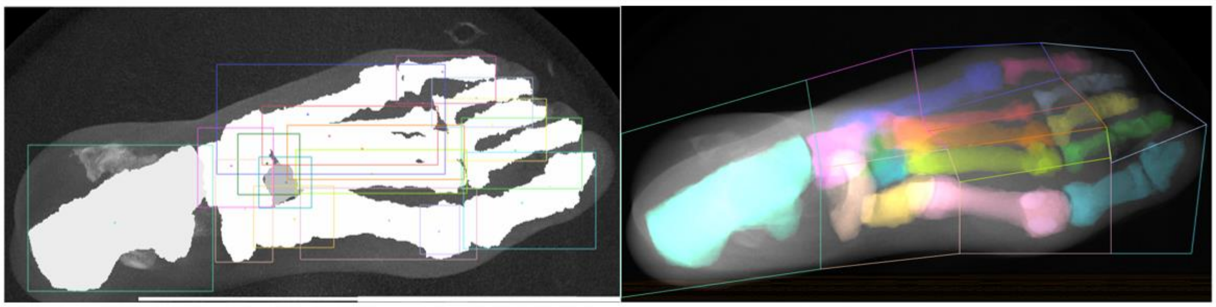

Figure 7-1: Left: Bone centroids and bounding boxes overlaid on project of CT intensity values through the interior-superior axis. Right: Plantar pressure mask defined by bony landmarks in the CT scan.

Each plantar pressure trial was registered to the summed projection of the CT along the superior-inferior axis. Using this summation-projection allows registration of the CT soft tissues to the outline of the plantar pressure. The CT projection was binarized using Otsu's method[317] to obtain the weighted skin outline, and the plantar pressure was binarized using a threshold of all sensors with pressure measurements over zero. Angular registration was performed by calculating the sum of absolute differences (SAD) metric across angles between -14 and 10 degrees in increments of 1 degree and selecting the angle for which the metric was minimized. Translations were calculated as the difference between the bounding boxes of the binarized, rotated CT and binarized plantar pressure map. The registration rotations and offsets were applied to the CT-generated masks to calculate the plantar pressure masks.

These masks were used to calculate peak plantar pressure, FTI, two definitions of PTI, pressure gradient (PPG) and pressure gradient angle (PGA). Mask overlays were compared visually to the 11 region built-in mask calculated by the novel automasking and multimask software. For variables that are reasonably expected to be similar between methods (Peak pressure, FTI, PTI_F), differences and percent differences were calculated between methods for each trial.

The pressure time integral was calculated as the spatial and temporal sum of all sensors in a region multiplied by the time step.

$$PTI = \sum_{v=1}^{T}\sum_{i=1}^{N}\sum_{j=1}^{M} P\left(x_{i,v}, y_{j,v}\right)(t_v - t_{v-1})$$

As all time steps are equal and thus the Δt term is constant, this can also be written as

$$PTI = \Delta t \sum_{t=1}^{T}\sum_{i=1}^{N}\sum_{j=1}^{M} P\left(x_{i,v}, y_{j,v}\right)$$

Similarly, the force-time integral was calculated as the spatial and temporal sum of the force measured by all sensors in a region multiplied by the time step, where the force is calculated by multiplying the pressure by the sensor area.

$$FTI = \Delta t \sum_{t=1}^{T}\sum_{i=1}^{N}\sum_{j=1}^{M} P\left(x_{i,v}, y_{j,v}\right) * A_{sensor}$$

A prior investigation used the force time integral to compute an alternative pressure time integral within the confines of commercial software. Their definition of the force time integral divided by the contact area is equivalent to the average pressure time integral over the mask area.

$$PTI_F = \frac{FTI}{CA} = \frac{\Delta t \sum_{t=1}^{T}\sum_{i=1}^{N}\sum_{j=1}^{M} P\left(x_{i,v}, y_{j,v}\right) * A_{sensor}}{\sum_{i=1}^{N}\sum_{j=1}^{M} A_{sensor}} = \frac{\sum_{sensor=1}^{N} PTI_{sensor}}{N}$$

For static trials, there is step-on pressure information that may not be informative when considering long-duration static loading. Therefore, these initial dynamic frames were removed by calculating the number of active sensors in each frame, identifying the time point where the number of active sensors reaches steady state as the point where the derivative of the number of active sensors is below 0.001, and taking only frames after the steady state point for parameter calculations. For dynamic trials, all frames were used for peak pressure, PTI, and FTI.

The PPG and PGA were calculated only for dynamic trials as previously reported[315,318,319]. The pressure gradient was calculated as the maximum of the difference between a pressure value and its surrounding 8-sensor neighborhood normalized by the distance between the centers of the sensors. The pressure gradient angle was calculated as the difference between the direction of the pressure gradient at each time step and the direction of the pressure gradient at the same sensor for the previous time step. The maximum of these time-varying values within a region is reported as the Max pressure gradient (MPG) and max pressure gradient angle (MPGA) for each subject. In order to avoid selection of the border pixels of the plantar pressure map, these pixels are removed from the analysis.

In order to compare differences between automasking methods, the peak pressure from each region of each dynamic trial was compared using both differences and percent error between matching trials, across all trials for each subject, and across subjects. To assess the effect of the removal of step-on frames from the static trials, the same metrics were calculated for static trials.

7.4 Results

The SAD-based registration of plantar pressure and CT soft tissue binary maps was qualitatively acceptable. Visually, the CT-based and commercial automasking created similar masking areas.

The first metatarsal, fifth metatarsal, and midfoot regions were the most different between methods, with occasional clear deviations in the hallux-toe boundary.

Overall, dynamic peak pressures using the commercial method were about 6.5% lower than dynamic peak pressures using the CT-based method (Table 7.4-1). Differences varied by region, but regional trends remained similar (Figure 7-2). FTI and PTI_F, which are calculated similarly between the two metrics, is 4.7% higher on average in dynamic trials using the CT method compared to the commercial method. Again, the deviation varies by region but regional trends remain intact (Figure 7-2).

Table 7.4-1: Average differences between the commercial method and the CT-based method by region and overall for both static and dynamic peak pressure, PTI, PTI_F, and FTI.

	Toes	**Forefoot**	**Midfoot**	**Hindfoot**	**total**	**overall average**
Peak, dynamic	-11%	-1%	14%	1%	1%	-6.5%
Peak, static	59%	32%	43%	25%	25%	29%
PTI, dynamic	-1613%	-1985%	-2230%	-7205%	-2199%	-2615%
PTI, static	-239%	-1217%	-666%	-4206%	-4075%	-1610%
PTI_F, dynamic	18%	12%	38%	-167%	-8%	-6.4%
PTI_F, static	70%	32%	65%	-142%	10%	18%
FTI, dynamic	1%	-7%	41%	-11%	0%	-4.7%
FTI, static	54%	34%	71%	27%	34%	33%

In contrast, the static pressures calculated by measuring only those frames which occurred after step-on were on average 29% lower than those calculated by the commercial software including step-on frames. Similarly, the PTI calculated as the sum of all pressures in a given region over time rather than just the peak pressures was 1610-2615% higher than those calculated as the sum of the peak pressures over time. The regional trends of the static and dynamic PTI differed between the two methods, with the heel sustaining higher total loads relative to the rest of the foot over the loading time in the CT-based method compared to higher summed peak pressures in the forefoot in the

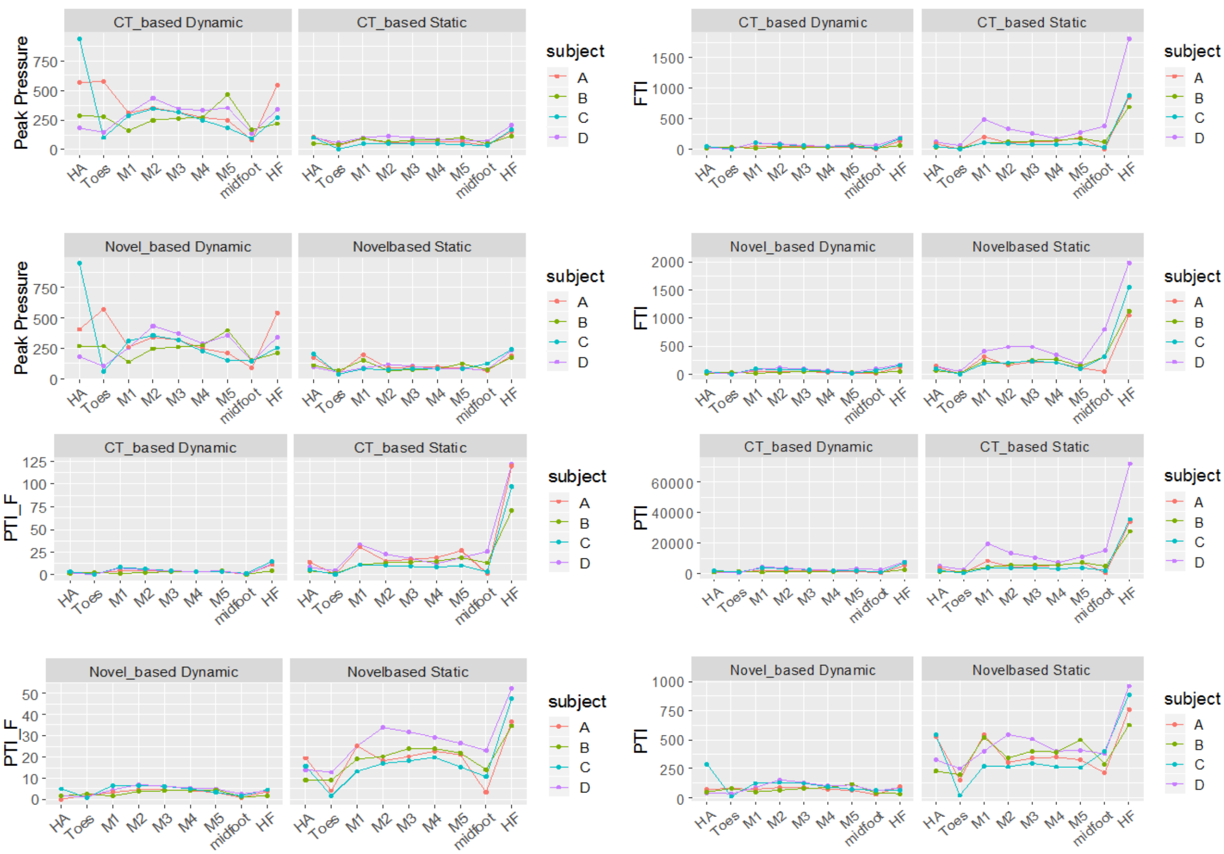

Figure 7-2: Per-subject regional peak pressure (top left)< FTI (Top right), PTI_F (bottom left) and PTI (bottom right) demonstrating similar trends for comparable dynamic metrics and differences in trends for static metrics and the different PTI definitions**.**

Table 7.4-2: MPPG and MGPA by region, averaged across all subjects

	HA	Toes	M1	M2	M3	M4	M5	LM	MM	HF
MPPG	55.2	41.7	31.4	28.2	27.1	23.8	42.7	13.5	3.6	35.2
MPGA	43.0	50.0	78.0	80.3	84.3	74.6	80.4	64.4	14.1	22.2

commercial method. These differences in regional PTI trends may also reflect a change in pattern due to the removal of the step-on frames in the static trials.

The calculated maximum peak pressure gradient and maximum pressure gradient angle (Table 7.4-2) are not available to calculate in the commercial software and therefore cannot be compared in the same way as peak pressure, PTI, and FTI.

While the locations of peak pressure, PTI, and FTI are often correlated, the locations of the MPGA and MPPG calculated over the entire pressure map are not always consistent with the location of the peak pressure (Figure 7-3).

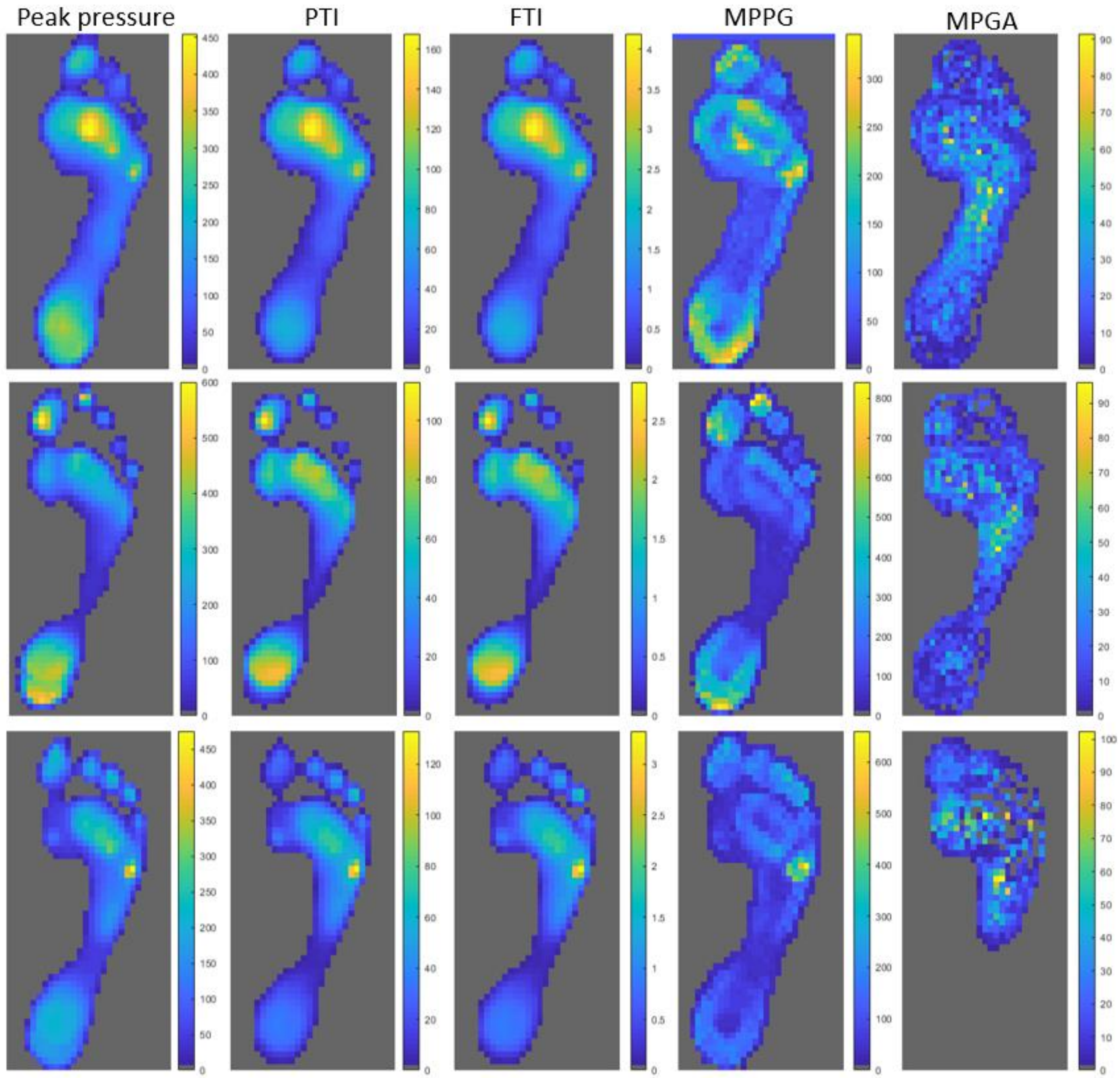

Figure 7-3: Spatial heat maps of peak pressure, PTI, FTI, MPPG, and MPGA for subjects A (top), B (middle), and D (bottom). Locations of peak values are sometimes but not always correlated between MPPG, MPGA, and peak pressure. Location of peak pressure is often correlated with location of peak PTI and FTI values

7.5 Discussion

This work presents a novel method to automatically calculate plantar pressure variables using segmented CT scans. Differences in peak pressure and FTI calculated using the two different methods were 6% of the total value on average. Outliers among these differences were often clustered in the values at the toes, the first and fifth metatarsals, and the midfoot-heel boundary, likely due to differences in the way that the masks are defined. The commercial mask appears to apply a relatively even horizontal distance to the metatarsal head areas. However, the metatarsal heads are not always distributed evenly in the soft tissue, particularly under load. The CT-projection method creates more variable metatarsal head widths and tends to place the first and fifth metatarsals closer to the sagittal midplane of the foot than the commercial software. This leads to larger first and fifth metatarsal areas and smaller second through fourth metatarsal areas. Additionally, the CT-based method calculates the midfoot-hindfoot border as the anterior boundary of the calcaneus, which places this boundary farther anterior than the commercial software. As a result, using the CT-based method, the midfoot values using are often lower and the hindfoot values higher than the commercial method.

The PTI calculated using all pressure values was two orders of magnitude higher than the value calculated by the commercial software using only peak values at each time step. There was a marked variation in regional trends between the two methods. The values of PTI using the sub-peak pressures were highest at the hindfoot in both static and dynamic conditions, followed by the first metatarsal, and lowest values at the toes, while the commercial PTI values were highest at the hindfoot for static acquisitions but at the hallux or second metatarsal for dynamic conditions. Differences between PTI values for high and low locations were also larger using the CT-based method. Furthermore, the regional pattern of the PTI and peak pressure using the commercial method are similar while using the CT-based method, the PTI is more similar in regional patterns to the FTI. These results indicate that there is an accumulation of higher sub-peak pressures at the hindfoot that are not captured by the commercial PTI metric, supporting the assertion of Melai et.

al [6]. Such high sub-peak loads could be indicative of cumulative damage during quiet activities of daily living that are not captured by the peak summation method.

Removing step-on frames from static load acquisitions moderately affected peak pressure values and regional pressure distributions in this small sample. However, the reduced peak pressures at the forefoot indicate that when these frames are not removed they may artificially increase the measured peak pressure for static acquisitions and may not reflect pressures commonly experienced during daily life as the static acquisition protocol is not a common motion. Measurement of these frames could incorrectly flag forefoot areas as high risk using static pressure thresholds or disrupt secondary calculations using static data. Applications where static plantar pressure is used for stiffness calculations [31] or other applications where true quiet stance is important should take care to ensure these frames are not included.

Prior work has based the calculation of pressure gradient and pressure gradient angle on only the location of the peak pressure[36,318,319]. However, the maximum pressure gradients and angles in this study did not always occur within the 8-pixel neighborhood of the peak plantar pressure. Use of a matrix approach for calculating MPPG and PGA allows visualization of PPG and PGA ‘maps’ which may better illustrate how the plantar pressure changes both spatially and temporally. Location of peak pressure and peak pressure gradient or peak pressure gradient angle taken together may explain more ulcer risk than location of peak pressure alone.

In some cases, the commercial automasking software incorrectly labelled toe regions. While the pre-defined CT-based mask regions are more box-like and less adaptable to the curves of regions like the toes, complete mislabeling of entire pressure regions is more unlikely. However, the CT-based method does suffer occasionally from assigning pixels on the borders of the regions incorrectly due to the rigid lines. In particular, the CT-based method often underestimates the hallux FTI and overestimates the toe pressure relative to the commercial method due to the curve of the tissue at that location. Use of the weighted CT scan lends additional credibility to the pressure map masking as it is better able to reflect the subject-specific relationship between soft tissue area and underlying bone geometry, which could be additionally useful for studies in patient populations prone to bone abnormalities, such as patients with diabetes.

There are several limitations to this work. First and foremost is the small sample size. While this sample is too small to validate statistical equivalence (peak pressure, FTI) or difference (PTI, removal of step-on frames), the calculated percent error and regional trends support the utility of this method. The use of segmented CTs limits the broader applicability of this method and contributes additional cost and concerns about radiation dosage. However, in cases where CT scans or MRI are already acquired and segmented for other outcomes of interest and where there is a desire for additional flexibility computing plantar pressure variables of interest, this methodology represents an efficient method for producing those results. As fields such as biplanar fluoroscopy and medical image processing advance, it may be more common to have a segmented bony anatomy available. Segmentation itself is also a significant time investment. However, automated tools are rapidly reducing the time required for this task and could be implemented for this method, as the calculation of bounding boxes does not require a high- quality segmentation. Finally, this method was only tested against a single commercial system and with normal foot anatomy. Many commercial systems calculate similar metrics using similar methods, making it likely that the CT-based method performs well relative to these methods as well. Bony deformities, such as claw toe and partial foot amputations that are common with diabetes, can create issues in masking regions of plantar pressure as there may be changes in the plantar pressure shape used to define the masks.

Use of the weighted CT scan reflects the subject-specific relationship between soft tissue area and underlying bone geometry, which may be more robust to these challenges. However, the current software relies on presence of all 16 segmented bones and would need to be adapted for the case of missing bones.

7.6 Conclusion

This work contributes an alternative automated method for plantar pressure analysis and spatially extends two variables to further explore the explanatory power of plantar pressure. This method could make newer variables like MPG and MPGA more accessible, and provides a framework from which to build additional plantar pressure-based analysis.

8 A 3-D characterization of diabetic and non-diabetic plantar Soft tissue *in vivo*

8.1 Abstract

Ulceration is a severe complication of diabetes that often precedes nontraumatic lower limb amputations in the diabetic population. While there are established general systemic risk factors for ulcer formation, the underlying mechanics of ulcer initiation remain unclear. Volumetric ultrasound scans were taken of the entire plantar soft tissue of four subjects (1 diabetic, 3 nondiabetic) in unloaded, unloaded shear wave elastography, and dual support loaded conditions. Plantar pressure and computed tomography scans were also acquired for validation and stiffness measurements. Loaded and unloaded scans were registered and internal deformations were measured using commercial digital volume correlation software. Vertical displacement, axial and principal strains, and tissue thickness were measured. Tissues were segmented from weighted ultrasound scans to obtain tissue-specific measurements and vertical displacement was registered to plantar pressure to obtain a stiffness map. Ultrasound thickness measurements and volume reconstruction were validated using computed tomography. Ultrasound volume measurements were 11-28% lower than computed tomography measurements. Plantar pressure, average shear wave speed and modulus measurements, and muscle volume measurements were comparable to prior work. Strain maps varied between subjects but demonstrated increased vertical strain in load bearing regions of the fat and skin, higher sagittal shear strain below the metatarsals and lower beneath the calcaneus in the fat and skin, and higher sagittal shear strain at the anterior plantar fascia. Stiffness was highest at the heel and metatarsals and values with within ranges of prior work using similar methods.

8.2 Introduction

Diabetes is a metabolic disease affecting over 34 million Americans[1]. As a systemic disease, diabetes is associated with a range of complications. In the foot, complications associated with diabetes include neuropathy, vascular disease, structural deformities, and ulceration. Ulcers are costly[3], painful, difficult to heal, and if not healed effectively, can lead to amputations[105].

Several clinical measurements have been linked to ulcer risk, including regular standard of care measurements like insulin use[149], less frequently adopted measurements like peak plantar pressure[8,320], and comorbidities like peripheral neuropathy[149], peripheral arterial disease[149] or foot bone deformity[149]. However, models based on these metrics can only predict if an ulcer will occur and not where, and may have sensitivity as low as 75% and specificity as low as 27%[321]. From a biological and mechanistic perspective, diabetes has been linked with increased tissue stiffness and modulus [22–24,35], and microstructural disruptions[56,110,322] in *ex vivo* testing, which could contribute to ulcer risk. However, there remain questions about how ulcers form and insufficient effective predictive measurements for early detection and prevention. In particular, while it has long been hypothesized that shear forces and strains are important in understand ulcer etiology[6], the majority of plantar mechanical measurements have been uniaxial.

Ultrasound is a popular choice in biomechanical plantar soft tissue assessments. Relative to computed tomography (CT) or magnetic resonance imaging (MRI), it is low-cost, portable, fast, and introduces less risk to the patient. Advances in signal processing, noise reduction, and transducer technology have improved the quality of ultrasound images, and advances such as shear wave elastography, which uses different acoustic techniques to estimate material modulus, have made ultrasound even more useful. However, most clinical ultrasound is planar or involves small swept volumes of up to 30^{o}. Recently, researchers have been extending the idea of swept volume ultrasound to larger volumes using larger mechanical translation systems[78,97,98,263,303] or instrumented transducers [94,323–325]. However, these volumetric applications are not load bearing and do not measure deformation.

The combination of applied load and ultrasonic measurement has been used to measure *in vivo* plantar tissue stiffness and deformation. These investigations have included both single-line send-receive ultrasound[34,35,37,181,182] and planar B-mode ultrasound imaging[104,183,326]. Methods of applying load include indentation normal to the plantar surface[34,35,37,181,182,326], static standing on a plate[187,192,304], cyclic loading with the transducer situated behind a plate[103], and single-step[104] conditions. These works often report uniaxial peak tissue deformation or stiffness or modulus from a stress-strain curve. However, these works do not report two-dimensional strain or displacement maps nor do they report lateral or shear strains.

The SWE modality does produce two dimensional stiffness maps based on the shear speed of sound through the material, which is related to the shear and elastic moduli. SWE has been used to describe changes in elastic moduli of the heel pad with depth[185], age[184], and heel pain[155]; improve predictive models for ulceration[90]; and inform material properties for finite element models[191]. However, while SWE values have demonstrated similar trends to finite element models[91] and mechanical testing (Appendix A), the relationship between SWE and prior work has not been established. Finally, while qualitative strain elastography has been used to evaluate the plantar fascia[189] and the plantar fat[327] in diabetic and non-diabetic populations, evaluation using quantitative SWE has not been reported.

The primary method of obtaining and reporting shear strain and two-dimensional strain maps are finite element models of the foot[191,203,204,328,329]. These models vary in complexity of geometries, tissues represented, constitutive models applied, and loading scenarios investigated. Finite element models are time consuming to create and validate and are typically focused on reporting the effects of changes to conditions such as footwear or tissue stiffness rather than comparisons between models of different subjects. While these are useful for understanding how changes in material properties can affect structural foot function, results can vary with mesh size and boundary conditions and it is difficult to assess the effect of the assumptions of the initial model on internal strain without an internal measurement for comparison.

Recently, two groups have used external MRI-compatible actuators to apply loads while acquiring three-dimensional MRI images. One group reported applied force and differences in calcaneus-to-plate differences to obtain a uniaxial estimate of stiffness for one diabetic and one non-diabetic subject[29]. The second group performed an elastic registration of a loaded and unloaded MRI scan of a single subject to measure internal deformation due to the applied load and reported the superior-inferior and anterior-posterior displacements as well as the maximum principal shear strain. They also used the resultant displacement maps to evaluate constitutive models used in a finite element analysis[202]. However, both of these works only report images of the heel pad and the actuator is only applied to the heel.

In aim of this work is to develop methods to better understand the multidimensional strain behavior of the plantar soft tissue using a novel load-bearing volumetric ultrasound device capable of obtaining loaded and unloaded volumetric images of the entire plantar soft tissue. We propose to calculate tissue-specific axial and shear strains for each anatomical axis as well as maximum and minimum principal and principal shear strains using digital volume correlation. We also propose calculation of tissue-specific stiffness using shear wave elastography (SWE). We also propose using plantar pressure and volumetric deformation to create tissue stiffness maps similar to plantar pressure maps. We plan to use these methods to evaluate diabetes-related changes in stiffness deformation and mechanics.

8.3 Methods

8.3.1 Demographics

Six (D=3, ND=3) age-matched male subjects were recruited for this IRB-approved protocol. Subjects were ambulatory, and those with neuropathy, recent injury to the lower limb, diagnosed peripheral vascular disease, or arthritis were excluded. Hba1c was recorded from the last clinical visit on record when applicable.

8.3.2 Initial protocol

Subjects first had measurements of height and weight taken. Then, subjects underwent a 10g (5.07) Semmes Weinstein monofilament test for sensation. Subjects who were not able to accurately locate the 10 contact sites of the monofilament were excluded from the study. Measurements of foot length and width were recorded in order to set scanning parameters. Finally, subjects were asked to walk across a 6 m path four times a normal speed to obtain the subjects normal self-selected walking speed.

8.3.3 Plantar pressure

Plantar pressure data was taken using the novel emed plantar pressure platform. Three to five trials each of static plantar pressure and dynamic plantar pressure were recorded for each foot. Dynamic trials were captured at a self-selected walking speed that matched previously recorded typical walking speed for each subject.

8.3.4 Ultrasound Scans

After plantar pressure collection, subjects were seated on the scanning machine described in Chapter 7 (Figure 8-1). The right foot was placed either in an isotonic (0.9% NaCl) water bath or on a custom polyacrylamide hydrogel coupling pad. In the case of polyacrylamide hydrogel pads, they were manufactured according to a previously reported protocol (Section 7) and within 2 hours of data collection, were removed from the CaCl storage solution, washed, and stored in an isotonic NaCl and glycerin solution to reduce irritation and drying associated with prolonged skin contact. The transducer was coupled to the underside of the plate using either a hydrogel burn pad secured with a polyurethane adhesive bandage, or a custom molded polyacrylamide hydrogel couplant (Figure 8-1). Unweighted structural scans were taken with B-mode ultrasound through a 1/8" HDPE plate using an SL18-5 transducer and an Aixplorer (Supersonic Imagine, Aix-enProvonce, France) using the MSK Foot & Ankle preset, 1660 m/s, Res (C1) or Pen, and HD. The images were taken with 0.3925 mm- 0.474mm spacing in the anterior-posterior direction. Subjects were instructed to relax their foot and hold it still. After the unweighted structural scans, an unweighted material scan was taken using shear wave elastography and 1.5mm-2.5mm spacing in the anterior-posterior direction. The SWE focus for the SWE images was set just deep to the superior extent of the SWE box. The SWE box was set to the maximum size allowed and positioned on the medial side of the image to allow overlap of SWE values. Three SWE images were taken at each step to allow the SWE signal to stabilize, based on previously reported reliability testing[330]. Weighted structural scans were taken with B-mode ultrasound through a 1/4" (6.35mm) HDPE plate. The structural scans took 9-10 minutes to complete depending on the length of the foot while the SWE scan took between 14-30 minutes to complete. In total 2 unweighted structural scans, one SWE scan, and one weighted structural scan were acquired. Subjects dried off their foot and rested it outside the scanning area between scans for between 5 and 15 minutes. Subjects typically took a break including walking around the test area between the unweighted and weighted scans as this required changing the scanner plate.

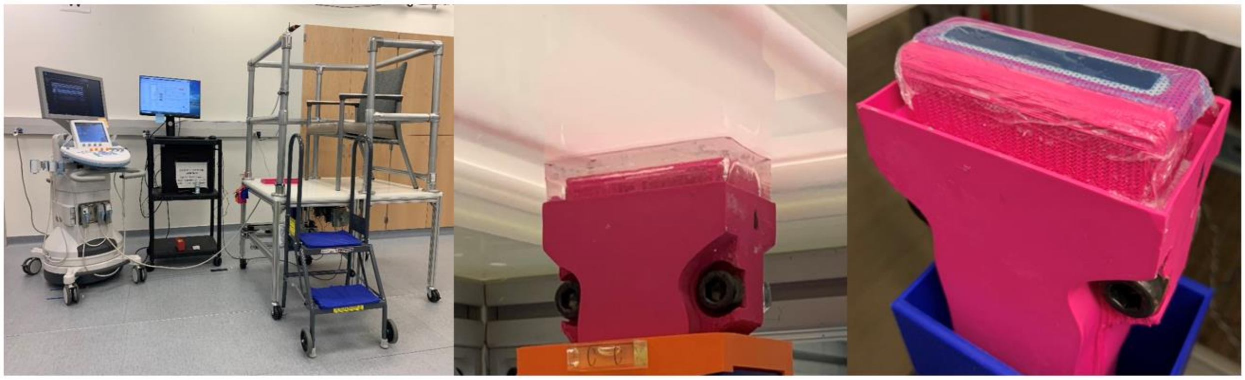

Figure 8-1: Left: setup for volumetric ultrasound scans. Subjects ascend the stairs and either sit in the chair or stand placing equal weight in the scanning area and the non-scanning area. The computer hosts the MATLAB-based control program and the system uses an Aixplorer commercial ultrasound machine.

8.3.5 CT

A computed tomography (CT) scan was taken using the CurveBeam Lineup (Hatfield,PA,USA) using the large field of view, small (C1) or standard patient preset, which uses 100kV (small) or 120kV (standard) and 5mA. In all, 17 bones (calcaneus, 5 metatarsals, 3 cuneiforms, cuboid, navicular, 5 phalanges, and sesamoids) were manually segmented from the right foot to use for validation of the thickness measurements as well as to automatically mask the plantar pressure measurements.

8.3.6 Ultrasound image registration and volume reconstruction

Ultrasound images were registered within-scan manually using a custom-developed graphical user interface (GUI). This user interface allows a user to align the images using different horizontal overlaps, vertical displacements, and rotations. It also allows the user to incrementally adjust the image anterior-posteriorly between the three passes of the scan in the case of movement or motor stalling. After manual medial-lateral registration, the scans were registered anterior-posteriorly between steps using normalized cross correlation to offset minor movements during the scan. The images were stitched by taking the maximum value of the image intensity in overlapping regions and normalized by the maximum intensity per column.

Shear wave elastography images were reconstructed by first registering the blue channel of the saved live screen images in the same manner as the B-mode scans. Then, the raw shear wave speed values saved from the research interface were positioned inside an empty matrix according to the SWE box size, image size, and SWE box position information saved from the research interface. Shear wave speed (SWS) values outside of the expected range based on the maximum rated modulus were removed and SWS matrices were up sampled to the resolution of the images using nearest neighbor interpolation prior to placement in the image area. A composite SWS map was created by taking the per-pixel average of the 3-4 SWS acquisitions taken at each step. Then the registration determined from the image data was used to reconstruct a volume of SWS values.

8.4 During the process of processing SWE images, mismatches between the recorded SWS using the 'last frame' acquisition mode and the 'last frame' image mode were identified (see Conclusion

Plantar soft tissue mechanics have long been of interest to biomechanics researchers and internal medicine clinicians treating patients with diabetes. The morbidities associated with diabetes-related plantar ulceration are significant, and the mechanical etiology of these wounds remains unclear, leaving a gap in knowledge that could aid prevention. The development of a load-bearing ultrasound-based volumetric plantar soft tissue scanner and the associated pipeline for measuring internal strain, internal modulus, muscle volume, and regional stiffness represent a new way to measure and understand this complex biological structure.

Supplemental Images). Therefore, SWS frames were manually compared to image frames and frames that did not match were removed from analysis. For all matching SWS values, these values were averaged within step and the average values were used for the registration and reconstruction.

Registration between scans of different types was performed manually using point-to-point registration in 3D Slicer. Points chosen included metatarsal heads, the base of the fifth metatarsal, and the inferior calcaneus for translation and rotation in the transverse, coronal, and sagittal planes, and the scanning plate for translation along the superior-inferior axis. Ultrasound volumes were registered so that the scanning plates were aligned. The transform estimated from slicer was transferred to MATLAB and used to transform the volumes before saving the file format required for digital volume correlation.

8.4.1 DVC

Registered weighted and unweighted ultrasound volumes were resized to a cubic voxel in MATLAB using built in function interp3 with the cubic method. Resized volumes were imported into StrainMaster digital volume correlation software (LaVision, Ypsilanti, MI). After determining best parameters (see below), displacement and strain along each anatomical axis, shear strain in each anatomical plane, principal strains, and the correlation value quality metric were exported from the software as a .dat file for subsequent analysis in MATLAB.

8.4.2 Segmentation

All visible intrinsic muscles, skin, plantar fat, visible bones, general soft tissue, and the scanning plate were manually segmented from the weighted scans, and soft tissues of interest for SWE analysis were manually segmented from unweighted scans using Mimics (Materialise, Leuven, Belgium). All foot bones and the load bearing plate were segmented from CT scans using thresholding tools available in Mimics.

8.4.3 Validation

8.4.3.1 Validation of ultrasound volumes

Segmentations from the CT scan and the matching ultrasound scan for each subject were imported into MATLAB and converted into label maps. The upper plate surface was identified as the first index in the superior-inferior direction where the voxel value of the binary plate label map changed from 0 to 1. The inferior bone surface was defined as the last index in the superior-inferior direction that was included in the bone mask for each position in the transverse plane. The distance between the bone and the plate was defined as the difference between the inferior bone index and the superior plate index for each spatial position in the transverse plane. This pixel value distance was then converted to millimeters as the CT and US have different resolution along the superior-inferior axis. Five bones were selected as they are the clearest in the ultrasound images: calcaneus, second metatarsal, fifth metatarsal, and the sesamoids.

The distance was qualitatively compared using scale-normalized heat maps. For a quantitative comparison, regions of interest (ROIs) were placed using a point-and-click GUI with standardized ROI sizes at the posterior calcaneus, second and fifth metatarsal heads, the base of the fifth metatarsal, and the sesamoids, as these are the clearest bone surfaces in the ultrasound images. Distance values within the ROIs were averaged for comparison and percent error was calculated for each location.

8.4.3.2 Validation of DVC

The commercial digital volume correlation software operates by performing sequential intensity-based correlations at different resolutions. These sequential correlations are in the form of one FFT-based correlation followed by four levels of direct correlation at different subsampled volumes. There are six parameters for each subsampling step: subvolume size, shape, overlap, peak search, binning, and passes. There are four additional parameters that can be varied for each run: correlation mode, FFT size, remove rigid body motion, and required valid voxel size. DVC was run to correlate the weighted and unweighted scans for two subjects using different combinations of the parameters (Table 8.4-1) in order to identify parameters to produce satisfactory results. The shape was set to circle, and the binning was set to 8^3 for step 1, 4^3 for step 2, 2^3 for step 3 and no binning for step 4. The different correlation modes are equivalent for processing a single step of deformation, and rigid body motion should have been removed with the initial manual registration, so this option was not used.

Parameters were chosen based on the following criteria:

Table 8.4-1: Values tested for each available DVC parameter.

FFT pre-shift size	64,80,96,128,144,160
Subvolume 1 size	48,64,80,96,128,160
Subvolume 2 size	32,40,48,64,80
Subvolume 3 size	16,20,24,28,32,40,48,56
Subvolume 4 size	8,12,16,20,24,28,32
1st search radius	16,24,32,40,48,56,64
2nd search radius	8,12,16,20,24,28,32
3rd search radius	4,6,8,10,12,14,16,20
4th search radius	2,3,4,6,7,8,10
Overlap 1,2,3	50,75
Overlap4	0,75
Number of passes step 1	2,3
Number of passes step 2,3,4	2,3,4
Required valid voxel %	10,20,30,40,50,70

1) Size of deformation to track

The software must be able to track the largest deformation, which means that the largest subvolume must be larger than the largest anticipated displacement. The maximum anticipated vertical displacement is on the order of 2cm(0.5) / 0.1668 ≈ 60 pixels (px). No reported measurements currently exist for the shear strain of the plantar soft tissue, however, Pai et. al used an estimate of 85% shear strain[23,198]. Using the formula $\gamma=x/h$ and the resolution of 0.1668, we can estimate that the x-displacement may be on the order of 0.85 * 2cm./.1668 mm/px = 100 px. For the range of resolutions in the DVC volumes, these values are between 60-65 px (vertical) and 101 – 110 px (lateral). Therefore, the maximum displacement searched by the program should be around 100px.

2) Spatial resolution and minimum subvolume size

The minimum subvolume size must be at least as small as the minimum desired resolution. In this case, the smallest layer of desired resolvability is the skin. The minimum desired resolution was empirically determined to be around 4 pixels. The tradeoff of small subvolumes is increased noise.

3) Computational load

The DVC program must store volumes in working memory in order to process them. As the license is not GPU processing compatible, all processing must be performed on a CPU. Additional memory must be read and written to disk, which increases computational time. The limitation of the current hardware is 136 GB RAM and 8 CPU cores.

4) Overlap, binning, shape, number of passes

The DVC program has several options for the parameters for each correlation step. Binning the volume is equivalent to down sampling using a mean averaging filter of the specified bin voxel dimensions. This reduces the required memory for larger subvolumes and search radii. The overlap specifies the degree to which tracked subvolumes should overlap. Overlapping subvolumes allows for finer spatial resolution of displacement vectors while still computing displacement over a larger subvolume. The shape parameter determines the shape of the subvolume as either cubic or a Gaussian-weighted sphere where the radius is equal to the subvolume size. The spherical option improves accuracy by including down-weighted information from farther voxels. The number of passes is the number of times the current step is repeated in a predictor corrector scheme. More passes can increase the accuracy but also increases the runtime of the evaluation.

In order to assess how changes in these parameters changed the outcome, the quality of the fit was assessed qualitatively by comparing the deformed volume remapped to the reference volume using the calculated displacement to the reference volume, and by assessing the biological likelihood of the resultant displacement map in the coronal plane at regular reference intervals.

8.4.4 Measurements

8.4.4.1 Plantar pressure

Plantar pressure scans were automatically analyzed using custom MATLAB code as described in Chapter 8. Briefly, novel pressure files and CT segmentations were loaded into MATLAB, and a 10-region mask was generated using the centroids and bounding boxes of the bone masks. The superior-inferior projection (transverse plane) of the CT scan was then registered to the area of the activated plantar pressure sensors using the sum of absolute differences metric.

Using the mask generated from the CT-pressure registration, three metrics (peak pressure, pressure time integral (PTI), force time integral (FTI), and pressure time integral relative to force (PTI_F)) are computed for the whole plantar area and for each region for static acquisitions, and likewise, five metrics (peak pressure, PTI, FTI, PTI_F, pressure gradient (MPPG), pressure gradient angle (MPGA)) are calculated for dynamic acquisitions. The pressure time integral and force time integral are computed using all sensors within a region over the length of the acquisition. The pressure gradient and pressure gradient angle are calculated using previously reported methods (Chapter 7.3).

8.4.4.2 Shear Wave Speed and Modulus

SWE images were registered to unweighted scans by first upsampling the image volume to the size of the unweighted volume, then applying rotation around the superior-inferior and anterior-posterior axes followed by translation and scale.

$$\begin{bmatrix} r_{AP} & r_{AP} & 0 & 0 \\ -r_{AP} & r_{AP} & 0 & 0 \\ 0 & 0 & 1 & 0 \\ 0 & 0 & 0 & 1 \end{bmatrix} \begin{bmatrix} r_{SI} & 0 & r_{SI} & 0 \\ 0 & 1 & 0 & 0 \\ r_{SI} & 0 & r_{SI} & 0 \\ 0 & 0 & 0 & 1 \end{bmatrix} \begin{bmatrix} 1 & 0 & 0 & T_{ML} \\ 0 & 1 & 0 & T_{SI} \\ 0 & 0 & 1 & T_{AP} \\ 0 & 0 & 0 & 1 \end{bmatrix} \begin{bmatrix} S_x & 0 & 0 & 0 \\ 0 & 1 & 0 & 0 \\ 0 & 0 & S_y & 0 \\ 0 & 0 & 0 & 1 \end{bmatrix}$$

Where the rotations around the anterior-posterior and superior-inferior axes are designated r_{AP} and r_{SI}, the translation along each axis is represented by T--, and the scale is represented by S_x and S_y. In order to mitigate interpolation effects on SWS values, the SWS values volume was interpolated using nearest neighbor interpolation in the coronal plane, where the resolution difference was less than a factor of 2, and for the anterior-posterior direction, where sampling was different by a factor of close to 6, the frames were inserted in the closest location of a blank volume. The aforementioned translation, scale, and rotation were inverted and applied to transform the segmentations of the ultrasound volumes to the SWS values to get tissue-specific values.

Figure 8-2: Regional separation of SWE volumes into toes, forefoot, midfoot, and hindfoot. The heatmap is a summation of the segmented structures showing where the regional boundaries are in

Tissue-masked volumes were converted to tissue-specific modulus values using density values available in the literature[331,332] (911, 1109, 1142 kg/m3 for fat, skin, and fascia respectively) and the standard conversion $E = 3\rho c^2$, where E is the elastic (Young's) modulus, ρ is the tissue density, and c is the shear speed of sound. The mean and standard deviation were taken over the entire tissue volume.

For larger tissue regions (skin and adipose tissue), the regional SWE parameters were calculated by distributing the image into 4 regions: toes, forefoot, midfoot, and hind foot (Figure 8-2), and calculating the average tissue SWS and modulus within these regions.

8.4.4.3 Muscle Volume

Muscle volumes were measured using the regionprops3 function in MATLAB on the label matrix defined by the segmented weighted volume and converted from voxels to cm^3 using the scan resolution.

8.4.4.4 Deformation

Displacement, strain, and correlation values were reconstructed from the coordinate-value output file into a volume of the same size as the segmented volume of the weighted scan using the input resolution of the volumes. Mask volumes for each tissue were created from the segmented volume, and masks were applied to the deformation values and average and maximum values were taken for each tissue along the inferior-superior axis to create maps in the transverse plane. The deformation and strain volumes were also colorized and overlaid on sliced from the weighted volume using custom MATLAB code.

8.4.4.5 Stiffness

Vertical displacement and average vertical force were calculated from DVC and plantar pressure values, respectively. Vertical displacement was taken as the maximum vertical displacement along the superior-inferior axis across the 3D spatial locations within the segmented soft tissue volume. Force was calculated as the average of all force values in a single spatial sensor location over the duration of a static pressure acquisition between the cutoff for step-on frames (7.3) and the last frame, where force is the pressure multiplied by the sensor area.

In order to create the stiffness map, several types of data needed to be co-registered. First, the transformation matrix that aligned the weighted B-mode volume with the unweighted B-mode volume for DVC was applied to the segmented weighted B-mode volume. Then, a 2D binary map of the weight-bearing area of the foot was created as all the pixels where the sum of the skin mask in the superior-inferior direction up to an empirically determined cutoff of 140 pixels (6.8-7.7 mm) is greater than zero. This 2D map of the skin area from the segmented weighted volume was then down sampled to the size of the plantar pressure and rigidly registered to the binary map of the area of active pressure sensors using step gradient descent and the mean squares metric.

The map was then upsampled according to the resolution of the DVC such that there was approximately 1 DVC result per pixel to avoid interpolation of DVC values. Plantar pressure was upsampled using nearest neighbor interpolation to best approximate the actual pressure.

The transformation matrix is:

$$\begin{bmatrix} S_x & 0 & 0 & 0 \\ 0 & 1 & 0 & 0 \\ 0 & 0 & S_y & 0 \\ 0 & 0 & 0 & 1 \end{bmatrix} \begin{bmatrix} T(2,2) & 0 & T(2,1) & 0 \\ 0 & 1 & 0 & 0 \\ T(1,2) & 0 & T(1,1) & 0 \\ T(3,2) & 0 & T(3,1) & 1 \end{bmatrix} \begin{bmatrix} S_x & 0 & 0 & 0 \\ 0 & 1 & 0 & 0 \\ 0 & 0 & S_y & 0 \\ 0 & 0 & 0 & 1 \end{bmatrix}$$

Where Sx and Sy are the stretch factors in the medial-lateral and anterior-posterior directions, respectively, and T is the transform determined by the binary skin map to plantar pressure registration. Stiffness was calculated as the average force divided by the vertical displacement for each spatial location.

8.5 Results

8.5.1 Data collection

Table 8.5-1: Quality, variable parameters, and issues with each type of data acquired for each of the six recruited subjects.

W US	SWE	CT	PP	Other
lower resolution (.474mm step) poor coupling at HA more superficial focus (difficult to segment deeper structures) medial side cut off poor coupling at medial heel	'last' (poor quality, values thrown out d/t difficulty matching, lower resolution) higher resolution (0.9mm step) medial side cut off	unweighted Large Fov, Lite	3 static	
higher resolution (0.415mm step) forefoot and center pass midfoot dark poor lateral transducer coupling	'last' (poor quality, values thrown out d/t difficulty matching, lower resolution) lower resolution (2.4mm step)	weighted Large Fov, regular	1 static	
				excluded
higher resolution (0.415mm step) motion (difficult to reconstruct	poor coupling (gel-foot & gel-plate) 'all' (higher quality, better matching, more data) lower resolution (2.4mm step)	weighted Large Fov, regular	1 static	
higher resolution (0.415mm step) dark (poor gain matching) high plate reflection	'all' (higher quality, better matching, more data) lower resolution (2.4mm step) dark (poor gain matching) high plate reflection	weighted Large Fov,	1 static	
				excluded

Subject	UW US
C1	lower resolution (.474mm step) more superficial focus (difficult to segment deeper medial side cut off
C2	higher resolution (0.415mm step) poor coupling on ends of transducer center pass dark cut off end of heel
D0	
D1	poor coupling (gel-foot & gel-plate) higher resolution (0.415mm step)
C3	higher resolution (0.415mm step) significant motion - difficult to dark (poor gain matching) high plate reflection
D00	

As a result of variations in ultrasound parameters, data collection protocols, subject motion, and exclusion criteria, data quality varied between subjects (Table 8.5-1). As a result, not all of the data was analyzed for all subjects.

8.5.2 Volume validation

Bone to plate distances measured from ultrasound volumes were 9-28% lower than those measured from the corresponding CT (Table 8.5-2). Errors for subjects C2 and C3 were lower than for C1.

Table 8.5-2: Average bone-to-plate distances at each measured location for each subject and the error of the ultrasound measurement.

	CA	M5 base	M5 head	M2	Ses1	Ses2	total
C1							
CT distance (mm)	18.44	13.58	8.51	14.17	12.59	12.87	
US distance (mm)	13.39	11.31	5.90	10.80	10.16	6.40	
difference (mm)	5.05	2.28	2.61	3.37	2.43	6.47	3.70
difference (%)	27%	17%	31%	24%	19%	50%	28%
C2							
CT distance (mm)	10.34	12.74	7.88	14.05	7.28	8.93	
US distance (mm)	9.01	13.13	6.96	10.83	7.77	7.31	
difference (mm)	1.33	-0.39	0.92	3.22	-0.49	1.62	1.04
difference (%)	13%	-3%	12%	23%	-7%	18%	9%
C3							
CT distance (mm)	10.74	15.55	9.10	14.98	11.29	7.46	
US distance (mm)	10.20	14.28	7.24	11.66	10.49	6.48	

difference (mm)	0.54	1.27	1.86	3.31	0.79	0.98	1.46
difference (%)	5%	8%	20%	22%	7%	13%	13%

8.5.3 Plantar pressure

Dynamic peak pressure, PTI, FTI, PTI_F, PPG, and MPGA, for the 4 subjects are measured (Figure 8-3). Peak values for all static variable occurred at the heel. Similarly, peak PTI_F, FTI, and PTI also occurred at the heel in the dynamic trials. However, peak overall pressure occurred at the hallux for two subjects and the heel and fifth metatarsal head for the two other subjects. The maximum pressure gradient occurred at the forefoot for two control subjects and at the fifth metatarsal head for the remaining control and diabetic subject. The maximum pressure gradient angle occurred at the metatarsal heads for all subjects.

Differences between groups were minimal. The single subject with diabetes demonstrated less variability across regions in temporal integral variables but a larger difference between regions in maximum pressure gradient angle.

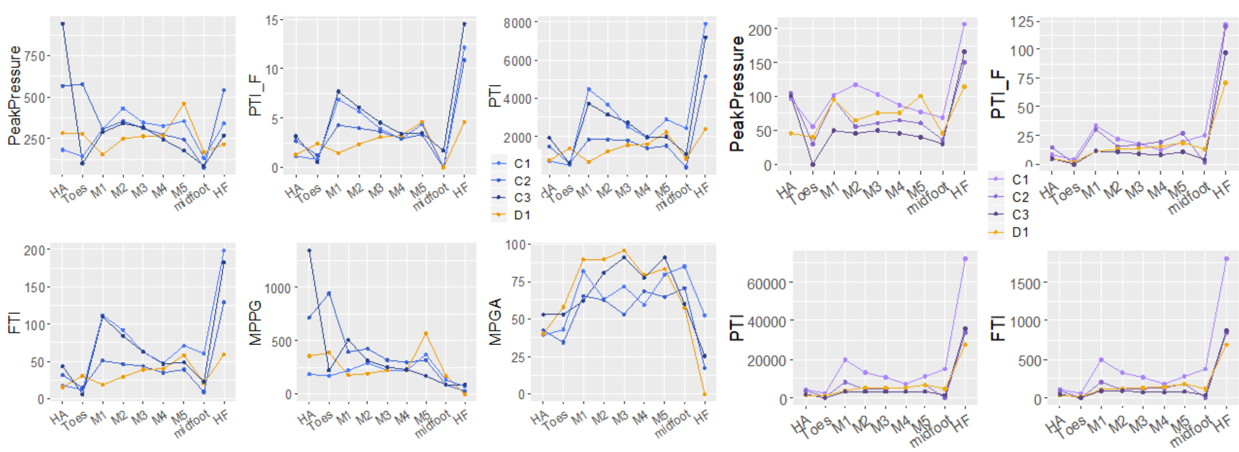

Figure 8-3: Dynamic (left, orange and blue) and static (right, purple and gold) regional pressure values for each measurement and subject. The sample size is too large and subject demographics too different to draw inferences. M1-5 = first through fifth metatarsals, HA = hallux, HF = hindfoot.

Figure 8-4: 3D rendering of segmented tissues from subject C2. Left: orthogonal view of all segmented tissues. Right: superficial to deep layers of plantar fascia and muscles.

8.5.4 Segmentation

The scanning plate, 11 bones, and 10 soft tissue structures were successfully segmented from the weighted ultrasound scan of C2, and a subset of those were segmented from the weighted and unweighted scans of other subjects (Table 8.5-3). All soft tissue not readily identifiable as one of the 10 structures was labeled as a general soft tissue (only pictured in the coronal overlays). The 3D model of the weighted segmentation for subject C2 is displayed (Figure 8-4).

Table 8.5-3: List of features segmented for subjects C1 and C2.

	C1		**C2**		**D1**	**C3**
	Weighted	Unweighted	Weighted	Unweighted	SWE	Weighted
Skin	x	x	x	x	x	
Adipose	x	x	x	x	x	
General soft tissue	x	x	x			
Plantar Fascia	x	x	x	x	x	
Hallux	x	X	x			x
Phalanx 2	x	X	x			x
Phalanx 3	x	X	x			x
Phalanx 4	x	X	x			x
Phalanx 5	x	X	x			x
Metatarsal 1	x	X	x			x
Metatarsal 2	x	X	x			x
Metatarsal 3	x	X	x			x
Metatarsal 4	x	X	x			x
Metatarsal 5	x	X	x			x
Cuboid	x		x			

Calcaneus	x	x	x	x
Medial cuneiform				
Intermediate cuneiform				
Lateral cuneiform				
Navicular				
Abductor Hallucis			x	
Flexor Digitorum Brevis	x		x	
Abductor Digiti Minimi	X		x	
Flexor Digiti Minimi Brevis	x		x	
Quadratus Plantae			x	
Adductor Hallucis			x	
Flexor Hallucis Brevis			x	
Plate	x	x	x	x

8.5.4.1 Muscle Volume

Fewer muscle volumes were segmented for subject C1 than C2 (Table 8.5-4). Of the muscles and soft tissues present in both segmentations, the skin, adipose, plantar fascia, and total soft tissue volume were larger in subject C1 than subject C2, consistent with the larger foot size of subject C1.

Table 8.5-4: Volume of segmented soft tissues from scans C1 and C2.

	C1 (cm^3)	**C2 (cm^3)**	**mean (cm^3)**
Skin	22.4	18.3	20.4
Adipose	111.0	102.8	106.9
Flexor Digitorum brevis	10.6	16.6	13.6
Plantar Fascia	7.0	5.6	6.3
Abductor Digiti minimi	3.6	5.9	4.7
Flexor Digiti Minimi Brevis	-	1.4	1.4
Abductor Hallucis	-	6.9	6.9
Adductor Hallucis	-	4.7	4.7
Quadratus Plantae	-	10.7	10.7
Flexor Hallucis Brevis	-	12.1	12.1
1st Lumbrical	-	0.1	0.1
All soft tissues	145.7	115.2	130.5

8.5.5 SWE

SWS values calculated from each tissue were determined for 3 subjects (Table 8.5-5).

Table 8.5-5: Average shear wave speed (SWS) and elastic modulus (E) calculated from shear wave volumes for each tissue in each region.

		Fat		**Skin**		**Plantar Fascia**	
Subject	Region	SWS (m/s)	E (kPa)	SWS (m/s)	E (kPa)	SWS (m/s)	E (kPa)
C1	All	3.22 (2.36)	43.4 (68.7)	2.71 (2.00)	37.8 (59.2)	0.05 (0.44)	0.68 (6.92)
C1	Toe	3.10 (2.28)	40.4 (62.0)	2.39 (2.08)	33.5 (62.3)	0.00	0.00
C1	Forefoot	3.67 (2.64)	55.8 (90.4)	3.35 (1.79)	48 (58.4)	0.06 (0.43)	0.66 (5.81)
C1	Midfoot	2.99 (2.00)	35.3 (52.3)	2.61 (1.82)	33.6 (49.5)	0.11 (0.64)	1.44 (10.54)
C1	Hindfoot	3.60 (2.96)	59.4 (87.8)	2.75 (2.26)	42.2 (70.7)	0.00	0.00
C2	All	4.58 (3.06)	82.7 (99.8)	4.04 (3.12)	86.7 (120.7)	0.08 (0.60)	1.25 (11.60)
C2	Toe	3.92 (2.94	65.5 (92.0)	3.96 (3.29)	88.3 (129.7)	0.00	0.00
C2	Forefoot	5.25 (3.42)	107.2 (123.5)	4.74 (2.84)	101.4 (117.1)	0.04 (.35)	0.43 (4.42)
C2	Midfoot	4.24 (2.63)	68.0 (81.3)	4.28 (2.87)	88.3 (109.5)	0.22 (.95)	3.28 (17.88)
C2	Hindfoot	4.74 (3.10)	87.6 (96.1)	2.68 (2.76)	49.3 (94)	0.07 (.61)	1.28 (15.07)
D1	All	3.40 (2.28)	45.8 (48.9)	3.31 (2.05)	50.5 (50.3)	0.01 (.15)	0.08 (3.06)
D1	Toe	2.24 (1.78)	22.5 (35.7)	2.25 (1.74)	26.9 (38.2)	0.00	0.00
D1	Forefoot	3.47 (1.81)	41.9 (32.5)	3.39 (1.91)	50.4 (42.9)	0.01 (.13)	0.06 (2.12)
D1	Midfoot	3.54 (2.44)	50.5 (54.5)	3.15 (1.92)	45.3 (47.6)	0.02 (.29)	0.29 (6.02)
D1	Hindfoot	3.46 (2.45)	49.2 (53.4)	3.69 (2.62)	68.1 (72.7)	0	0

The shear wave speed and modulus were generally lower in the toes and midfoot and higher on the relatively higher load bearing forefoot (metatarsal heads) and hindfoot. This pattern was most clearly visible in the fate and less pronounced in the skin. The signal in the plantar fascia was too poor to obtain meaningful values. Differences between control subjects (C1,C2) were larger than differences between diabetic (D1) and control subjects. Standard deviations for all values were similar to or larger than mean values.

8.5.6 DVC

8.5.6.1 Sensitivity analysis

Representative remapped volume, displacement, and mean compression maps can be found in Appendix C.

Runs with an FFT size less than 128^3 voxels did not perform well. Similarly, runs with an initial sub volume size of less than 96^3 voxels also did not perform well. Runs with a larger FFT size than 128^3 voxels did not appear to perform better. Runs with a minimum search radius larger than 6 voxels did not perform well. Runs with smaller search radii for each subvolume performed marginally better than those with larger search radii at higher level steps. Memory usage and run time were inversely related to the ratio of the effective subvolume size to the effective search radius (Figure 8-5), where the effective subvolume size and search radius are those parameters divided by the binning for that step. These results effectively narrow the useable search parameters for DVC of the ultrasound volumes to sequential subvolumes between 128^3 and 8^3 with a final search radius of 2-4, and suggest use of smaller search radii at higher level steps, further reducing the search area.

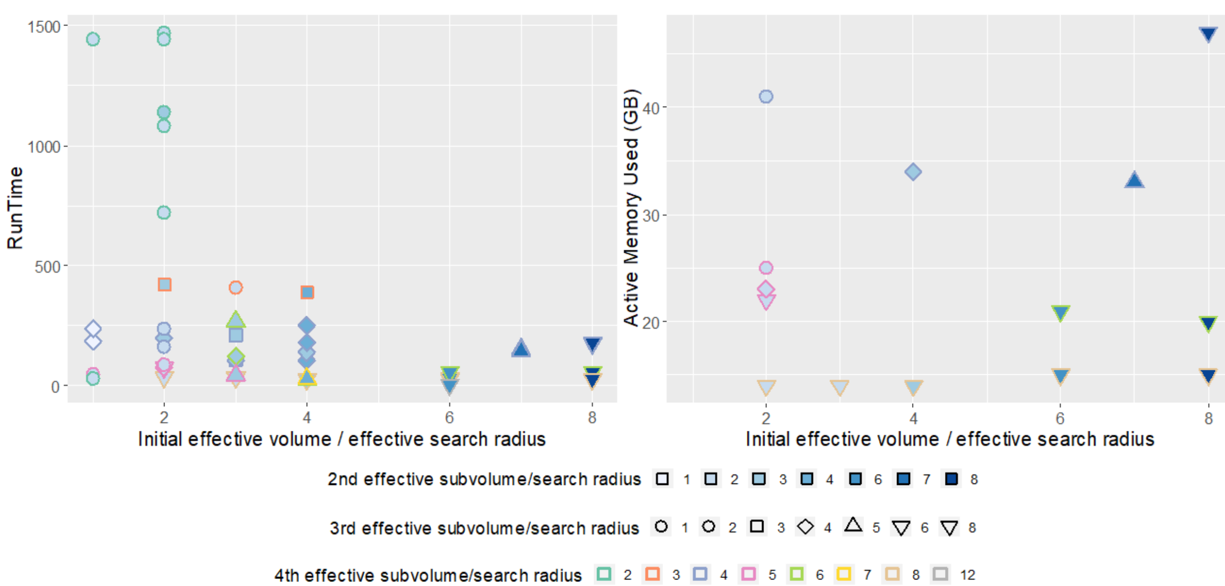

Figure 8-5: Effect of subvolume size and search radius on run time and active memory usage.

The run with the best combination of performance metrics, though not the best overall performance in every metric, for both subjects C1 and C2 was 128 FFT, 128 voxel subvolume with an 8^3 binning and 16 voxel search radius, 64 voxel subvolume with a 4^3 binning and 8 voxel search radius, 32 voxel subvolume with a 2^3 binned and 4 voxel search radius, and 8 voxel subvolume with a 2 voxel search radius. This set of parameters ran for around 3 hours for each subject and used 41-47 GB of RAM. This run was used for subsequent calculations.

8.5.6.2 Deformation

Average axial and shear strains for all three axes, average maximum principal strain, and average vertical displacement for all fat and skin were calculated (Figure 8-6). Similar maps for

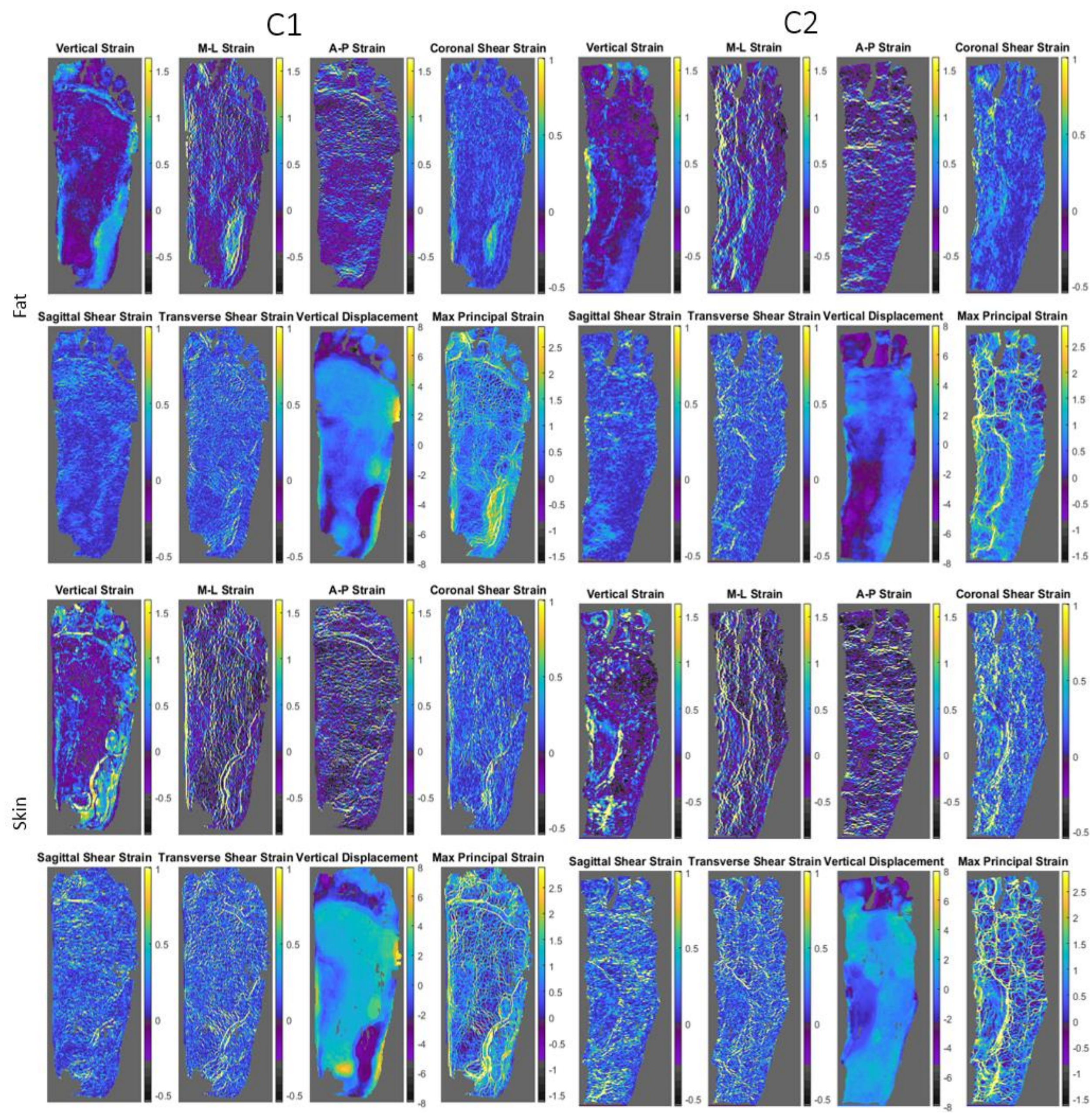

Figure 8-6: Average vertical, medial-lateral, anterior-posterior, and shear strains, maximum vertical displacement, and maximum principal strain for the fat and skin of subjects C1 and C2.

additional tissues can be found in the supplemental images. There were large variations in strain and displacement patterns between subjects. Strain maps from both subjects demonstrated negative vertical strain along the primary load bearing locations (metatarsal heads, lateral midfoot, and heel) of the fat and skin, higher sagittal shear strain at the submetatarsal fat and skin, lower sagittal shear strain at the subcalcaneal fat and skin, and higher sagittal shear strain in the distal plantar fascia.

Within the flexor digitorum brevis, there was an anterior-medial gradient of vertical displacement in both subjects, with higher magnitude displacement at the posterior-lateral end and lower magnitude displacement at the anterior-medial side.

8.5.6.3 *Stiffness*

The measured stiffness was around 0.5 N/mm, with higher values in the heel and metatarsal heads and noise particularly on the lateral edge of the foot (Figure 8-7).

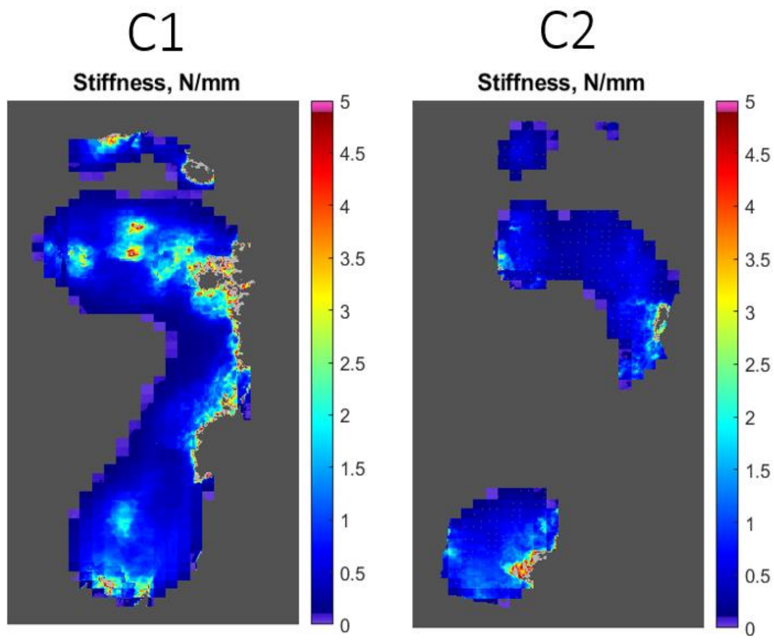

Figure 8-7: Spatial stiffness heat maps calculated from DVC-based deformation and registered plantar pressure.

8.6 Discussion

8.6.1 Validation

The ultrasound volume bone-to-plate distance was 11% (weighted) to 28% (unweighted) smaller than the bone-to-plate distance measured using CT. The magnitude of this difference was between 0.5 and 3 mm in different regions, and the total ultrasound-measured tissue thicknesses ranged from 5.9 -14.28mm across subjects and locations. The plantar soft tissue has previously been reported as 7.2 -27.0 mm at the heel unloaded[333] , and has previously been reported to undergo 42-60% compression during barefoot locomotion[186,197,198] and 28-38% compression during shod walking. As a result the measured tissue thicknesses are within previously reported ranges accounting for the weight of the lower leg (subject C1) and quiet stance (subjects C2, C3).

While the absolute values obtained via the ultrasound scan bone-to-plate distance were within the range of previously reported values, the ultrasound volumes generally underestimated the bone-to-plate distance relative to the CT. This underestimate may be related to a mismatched assumed speed of sound. The maximum speed of sound available on the commercial machine is 1660 m/s. The acoustic velocity of HDPE, from which the load bearing scanning surface is made, has been reported in the range of 2430 m/s. The weight bearing scan in particular uses a relatively thick layer of HDPE at ¼" or around 6mm. This is approximately 30% of the thickness of the plantar soft tissue. This makes the bulk speed of sound of the plate-tissue complex higher and can lead to errors in the reconstruction if the assumed speed of sound is lower than the actual time of flight. Distance in ultrasound images is typically reconstructed as $d=c*t/2$, where c is the speed of sound, t is the time of flight for both send and receive, and d is the distance calculated. If the actual speed of sound is higher than the assumed speed of sound, the reflected wave will return sooner and the distance recorded will be smaller. This could create an underestimate similar to what is reported here. This hypothesis is further supported by the appearance of point scatterers, which, particularly in the weighted scan, appear elongated and slightly curved downward. This artifact occurs when the speed of sound assumed for reconstruction is lower than the appropriate speed of sound for reconstruction.

Subject C1 underwent an unweighted CT scan, which required the unweighted US volume for comparison. Unfortunately, C1's ultrasound scan was taken with a shallower focus, making the bone boundaries more difficult to decipher. This likely introduced error into the distance measurement and could account for the larger discrepancy between the CT and US volumes. As this is now a known issue that was corrected in subsequent scans it is unlikely to create problems in the future. Another potential factor for the large differences in the validation differences for C1 was the large FOV, light setting of the CT. This setting reduced radiation dose but increases noise in the CT image. In particular, bones nearest to the plate were grainier and less bright. As a result, the bottom surface of the bones as segmented via CT may be less accurate than those segmented from Large FOV, regular CT scans.

Finally, the CT scan and Ultrasound Scan were not acquired at the same time. This could introduce additional error as the subject may have loaded the foot of interest slightly more or less in one scan versus the other and the subject walked between the lab spaces prior to the CT scan being taken. A future validation could consider developing a device to take both scans at the same time or to test the scanner distance measurement using phantoms or other more controllable conditions to develop a more rigorous bound on the error between the measurements.

8.6.2 Plantar Pressure

Differences between groups cannot be measured within this study population due to the small number of subjects and the height, weight, foot length, and foot width of the single subject with diabetes falling at or more than one standard deviation below the mean of the control group. However, absolute values of calculated variables fall within similar ranges of prior measurements in groups with and without diabetes, with the exception of the PTI, which is calculated differently than in prior work (Table 8.6-1). In concordance with prior work, peak pressures from static trials were lower than peak pressures from dynamic trials. Regionally, peak plantar pressures tend to be higher at the forefoot and hindfoot and lower in the midfoot, which is replicated in these results.

Plantar pressure is an established metric to assess ulceration risk. While the interpretation of these results are limited due to the sample population, integration of plantar pressure into the protocol and workflow of volumetric ultrasound scans enables comparisons between the study population and prior work establishing risk factors for ulceration.

Table 8.6-1: Comparison of prior plantar pressure values to the current work.

	Author	trial type	unit	Hallux		Toes		Forefoot		Midfoot		Hindfoot		Whole foot	
				D	ND	D	ND	D	ND	D	ND	DC	ND	DC	ND
peak	*current*	*dynamic*	kPa	*285*	*564*	*278*	*274*	*281*	*310*	*170*	*103*	*217*	*385*	*463*	*651*
	Melai 2011[316]	dynamic	kPa	514	355			448	364	165	118	419	359		
	Stess 1997[334]	dynamic	kPa					407							
	Fernando 2017[335]	dynamic	kPa			25	21	55	46	30	22				
	Falzon 2017[336]	dynamic	kPa	230				265				240			
	Lung 2016[319]	dynamic	kPa	500	300			450	350			275	275		
	Fawzy 2014[337]	dynamic	kPa					293				239			
	Mueller 2008[338]	dynamic	kPa						739				325		
	Caselli 2002[339]	dynamic	kPa					294	323			245	225		
	Fang 2013[340]	dynamic	kPa											459	468
peak	*current*	*static*	kPa	*45*	*100*	*40*	*28.3*	*100*	*82.2*	*45*	*44.4*	*115*	*173.9*	*115*	*173.9*
	Fawzy 2014[337]	static	kPa											114	
PTI	*current (all)*	*dynamic*	kPa-s	*742*	*1358*	*1232*	*489*	*1443*	*2487*	*824*	*1300*				
	current (novel)	*dynamic*	kPa-s	*35*	*87*	*70*	*37*	*82*	*100*	*54*	*60*	*79*	*40*	*170*	*253*
	Fernando 2016[335]	dynamic	kPa-s			6	5			10	6				
	Falzon 2017[336]	dynamic	kPa-s	38				51				48			
	Stess 1997[334]	dynamic	kPa-s	150				185							
	Sinacore 2008[341]	dynamic	kPa-s								3				
	Fang 2013[340]	dynamic	kPa-s											78	82
FTI	*current*	*dynamic*	N-s/kg	0.31	0.37	0.58	0.14	3.49	3.51	0.39	0.34	1.11	1.67	5.86	6.02
	current	*static*	N-s/kg	0.78	0.94	0.30	0.19	12.89	9.53	2.38	1.38	12.89	12.28	29.19	24.32
	Bus 2005[342]	dynamic	N-s/kg												
	Waldecker 2012[343]	dynamic	%BW-s		4.5		9		34		3		16		
	Sinacore 2008[344]	dynamic	N-s								16				
	Fang 2013[340]	dynamic	%BW-s											57.5	54.8
MPPG	*current*	*dynamic*	kPa/mm	36	74.5	38.7	44.7	56.7	41.5	16.8	10.2	23.7	46.7	56.7	74.4
	Lung 2016[315]	dynamic	kPa/mm	105	45			62.5	40			25	20		
	Mueller 2008[338]	dynamic	kPa/mm						68				7		
	Lung 2022[319]	dynamic	kPa/mm		50				61				38		
PGA	*current*	*dynamic*	°	40.3	44.9			87.4	71.3	57.2	71.58	0	31.7	7.5	40.8
	Lung 2016[315]	dynamic	°	20	40			50	55			65	75		
	Lung 2022[319]	dynamic	°		30				55						

8.6.3 SWE

The elastic modulus and shear wave speed values calculated for the plantar fat and skin are higher than values previously reported (Table 8.6-2). This increase could be partly due to the HDPE plate, which may affect the image tracking used to calculate the speed of sound. This increase may also be related to the compression on the foot in the ‘unloaded’ state. While most SWE studies ensure that the tissue is completely unloaded, the plantar tissue in the unloaded scan is bearing the weight of the lower leg and foot. When a material is compressed, the density is increased and sound waves are typically able to move through the material faster, increasing the speed of sound through the material. The values calculated for the plantar fascia are significantly lower than previously reported values. This disparity is likely due to the lack of good signal in the plantar fascia of the subjects analyzed. The ‘last’ frame acquisition issue affected both C1 and C2, and C1 additionally suffered from the superficial focus, both of which reduced useable SWE signals in the tissue. While SWE signal was strong in the scan for D1, that acquisition suffered from poor coupling, making it difficult to segment the tissues effectively and disrupting signal in key areas.

Prior work has investigated regional differences in the mechanical properties of the plantar soft tissues using *ex vivo* and indentation methods (Figure 8-8). Pai et. al reported highest modulus and energy loss in compression of the plantar fat beneath the first metatarsal head, and decreasing modulus and energy loss moving through the third and fifth metatarsals, hallux, lateral midfoot, and calcaneus[22]. The same group reported that the compressive modulus of the skin was lowest at the metatarsal heads, higher at the hallux, and highest in the lateral midfoot and calcaneus[24]. While the SWE data support the finding of higher modulus in the forefoot plantar fat, the other regional trends are in contrast. Regional data from normal (compressive) indentation tests vary, with some studies reporting higher moduli[182] at the hindfoot and others reporting higher moduli at the forefoot[35,357](Figure 8-8). The most similar trends are found between initial shear moduli of the

Table 8.6-2: Comparison of prior measurements of the shear wave speed and elastic modulus from shear wave elastography to the current work.

Author	Tissue type	SWS (m/s)	E (kPa)
current	*fat (D)*	*3.4*	*45.8*
current	*fat (ND)*	*3.9*	*63.1*
Mo[191]	fat (hallux)		12.9
Mo	fat (macrochambers)		10.8
Wu[184]	fat (macrochambers)		21.7
Lin[155]	fat (macrochambers)		26.3
Mo	fat (microchambers)		18.8
Wu	fat (microchambers)		103.8
Lin	fat (microchambers)		60.9
Mo	fat (MTH1)		11.5
Mo	fat (MTH4)		13.8
Mo	fat (whole heel pad)		12.2
Wu	fat (whole heel pad)		39.4
Lin	fat (whole heel pad)		31.8
current	*plantar fascia (D)*	*0.01*	*0.08*
current	*plantar fascia (ND)*	*0.07*	*0.97*
Alviti[345]	plantar fascia	5.13	
Beydogan[346]	plantar fascia	4.78	
Gatz[347]	plantar fascia		124.1
Gatz	plantar fascia		82.23
Schillizzi[348]	plantar fascia	5.04	
Baur[349]	plantar fascia	6.5	150
Chino[350]	plantar fascia (proximal)	5.58	
Chino	plantar fascia (distal)	8.8	
Jiang[351]	plantar fascia		58.14
Chen[352]	plantar fascia	6.44	
current	*skin (D)*	*3.31*	*50.5*
current	*skin (ND)*	*3.38*	*62.21*
Yang [353]	Skin (finger)		35.5
Yang [354]	Skin (finger)		30.3
Xiang[355]	Skin (finger)		34.97
Sobolewski[356]	Skin (finger)		28.25
Sobolewski	Skin (foot)		33.97

fat reported by Pai et. al and the moduli derived from SWE, demonstrating increased modulus at the forefoot and hindfoot and lower modulus at the toe and midfoot.

All of the moduli reported from SWE are lower than those reported from mechanical and indentation tests. Prior work comparing mechanical and SWE methods have demonstrated similar trends but lower absolute values[91] (Appendix A.2). This is likely due in part to the lower displacement initiated during SWE propagation, lower compression during SWE acquisition, and nonlinear viscoelastic nature of biological tissue. Additional work is required in comparing SWE and mechanical modulus values for direct comparison between studies using different techniques.

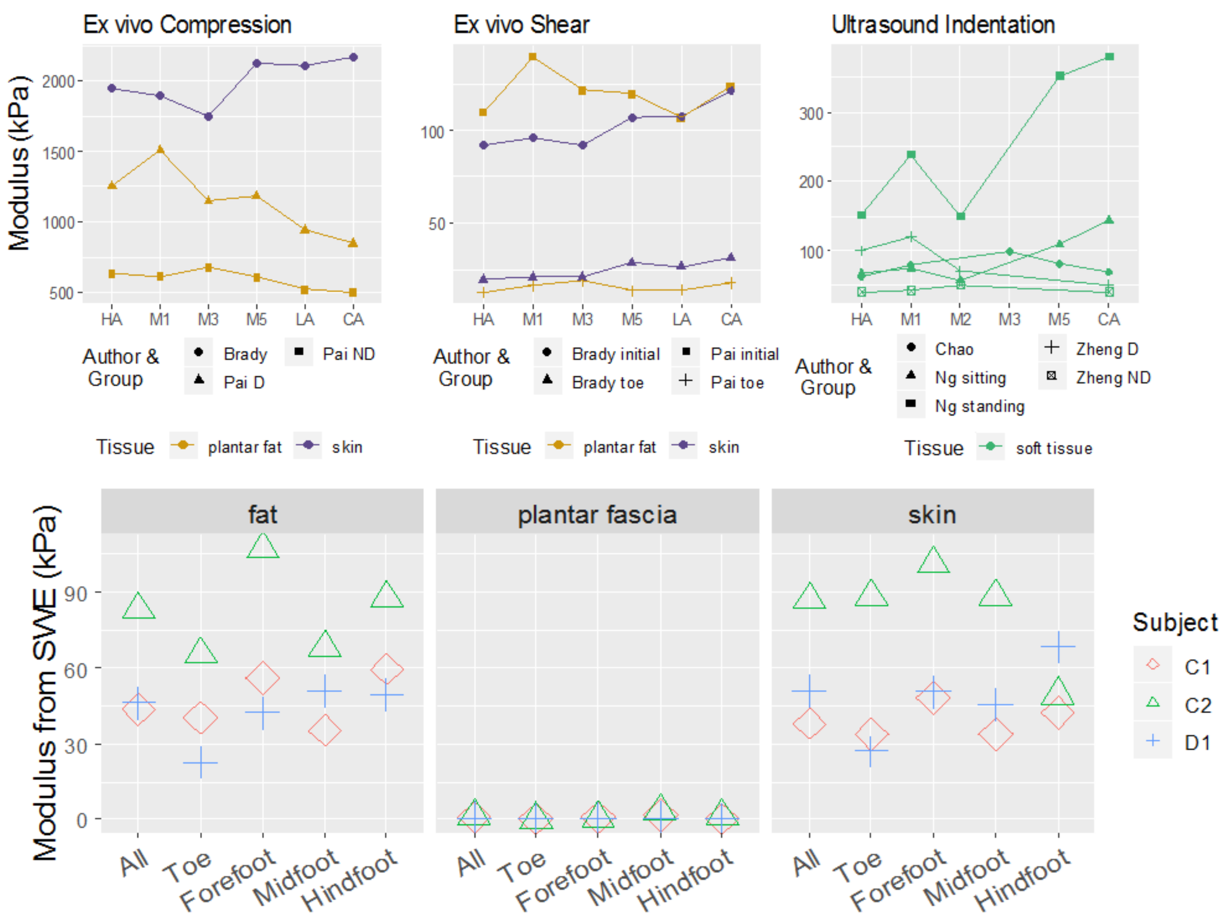

Figure 8-8: Comparison of prior moduli measured using mechanical and indentation methods to moduli measured using SWE from the current work.

8.6.4 Segmentation

11 bones and 10 different soft tissue structures were successfully segmented from the weighted ultrasound scans for subject C1 and C2, demonstrating the feasibility of weight bearing volumetric ultrasound for volumetric analyses or finite element modelling. One appreciable deterrent from use of volumetric ultrasound is the lack of available tools to aid segmentation in this modality. Whereas MRI and CT naturally lend themselves to intensity displays wherein different tissues are typically segmented at least initially by thresholding based on different intensities, the differentiation of tissues on ultrasound relies on bright boundaries and textural differences. Therefore, commercially available and open source programs for segmenting medical images are currently ill equipped to reduce the manual burden of segmentation. As a result, these segmentations must be performed manually by a user with significant knowledge of both ultrasound and the plantar anatomy and with access to reference illustrations at great temporal cost. An important area of future work is to reduce the time required to perform these segmentations through use of computational methods like texture-based feature descriptors or convolutional neural networks. Such methods have previously been investigated for segmentation of ultrasound images and volumes in whole breast ultrasound [78,358–361].

The segmentations demonstrated in this work have not been validated relative to a different modality and the boundaries are not consistently smooth. There is some trained guesswork involved in the boundaries displayed here. This would likely be improved by further additional fine tuning of the ultrasound acquisition parameters and could potentially be alleviated with a more customizable ultrasound sequence. Additionally, future work on this area should devise a validation study similar to the one performed here with CT in which soft tissue volumes segmented from unweighted scans are compared to scans of the same subject using another soft tissue imaging modality such as MRI which can be segmented more easily using thresholding tools currently available in medical image viewing software. These scans could also provide a ‘gold standard’ external validation against which to compare automated segmentation methods.

8.6.4.1 Muscle volume

Smaller and deeper muscles, such as the abductor hallucis and adductor hallucis, lumbricals, and flexor digiti minimi brevis may be underestimated in this analysis, likely in part due to the reduction in clarity with depth. More superficial muscles like the flexor digitorum brevis and quadratus plantae are closer to previously reported values (Table 8.6-3). The reported value for total muscle volume is the sum of all muscle volumes in C2. However, this value does not include most lumbricals and excludes all interossei, which are often included in other studies. Therefore, a direct comparison between the current work and some prior work is difficult[362–364]. However, Kura et. al. similarly report only individual muscle volumes and comparison of the muscle volumes reported in the current work and those in the work of Kura et. al yields a relatively similar sum of muscle volumes[365].

Table 8.6-3: Comparison of prior muscle volume measurements to those obtained using segmentations of ultrasound volumes.

paper	units	AbdM	AbdH	AddH	FDB	FDMB	FHB	QP	Lumbrical	All
C2 (weighted)	*cm3*	*5.9*	*6.9*	*4.7*	*16.6*	*1.4*	*12.1*	*10.7*	*0.1*	*58.4**
Kusagawa 2022[366]	cm3	13.8	18.7	13.8	15.4		12.9	9.8		85.9
Kura 1997[367]	cm3	8.8	15.2	10.2	11.0	3.4	6.5	8.0	0.6	65.2*
Abe 2016[368]	cm3				9.3					
Chang 2012[369]	cm3									110
Kimura 2020[364]	cm3									115

The current work uses a weighted scan while the prior work does not. This could also contribute to the discrepancies (Table 8.6-3) as muscles are expected to deform with weightbearing and are not perfectly incompressible. Ultimately, additional validation experiments and further refining of focus depth, total image depth, and brightness and power parameters should be undertaken for reliable use of these ultrasound volumes for muscle volume study.

8.6.5 Deformation

This work presents comprehensive volumetric strain vectors derived from the deformation from a seated to a static standing state. Previously, attempts to obtain this information have involved subject-specific finite element models and partial foot MRI analyses.

Using a finite element model consisting of 30 bones, 134 ligaments, and plantar fascia modeled as linear elastic with varying moduli and general soft tissue modeled as hyperelastic second-order polynomial, Chen at. al. found that internal strain at the level of the metatarsal heads was non-uniformly distributed, with higher magnitude displacement at the fifth metatarsal than at the first[219]. The pattern in vertical displacement for both C1 and C2 differed in that maximum vertical displacement was located under the second and third metatarsals rather than the fifth (Figure 8-9, top left). The gradient of displacement was also inverted due to different definitions of load (plate moving up in Chen 2010, bones moving down in the present work). In the ultrasound volume DVC results, despite care taken to align the plates, the DVC vertical displacement results indicate movement in the superior direction near the plate face that could interfere with comparison of these gradients. Future work should investigate in greater detail the sensitivity of the DVC output to the loaded-unloaded registration to ensure that values close to the plate are representative of true motion.

Using a finite element model consisting of 30 bones, 134 ligaments, plantar fascia, Achilles, and extrinsic flexors represented as linear elastic materials with varying moduli surrounded by a general bulk soft tissue represented by an Ogden hyperelastic model, Chen et. al determined that plantar soft tissue thickness is positively correlated with minimum principal strain, and demonstrated that minimum principal strain occurs under the metatarsophalangeal joint for the second metatarsal head[329]. Measurements under the second metatarsal head from subject C1 demonstrated the opposite pattern, with the maximum value of the minimum principal strain occurring under the metatarsophalangeal joint, while from subject C2, there was a slightly but not substantially or uniformly lower value of minimum principal strain under the second metatarsal head and the measurements overall were noisy(Figure 8-9, top right). The maximum magnitude of the strains reported for subjects C1 and C2 are also about 50% higher than those reported in the literature[329]. The magnitude of minimum principal strain at the second metatarsal head of subject C1, while not the minim value for the region, is similar in value to those obtained by Chen et. al using a 7.6mm – 10.2mm tissue thickness, and the tissue thickness at the second metatarsal head for subject C1 is about 10 mm. The magnitude of minimum principal strain at the second metatarsal head of subject C2, is larger in value than those obtained by Chen et. al using a the smallest (2.5mm) tissue thickness, and the tissue thickness at the second metatarsal head for subject C2 is also about 10 mm. This finite element model was performed to study different insole conditions, so it is possible that the model is not directly comparable to the barefoot ultrasound volume correlation.

Focusing on the plantar fascia, Peng et. al created a muscle-driven flatfoot finite element model using 20 bones, ligaments, and plantar fascia modeled as linear elastic materials, general bulk soft tissue modeled as a second order polynomial hyperelastic material, and skin modeled as a first-order Odgen hyperelastic material[203]. They simulated different orthotic conditions with variations in arch height, inclination angle, heel cup height, and material stiffness. Reported strain varied from 0 – 1% stretch in the longitudinal direction and was higher on the medial side of the fascia and lower on the lateral side. The longitudinal strain maps of the plantar fascia of subject C1 and

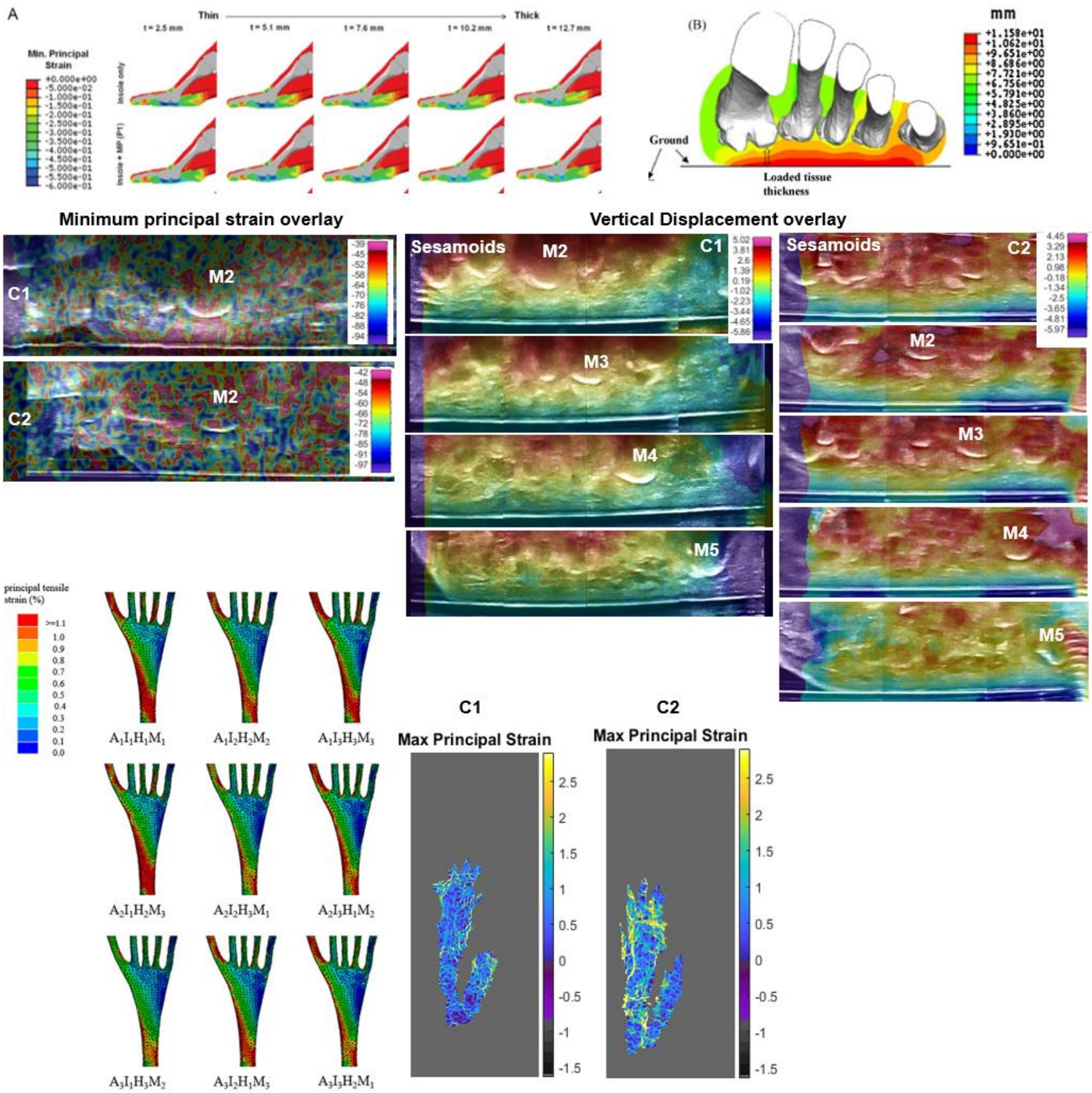

Figure 8-9: Top left: Minimum principal strain under the second metatarsal head from Chen (2015, reproduced with permission) and from subjects C1 and C2. Strain for subjects C1 and C2 is in units of %. Right: Vertical displacement under the metatarsal heads in Chen (2010, reproduced with permisson) and for subjects C1 and C2. Chen (2015) chose the bones as fixed while we define the plate as fixed. Bottom Left: Principal strain in the plantar fascia under different orthotic conditions from Peng (2022 reproduced under creative commons license) and from subjects C1 and C2 (units in %). Peng (2022) does not include the lateral branch but does include the tendon slips.

C2 during barefoot static loading do not display any anterior-posterior or medial-lateral variation (Figure 8-9, bottom left). The difference between these results could be related to the difference in footwear conditions between the model and the *in vivo* measurement. The presence of an arched insole would encourage additional stretching of the plantar fascia around the arch shape and likely promote a medial-lateral strain gradient as the arch support sloped down laterally. Both C1 and C2 were acquired in a water bath condition and therefore, there was no support or external interference in the medial arch. Weighted volumetric ultrasound scans using molded gel couplants could have more similar effects to those reported by Peng et. al., and the effect of the gel couplant on mechanical results should be considered in future validation of the ultrasound volumes and deformation.

Using a model consisting of fat modeled as a first order Ogden hyperelastic material, skin modeled as an Isihara's Law hyperelastic material, bulk intrinsic muscles modeled as Yeoh's law hyperelastic, and the calcaneus modeled as rigid, Trebbi et. al. compared internal strain patterns at the heel to those obtained using MRI[204]. This group also compared other constitutive models for the same tissue groups. Unlike the models presented in Trebbi 2021, the maximum principal shear strain maps of subjects C1 and C2 do not demonstrate any regional gradients at the inferior point of the calcaneus, nor are there clear gradients in this variable throughout the volume (Figure 8-11). Shear strain has long been hypothesized as a means of injury initiation in the development of plantar ulcers[6], making high shear strains a feature of interest. Further investigation should be performed into the heterogeneity of the maximum shear strain in the ultrasound-based deformation to better understand how shear strain may be related to the overall tissue mechanics.

Using a model of 26 bones, plantar fascia, 53 ligaments, a 3 layer model of the plantar soft tissue, and skin modeled with a variety of element shapes and types as linear elastic (bone, tendons, ligaments, fascia) or first order Ogden hyperelastic (plantar soft tissue) Mo et. al, described the effect of different plantar soft tissue thicknesses and moduli on the compressive strain at the heel[191]. They found that increased tissue thickness at the heel resulted in increased compressive strain while increased stiffness led to decreased compressive strain. The tissue thickness at the heel of subject C1 from the CT scan measurements was 18.44mm while for subject C1 was 10.34 mm. These correspond roughly to the largest and smallest thicknesses studied by Mo et. al. Unfortunately, SWE signal at the heel of subject C1 was poor, so comparison of moduli between the two subjects is difficult, but the stiffness from the maps created using DVC and plantar pressure suggest similar stiffnesses between the two subjects with that of C1 slightly elevated. From this, C1 would be expected to have higher compressive strain at the heel than subject C2 based on the results of Mo et. al. While the strain maps are heterogeneous, the values at the calcaneus of C1 are lower on average than those of subject C2, indicating more compressive strain, in agreement with the finite element model (Figure 8-10).

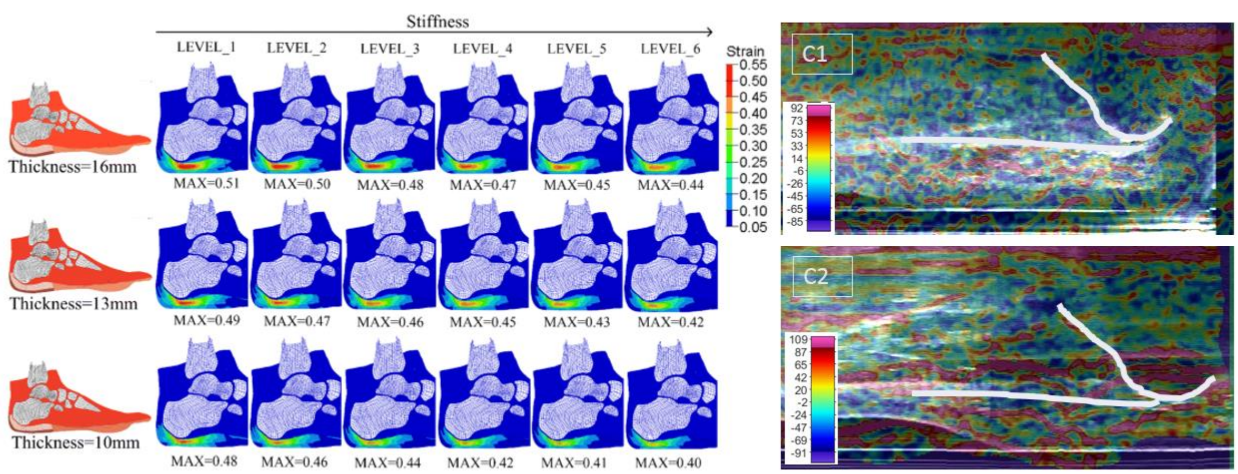

Figure 8-10: Left, effect of tissue thickness and stiffness on compressive strain from Mo et. al. (2019, Annals biomed Eng 47:12, 2364, reproduced with permission) units in mm/mm. Right. Compressive strain measured using DVC of ultrasound volumes. Units in %.

Recognizing the limitations of uniaxial measurements and computational models, two groups have used MRI to make *in vivo* volumetric strain measurements. Trebbi et. al developed an MRI-compatible normal and shear loading device for the heel capable of applying up to 15N in normal

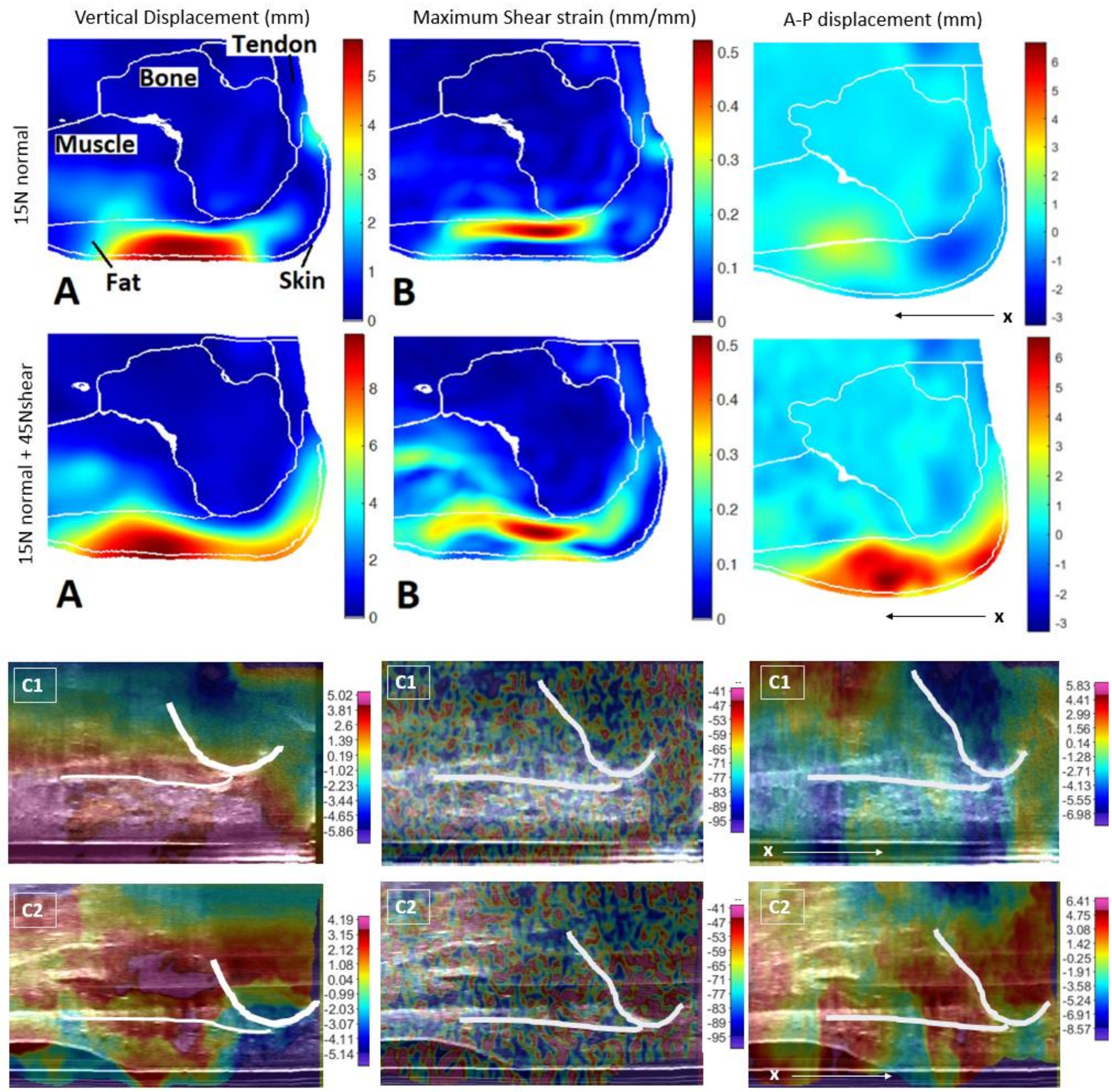

Figure 8-11: Left : Vertical displacement measured by Trebbi (2022, Med Eng & Phys 108, 1-10, reproduced with permission) compared to vertical displacement in subjects C1 and C2 at the heel. Middle: Maximum shear strain measured by Trebbi (2022, Med Eng & Phys 108, 1-10, reproduced with permission) compared to maximum shear strain in in subjects C1 and C2 at the heel. Right: Anterior-posterior displacement measured by Trebbi (2021, Med Eng & Phys 98,25-132, reproduced with permission) compared to anterior-posterior displacement in subjects C1 and C2 at the heel. Note the difference in definition of the anterior-posterior axis between studies. Units for subject C1 and C2 are mm, %, mm**.**

and 45N in shear, and acquired loaded and unloaded 3T scans of a single subject (healthy control, 40 y/o, bodyweight not reported)[202,217]. The resulting scan had a resolution of 0.3125x0.375x0.3125mm. The calcaneus of the loaded and unloaded volumes were rigidly registered and deformable registration was performed using open-source software. The authors reported maps of inferior-superior and anterior-posterior displacement[202] as well as vertical and maximum shear strain[217] under low normal (14.9N) and low normal- high shear (15.9 N / 45 N) conditions. The displacement maps generated from DVC of subjects C1 and C2 are more similar in vertical and longitudinal displacement to the normal + shear condition (Figure 8-11). However, while Trebbi et. al report a clear gradient of maximum Green Lagrange shear strain at the anterior-inferior calcaneus, the maximum shear strain measured for subjects C1 and C2 does not form clear gradients at the heel.

Williams et. al[29] developed an MRI-compatible loading device to apply load normal to the heel and used gated-MRI imaging to obtain dynamic loading information for 8 loading steps from 0% to 25% bodyweight at a rate of 0.2Hz. The resulting scans had a resolution of 1mm^3. Applied load was measured using a calibrated pressure sensor and displacement was measured from the MRI as the distance between the platen and the inferior aspect of the calcaneus. Gated MRI was acquired for one subject with diabetes and one without. The authors reported displacement of 3-4.2 mm and stiffness of 20-57 N/mm for strains from 16% to 22% for the control subject and displacement of 3-4.1 mm and stiffness of 70-114 N/mm strains from 16% to 22% for the subject with Type I diabetes. Given that the applied loads are ¼ BW at maximum, it is difficult to compare this work the ½ BW loading applied during the volumetric ultrasound scans. However, the slightly lower displacements support the displacements measured in the volumetric ultrasound. However, the reported stiffnesses are about 10X those reported for the volumetric scan-plantar pressure analysis.

In contrast to these MRI loading devices, the volumetric ultrasound scans represent real loading scenarios in which the subject is applying normal muscle tension and complex loading. This advantage is clearly demonstrated in comparison to the pure normal and normal plus shear measurements of Trebbi et. al[202]. While they do not report the body weight of the subject measured, the 15N normal load is likely less than 5% bodyweight, and the combined 15N plus 45 N load is likely less than ¼ BW. While Williams et. al did apply 23% BW, they noted substantial discomfort to the subjects. In contrast, in the weight bearing ultrasound scanner, subjects sustain their own bodyweight in a comfortable stance and can apply ½ BW or more load to their foot without discomfort. Another advantage of the ultrasound scans is the application of load to and imaging of the entire plantar soft tissue. Both Trebbi et. al and Williams et. al apply load only to the heel due to limitations of the load applying device and the MRI scanner. In contrast, the weight bearing ultrasound scanner can measure deformation across the entire plantar surface in biomechanically realistic loading scenarios. Additionally, the ultrasound scanning device is inexpensive to manufacture, allowing in-house storage that facilitates scheduling relative to MRI which is often costly and difficult to access.

The maximum principal strain occurred at a different location in each subject. However, the pattern of maximum strain was consistent between fat, skin, and the total tissue. The maximum principal strain for subject C2 traced along the medial boundary of the load bearing midfoot while the maximum principal strain for subject C1 occurred on the lateral edge of the load bearing hindfoot. The locations of these strains correlate with regions of high but not peak medial-lateral and vertical strain. While these locations do not correlate to high plantar pressure, the maximum principal strain could be a patient-specific biomarker that might inform localized tissue injury risk.

The minimum principal strain occurred in the submetatarsal fat while the subcalcaneal fat experienced a lower magnitude minimum principal strain, correlated to more compression of the fat at the forefoot and less at the heel (Figure 8-12). The heel pad is composed of almost entirely fat while the tissue under the metatarsal heads contains several tendons which make up a substantial portion of the bone to plate distance. Plantar fat is typically more compressible than tendon, so it makes intuitive sense that the fat in that region would undergo more compression. In the skin, the minimum principal strain occurred throughout the load bearing area and was higher magnitude than minimum principal strain in the fat. With regards to the total tissue area, the highest magnitude minimum principal strain occurred at both the submetatarsal and subcalcaneal regions. The minimum principal strain largely corresponds to both load bearing regions and common regions of ulceration[50].

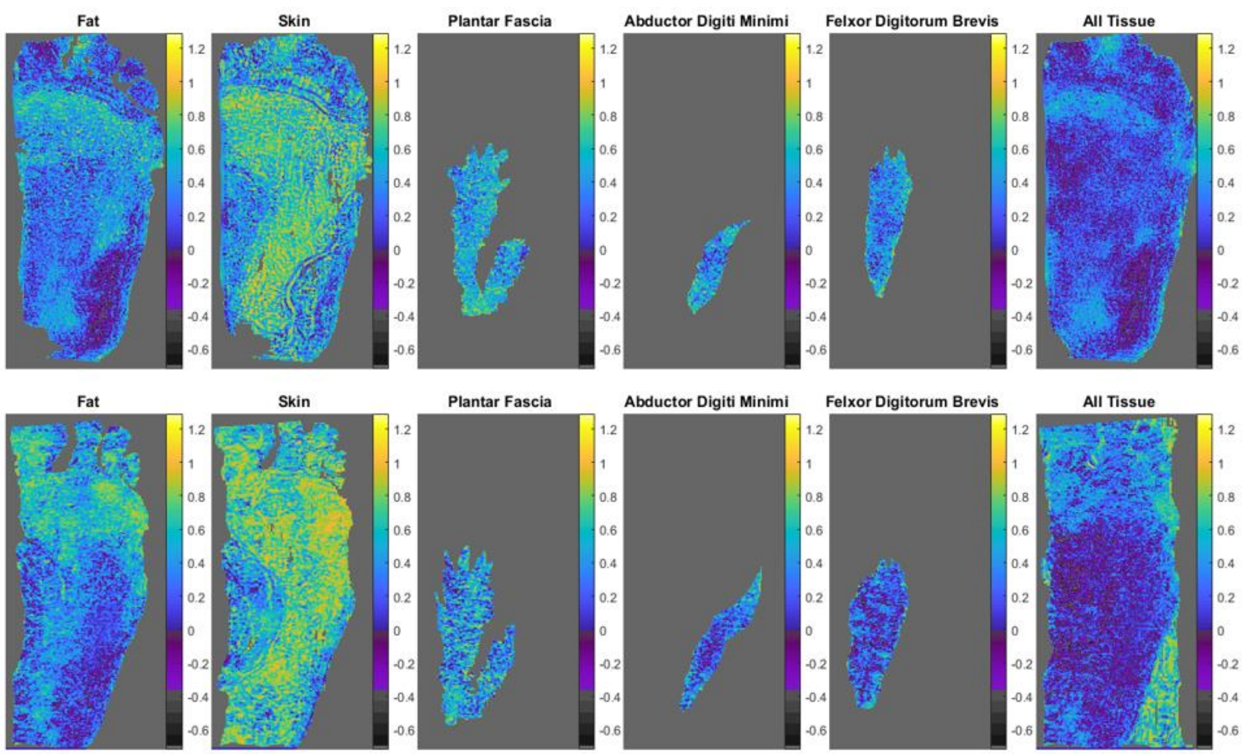

Figure 8-12: Minimum principal strain for each tissue. The top row is results for subject C1. The bottom row is results for subject C2.

For decades, finite element models have been the standard for estimating internal strain deformation in the plantar soft tissue due to the difficulty of making these measurements *in vivo*. However, these methods are expensive in manual labor, time, and computational power. Finite element models of the foot are also difficult to create and validate due to the complexity of the geometry, the complexity of the constitutive models required to correctly model biological soft tissues, and the difficulty of making *in vivo* measurements that will act as validation for finite element models. Finite element models are sensitive to mesh sizes and the outputs of finite element models are not always of high confidence. While DVC methods cannot directly measure internal stresses, the measurement of internal strain allows researchers to not only make direct measurements of complex three-dimensional strains and the differences therein related to pathologies, but is another tool for more rigorously validating the output of the finite element models. The estimated time required to process a single subject through tissue-specific ultrasound-based DVC analysis is about 1-2 weeks, of which most is spent on manual stitching, registration, and segmentation. If these tools can be automated, there is potential for obtaining patient-specific internal strain in a more temporally and computationally efficient manner.

8.6.6 Stiffness

While there were regions of higher force and displacement, these areas tended to be correlated so that the overall variation in stiffness was less than 5N/mm (Figure 8-13). Regions of higher stiffness on the outer edges of the heel, metatarsal head areas, and hallux were likely due in part to noise in the displacement measurement. Additional mean or median filtering could reduce the noise to create a less variable map. Higher values, missing values, and general noise on the lateral edges of the foot may be related to the curve of the plate creating lower displacement values as the displacement is measured in differences between pixel locations, and the bending of the plate under loading is more severe toward the lateral edge of the foot, making the location of the lateral edge of the foot more superior relative to the middle of the foot in the weighted condition. Future work should investigate a correction method for these values, such as calculating displacement from the bone rather than the plate, calculating plate displacement and applying it as an offset to the calculated displacement, or changing the material or geometry of the scanning plate to reduce bending.

Prior work has investigated the stiffness of the plantar soft tissue using a variety of *in vivo* and *ex vivo* point measurements. Prior impact testing applied loads of 223 – 676 N *in vivo* and 1200 – 2000 N *ex vivo* and reported stiffnesses of 8-25 kN/m (initial stiffness, *in vivo*), 100-175 (final stiffness, *in vivo*), and 900-1160 kN/m (final stiffness, *ex vivo)*[333]. Previous work instrumenting a shoe to measure dynamic stiffness during walking measured the plantar stiffness at the heel at 26-40 N/mm[306]. Prior work using imaging indentation[27,370,371], non-imaging indentation[372], optical coherence tomography air jet[373] and imaging and plantar pressure[31] systems have measured the plantar stiffness at 0.12 – 1.8 N/mm. Stiffnesses of 0.3-1 N/mm at the metatarsal heads, 0.3-0.5 N/mm at the hallux and 0.5-1.1N/mm at the heel measured using the approach described here are similar to values previously obtained using indentation and imaging systems at those same sites. Stiffnesses measured in the present work using DVC deformation and static plantar pressure are expected to be more similar to the values measured using plantar pressure and indentation systems and lower than stiffness measured using impact testing and walking measurements due to the use of static plantar pressure loads rather than the higher dynamic loads that impact tests attempt to match.

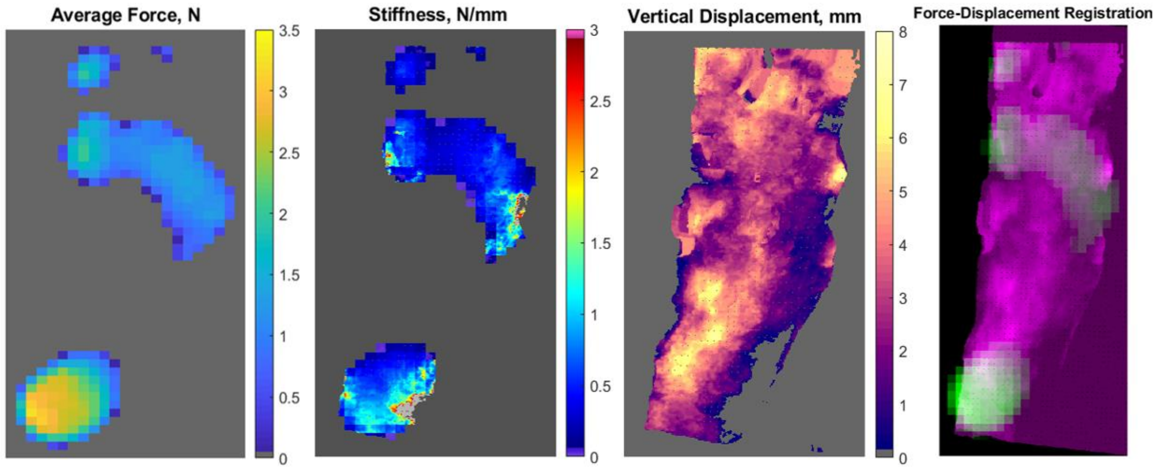

Figure 8-13: Comparison of plantar pressure, stiffness, and vertical displacement values and an overlay of registered plantar pressure (green) and displacement (purple)

All of the prior work mentioned measured stiffness in point locations. The extension of stiffness measurements to a two-dimensional map opens the potential to create new descriptive statistics and better understand the spatial changes in the mechanics of the plantar soft tissue with diabetes. Similar to plantar pressure, gradients, local summary variables, and other summarizations of stiffness data could be used to better assess the risk of tissue injury or assess changes in stiffness patterns with diabetes. Stiffness information could also be used to design custom offloading insoles in a similar way to recent work using plantar pressure[374].

8.7 Conclusion

Plantar soft tissue mechanics have long been of interest to biomechanics researchers and internal medicine clinicians treating patients with diabetes. The morbidities associated with diabetes-related plantar ulceration are significant, and the mechanical etiology of these wounds remains unclear, leaving a gap in knowledge that could aid prevention. The development of a load-bearing ultrasound-based volumetric plantar soft tissue scanner and the associated pipeline for measuring internal strain, internal modulus, muscle volume, and regional stiffness represent a new way to measure and understand this complex biological structure.

8.8 Supplemental Images

These images add additional information regarding the methods and results presented in chapter 8.

8.8.1 SWE errors

During acquisition of SWE volume scans, both a B-mode image with the SWE overlay was acquired from the commercial ultrasound display using the ‘getLiveImage’ command and the ‘last’ option, which should save the most recent image. Immediately after, a ‘getSWE’ acquisition was performed using the ‘last’ option, which should save the most recent SWE map. The image and SWE map were saved to a structure along with the time of acquisition so that the two types of data could be easily correlated.

When comparing the recolored SWE map to the overlaid SWE map, it became clear that the values did not always match (Figure 8-14), leading to a change in the protocol and manual matching of frames for subjects C1 and C2.

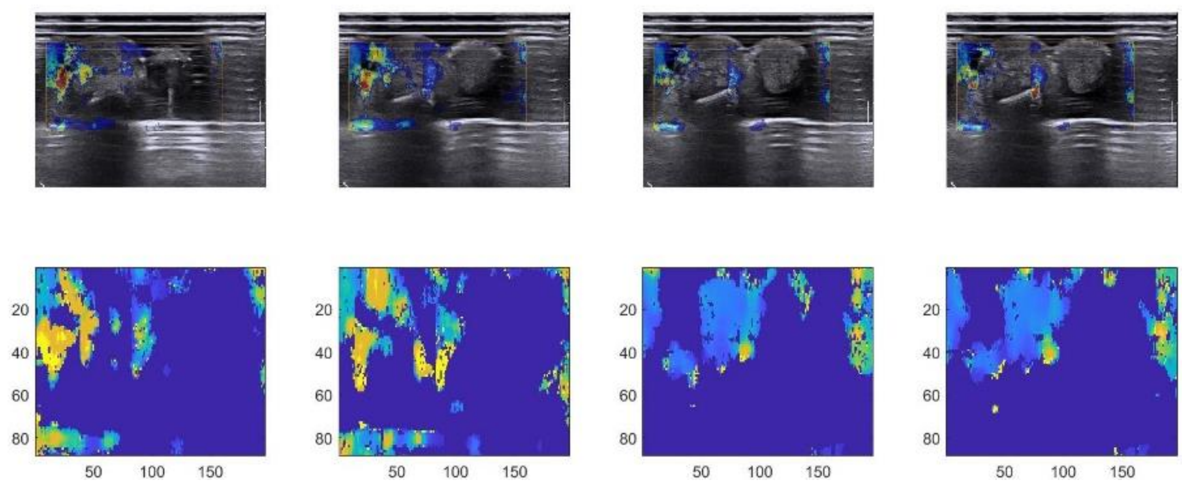

Figure 8-14 Example of shear wave speed ‘images’ that do not match the shear wave map on the last acquired frame.

8.8.2 Validation

Ultrasound and CT bone-to-plate distances were compared visually using color heat maps and quantitatively by matching standardized-sized ROIs placed by a user at corresponding locations.

Identifying locations on the less complete ultrasound bone segmentations is challenging, and the ROIs are restricted to locations easily segmentable on ultrasound scans.

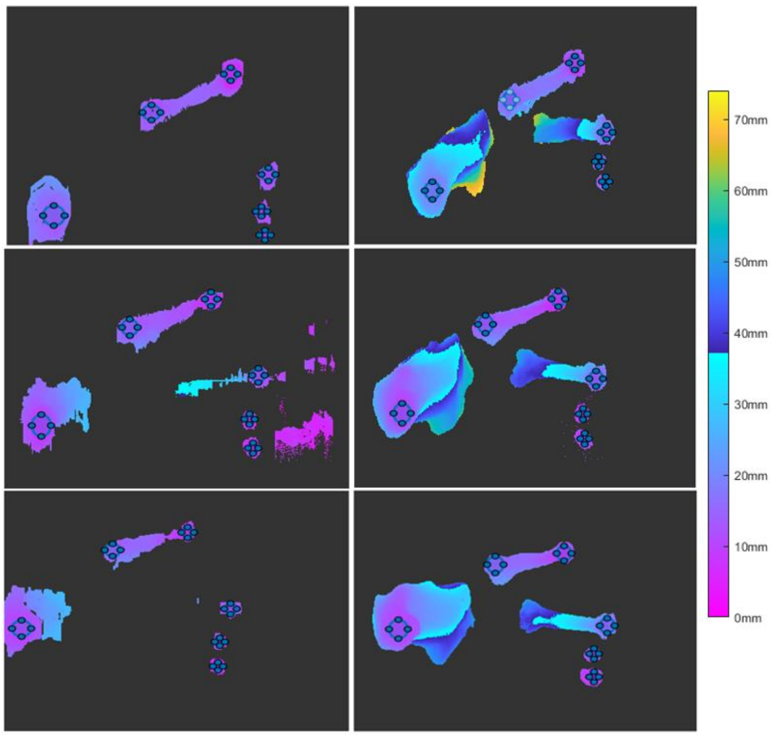

Figure 8-15 Bone to plate distances for ultrasound (Left) and CT (Right) and ROIs used for validation measurements. From top to bottom: C1, C2, C3. The scans for subject D1 were not clean enough to segment the required bones with accuracy.

8.8.3 SWE transverse maps

SWE signal is noisy by nature, and there were issues with the acquisition of the SWE values for several subjects, as previously described. With a clean scan, regional and tissue-specific variations in SWS and SWE-derived modulus values could be assessed in a similar way to strain and displacement by visualizing averages along the superior-inferior axis in the transverse plane.

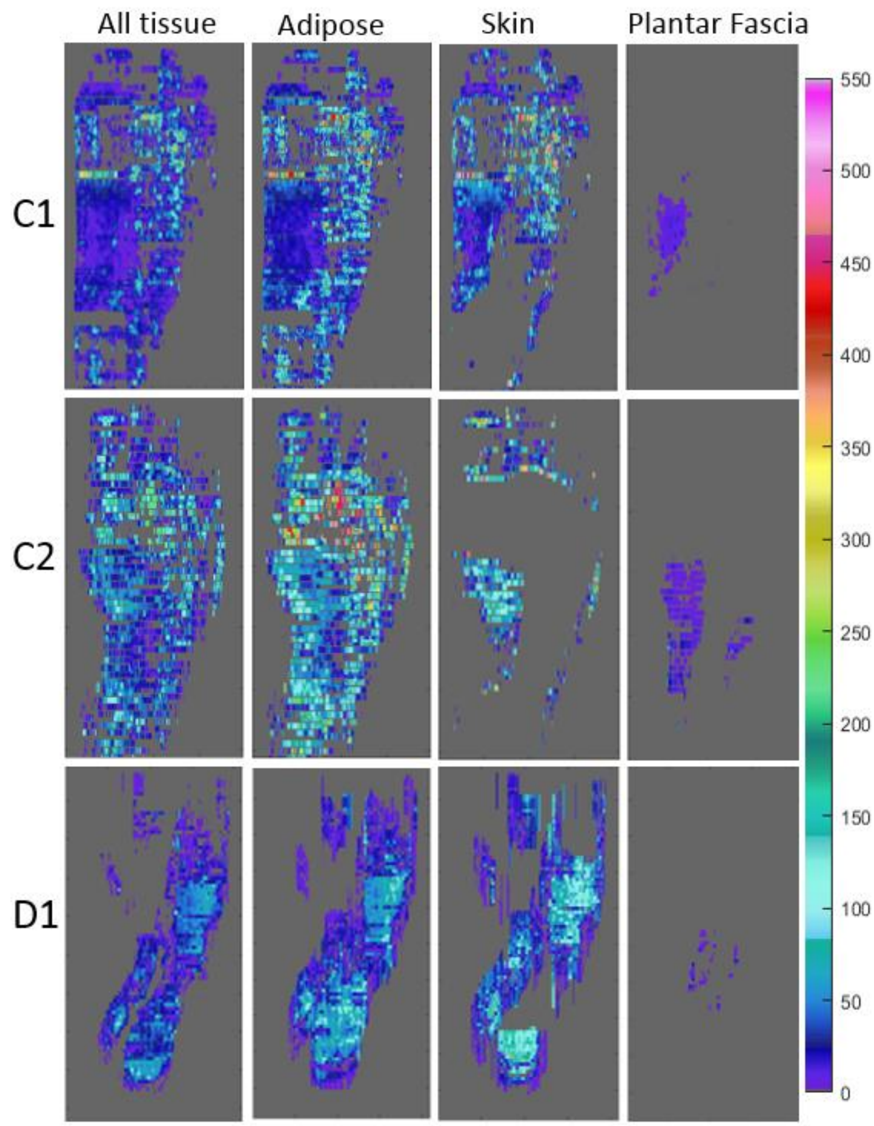

Figure 8-16 Transverse plane map of regional tissue-specific modulus calculated from shear wave speed. Values are averaged along the inferior-superior direction through the thickness of the specified tissue. The quality of shear wave data for subjects C1 and C2 is affected by a discrepancy in the manufacturer-provided research package. The quality of shear wave data and tissue-specific segmentation for subject D1 is affected by issues with ultrasound coupling.

8.8.4 Tissue-specific strain and displacement

DVC results were highlighted for skin and fat in the text. However, additional tissue-specific strains were visualized and are presented here.

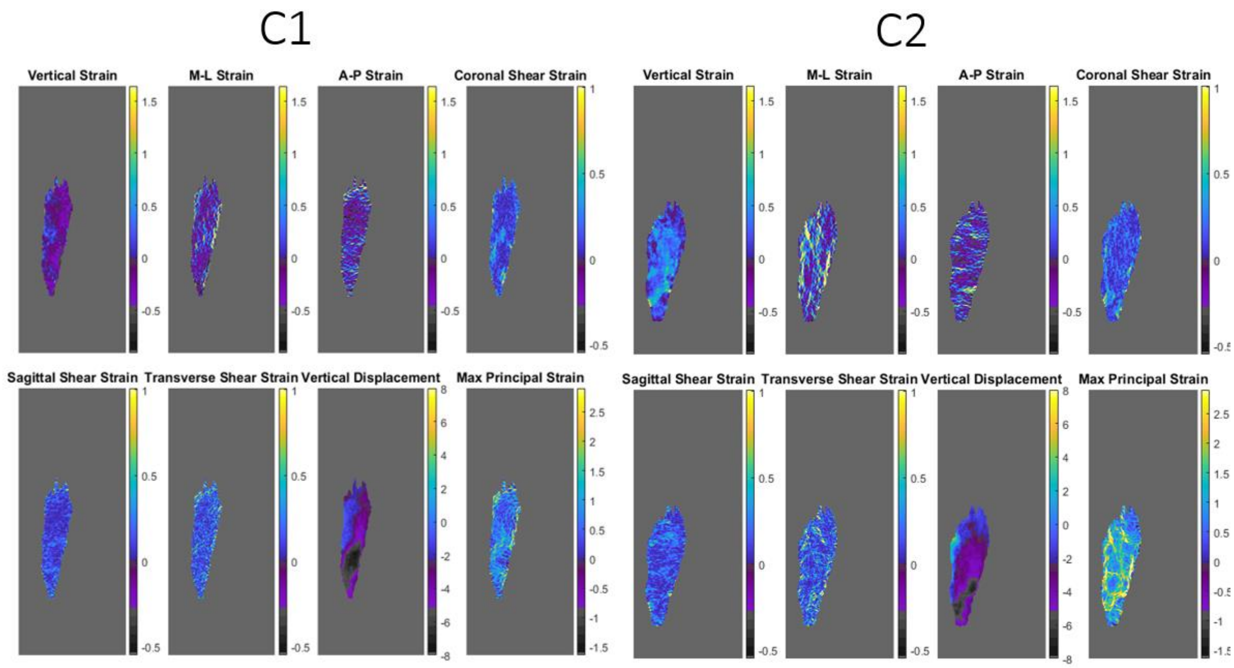

Figure 8-17 Strain and vertical displacement of the flexor digitorum brevis, displayed as a maximum value in the transverse plane. For each image, top = anterior, bottom = posterior, Left = medial, right = lateral.

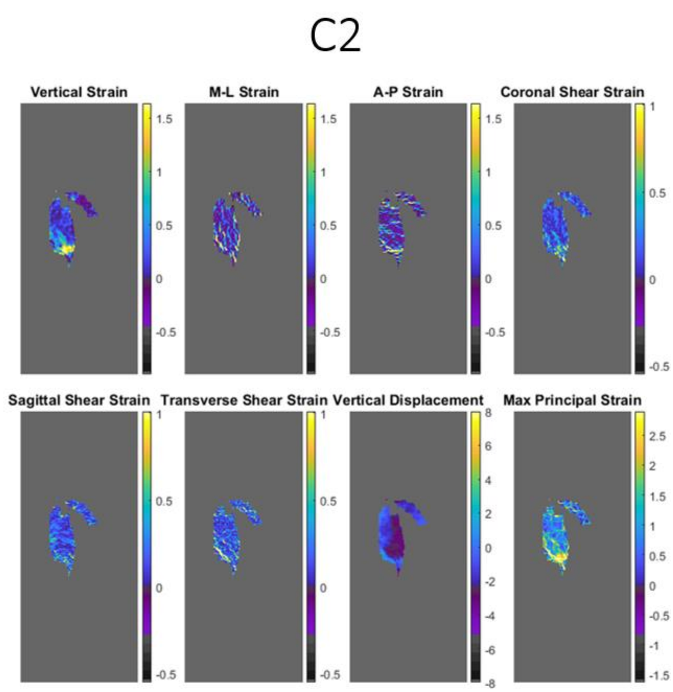

Figure 8-18 Strain and vertical displacement of the adductor hallucis, displayed as a maximum value in the transverse plane. For each image, top = anterior, bottom = posterior, Left = medial,

right = lateral. The scans for subject C1 were performed with a focus too superficial to accurately resolve this muscle.

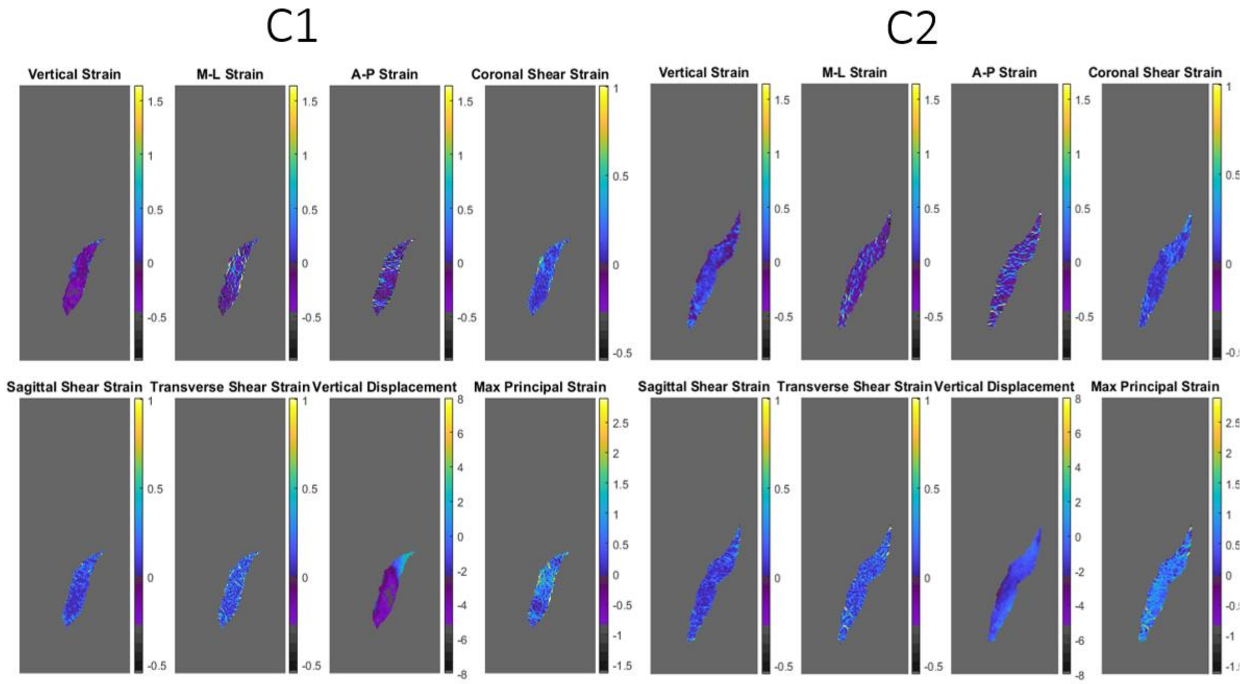

Figure 8-19 Strain and vertical displacement of the abductor digiti minimi, displayed as a maximum value in the transverse plane. For each image, top = anterior, bottom = posterior, Left = medial, right = lateral.

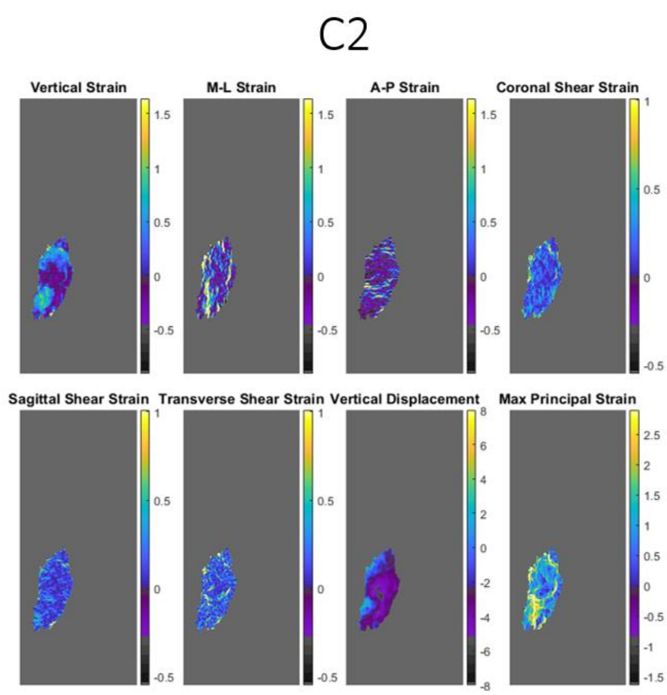

Figure 8-20 Strain and vertical displacement of the quadratus plantae, displayed as a maximum value in the transverse plane. For each image, top = anterior, bottom = posterior, Left = medial,

right = lateral. The scans for subject C1 were performed with a focus too superficial to accurately resolve this muscle.

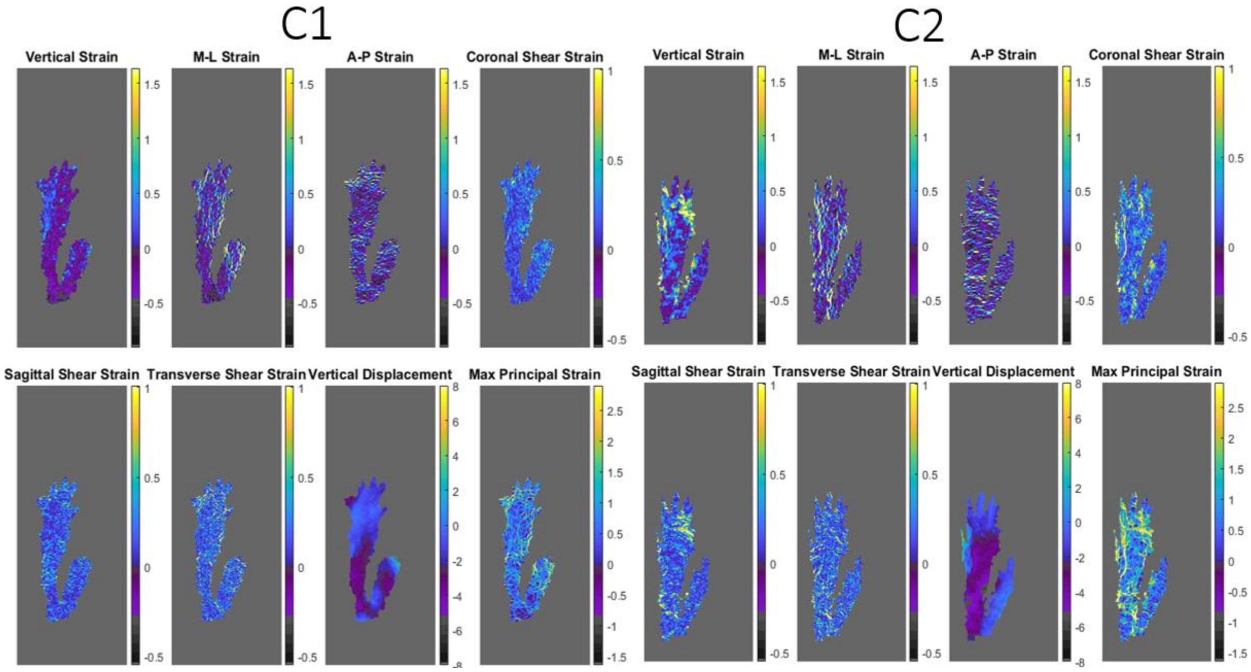

Figure 8-21 Strain and vertical displacement of the plantar fascia, displayed as a maximum value in the transverse plane. For each image, top = anterior, bottom = posterior, left = medial, right = lateral.

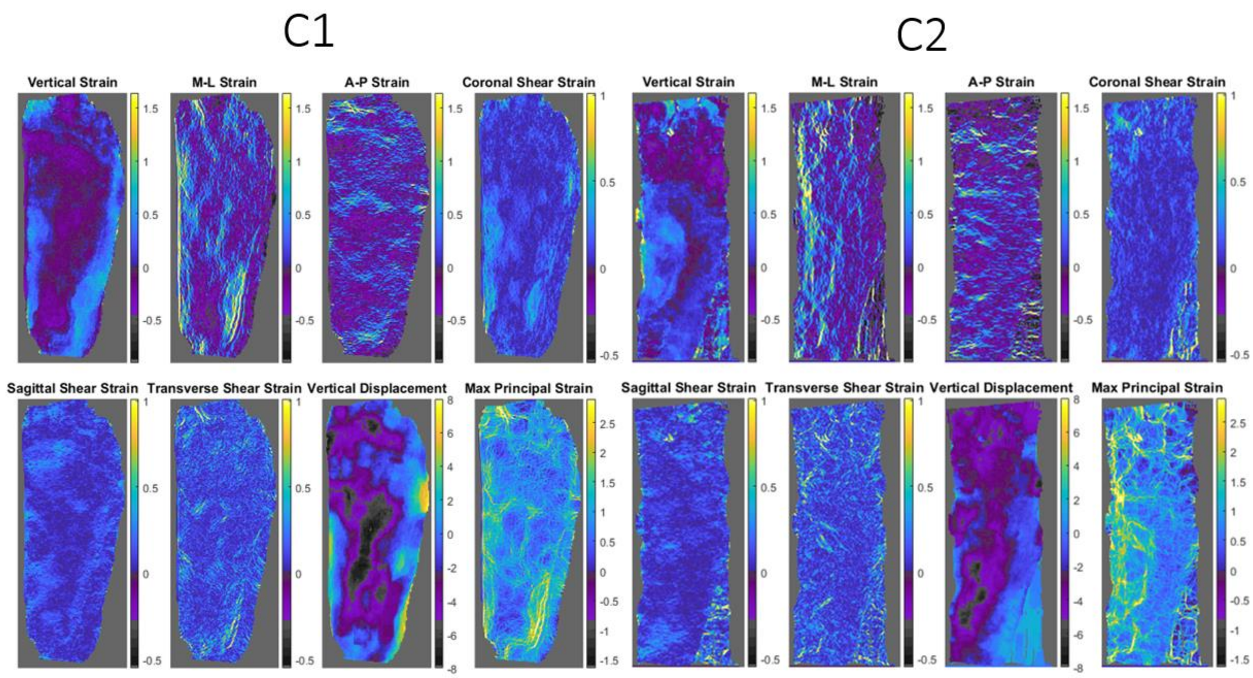

Figure 8-22 Strain and vertical displacement of the total soft tissue volume, displayed as a maximum value in the transverse plane. For each image, top = anterior, bottom = posterior, left = medial, right = lateral.

9 Insights and Future Directions

This work presents development and applications of methods to assess microstructural, macrostructural, and mechanical changes in the plantar soft tissue associated with diabetes.

9.1 Microstructure

The microstructural aims of this work were to:

µSA1) Develop a method for automated segmentation of different plantar soft tissues from microscopy slides.

µSA2) Investigate attention mechanisms in order to guide selection of areas and morphological parameters of interest with relation to diabetes.

μSA3) Use automated processing to quantify morphological changes to the microstructure of plantar soft tissue.

To address **μSA1**, texture-based feature descriptors and techniques including regression trees and support vector machines were compared to a Unet for the task of segmenting five microstructural tissue components from fixed plantar soft tissue sections stained using a modified Hart stain for elastin. In agreement with contemporary work, the Unet performed better than the other statistical machine learning methods, and the Unet achieved accuracy deemed acceptable for subsequent morphological analysis. One of the highlighted successes of this work was the ability to discriminate small septal walls so that a comprehensive area analysis of adipose chambers within the plantar fat could be automated.

To address **μSA2**, an axial-deeplab network with a ResNet26 backbone was employed to classify histological images as diabetic or nondiabetic, and the attention layer for each inference was overlaid on the input image. Unfortunately, the hardware limitations required the images to be down sampled by a factor of more than 10, and the resulting attention layer was downsampled further, making the attention information broad and difficult to correlate to small images features common in histology.

To address **μSA3**, the Unet from **μSA1** was employed to segment 323 histology images into five tissue classes, and the resulting segmented images were used to create label masks for morphological analysis. This largely automated method was used to determine that the adipose chambers in the superficial layer of plantar fat are smaller than the chambers in the deeper layer of adipose fat, and that the size of deeper chambers is decreased and the size of superficial chambers is increased with diabetes. This adds quantitative validation to prior qualitative observations of differences in chamber size with depth, and adds additional new information about the microstructural changes associated with diabetes. This change in microstructure may have implications for tissue injury, as the combination of thicker, frayed septal walls and smaller adipose chambers in the thicker deep layer of plantar fat could partially explain the higher modulus previously measured[22,23]. The potential for increased stress in deeper layers of plantar fat and reduced load resistance in the superficial layer could create stress and strain patterns in contrast to those that form in non-diabetic tissue and make the tissue more susceptible to injury.

The microstructural basis for macromechanical properties is well-established in classic engineering and materials disciplines, but is not always a focus of biomechanical inquiry due to the large range of skills required to bridge the two fields. However, integration of both approaches helps to provide broader understanding of pathological changes, such as those associated with diabetes. Often clinical treatments are a combination of pharmacochemical and manual or biomechanical approaches, and a more in-depth understanding of how the two work together can help optimize these combinations.

One of the challenges associated with performing microstructural analyses is the time-consuming manual measurement of repetitive structures at different locations and carefully selecting measurements and locations to avoid biasing two-dimensional measurements of three-dimensional structures[55,110]. Much work, including the work reported in chapters 3 and 4 aims to mitigate this challenge through computational methods. Various groups are also pioneering the field of three-dimensional microscopy[375,376] and using computational techniques to apply various staining appearances[377–379]. All of these techniques can help streamline the workflow associated with microscopic structural study and may enable more comprehensive descriptive and quantitative analyses.

However, while human processing is effective and efficient at discriminating differences based on texture, this has historically been a challenge for computational methods, as noted in chapters 3 and 8. Deep convolutional neural networks have begun to bridge this gap in image processing, but for medical applications, the decision making process is important. The addition of attention and interpretability methods to medical image processing pipelines is starting to address this concern as well. The emerging field of interpretable neural networks have the potential to improve the confidence in and applicability of these types of models to understanding of biological structures and improving clinical care.

Future work building on the investigations presented in chapters 3 and 4 should pursue larger GPU units to allow processing of higher resolution images and more fine-grained attention. Another way that this work could be expanded to provide additional insight is through using the additional two stains used on samples from the same work[55]. These could be used to develop stain-agnostic segmentation methods[380,381] or to identify differences in attention based on stains used to emphasize different structures. Three-dimensional microscopy could extend these insights to better describe the complexity of the three-dimensional structure of the adipose tissue. Such an analysis could provide richer information about the way that the adipose-septal wall relationship changes with diabetes and location and how that creates a material with a higher elastic modulus. An expansion of the work in[24,56] to allow regression between mechanical and image data with attention could be used to better correlate microstructural changes with mechanics as in both of those analyses the mechanical, microstructural, and biochemical data did not show strong associations.

9.2 Macrostructure and Mechanics

The macrostructural and mechanical aims of this work were to:

mmSA1) Develop a mechanical system and the necessary software to generate a three-dimensional scan of the entire plantar soft tissue, using B-mode ultrasound for structural information and shear wave elastography for tissue properties.

mmSA2) Collect plantar soft tissue scans for 7 diabetic non-neuropathic subjects and 7 non-diabetic subjects.

mmSA3) Analyze these scans using segmentation and strain information calculated with digital volume correlation as well as an interpretable classification neural network.

To address **mmSA1**, an elevated scanning platform was constructed featuring a motorized two-axis horizontal translation system, an acoustically transparent load-bearing plate, and custom-molded coupling gels. The ability to acquire volumetric scans of the plantar soft tissue under normal loading addresses many of the limitations associated with prior work using uniaxial force or bi-axial force, single-line or planar imaging, supine acquisitions, or partial foot analysis. This technology has the potential to advance research in several areas of foot biomechanics including but not limited to diabetes, plantar fasciitis, and heel pain.

To address **mmSA2**, the volumetric scanner was used to collect loaded, unloaded, and SWE scans for 3 non-diabetic and 1 diabetic subject. While this is fewer subjects than initially intended, and the sample size is too small to draw meaningful inference about population differences, the methods developed will enable additional future data collection with minimal startup time.

To address **mmSA3**, the loaded and unloaded scans were processed using digital volume correlation and displacement and normal and shear strain were extracted for the three anatomical axes. Scans were compared to computed tomography to assess the accuracy of measurements through the acoustically transparent plate, displacements were correlated with plantar pressure to obtain regional stiffness maps, and scans were segmented to obtain tissue-specific strain and SWE values as well as to assess tissue morphology. While the sample size was insufficient to process scans using the neural networks proposed, the development of the analysis methods described allow future work using volumetric ultrasound scans to be directly compared to prior work and expands prior measurements into two (stiffness) or three (modulus, strain) dimensions. The introduction of additional dimensions to previously devised measurements allows interrogation of previously unmeasured quantities and the evaluation of long-standing hypothesis about the mechanical etiology of plantar ulceration.

There are many directions that this work could be taken. A few of the limitations of and possible improvements to this work are enumerated below.

9.2.1 Scanner Hardware

A current limitation of the scanner hardware is the time required to obtain a scan. The longitudinal resolution is restricted to a minimum of 0.4-0.5mm depending on the length of the foot due to concerns about subject motion, exposure to moisture, and overall data collection time. This limits the number of scans that can be taken in one data collection session to the two unweighted B-mode, one SWE, and one weighted B-mode scans described previously. The long scan time also makes it more difficult to translate this technology to clinical practice. There are several ways that the scan time could be reduced. One way would be to change the transducer technology. Custom transducer arrays can be manufactured in different geometries and with different numbers of elements. One possible design solution would be a wider transducer array with more elements to eliminate the need for multiple passes. This could reduce the scan time from 9-14 minutes to 3-4.5 minutes at the current resolution. The present transducer is 50mm wide and has 256 elements. An analysis of 1.2 million foot measurements reported widths ranging from 70 -130mm with averages ranging from 85 to 110 across different foot lengths[382]. A custom-designed transducer with a width of 110mm would be able to scan most feet in one longitudinal pass. Based on the metrics of the current transducer, such a design would require around 570 elements. Currently available matrix array technology, which allow acquisition of small volumes at similar frame rates to linear array transducers, include transducers with up to 1024 elements, seemingly indicating the feasibility of this idea. Another idea would be to use multiple commercially available linear arrays and sync or stagger their acquisitions. To again allow acquisition of more than one area per motor move or to reduce the number of passes required for a full scan. However, both of these solutions would require use of a research ultrasound to allow the use of a custom transducer, and therefore would require a significant investment in ultrasound processing schemes. This would also increase the cost of the system and could reduce the ease of translation to other research groups and clinicians. However, the reduction in acquisition time could enable acquisition of more types of data such as different loading rates (0, 25%, 50%, 100% BW) or conditions, could reduce medial-lateral bending of the plate, and could increase scan resolution. In the case of a single, wide linear array, such a change in hardware would also substantially reduce time required to reconstruct the volumes, assuming similar temporal reconstruction of send-receive signals as is currently available on commercial machines, as there would no longer be a need for stitching multiple passes together.

Use of a research ultrasound rather than a commercial ultrasound could also allow more customization of sequences, which may be able to overcome some of the limitations of the interfering plate. However, this would again require substantial time to develop, validate, and assess for safety.

The current scanner is quite large and elevated, in part due to the geometry of the transducer. A future iteration of the scanner could be made more portable by creating a transducer with a custom, flat housing and cables and electrical components lateral to the transducer face rather than inferior to it. A reduction in the height of the scanner would allow it to be used without the elevated platform, making it easier to integrate into different research and clinical protocols. This would also make it easier to store and move.

9.2.2 Scanner Software

The processing pipeline for the volumetric ultrasound scans is at this point largely manual. However, there are many examples in the literature of groups developing more automated methods for many of these tasks. The most time-consuming task in the pipeline is segmenting the ultrasound volumes. Current medical imaging software is designed for CT and MRI scans, in which different tissues typically appear with relatively uniform intensity within a tissue that is different from the intensity of a different tissue. Most segmentation methods take advantage of this property and are based on thresholding techniques. However, in ultrasound, tissues are differentiated by their texture and reflective boundaries rather than uniform intensity, making most commercially available tools a poor fit. As a result, manual segmentation involves manually drawing in tissue boundaries. However, several groups have published work addressing the problem of ultrasound segmentation. Neural networks have been implemented for segmentation of automated whole breast ultrasound (AWBUS) volumes using methods from basic encoder-decoder networks[359] to more recent attention-based methods[358,360,383]. In planar ultrasound, segmentation algorithms have been applied to the kidney[384], prostate[385], vessels and nerves[386]. Future work on this project should investigate training a neural network for the specific difficult task of segmenting the soft tissues from the ultrasound volumes. Unet variants have proven performant for difficult textural segmentation tasks[174], and the Unet encoder-decoder structure has even been developed into a versatile hyperparameter optimization automated method designed specifically for medical images[80].

A similarly temporally expensive task is stitching the ultrasound volumes. This is also done manually by stepping through each longitudinal position and making small adjustments to align images from different passes. Various groups have investigated automated methods for stitching ultrasound volumes from a variety of acquisition types. Many methods are based on the three-dimensional tracking of an instrumented ultrasound probe so that the exact position of the transducer can be used to accurately place the image in the volume[324,325,387,388], however, there have also been image processing approaches[307,389–392]. Future work on this project should prioritize automating the stitching process.

Finally, another area of computational interest is developing an attention network to perform classification of ultrasound volumes. There are a variety of ways this could be implemented and numerous potential insights that could be derived. One method would be taking loaded or unloaded ultrasound volumes, or both, and developing a classification or regression network based on other metrics associated with ulcer risk. This could be an effective way to translate an image volume to a meaningful metric. Addition of attention to such a network could further help identify image features associated with increased risk. Those features could be applied to two-dimensional ultrasound clinically as a biomarker for predicting and preventing ulceration. This would be an additionally useful approach in a longitudinal follow up study where volumetric ultrasound structural, deformation, and SWE stiffness features could be correlated with ulcer development. A similar approach could be applied to graded progression of comorbidities such as neuropathy to better assess how progression of these pathologies changes structural and material characteristics. Finally, a network capable of using multimodal input such as CT, plantar pressure, loaded and unloaded volumes or deformation values, and SWE volumes could help identify the combination of metrics most useful for assessing ulcer risk and predicting future ulceration.

10 References

1. CDC: National Diabetes Statistics Report 2020. Estimates of diabetes and its burden in the United States. Atlanta, GA; 2020.
2. Raghupathi W and Raghupathi V: An Empirical Study of Chronic Diseases in the United States: A Visual Analytics Approach. Int. J. Environ. Res. Public Health 2018; **15**: 431. Available at: https://pubmed.ncbi.nlm.nih.gov/29494555.
3. Rice JB, Desai U, Cummings AKG, Birnbaum HG, Skornicki M and Parsons NB: Burden of Diabetic Foot Ulcers for Medicare and Private Insurers. Diabetes Care 2014; **37**: 651 LP – 658. Available at: http://care.diabetesjournals.org/content/37/3/651.abstract.
4. Armstrong DG, Boulton AJM and Bus SA: Diabetic Foot Ulcers and Their Recurrence. Edited by JR Ingelfinger. N. Engl. J. Med. 2017; **376**: 2367–2375. Available at: https://doi.org/10.1056/NEJMra1615439.
5. Bus SA, Lavery LA, Monteiro-Soares M, Rasmussen A, Raspovic A, Sacco ICN and Netten JJ: Guidelines on the prevention of foot ulcers in persons with diabetes (IWGDF 2019 update). Diabetes. Metab. Res. Rev. 2020; **36**: 1–18. Available at: https://onlinelibrary.wiley.com/doi/10.1002/dmrr.3269.
6. Delbridge L, Ctercteko G, Fowler C, Reeve TS and Le Quesne LP: The aetiology of diabetic neuropathic ulceration of the foot. Br. J. Surg. 1985; **72**: 1–6.
7. Bus SA, Armstrong DG, Gooday C, Jarl G, Caravaggi C, Viswanathan V and Lazzarini PA: Guidelines on offloading foot ulcers in persons with diabetes (IWGDF 2019 update). Diabetes. Metab. Res. Rev. 2020; **36**. Available at: https://onlinelibrary.wiley.com/doi/10.1002/dmrr.3274.
8. Veves A, Murray HJ, Young MJ and Boulton AJM: The risk of foot ulceration in diabetic

patients with high foot pressure: a prospective study. Diabetologia 1992; **35**: 660–663.

9. Ledoux WR, Shofer JB, Cowley MS, Ahroni JH, Cohen V and Boyko EJ: Diabetic foot ulcer incidence in relation to plantar pressure magnitude and measurement location. J. Diabetes Complications 2013; **27**: 621–626. Available at: http://dx.doi.org/10.1016/j.jdiacomp.2013.07.004.

10. Murray HJ, Young MJ, Hollis S and Boulton AJM: The Association Between Callus Formation, High Pressures and Neuropathy in Diabetic Foot Ulceration. Diabet. Med. 1996; **13**: 979–982. Available at: https://onlinelibrary.wiley.com/doi/10.1002/(SICI)1096-9136(199611)13:11%3C979::AID-DIA267%3E3.0.CO;2-A.

11. Jenkins D: Hollinshead's Functional Anatomy of the limb and back.; 2009.

12. Blechschmidt E: The Structure of the Calcaneal Padding.; 1982.

13. Jahss MH, Kummer F and Michelson JD: Investigations into the fat pads of the sole of the foot: heel pressure studies. Foot Ankle 1992; **13**: 227–32. Available at: http://www.ncbi.nlm.nih.gov/pubmed/1624185, accessed July 26, 2020.

14. Hsu C-C, Tsai W-C, Wang C-L, Pao S-H, Shau Y-W and Chuan Y-S: Microchambers and macrochambers in heel pads: are they functionally different? J. Appl. Physiol. 2007; **102**: 2227–2231. Available at: http://www.physiology.org/doi/10.1152/japplphysiol.01137.2006, accessed August 3, 2018.

15. Wu C-H, Lin C-Y, Hsiao M-Y, Cheng Y-H, Chen W-S and Wang T-G: Altered stiffness of microchamber and macrochamber layers in the aged heel pad: Shear wave ultrasound elastography evaluation. J. Formos. Med. Assoc. 2018; **117**: 434–439. Available at: https://www.sciencedirect.com/science/article/pii/S0929664617301511, accessed

December 10, 2018.

16. Hsu C-C, Tsai W-C, Hsiao T-Y, Tseng F-Y, Shau Y-W, Wang C-L and Lin S-C: Diabetic effects on microchambers and macrochambers tissue properties in human heel pads. Clin. Biomech. 2009; **24**: 682–686. Available at: https://www.sciencedirect.com/science/article/pii/S0268003309001533?via%3Dihub, accessed August 3, 2018.

17. Bell EA, Hibbert JE and Domire ZJ: Measurement of intrinsic foot stiffness in minimally and traditionally shod runners using ultrasound elastography: A pilot study. J. Sports Sci. 2020; **38**: 1516–1523. Available at: https://doi.org/10.1080/02640414.2020.1746595.

18. Miller-Young JE, Duncan NA and Baroud G: Material properties of the human calcaneal fat pad in compression: Experiment and theory. J. Biomech. 2002; **35**: 1523–1531.

19. Seyfi B, Fatouraee N and Samani A: A novel micro-to-macro structural approach for mechanical characterization of adipose tissue extracellular matrix. J. Mech. Behav. Biomed. Mater. 2018; **77**: 140–147. Available at: https://www.sciencedirect.com/science/article/pii/S1751616117303909.

20. Fontanella CG, Nalesso F, Carniel EL and Natali AN: Biomechanical behavior of plantar fat pad in healthy and degenerative foot conditions. Med. Biol. Eng. Comput. 2016; **54**: 653–661. Available at: http://link.springer.com/10.1007/s11517-015-1356-x.

21. Johnson LK, Richburg C, Lew M, Ledoux WR, Aubin PM and Rombokas E: 3D Printed lattice microstructures to mimic soft biological materials. Bioinspiration and Biomimetics 2019; **14**.

22. Pai S and Ledoux WR: The compressive mechanical properties of diabetic and non-diabetic plantar soft tissue. J. Biomech. 2010; **43**: 1754–1760. Available at:

https://pubmed.ncbi.nlm.nih.gov/20207359.

23. Pai S and Ledoux WR: The shear mechanical properties of diabetic and non-diabetic plantar soft tissue. J. Biomech. 2012; **45**: 364–370. Available at: https://www.sciencedirect.com/science/article/pii/S0021929011006555.

24. Brady L, Pai S, Iaquinto JM, Wang Y-N and Ledoux WR: The compressive, shear, biochemical, and histological characteristics of diabetic and non-diabetic plantar skin are minimally different. J. Biomech. 2021; **129**: 110797. Available at: https://linkinghub.elsevier.com/retrieve/pii/S0021929021005595.

25. Ledoux WR and Blevins JJ: The compressive material properties of the plantar soft tissue. J. Biomech. 2007; **40**: 2975–2981.

26. Chen Y: The influence of diabetes on mechanical properties of skin. ProQuest Diss. Theses 2003. Available at: https://www.proquest.com/dissertations-theses/influence-diabetes-on-mechanical-properties-skin/docview/305264701/se-2?accountid=14784.

27. Gefen A, Megido-Ravid M, Azariah M, Itzchak Y and Arcan M: Integration of plantar soft tissue stiffness measurements in routine MRI of the diabetic foot.; 2001. Available at: www.elsevier.com/locate/clinbiomech.

28. Cheung YY, Doyley M, Miller TB, Kennedy F, Lynch F, Wrobel JS, Paulson K, Weaver J and Cheung Y: Magnetic Resonance Elastography of the Plantar Fat Pads Preliminary Study in Diabetic Patients and Asymptomatic Volunteers.; 2006. Available at: http://journals.lww.com/jcat.

29. Williams ED, Stebbins MJ, Cavanagh PR, Haynor DR, Chu B, Fassbind MJ, Isvilanonda V and Ledoux WR: A preliminary study of patient-specific mechanical properties of diabetic and healthy plantar soft tissue from gated magnetic resonance imaging. Proc. Inst.

Mech. Eng. Part H J. Eng. Med. 2017; **231**: 625–633.

30. Brash PD, Foster[2] J, Vennart[2] W, Anthony[3] P and Tooke JE: Magnetic resonance imaging techniques demonstrate soft tissue damage in the diabetic foot.

31. Mueller MJ, Hastings M, Commean PK, Smith KE, Pilgram TK, Robertson D and Johnson J: Forefoot structural predictors of plantar pressures during walking in people with diabetes and peripheral neuropathy. J. Biomech. 2003; **36**: 1009–1017. Available at: https://linkinghub.elsevier.com/retrieve/pii/S0021929003000782.

32. Robertson DD, Mueller MJ, Smith KE, Commean PK, Pilgram T and Johnson JE: Structural Changes in the Forefoot of Individuals with Diabetes and a Prior Plantar Ulcer. JBJS 2002; **84**. Available at: https://journals.lww.com/jbjsjournal/Fulltext/2002/08000/Structural_Changes_in_the_Forefoot_of_Individuals.16.aspx.

33. Wearing SC, Hooper SL, Dubois P, Smeather JE and Dietze A: Force–Deformation Properties of the Human Heel Pad during Barefoot Walking. Med. Sci. Sport. Exerc. 2014; **46**: 1588–1594. Available at: https://journals.lww.com/00005768-201408000-00014.

34. Sun J-H, Cheng BK, Zheng Y-P, Huang Y-P, Leung JY and Cheing GL: Changes in the Thickness and Stiffness of Plantar Soft Tissues in People With Diabetic Peripheral Neuropathy. Arch. Phys. Med. Rehabil. 2011; **92**: 1484–1489. Available at: https://linkinghub.elsevier.com/retrieve/pii/S0003999311001651.

35. Chao CYL, Zheng Y-P and Cheing GLY: Epidermal Thickness and Biomechanical Properties of Plantar Tissues in Diabetic Foot. Ultrasound Med. Biol. 2011; **37**: 1029–1038. Available at: https://linkinghub.elsevier.com/retrieve/pii/S0301562911002018.

36. Jan Y-K, Lung C-W, Cuaderes E, Rong D and Boyce K: Effect of viscoelastic properties of plantar soft tissues on plantar pressures at the first metatarsal head in diabetics with peripheral neuropathy. Physiol. Meas. 2013; **34**: 53–66. Available at: https://iopscience.iop.org/article/10.1088/0967-3334/34/1/53.

37. Xiong S, Goonetilleke RS, Witana CP and Rodrigo WDAS: An indentation apparatus for evaluating discomfort and pain thresholds in conjunction with mechanical properties of foot tissue in vivo. J. Rehabil. Res. Dev. 2010; **47**: 629. Available at: http://www.rehab.research.va.gov/jour/10/477/pdf/xiong.pdf.

38. Zwaferink JBJ, Custers W, Paardekooper I, Berendsen HA and Bus SA: Optimizing footwear for the diabetic foot: Data-driven custom-made footwear concepts and their effect on pressure relief to prevent diabetic foot ulceration. PLoS One 2020; **15**: 90–98. Available at: http://dx.doi.org/10.1371/journal.pone.0224010.

39. Shaulian H, Gefen A, Solomonow-Avnon D and Wolf A: Finite element-based method for determining an optimal offloading design for treating and preventing heel ulcers. Comput. Biol. Med. 2021; **131**: 104261. Available at: https://doi.org/10.1016/j.compbiomed.2021.104261.

40. Ibrahim M, El Hilaly R, Taher M and Morsy A: A pilot study to assess the effectiveness of orthotic insoles on the reduction of plantar soft tissue strain. Clin. Biomech. 2013; **28**: 68–72. Available at: https://www.sciencedirect.com/science/article/pii/S0268003312002227, accessed October 8, 2018.

41. Guiotto A, Sawacha Z, Guarneri G, Avogaro A and Cobelli C: 3D finite element model of the diabetic neuropathic foot: A gait analysis driven approach. J. Biomech. 2014; **47**:

3064–3071. Available at: http://dx.doi.org/10.1016/j.jbiomech.2014.06.029.

42. Boulton AJM, Hardisty CA, Betts RP, Franks CI, Worth RC, Ward JD and Duckworth T: Dynamic Foot Pressure and Other Studies as Diagnostic and Management Aids in Diabetic Neuropathy. Diabetes Care 1983; **6**: 26–33. Available at: https://care.diabetesjournals.org/content/6/1/26.

43. M. Y, A. E, G. B, G.B. H, L. B and B.L. D: Peak plantar pressure and shear locations: Relevance to diabetic patients. Diabetes Care 2007; **30**: 2643–2645. Available at: http://care.diabetesjournals.org/cgi/reprint/30/10/2643%5Cnhttp://ovidsp.ovid.com/ovidweb.cgi?T=JS&PAGE=reference&D=emed8&NEWS=N&AN=2007494264.

44. Gefen A: Plantar soft tissue loading under the medial metatarsals in the standing diabetic foot. Med. Eng. Phys. 2003; **25**: 491–499. Available at: https://www.sciencedirect.com/science/article/pii/S1350453303000298, accessed October 8, 2018.

45. Luboz V, Perrier A, Stavness I, Lloyd J, Bucki M, … Cannard F: Foot ulcer prevention using biomechanical modelling To cite this version : HAL Id : hal-01092588. 2014.

46. Fontanella CG, Nalesso F, Carniel EL and Natali AN: Biomechanical behavior of plantar fat pad in healthy and degenerative foot conditions. Med. Biol. Eng. Comput. 2016; **54**: 653–661.

47. Behforootan S, Chatzistergos PE, Chockalingam N and Naemi R: A clinically applicable non-invasive method to quantitatively assess the visco-hyperelastic properties of human heel pad, implications for assessing the risk of mechanical trauma. J. Mech. Behav. Biomed. Mater. 2017; **68**: 287–295. Available at: http://linkinghub.elsevier.com/retrieve/pii/S175161611730067X, accessed March 9, 2017.

48. Martínez Bocanegra MA, Bayod J, Vidal-Lesso A, de Bengoa Vallejo RB and Tobar AM: Assessment of Plantar Pressure in a Foot Finite Element Model Considering a Sliding Contact Between Soft Tissues. In: IFMBE Proceedings.Vol 75. Springer 2020; pp 874–883.

49. Behforootan S, Chatzistergos P, Naemi R and Chockalingam N: Finite element modelling of the foot for clinical application: A systematic review. Med. Eng. Phys. 2017; **39**: 1–11. Available at: https://linkinghub.elsevier.com/retrieve/pii/S1350453316302570, accessed November 24, 2019.

50. Eli Isakov, Nikolay Budoragin, Shoshana Shenhav, MSc IM, Asher Korzets and Zeev Susak: Anatomic sites of foot lesions resulting in amputation among diabetics and non-diabetics. Am. J. Phys. Med. Rehabil. 1995; **74**: 130–133.

51. Cowley MS, Boyko EJ, Shofer JB, Ahroni JH and Ledoux WR: Foot ulcer risk and location in relation to prospective clinical assessment of foot shape and mobility among persons with diabetes. Diabetes Res. Clin. Pract. 2008; **82**: 226–232. Available at: https://linkinghub.elsevier.com/retrieve/pii/S016882270800380X.

52. Andreassen TT, Seyer-Hansen K and Oxlund H: Biomechanical changes in connective tissues induced by experimental diabetes. Acta Endocrinol. (Copenh). 1981; **98**: 432–436. Available at: https://eje.bioscientifica.com/view/journals/eje/98/3/acta_98_3_019.xml.

53. Kawaguchi M, Techigawara M, Ishihata T, Asakura T, Saito F, Maehara K and Maruyama Y: A comparison of ultrastructural changes on endomyocardial biopsy specimens obtained from patients with diabetes mellitus with and without hypertension. Heart Vessels 1997; **12**: 267–274. Available at: https://doi.org/10.1007/BF02766802.

54. Reihsner R, Melling M, Pfeiler W and Menzel E-J: Alterations of biochemical and two-

dimensional biomechanical properties of human skin in diabetes mellitus as compared to effects of in vitro non-enzymatic glycation. Clin. Biomech. 2000; **15**: 379–386. Available at: https://linkinghub.elsevier.com/retrieve/pii/S0268003399000856.

55. Wang Y-N, Lee K, Shofer JB and Ledoux WR: Histomorphological and biochemical properties of plantar soft tissue in diabetes. Foot 2017; **33**: 1–6. Available at: https://linkinghub.elsevier.com/retrieve/pii/S0958259217300044.

56. Ledoux WR, Pai S, Shofer JB and Wang YN: The association between mechanical and biochemical/histological characteristics in diabetic and non-diabetic plantar soft tissue. J. Biomech. 2016; **49**: 3328–3333. Available at: http://dx.doi.org/10.1016/j.jbiomech.2016.08.021.

57. Zheng Y., Choi YK., Wong K, Chan S and Mak AF.: Biomechanical assessment of plantar foot tissue in diabetic patients using an ultrasound indentation system. Ultrasound Med. Biol. 2000; **26**: 451–456. Available at: https://linkinghub.elsevier.com/retrieve/pii/S0301562999001635.

58. Rivlin RS: Large elastic deformations of isotropic materials IV. further developments of the general theory. Philos. Trans. R. Soc. London. Ser. A, Math. Phys. Sci. 1948; **241**: 379–397. Available at: https://royalsocietypublishing.org/doi/10.1098/rsta.1948.0024.

59. Ogden RW: Large Deformation Isotropic Elasticity - On the Correlation of Theory and Experiment for Incompressible Rubberlike Solids. Proc. R. Soc. Lond. A. Math. Phys. Sci. 1972; **326**: 565–584. Available at: http://www.jstor.org/stable/77930.

60. Arruda EM and Boyce MC: A three-dimensional constitutive model for the large stretch behavior of rubber elastic materials. J. Mech. Phys. Solids 1993; **41**: 389–412.

61. Fung Y-C: Bioviscoelastic Solids. In: Biomechanics: Mechanical Properties of Living

Tissues. New York, NY: Springer New York 1993; pp 242–320. Available at: https://doi.org/10.1007/978-1-4757-2257-4_7.

62. Galarraga M, Campión J, Munõz-Barrutia A, Boqué N, Moreno H, Martínez JA, Milagro F and Ortiz-de-Solórzano C: Adiposoft: Automated software for the analysis of white adipose tissue cellularity in histological sections. J. Lipid Res. 2012; **53**: 2791–2796.

63. Abreu-Vieira G, Fischer AW, Mattsson C, De Jong JMA, Shabalina IG, Rydén M, Laurencikiene J, Arner P, Cannon B, Nedergaard J and Petrovic N: Cidea improves the metabolic profile through expansion of adipose tissue. Nat. Commun. 2015; **6**.

64. Bursać BN, Vasiljević AD, Nestorović NM, Veličković NA, Vojnović Milutinović DD, Matić GM and Djordjevic AD: High-fructose diet leads to visceral adiposity and hypothalamic leptin resistance in male rats — do glucocorticoids play a role? J. Nutr. Biochem. 2014; **25**: 446–455. Available at: https://www.sciencedirect.com/science/article/pii/S0955286314000023.

65. Dirkes RK, Welly RJ, Mao J, Kinkade J, Vieira-Potter VJ, Rosenfeld CS and Bruzina PS: Gestational and lactational exposure to BPA, but not BPS, negatively impacts trabecular microarchitecture and cortical geometry in adult male offspring. Bone Reports 2021; **15**: 101147. Available at: https://www.sciencedirect.com/science/article/pii/S2352187221004046.

66. van Tilborg E, van Kammen CM, de Theije CGM, van Meer MPA, Dijkhuizen RM and Nijboer CH: A quantitative method for microstructural analysis of myelinated axons in the injured rodent brain. Sci. Rep. 2017; **7**: 16492. Available at: https://pubmed.ncbi.nlm.nih.gov/29184182.

67. Fonck E, Feigl GG, Fasel J, Sage D, Unser M, Rüfenacht DA and Stergiopulos N: Effect

of aging on elastin functionality in human cerebral arteries. Stroke 2009; **40**: 2552–2556.

68. R V and K RR: a Semi - Automated Morphometric Assessment of Nuclei in Pap Smears Using Imagej. J. Evol. Med. Dent. Sci. 2015; **4**: 5363–5370.

69. Hedberg-Buenz A, Christopher MA, Lewis CJ, Meyer KJ, Rudd DS, … Anderson MG: RetFM-J, an ImageJ-based module for automated counting and quantifying features of nuclei in retinal whole-mounts. Exp. Eye Res. 2016; **146**: 386–392. Available at: https://www.sciencedirect.com/science/article/pii/S0014483515002535.

70. Gad AR, Hussein Hassan NM, Abul Seoud RA and Nassef TM: Automatic Machine Learning Classification of Alzheimer's Disease Based on Selected Slices from 3D Magnetic Resonance Imagining. Int. J. Biomed. Sci. Eng. 2016; **4**: 50–54. Available at: http://www.sciencepublishinggroup.com/j/ijbse, accessed April 23, 2019.

71. Awan R, Sirinukunwattana K, Epstein D, Jefferyes S, Qidwai U, Aftab Z, Mujeeb I, Snead D and Rajpoot N: Glandular Morphometrics for Objective Grading of Colorectal Adenocarcinoma Histology Images. Sci. Rep. 2017; **7**: 16852. Available at: http://www.nature.com/articles/s41598-017-16516-w, accessed January 8, 2019.

72. Mercan E, Mehta S, Bartlett J, Weaver DL, Elmore JG and Shapiro LG: Automated Diagnosis of Breast Cancer and Pre-invasive Lesions on Digital Whole Slide Images.

73. Salinas P, Sanhueza J and Sandoval C: Color-Based Segmentation vs. Stereology: A Simple Comparison Between Two Semi-Automated Methods of Image Analysis for the Quantification of Collagen Segmentación Basada en Colores vs. Estereología: Una Comparación Simple entre Dos Métodos Semiautomáticos .; 2018. Available at: https://scielo.conicyt.cl/pdf/ijmorphol/v36n3/0717-9502-ijmorphol-36-03-01118.pdf, accessed December 12, 2018.

74. Simonyan K and Zisserman A: Very Deep Convolutional Networks for Large-Scale Image Recognition. CoRR 2015; **abs/1409.1**.

75. Krizhevsky A, Sutskever I and Hinton GE: ImageNet Classification with Deep Convolutional Neural Networks. In: Advances in Neural Information Processing Systems. Edited by F Pereira, CJC Burges, L Bottou and KQ Weinberger. Vol 25. Curran Associates, Inc. 2012. Available at: https://proceedings.neurips.cc/paper/2012/file/c399862d3b9d6b76c8436e924a68c45b-Paper.pdf.

76. Yan Z, Yang X and Cheng K-TT: A Deep Model with Shape-Preserving Loss for Gland Instance Segmentation. In: Springer, Cham 2018; pp 138–146. Available at: http://link.springer.com/10.1007/978-3-030-00934-2_16, accessed January 8, 2019.

77. Ronneberger O, Fischer P and Brox T: U-Net: Convolutional Networks for Biomedical Image Segmentation. Available at: http://lmb.informatik.uni-freiburg.de/, accessed September 25, 2018.

78. Xu Y, Wang Y, Yuan J, Cheng Q, Wang X and Carson PL: Medical breast ultrasound image segmentation by machine learning. Ultrasonics 2019; **91**: 1–9. Available at: https://www.sciencedirect.com/science/article/pii/S0041624X18302257, accessed October 3, 2018.

79. Islam J and Zhang Y: Early Diagnosis of Alzheimer's Disease: A Neuroimaging Study with Deep Learning Architectures. Available at: http://openaccess.thecvf.com/content_cvpr_2018_workshops/papers/w36/Islam_Early_Diagnosis_of_CVPR_2018_paper.pdf, accessed April 23, 2019.

80. Isensee F, Jaeger PF, Kohl SAA, Petersen J and Maier-Hein KH: nnU-Net: a self-

configuring method for deep learning-based biomedical image segmentation. Nat. Methods 2021; **18**: 203–211. Available at: http://dx.doi.org/10.1038/s41592-020-01008-z.

81. Cai Y and Wang Y: MA-Unet: An improved version of Unet based on multi-scale and attention mechanism for medical image segmentation. 2020. Available at: http://arxiv.org/abs/2012.10952.

82. Jin D, Zhou B, Han Y, Ren J, Han T, … Liu Y: Generalizable, Reproducible, and Neuroscientifically Interpretable Imaging Biomarkers for Alzheimer's Disease. Adv. Sci. 2020; **7**: 2000675. Available at: https://doi.org/10.1002/advs.202000675.

83. Bercoff J, Tanter M and Fink M: Supersonic shear imaging: a new technique for soft tissue elasticity mapping. IEEE Trans. Ultrason. Ferroelectr. Freq. Control 2004; **51**: 396–409. Available at: http://ieeexplore.ieee.org/document/1320804/.

84. Sigrist RMS, Liau J, Kaffas A El, Chammas MC and Willmann JK: Ultrasound elastography: Review of techniques and clinical applications. Theranostics 2017; **7**: 1303–1329.

85. Cosgrove DO, Berg WA, Doré CJ, Skyba DM, Henry J-P, Gay J, Cohen-Bacrie C and Group the BS: Shear wave elastography for breast masses is highly reproducible. Eur. Radiol. 2012; **22**: 1023–1032. Available at: http://link.springer.com/10.1007/s00330-011-2340-y, accessed December 18, 2018.

86. Lifshitz EM, Kosevich AM and Pitaevskii LP: CHAPTER III - ELASTIC WAVES. In: Theory of Elasticity (Third Edition). Edited by EM LIFSHITZ, AM KOSEVICH and LP PITAEVSKII. Third Edit. Oxford: Butterworth-Heinemann 1986; pp 87–107. Available at: https://www.sciencedirect.com/science/article/pii/B9780080570693500103.

87. Hamilton MF, Ilinskii YA and Zabolotskaya EA: Separation of compressibility and shear

deformation in the elastic energy density (L). J. Acoust. Soc. Am. 2004; **116**: 41–44. Available at: https://doi.org/10.1121/1.1736652.

88. Zabolotskaya EA, Hamilton MF, Ilinskii YA and Meegan GD: Modeling of nonlinear shear waves in soft solids. J. Acoust. Soc. Am. 2004; **116**: 2807–2813. Available at: https://doi.org/10.1121/1.1802533.

89. Gennisson J-L, Rénier M, Catheline S, Barrière C, Bercoff J, Tanter M and Fink M: Acoustoelasticity in soft solids: Assessment of the nonlinear shear modulus with the acoustic radiation force. J. Acoust. Soc. Am. 2007; **122**: 3211–3219. Available at: http://asa.scitation.org/doi/10.1121/1.2793605, accessed May 21, 2018.

90. Naemi R, Chatzistergos P, Suresh S, Sundar L, Chockalingam N and Ramachandran A: Can plantar soft tissue mechanics enhance prognosis of diabetic foot ulcer? Diabetes Res. Clin. Pract. 2017; **126**: 182–191. Available at: https://www.sciencedirect.com/science/article/pii/S0168822716315340?via%3Dihub, accessed May 21, 2018.

91. Chatzistergos PE, Behforootan S, Allan D, Naemi R and Chockalingam N: Shear wave elastography can assess the in-vivo nonlinear mechanical behavior of heel-pad. J. Biomech. 2018; **80**: 144–150. Available at: https://www.sciencedirect.com/science/article/pii/S0021929018307243?via%3Dihub#b0060, accessed December 19, 2018.

92. Lin C-Y, Chen P-Y, Shau Y-W, Tai H-C and Wang C-L: Spatial-dependent mechanical properties of the heel pad by shear wave elastography. J. Biomech. 2017; **53**: 191–195. Available at: http://linkinghub.elsevier.com/retrieve/pii/S0021929017300052, accessed March 9, 2017.

93. Mo F, Li J, Yang Z, Zhou S and Behr M: In Vivo Measurement of Plantar Tissue Characteristics and Its Indication for Foot Modeling. Ann. Biomed. Eng. 2019. Available at: https://doi.org/10.1007/s10439-019-02314-0, accessed November 23, 2019.

94. Noorkoiv M, Theis N and Lavelle G: A comparison of 3D ultrasound to MRI for the measurement and estimation of gastrocnemius muscle volume in adults and young people with and without cerebral palsy. Clin. Anat. 2019; **32**: 319–327. Available at: https://onlinelibrary.wiley.com/doi/10.1002/ca.23314.

95. Nicosia L, Ferrari F, Bozzini AC, Latronico A, Trentin C, Meneghetti L, Pesapane F, Pizzamiglio M, Balesetreri N and Cassano E: Automatic breast ultrasound: state of the art and future perspectives. Ecancermedicalscience 2020; **14**: 1062. Available at: https://pubmed.ncbi.nlm.nih.gov/32728378.

96. van Zelst JCM and Mann RM: Automated Three-dimensional Breast US for Screening: Technique, Artifacts, and Lesion Characterization. RadioGraphics 2018; **38**: 663–683. Available at: https://doi.org/10.1148/rg.2018170162.

97. Ranger BJ, Feigin M, Pestrov N, Zhang X, Lempitsky V, Herr HM and Anthony BW: Motion compensation in a tomographic ultrasound imaging system: Toward volumetric scans of a limb for prosthetic socket design. Proc. Annu. Int. Conf. IEEE Eng. Med. Biol. Soc. EMBS 2015; **2015-Novem**: 7204–7207.

98. Ranger BJ, Feigin M, Zhang X, Moerman KM, Herr H and Anthony BW: 3D Ultrasound Imaging of Residual Limbs With Camera-Based Motion Compensation. IEEE Trans. Neural Syst. Rehabil. Eng. 2019; **27**: 207–217. Available at: https://ieeexplore.ieee.org/document/8624620/.

99. Weide G, Huijing PA, Maas JC, Becher JG, Harlaar J and Jaspers RT: Medial

gastrocnemius muscle growth during adolescence is mediated by increased fascicle diameter rather than by longitudinal fascicle growth. J. Anat. 2015; **226**: 530–541. Available at: https://pubmed.ncbi.nlm.nih.gov/25879671.

100. Bénard MR, Harlaar J, Becher JG, Huijing PA and Jaspers RT: Effects of growth on geometry of gastrocnemius muscle in children: a three-dimensional ultrasound analysis. J. Anat. 2011; **219**: 388–402.

101. Huijing PA, Bénard MR, Harlaar J, Jaspers RT and Becher JG: Movement within foot and ankle joint in children with spastic cerebral palsy: A 3-dimensional ultrasound analysis of medial gastrocnemius length with correction for effects of foot deformation. BMC Musculoskelet. Disord. 2013; **14**.

102. Ahanchian N, Nester CJ, Howard D, Ren L and Parker D: Estimating the material properties of heel pad sub-layers using inverse Finite Element Analysis. Med. Eng. Phys. 2017; **40**: 11–19. Available at: http://www.sciencedirect.com/science/article/pii/S1350453316302788, accessed July 11, 2017.

103. Parker D, Cooper G, Pearson S, Crofts G, Howard D, Busby P and Nester C: A device for characterising the mechanical properties of the plantar soft tissue of the foot. Med. Eng. Phys. 2015; **37**: 1098–1104. Available at: http://dx.doi.org/10.1016/j.medengphy.2015.08.008.

104. Cavanagh PR: Plantar soft tissue thickness during ground contact in walking. J. Biomech. 1999; **32**: 623–628. Available at: https://linkinghub.elsevier.com/retrieve/pii/S0021929099000287.

105. Pecoraro RE, Reiber GE and Burgess EM: Pathways to diabetic limb amputation. Basis

for prevention. Diabetes Care 1990; **13**: 513–21. Available at: http://www.ncbi.nlm.nih.gov/pubmed/2351029, accessed July 26, 2020.

106. Geiss LS, Li Y, Hora I, Albright A, Rolka D and Gregg EW: Resurgence of diabetes-related nontraumatic lower-extremity amputation in the young and middle-aged adult U.S. Population. Diabetes Care 2019; **42**: 50–54.

107. Buschmann WR, Jahss MH, Kummer F, Desai P, Gee R 0 and Ricci JL: Histology and Histomorphometric Analysis of the Normal and Atrophic Heel Fat Pad.; 1995.

108. Manorama A, Meyer R, Wiseman R and Bush TR: Quantifying the effects of external shear loads on arterial and venous blood flow: Implications for pressure ulcer development. Clin. Biomech. 2013; **28**: 574–578.

109. Yavuz M: American Society of Biomechanics Clinical Biomechanics Award 2012: plantar shear stress distributions in diabetic patients with and without neuropathy. Clin. Biomech. (Bristol, Avon) 2014; **29**: 223–9. Available at: http://www.ncbi.nlm.nih.gov/pubmed/24332719, accessed July 26, 2020.

110. Wang Y-N, Lee K and Ledoux WR: Histomorphological evaluation of diabetic and non-diabetic plantar soft tissue. Foot ankle Int. 2011; **32**: 802–10. Available at: http://www.ncbi.nlm.nih.gov/pubmed/22049867, accessed July 26, 2020.

111. Aresta G, Araújo T, Kwok S, Chennamsetty SS, Safwan M, … Aguiar P: BACH: Grand challenge on breast cancer histology images. Med. Image Anal. 2019; **56**: 122–139. Available at: https://www.sciencedirect.com/science/article/pii/S1361841518307941?casa_token=aU6f-D75_2QAAAAA:rVku2px0OBRIXoepSd6BB3USSNg-3QKqssweYEe3HLMpGE_02aV9C9nSyeSBG0XHhtxmfWyB8Q, accessed July 26,

2020.

112. Sirinukunwattana K, Pluim JPW, Chen H, Qi X, Heng P-A, … Rajpoot NM: Gland segmentation in colon histology images: The glas challenge contest. Med. Image Anal. 2017; **35**: 489–502. Available at: https://www.sciencedirect.com/science/article/pii/S1361841516301542, accessed January 8, 2019.

113. Kather JN, Weis C-A, Bianconi F, Melchers SM, Schad LR, Gaiser T, Marx A and Zöllner FG: Multi-class texture analysis in colorectal cancer histology. Sci. Rep. 2016; **6**: 27988. Available at: http://dx.doi.org/10.1038/srep27988.

114. Komura D and Ishikawa S: Machine Learning Methods for Histopathological Image Analysis. Comput. Struct. Biotechnol. J. 2018; **16**: 34–42.

115. Urdal J, Engan K, Kvikstad V and Jansseny EAM: Prognostic prediction of histopathological images by local binary patterns and RUSBoost. 25th Eur. Signal Process. Conf. EUSIPCO 2017 2017; **2017-Janua**: 2349–2353.

116. Belsare AD and Mushrif MM: Images using Texture Feature Analysis. Ieee 2015: 2–6.

117. Keller BM, Gastounioti A, Batiste RC, Kontos D and Feldman MD: Preliminary evaluation of a fully automated quantitative framework for characterizing general breast tissue histology via color histogram and color texture analysis. In: Medical Imaging 2016: Digital Pathology. Edited by MN Gurcan and A Madabhushi. Vol 9791. SPIE 2016; pp 69–74. Available at: https://doi.org/10.1117/12.2217094.

118. Bhattacharjee S, Kim CH, Park HG, Prakash D, Madusanka N, Cho NH and Choi HK: Multi-features classification of prostate carcinoma observed in histological sections: Analysis of wavelet-based texture and colour features. Cancers (Basel). 2019; **11**.

119. Rachapudi V and Devi GL: Improved convolutional neural network in remote sensing image classification. Evol. Intell. 2020.

120. Bianconi F, Bello-Cerezo R and Napoletano P: Improved opponent color local binary patterns: an effective local image descriptor for color texture classification. 2017; **27**: 011002-27–10. Available at: http://dx.doi.org/10.1117/1.JEI.27.1.011002.

121. Porebski A and Hoang VT: Multi-color space local binary pattern-based feature selection for texture classification. J. Electron. Imaging 2018; **27**: 1.

122. Li X and Plataniotis KN: Novel chromaticity similarity based color texture descriptor for digital pathology image analysis. PLoS One 2018; **13**: 1–19.

123. Herve N, Servais A, Thervet E, Olivo-Marin J-C and Meas-Yedid V: STATISTICAL COLOR TEXTURE DESCRIPTORS FOR HISTOLOGICAL IMAGES ANALYSIS Nicolas Herv ´ Institut Pasteur , Quantitative Image Analysis Unit , URA CNRS 2582 , 75015 Paris , France Departments of Nephrology and Renal Transplantation , Necker Hospital , 75015. IEEE Int. Symp. Biomed. Imaging 2011: 724–727.

124. Di Ruberto C and Putzu L: A Feature Learning Framework for Histology Images Classification. In: Emerging Trends in Applications and Infrastructures for Computational Biology, Bioinformatics, and Systems Biology: Systems and Applications. Elsevier Inc. 2016; pp 37–48.

125. Bouatmane S, Nekhoul B, Bouridane A and Tanougast C: Classification of Prostatic Tissues using Feature Selection Methods.; 2007. Available at: www.springerlink.com.

126. Bándi P, Van De Loo R, Intezar M, Geijs D, Ciompi F, Van Ginneken B, Van Der Laak J and Litjens G: COMPARISON OF DIFFERENT METHODS FOR TISSUE SEGMENTATION IN HISTOPATHOLOGICAL WHOLE-SLIDE IMAGES. In: IEEE

International Symposium on Biomedical Imaging. Melbourne 2017; pp 591–595. Available at: https://arxiv.org/abs/1703.05990.

127. Manivannan S, Li W, Zhang J, Trucco E and McKenna SJ: Structure Prediction for Gland Segmentation With Hand-Crafted and Deep Convolutional Features. IEEE Trans. Med. Imaging 2018; **37**: 210–221. Available at: http://ieeexplore.ieee.org/document/8030141/, accessed January 8, 2019.

128. Oskal KRJ, Risdal M, Janssen EAM, Undersrud ES and Gulsrud TO: A U-net based approach to epidermal tissue segmentation in whole slide histopathological images. SN Appl. Sci. 2019; **1**: 672. Available at: http://link.springer.com/10.1007/s42452-019-0694-y, accessed July 29, 2020.

129. Xiao Y, Decencière E, Velasco-Forero S, Burdin H, Bornschlögl T, Bernerd F, Warrick E and Baldeweck T: A NEW COLOR AUGMENTATION METHOD FOR DEEP LEARNING SEGMENTATION OF HISTOLOGICAL IMAGES.; 2019.

130. Mavuduru A, Halicek M, Shahedi M, Little J V., Chen AY, Myers LL and Fei B: Using a 22-layer U-Net to perform segmentation of squamous cell carcinoma on digitized head and neck histological images. In: SPIE-Intl Soc Optical Eng 2020; pp 35.

131. Kalapahar A, Silva-Rodríguez J, Colomer A, López-Mir F and Naranjo V: Gleason Grading of Histology Prostate Images through Semantic Segmentation via Residual U-Net. 2020. Available at: http://arxiv.org/abs/2005.11368, accessed July 29, 2020.

132. Zeng Z, Xie W, Zhang Y and Lu Y: RIC-Unet: An Improved Neural Network Based on Unet for Nuclei Segmentation in Histology Images. IEEE Access 2019; **7**: 21420–21428. Available at: https://ieeexplore.ieee.org/document/8632907/, accessed July 29, 2020.

133. Zhang J, Jin Y, Xu J, Xu X and Zhang Y: MDU-Net: Multi-scale Densely Connected U-

Net for biomedical image segmentation. 2018. Available at: http://arxiv.org/abs/1812.00352, accessed January 8, 2019.

134. Zhou Z, Siddiquee MMR, Tajbakhsh N and Liang J: UNet++: Redesigning Skip Connections to Exploit Multiscale Features in Image Segmentation. IEEE Trans. Med. Imaging 2020; **39**: 1856–1867. Available at: https://ieeexplore.ieee.org/document/8932614.

135. Lin D, Li Y, Nwe TL, Dong S and Oo ZM: RefineU-Net: Improved U-Net with progressive global feedbacks and residual attention guided local refinement for medical image segmentation. Pattern Recognit. Lett. 2020; **138**: 267–275. Available at: https://doi.org/10.1016/j.patrec.2020.07.013.

136. Rączkowski Ł, Możejko M, Zambonelli J and Szczurek E: ARA: accurate, reliable and active histopathological image classification framework with Bayesian deep learning. Sci. Rep. 2019; **9**: 1–12.

137. Wetteland R, Engan K, Eftestøl T, Kvikstad V and Janssen EAM: A Multiscale Approach for Whole-Slide Image Segmentation of five Tissue Classes in Urothelial Carcinoma Slides. Technol. Cancer Res. Treat. 2020; **19**: 153303382094678. Available at: http://journals.sagepub.com/doi/10.1177/1533033820946787.

138. Laws KI: TEXTURED IMAGE SEGMENTATION.; 1980.

139. Ahonen T, Matas J, He C and Pietikäinen M: Rotation Invariant Image Description with Local Binary Pattern Histogram Fourier Features. In: Image Analysis: 16th Scandinavian Conference, SCIA 2009, Oslo, Norway, June 15-18, 2009. Proceedings. Edited by A-B Salberg, JY Hardeberg and R Jenssen. Berlin, Heidelberg: Springer Berlin Heidelberg 2009; pp 61–70. Available at: https://doi.org/10.1007/978-3-642-02230-2_7.

140. Kononenko I, Šimec E and Robnik-Šikonja M: Overcoming the Myopia of Inductive Learning Algorithms with RELIEFF. Appl. Intell. 1997; **7**: 39–55. Available at: https://doi.org/10.1023/A:1008280620621.

141. Achanta R and Süsstrunk S: Superpixels and polygons using simple non-iterative clustering. In: Proceedings - 30th IEEE Conference on Computer Vision and Pattern Recognition, CVPR 2017. 2017.

142. Gorodkin J: Comparing two K-category assignments by a K-category correlation coefficient. Comput. Biol. Chem. 2004; **28**: 367–374. Available at: https://www.sciencedirect.com/science/article/pii/S1476927104000799.

143. Dice LR: Measures of the Amount of Ecologic Association Between Species. Ecology 1945; **26**: 297–302. Available at: http://www.jstor.org/stable/1932409.

144. Schindelin J, Arganda-Carreras I, Frise E, Kaynig V, Longair M, … Cardona A: Fiji: An open-source platform for biological-image analysis. Nat. Methods 2012; **9**: 676–682.

145. Kingma DP and Ba J: Adam: A Method for Stochastic Optimization. 2014. Available at: http://arxiv.org/abs/1412.6980, accessed July 29, 2020.

146. Jia Y, Shelhamer E, Donahue J, Karayev S, Long J, Girshick R, Guadarrama S and Darrell T: Caffe: Convolutional Architecture for Fast Feature Embedding. 2014. Available at: http://arxiv.org/abs/1408.5093, accessed July 27, 2020.

147. Csurka G, Larlus D and Perronnin F: What is a good evaluation measure for semantic segmentation? BMVC 2013 - Electron. Proc. Br. Mach. Vis. Conf. 2013 2013; **82**: 2009.

148. Fernandez-Moral E, Martins R, Wolf D and Rives P: A New Metric for Evaluating Semantic Segmentation: Leveraging Global and Contour Accuracy. In: 2018 IEEE Intelligent Vehicles Symposium (IV). IEEE 2018; pp 1051–1056. Available at:

https://ieeexplore.ieee.org/document/8500497/, accessed August 3, 2020.

149. Boyko EJ; and Ahroni JH: A prospective study of risk factors for diabetic foot ulcer: The Seattle Diabetic Foot Study.

150. Forssén PE: Maximally stable colour regions for recognition and matching. Proc. IEEE Comput. Soc. Conf. Comput. Vis. Pattern Recognit. 2007: 0–7.

151. Sirinukunwattana K, Alham NK, Verrill C and Rittscher J: Improving Whole Slide Segmentation Through Visual Context-A Systematic Study. Available at: https://arxiv.org/pdf/1806.04259.pdf, accessed January 8, 2019.

152. Segato dos Santos, Luiz Fernando, Neves, Leandro Alves, Rozendo GB, Ribeiro MG, Zanchetta do Nascimento M and Azevedo Tosta TA: Multidimensional and fuzzy sample entropy (SampEnMF) for quantifying H&E histological images of colorectal cancer. Comput. Biol. Med. 2018; **103**: 148–160. Available at: https://www.sciencedirect.com/science/article/pii/S0010482518303123.

153. Hatt M, Cheze C, Turzo A, Roux C and Oncology IT: Approach for Volume Determination in PET. Contract 2009; **28**: 881–893.

154. Kleczek P, Jaworek-Korjakowska J and Gorgon M: A novel method for tissue segmentation in high-resolution H&E-stained histopathological whole-slide images. Comput. Med. Imaging Graph. 2020; **79**: 101686. Available at: https://doi.org/10.1016/j.compmedimag.2019.101686.

155. Lin C-Y, Lin C-C, Chou Y-C, Chen P-Y and Wang C-L: Heel Pad Stiffness in Plantar Heel Pain by Shear Wave Elastography. Ultrasound Med. Biol. 2015; **41**: 2890–2898. Available at: https://www.sciencedirect.com/science/article/pii/S0301562915004263, accessed December 10, 2018.

156. Hsu T-C, Lee Y-S and Shau Y-W: Biomechanics of the heel pad for type 2 diabetic patients. Clin. Biomech. 2002; **17**: 291–296. Available at: https://linkinghub.elsevier.com/retrieve/pii/S0268003302000189.

157. Hanna W, Friesen D, Bombardier C, Gladman D and Hanna A: Pathologic features of diabetic thick skin. J. Am. Acad. Dermatol. 1987; **16**: 546–553. Available at: https://linkinghub.elsevier.com/retrieve/pii/S0190962287700723.

158. Collier A, Patrick AW, Bell D, Matthews DM, Maclntyre CCA, Ewing DJ and Clarke BF: Relationship of Skin Thickness to Duration of Diabetes, Glycemic Control, and Diabetic Complications in Male IDDM Patients. Diabetes Care 1989; **12**: 309–312. Available at: http://care.diabetesjournals.org/cgi/doi/10.2337/diacare.12.5.309.

159. Huntley AC and Walter RM: Quantitative determination of skin thickness in diabetes mellitus: relationship to disease parameters. J. Med. 1990; **21**: 257–64. Available at: http://www.ncbi.nlm.nih.gov/pubmed/2079616.

160. Hsu T-C, Wang C-L, Shau Y-W, Tang F-T, Li K-L and Chen C-Y: Altered heel-pad mechanical properties in patients with Type 2 diabetes mellitus. Diabet. Med. 2000; **17**: 854–859. Available at: http://doi.wiley.com/10.1046/j.1464-5491.2000.00394.x.

161. Hsu C-C, Tsai W-C, Shau Y-W, Lee K-L and Hu C-F: Altered energy dissipation ratio of the plantar soft tissues under the metatarsal heads in patients with type 2 diabetes mellitus: A pilot study. Clin. Biomech. 2007; **22**: 67–73. Available at: https://linkinghub.elsevier.com/retrieve/pii/S0268003306001306.

162. Araújo T, Aresta G, Castro E, Rouco J, Aguiar P, Eloy C, Polónia A and Campilho A: Classification of breast cancer histology images using Convolutional Neural Networks. PLoS One 2017; **12**: 1–14. Available at: https://doi.org/10.1371/journal.pone.0177544.

163. Ker J, Bai Y, Lee HY, Rao J and Wang L: Automated brain histology classification using machine learning. J. Clin. Neurosci. 2019; **66**: 239–245. Available at: https://www.sciencedirect.com/science/article/pii/S0967586819306563.

164. Halicek M, Shahedi M, Little J V, Chen AY, Myers LL, Sumer BD and Fei B: Head and Neck Cancer Detection in Digitized Whole-Slide Histology Using Convolutional Neural Networks. Sci. Rep. 2019; **9**: 14043. Available at: https://doi.org/10.1038/s41598-019-50313-x.

165. Silva-Rodríguez J, Colomer A and Naranjo V: WeGleNet: A weakly-supervised convolutional neural network for the semantic segmentation of Gleason grades in prostate histology images. Comput. Med. Imaging Graph. 2021; **88**: 101846. Available at: https://linkinghub.elsevier.com/retrieve/pii/S0895611120301415.

166. Heinemann F, Birk G, Schoenberger T and Stierstorfer B: Deep neural network based histological scoring of lung fibrosis and inflammation in the mouse model system. Edited by R Hurst. PLoS One 2018; **13**: e0202708. Available at: https://dx.plos.org/10.1371/journal.pone.0202708, accessed January 8, 2019.

167. Yu Y, Wang J, Ng CW, Ma Y, Mo S, … Yu H: Deep learning enables automated scoring of liver fibrosis stages. Sci. Rep. 2018; **8**: 16016. Available at: http://www.nature.com/articles/s41598-018-34300-2, accessed March 25, 2019.

168. MORTENSEN M: ANTECEDENTS AND CONSEQUENCES OF TEAM BOUNDARY DISAGREEMENT. Acad. Manag. Proc. 2004; **2004**: M1–M6. Available at: http://journals.aom.org/doi/10.5465/ambpp.2004.13862426.

169. Erhan D, Bengio Y, Courville AC and Vincent P: Visualizing Higher-Layer Features of a Deep Network. In: 2009.

170. Wang H, Wang Z, Du M, Yang F, Zhang Z, Ding S, Mardziel P and Hu X: Score-CAM: Score-Weighted Visual Explanations for Convolutional Neural Networks. In: 2020 IEEE/CVF Conference on Computer Vision and Pattern Recognition Workshops (CVPRW).Vol 2020-June. IEEE 2020; pp 111–119. Available at: https://ieeexplore.ieee.org/document/9150840/.

171. Li Z, Tao R, Wu Q and Li B: DA-RefineNet: Dual-inputs Attention RefineNet for Whole Slide Image Segmentation. In: 2020 25th International Conference on Pattern Recognition (ICPR). IEEE 2021; pp 1918–1925. Available at: https://ieeexplore.ieee.org/document/9412546/.

172. Li J, Li W, Sisk A, Ye H, Wallace WD, Speier W and Arnold CW: A multi-resolution model for histopathology image classification and localization with multiple instance learning. Comput. Biol. Med. 2021; **131**: 104253. Available at: https://linkinghub.elsevier.com/retrieve/pii/S0010482521000470.

173. Sun H, Zeng X, Xu T, Peng G and Ma Y: Computer-Aided Diagnosis in Histopathological Images of the Endometrium Using a Convolutional Neural Network and Attention Mechanisms. IEEE J. Biomed. Heal. Informatics 2020; **24**: 1664–1676. Available at: https://ieeexplore.ieee.org/document/8854180/.

174. Brady L, Wang Y-N, Rombokas E and Ledoux WR: Comparison of texture-based classification and deep learning for plantar soft tissue histology segmentation. Comput. Biol. Med. 2021; **134**: 104491. Available at: https://linkinghub.elsevier.com/retrieve/pii/S0010482521002857.

175. Wang H, Zhu Y, Green B, Adam H, Yuille A and Chen LC: Axial-DeepLab: Stand-Alone Axial-Attention for Panoptic Segmentation. arXiv 2020. Available at:

https://arxiv.org/abs/2003.07853, accessed February 13, 2022.

176. R Core Team: R: A Language and Environment for Statistical Computing. 2019. Available at: https://www.r-project.org/.

177. Bates D, Mächler M, Bolker B and Walker S: Fitting Linear Mixed-Effects Models Using lme4. J. Stat. Software; Vol 1, Issue 1 2015. Available at: https://www.jstatsoft.org/v067/i01.

178. Searle SR, Speed FM and Milliken GA: Population Marginal Means in the Linear Model: An Alternative to Least Squares Means. Am. Stat. 1980; **34**: 216–221. Available at: https://www.tandfonline.com/doi/abs/10.1080/00031305.1980.10483031.

179. Pai S and Ledoux WR: The quasi-linear viscoelastic properties of diabetic and non-diabetic plantar soft tissue. Ann. Biomed. Eng. 2011; **39**: 1517–1527. Available at: https://pubmed.ncbi.nlm.nih.gov/21327701.

180. Timár F, Soós G, Szende B and Horváth A: Interdigitation index - a parameter for differentiating between young and older skin specimens. Ski. Res. Technol. 2000; **6**: 17–20. Available at: http://doi.wiley.com/10.1034/j.1600-0846.2000.006001017.x.

181. Zheng Y, Choi Y, Wong K, Chan S and Mak AF.: Biomechanical Assessment of Plantar Foot Tissue in Diabetic Patients using an Ultrasound Indentation System Indentation Test of Plantar Tissue. Ultrasound Med. Biol. 2000; **26**: 451–456. Available at: https://linkinghub.elsevier.com/retrieve/pii/S0301562999001635.

182. Ng TKW, Zheng YP, Kwan RLC and Cheing GLY: An innovative ultrasound foot scanner system for measuring the change in biomechanical properties of plantar tissue from sitting to standing. Int. J. Rehabil. Res. 2015; **38**: 68–73.

183. Kawchuk GN and Elliott PD: Validation of displacement measurements obtained from

ultrasonic images during indentation testing. Ultrasound Med. Biol. 1998; **24**: 105–111.

184. Wu C-H, Lin C-Y, Hsiao M-Y, Cheng Y-H, Chen W-S and Wang T-G: Altered stiffness of microchamber and macrochamber layers in the aged heel pad: Shear wave ultrasound elastography evaluation. J. Formos. Med. Assoc. 2018; **117**: 434–439. Available at: https://www.sciencedirect.com/science/article/pii/S0929664617301511?via%3Dihub, accessed May 21, 2018.

185. Lin C-Y, Chen P-Y, Shau Y-W, Tai H-C and Wang C-L: Spatial-dependent mechanical properties of the heel pad by shear wave elastography. J. Biomech. 2017; **53**: 191–195. Available at: https://www.sciencedirect.com/science/article/pii/S0021929017300052?via%3Dihub, accessed May 21, 2018.

186. Yang XG, Teng ZL, Zhang ZM, Wang K, Huang R, … Geng X: Comparison of material properties of heel pad between adults with and without type 2 diabetes history: An in-vivo investigation during gait. Front. Endocrinol. (Lausanne). 2022; **13**.

187. Matsumoto M, Maemichi T, Wada M, Niwa Y, Inagaki S, Okunuki T, Ichikawa S and Kumai T: Ultrasonic Evaluation of the Heel Fat Pad under Weight-Bearing Conditions Using a Polymethylpentene Resin Plate: Part 1. Ultrasound Med. Biol. 2022; **48**: 358–372.

188. Kim M, Choi YS, You M-W, Kim JS and Young KW: Sonoelastography in the Evaluation of Plantar Fasciitis Treatment. Ultrasound Q. 2016; **32**: 327–332. Available at: https://journals.lww.com/00013644-201612000-00003.

189. Harish C. S, Dixit R, Singh S and Garg S: Evaluation of the plantar fascia in patients with diabetes mellitus: the role of sonoelastography. Polish J. Radiol. 2022; **87**: 500–505. Available at: https://www.termedia.pl/doi/10.5114/pjr.2022.119474.

190. Kwan RL-C, Zheng Y-P and Cheing GL-Y: The effect of aging on the biomechanical properties of plantar soft tissues. Clin. Biomech. 2010; **25**: 601–605. Available at: https://linkinghub.elsevier.com/retrieve/pii/S0268003310001014.

191. Mo F, Li J, Yang Z, Zhou S and Behr M: In Vivo Measurement of Plantar Tissue Characteristics and Its Indication for Foot Modeling. Ann. Biomed. Eng. 2019; **47**: 2356–2371. Available at: http://link.springer.com/10.1007/s10439-019-02314-0.

192. Matsumoto M, Maemichi T, Wada M, Niwa Y, Inagaki S, Taguchi A, Okunuki T, Tanaka H and Kumai T: Ultrasonic Evaluation of the Heel Fat Pad Under Loading Conditions Using a Polymethylpentene Resin Plate: Part 2. Reliability and Agreement Study. Ultrasound Med. Biol. 2023; **49**: 460–472.

193. Liu Z, Maemichi T, Matsumoto M, Okunuki T, Tanaka H, Katsutani H, Li Y and Kumai T: Change in the sub-sesamoid soft tissue thickness under different loading conditions.

194. Bygrave CJ and Betts RP: The plantar tissue thickness in the foot: a new ultrasound technique for loadbearing measurements and a metatarsal head depth study.; 1992.

195. Matteoli S: Diagnosis of Heel Pad Injuries. 2012.

196. Ng TK-W, Zheng Y-P, Kwan RL-C and Cheing GL-Y: An innovative ultrasound foot scanner system for measuring the change in biomechanical properties of plantar tissue from sitting to standing. Int. J. Rehabil. Res. 2015; **38**: 68–73. Available at: https://journals.lww.com/00004356-201503000-00009.

197. De Clercq D, Aerts P and Kunnen M: The mechanical characteristics of the human heel pad during foot strike in running: An in vivo cineradiographic study. J. Biomech. 1994; **27**: 1213–1222. Available at: https://linkinghub.elsevier.com/retrieve/pii/0021929094902755.

198. Pai S: Preliminary In Vivo Plantar Soft Tissue Shear Strain Estimates. 2011.

199. Weaver JB, Miller TB, Perrinez PR, Doyley MM, Wang H, Cheung YY, Wrobel JS, Comi RJ, Kennedy FE and Paulsen KD: MR elastographic methods for the evaluation of plantar fat pads: preliminary comparison of the shear modulus for shearing deformation and compressive deformation in normal subjects. In: Medical Imaging 2006: Physiology, Function, and Structure from Medical Images.Vol 6143. SPIE 2006; pp 61430Y.

200. Petre M, Erdemir A and Cavanagh PR: An MRI-compatible foot-loading device for assessment of internal tissue deformation. J. Biomech. 2008; **41**: 470–474. Available at: https://www.sciencedirect.com/science/article/pii/S0021929007003934, accessed October 8, 2018.

201. Williams ED, Stebbins MJ, Cavanagh PR, Haynor DR, Chu B, Fassbind MJ, Isvilanonda V and Ledoux WR: The design and validation of a magnetic resonance imaging-compatible device for obtaining mechanical properties of plantar soft tissue via gated acquisition. Proc. Inst. Mech. Eng. Part H J. Eng. Med. 2015; **229**: 732–742.

202. Trebbi A, Perrier A, Bailet M and Payan Y: MR-compatible loading device for assessment of heel pad internal tissue displacements under shearing load. Med. Eng. Phys. 2021; **98**: 125–132.

203. Peng Y, Wang Y, Wong DWC, Chen TLW, Chen SF, Zhang G, Tan Q and Zhang M: Different Design Feature Combinations of Flatfoot Orthosis on Plantar Fascia Strain and Plantar Pressure: A Muscle-Driven Finite Element Analysis With Taguchi Method. Front. Bioeng. Biotechnol. 2022; **10**.

204. Trebbi A, Fougeron N and Payan Y: Definition and evaluation of a finite element model of the human heel for diabetic foot ulcer prevention under shearing loads. Med. Eng. Phys.

2023; **118**.

205. Chen W-M, Lee S-J and Lee PVS: The in vivo plantar soft tissue mechanical property under the metatarsal head: implications of tissues′ joint-angle dependent response in foot finite element modeling. J. Mech. Behav. Biomed. Mater. 2014; **40**: 264–274. Available at: https://www.sciencedirect.com/science/article/pii/S1751616114002914, accessed October 8, 2018.

206. Behforootan S, Chatzistergos PE, Chockalingam N and Naemi R: A Simulation of the Viscoelastic Behaviour of Heel Pad During Weight-Bearing Activities of Daily Living. Ann. Biomed. Eng. 2017; **45**: 2750–2761. Available at: http://link.springer.com/10.1007/s10439-017-1918-1, accessed May 21, 2018.

207. Jurca A, Žabkar J and Džeroski S: Analysis of 1.2 million foot scans from North America, Europe and Asia. Sci. Rep. 2019; **9**: 19155. Available at: https://www.nature.com/articles/s41598-019-55432-z.

208. Rome K, Campbell R, Flint A and Haslock I: Heel Pad Thickness-A Contributing Factor Associated with Plantar Heel Pain in Young Adults.; 2002.

209. Isvilanonda V, Iaquinto JM, Pai S, Mackenzie-Helnwein P and Ledoux WR: Hyperelastic compressive mechanical properties of the subcalcaneal soft tissue: An inverse finite element analysis. J. Biomech. 2016; **49**: 1186–1191. Available at: https://linkinghub.elsevier.com/retrieve/pii/S0021929016302639.

210. Isvilanonda V: Finite Element Modeling of the Foot. 2015.

211. Reddy PN, Cooper G, Weightman A, Hodson-Tole E and Reeves ND: Walking cadence affects rate of plantar foot temperature change but not final temperature in younger and older adults. Gait Posture 2017; **52**: 272–279.

212. Beach C, Cooper G, Weightman A, Hodson-Tole EF, Reeves ND and Casson AJ: Monitoring of Dynamic Plantar Foot Temperatures in Diabetes with Personalised 3D-Printed Wearables. Sensors 2021; **21**: 1717. Available at: https://www.mdpi.com/1424-8220/21/5/1717.

213. Fedorov A, Beichel R, Kalpathy-Cramer J, Finet J, Fillion-Robin J-C, … Kikinis R: 3D Slicer as an image computing platform for the Quantitative Imaging Network. Magn. Reson. Imaging 2012; **30**: 1323–41. Available at: http://www.ncbi.nlm.nih.gov/pubmed/3466397.

214. Akhmanova M, Osidak E, Domogatsky S, Rodin S and Domogatskaya A: Physical, Spatial, and Molecular Aspects of Extracellular Matrix of In Vivo Niches and Artificial Scaffolds Relevant to Stem Cells Research. Stem Cells Int. 2015; **2015**: 1–35. Available at: http://www.hindawi.com/journals/sci/2015/167025/.

215. Duck FA: Mechanical Properties of Tissue. In: Physical Properties of Tissues. Elsevier 1990; pp 137–165.

216. Williams ED, Stebbins MJ, Cavanagh PR, Haynor DR, Chu B, Fassbind MJ, Isvilanonda V and Ledoux WR: A preliminary study of patient-specific mechanical properties of diabetic and healthy plantar soft tissue from gated magnetic resonance imaging. Proc. Inst. Mech. Eng. Part H J. Eng. Med. 2017; **231**: 625–633.

217. Trebbi A, Mukhina E, Rohan PY, Connesson N, Bailet M, Perrier A and Payan Y: MR-based quantitative measurement of human soft tissue internal strains for pressure ulcer prevention. Med. Eng. Phys. 2022; **108**: 1–10.

218. Chen W-M, Lee PV-S, Lee S-J and Lee T: Investigation of Plantar Barefoot Pressure and Soft-tissue Internal Stress: A Three-Dimensional Finite Element Analysis. In: 13th

International Conference on Biomedical Engineering. Berlin, Heidelberg: Springer Berlin Heidelberg 2009; pp 1817–1820. Available at: http://link.springer.com/10.1007/978-3-540-92841-6_451, accessed October 8, 2018.

219. Chen W-M, Lee T, Lee PV-S, Lee JW and Lee S-J: Effects of internal stress concentrations in plantar soft-tissue—A preliminary three-dimensional finite element analysis. Med. Eng. Phys. 2010; **32**: 324–331. Available at: https://www.sciencedirect.com/science/article/pii/S1350453310000020, accessed October 3, 2018.

220. Rome K: Mechanical properties of the heel pad: Current theory and review of the literature. Foot 1998; **8**: 179–185.

221. Al-Zogbi L, Bock B, Schaffer S, Fleiter T and Krieger A: A 3-D-Printed Patient-Specific Ultrasound Phantom for FAST Scan. Ultrasound Med. Biol. 2021; **47**: 820–832. Available at: https://linkinghub.elsevier.com/retrieve/pii/S0301562920304932.

222. Svendsen MBS, Ghulam QM, Zielinski AH, Lachenmeier C and Eiberg JP: Validation of an assessment tool for estimation of abdominal aortic aneurysm compression in diagnostic ultrasound. Ultrasonics 2021; **116**: 106484. Available at: https://linkinghub.elsevier.com/retrieve/pii/S0041624X21001153.

223. Flores Rivera AR: Risk factors for amputation in diabetic patients: a case-control study. Arch. Med. Res. 1998; **29**: 179—184. Available at: http://europepmc.org/abstract/MED/9650335.

224. Schmidt D, Germano AMC and Milani TL: Effects of water immersion on sensitivity and plantar skin properties. Neurosci. Lett. 2018; **686**: 41–46. Available at: https://www.sciencedirect.com/science/article/pii/S0304394018305937, accessed

December 10, 2018.

225. Wildnauer RH, Bothwell JW and Douglass AB: Stratum Corneum Biomechanical Properties I. Influence of Relative Humidity on Normal and Extracted Human Stratum Corneum. J. Invest. Dermatol. 1971; **56**: 72–78.

226. Robinson M, Visscher M, Laruffa A and Wickett R: Natural moisturizing factors (NMF) in the stratum corneum (SC). II. Regeneration of NMF over time after soaking. J. Cosmet. Sci. 2010; **61**: 23–9.

227. Spears MJ, McKillop K, Marshall JL, Stone KJ, Lilly NA, Warner RR and Boissy YL: Water Disrupts Stratum Corneum Lipid Lamellae: Damage is Similar to Surfactants1. J. Invest. Dermatol. 1999; **113**: 960–966.

228. Pavan TZ, Madsen EL, Frank GR, Jiang J, Carneiro AAO and Hall TJ: A nonlinear elasticity phantom containing spherical inclusions. Phys. Med. Biol. 2012; **57**: 4787–4804. Available at: http://stacks.iop.org/0031-9155/57/i=15/a=4787?key=crossref.e2fc64bd1cbaf1ec58be449c760c36cb, accessed May 29, 2018.

229. Madsen EL, Zagzebski JA, Banjavie RA and Jutila RE: Tissue mimicking materials for ultrasound phantoms. Med. Phys. 1978; **5**: 391–394. Available at: https://doi.org/10.1118/1.594483.

230. Chen L, Zeng G, Guo D, Liu J, Zhang X, Lin S and Zhang K: Soft elastic hydrogel couplants for ultrasonography. Mater. Sci. Eng. C 2021; **119**: 111609. Available at: https://linkinghub.elsevier.com/retrieve/pii/S092849312033527X.

231. Yengul SS, Barbone PE and Madore B: Dispersion in Tissue-Mimicking Gels Measured with Shear Wave Elastography and Torsional Vibration Rheometry. Ultrasound Med.

Biol. 2019; **45**: 586–604. Available at: https://www.sciencedirect.com/science/article/pii/S0301562918302783#bib0017, accessed April 27, 2019.

232. Anderson PG, Rouze NC and Palmeri ML: Effect of Graphite Concentration on Shear-Wave Speed in Gelatin-Based Tissue-Mimicking Phantoms. Ultrason. Imaging 2011; **33**: 134–142. Available at: http://journals.sagepub.com/doi/10.1177/016173461103300204.

233. Jacob X, Catheline S, Gennisson J-L, Barrière C, Royer D and Fink M: Nonlinear shear wave interaction in soft solids. J. Acoust. Soc. Am. 2007; **122**: 1917–1926. Available at: https://pubs.aip.org/jasa/article/122/4/1917/982779/Nonlinear-shear-wave-interaction-in-soft-solids.

234. Latorre-Ossa H, Gennisson J, De Brosses E and Tanter M: Quantitative imaging of nonlinear shear modulus by combining static elastography and shear wave elastography. IEEE Trans. Ultrason. Ferroelectr. Freq. Control 2012; **59**: 833–839. Available at: http://ieeexplore.ieee.org/document/6189191/, accessed May 21, 2018.

235. Bernal M, Chammings F, Couade M, Bercoff J, Tanter M and Gennisson J-L: <italic>In Vivo</italic> Quantification of the Nonlinear Shear Modulus in Breast Lesions: Feasibility Study. IEEE Trans. Ultrason. Ferroelectr. Freq. Control 2016; **63**: 101–109. Available at: http://ieeexplore.ieee.org/document/7336552/, accessed May 21, 2018.

236. Dunmire B, Kucewicz JC, Mitchell SB, Crum LA and Sekins KM: Characterizing an Agar/Gelatin phantom for image guided dosing and feedback control of high-intensity focused ultrasound. Ultrasound Med. Biol. 2013; **39**: 300–311.

237. Movahed P, Kreider W, Maxwell AD, Hutchens SB and Freund JB: Cavitation-induced

damage of soft materials by focused ultrasound bursts: A fracture-based bubble dynamics model. J. Acoust. Soc. Am. 2016; **140**: 1374–1386.

238. Movahed P, Kreider W, Maxwell AD, Dunmire B and Freund JB: Ultrasound-Induced Bubble Clusters in Tissue-Mimicking Agar Phantoms. Ultrasound Med. Biol. 2017; **43**: 2318–2328.

239. Sboros V, Moran CM, Anderson T, Gatzoulis L, Criton A, Averkiou M, Pye SD and McDicken WN: An in vitro system for the study of ultrasound contrast agents using a commercial imaging system. Phys. Med. Biol. 2001; **46**: 3301–3321. Available at: https://iopscience.iop.org/article/10.1088/0031-9155/46/12/316.

240. Ophir J, Makland N and Jager Pa: "Tissue Mimicking Materials for Ultrasound Phan toms''."; 1981.

241. Pogue BW and Patterson MS: Review of tissue simulating phantoms for optical spectroscopy, imaging and dosimetry. J. Biomed. Opt. 2006; **11**: 041102.

242. Wang C, Chen X, Wang L, Makihata M, Liu H-C, Zhou T and Zhao X: Bioadhesive ultrasound for long-term continuous imaging of diverse organs.; 2022. Available at: https://www.science.org.

243. Aoyagi M and Hiraguri T: Ultrasound Phantom Using Sodium Alginate as a Gelling Agent. J. Ultrasound Med. 2017; **36**: 2345–2353. Available at: https://onlinelibrary.wiley.com/doi/10.1002/jum.14252.

244. Baba M, Matsumoto K, Yamasaki N, Shindo H, Yano H, … Nagayasu T: Development of a Tailored Thyroid Gland Phantom for Fine-Needle Aspiration Cytology by Three-Dimensional Printing. J. Surg. Educ. 2017; **74**: 1039–1046. Available at: https://linkinghub.elsevier.com/retrieve/pii/S1931720416302288.

245. Nanda Kumar Y, Singh Z, Wang Y-N, Schade GR, Kreider W, Bruce M, Vlaisavljevich E, Khokhlova TD and Maxwell AD: Development of Tough Hydrogel Phantoms to Mimic Fibrous Tissue for Focused Ultrasound Therapies. Ultrasound Med. Biol. 2022; **48**: 1762–1777.

246. Kuth S, Karakaya E, Reiter N, Schmidt L, Paulsen F, Teßmar J, Budday S and Boccaccini AR: Oxidized Hyaluronic Acid-Gelatin-Based Hydrogels for Tissue Engineering and Soft Tissue Mimicking. Tissue Eng. Part C Methods 2022; **28**: 301–313.

247. Cortela GA, Negreira CA and Pereira WCA: Durability study of a gellan gum-based tissue-mimicking phantom for ultrasonic thermal therapy. J. Acoust. Soc. Am. 2020; **147**: 1531–1545.

248. Troia A, Cuccaro R and Schiavi A: Independent tuning of acoustic and mechanical properties of phantoms for biomedical applications of ultrasound. Biomed. Phys. Eng. Express 2017; **3**: 025011. Available at: https://iopscience.iop.org/article/10.1088/2057-1976/aa5ed0.

249. King RL, Liu Y, Maruvada S, Herman BA, Wear KA and Harris GR: Development and characterization of a tissue-mimicking material for high-intensity focused ultrasound. IEEE Trans. Ultrason. Ferroelectr. Freq. Control 2011; **58**: 1397–1405.

250. Chen P, Pollet AMAO, Panfilova A, Zhou M, Turco S, den Toonder JMJ and Mischi M: Acoustic characterization of tissue-mimicking materials for ultrasound perfusion imaging research. Ultrasound Med. Biol. 2022; **48**: 124–142. Available at: https://linkinghub.elsevier.com/retrieve/pii/S030156292100380X.

251. Cabrelli LC, Grillo FW, Sampaio DRT, Carneiro AAO and Pavan TZ: Acoustic and Elastic Properties of Glycerol in Oil-Based Gel Phantoms. Ultrasound Med. Biol. 2017;

43: 2086–2094.

252. Ilvio S, Vieira L, Pavan TZ, Junior JE and Carneiro AAO: PARAFFIN-GEL TISSUE-MIMICKING MATERIAL FOR ULTRASOUND-GUIDED NEEDLE BIOPSY PHANTOM. 2013. Available at: http://dx.doi.org/10.1016/j.ultrasmedbio.2013.06.008, accessed March 26, 2019.

253. Robertson J, Leen E, Goldberg JA, Angerson WJ, Sutherland GR and McArdle C: Flow measurement using duplex Doppler ultrasound: haemodynamic changes in patients with colorectal liver metastases.; 1992.

254. Zell K, Sperl JI, Vogel MW, Niessner R and Haisch C: Acoustical properties of selected tissue phantom materials for ultrasound imaging. Phys. Med. Biol. 2007; **52**: N475–N484.

255. Mori T, Ishikawa N and Mimura H: Bioequivalent and Non-Aqueous Polyurethane Gel for Ultrasound Phantom. J. Chem. Eng. JAPAN 2022; **55**: 21we117.

256. Culjat MO, Goldenberg D, Tewari P and Singh RS: A Review of Tissue Substitutes for Ultrasound Imaging. Ultrasound Med. Biol. 2010; **36**: 861–873. Available at: https://linkinghub.elsevier.com/retrieve/pii/S030156291000075X.

257. Poepping TL, Nikolov HN, Thorne ML and Holdsworth DW: A thin-walled carotid vessel phantom for Doppler ultrasound flow studies. Ultrasound Med. Biol. 2004; **30**: 1067–1078.

258. Tsou JK, Liu J, Barakat AI and Insana MF: Role of Ultrasonic Shear Rate Estimation Errors in Assessing Inflammatory Response and Vascular Risk. Ultrasound Med. Biol. 2008; **34**: 963–972. Available at: https://linkinghub.elsevier.com/retrieve/pii/S0301562907005704.

259. Culjat MO, Goldenberg D, Tewari P and Singh RS: A Review of Tissue Substitutes for

Ultrasound Imaging. Ultrasound Med. Biol. 2010; **36**: 861–873.

260. Chen SJS, Hellier P, Marchal M, Gauvrit JY, Carpentier R, Morandi X and Collins DL: An anthropomorphic polyvinyl alcohol brain phantom based on Colin27 for use in multimodal imaging. Med. Phys. 2012; **39**: 554–561.

261. Minton JA, Iravani A and Azizeh-Mitra Yousefi: Improving the homogeneity of tissue-mimicking cryogel phantoms for medical imaging. Med. Phys. 2012; **39**: 6796–6807.

262. Elvira L, Durán C, Higuti RT, Tiago MM, Ibáñez A, Parrilla M, Valverde E, Jiménez J and Bassat Q: Development and Characterization of Medical Phantoms for Ultrasound Imaging Based on Customizable and Mouldable Polyvinyl Alcohol Cryogel-Based Materials and 3-D Printing: Application to High-Frequency Cranial Ultrasonography in Infants. Ultrasound Med. Biol. 2019; **45**: 2226–2241. Available at: http://www.ncbi.nlm.nih.gov/pubmed/31128769.

263. Koch A, Genser M, Stiller F, Lerch R and Ermert H: A new 3D-tomographic ultrasound imaging concept for breast cancer and rheumatoid arthritis diagnostics avoiding water bath techniques. In: 2013 IEEE International Ultrasonics Symposium (IUS). IEEE 2013; pp 655–658. Available at: http://ieeexplore.ieee.org/document/6724891/.

264. Lee W, Lee SD, Park MY, Yang J and Yoo S-S: Evaluation of polyvinyl alcohol cryogel as an acoustic coupling medium for low-intensity transcranial focused ultrasound. Int. J. Imaging Syst. Technol. 2014; **24**: 332–338. Available at: https://onlinelibrary.wiley.com/doi/10.1002/ima.22110.

265. Prokop AF, Vaezy S, Noble ML, Kaczkowski PJ, Martin RW and Crum LA: Polyacrylamide gel as an acoustic coupling medium for focused ultrasound therapy. Ultrasound Med. Biol. 2003; **29**: 1351–1358.

266. Yi J, Nguyen K-CT, Wang W, Yang W, Pan M, Lou E, Major PW, Le LH and Zeng H: Polyacrylamide/Alginate double-network tough hydrogels for intraoral ultrasound imaging. J. Colloid Interface Sci. 2020; **578**: 598–607.

267. Lorenzato C, Cernicanu A, Meyre M-E, Germain M, Pottier A, Levy L, de Senneville BD, Bos C, Moonen C and Smirnov P: MRI contrast variation of thermosensitive magnetoliposomes triggered by focused ultrasound: a tool for image-guided local drug delivery. Contrast Media Mol. Imaging 2013; **8**: 185–192.

268. Choi MJ, Guntur SR, Lee K IL, Paeng DG and Coleman A: An optically transparent tissue mimicking phantom for monitoring the thermal lesion produced by high intensity focused ultrasound. J. Acoust. Soc. Am. 2012; **131**: 3364–3364.

269. Cao R, Huang Z, Varghese T and Nabi G: Tissue mimicking materials for the detection of prostate cancer using shear wave elastography: A validation study. Med. Phys. 2013; **40**: 022903. Available at: http://doi.wiley.com/10.1118/1.4773315, accessed May 17, 2018.

270. Ling T, Jin Q, Yao H and Zheng H: Design and Characterization of a Tissue-Mimicking Phantom for Ultrasonic Elastography. In: 2010 4th International Conference on Bioinformatics and Biomedical Engineering. IEEE 2010; pp 1–4. Available at: http://ieeexplore.ieee.org/document/5515427/.

271. de Carvalho IM, Basto RLQ, Infantosi AFC, von Kruger MA and de A. Pereira WC: Breast ultrasound phantom for image segmentation assessment. In: 2009 IEEE International Ultrasonics Symposium. IEEE 2009; pp 2484–2487. Available at: https://ieeexplore.ieee.org/document/5441417/.

272. Liu D, Jiang P, Wang Y, Lu Y, Wu J, Xu X, Ji Z, Sun C, Wang X and Liu W: Engineering Tridimensional Hydrogel Tissue and Organ Phantoms with Tunable Springiness. Adv.

Funct. Mater. 2023; **33**. Available at: https://onlinelibrary.wiley.com/doi/10.1002/adfm.202214885.

273. Moehring MA and Ritcey JA: Sizing emboli in blood using pulse Doppler ultrasound. I. Verification of the EBR model. IEEE Trans. Biomed. Eng. 1996; **43**: 572–580.

274. Hungr N, Long J, Beix V and Troccaz J: A realistic deformable prostate phantom for multimodal imaging and needle-insertion procedures. Med. Phys. 2012; **39**: 2031–2041. Available at: https://aapm.onlinelibrary.wiley.com/doi/10.1118/1.3692179.

275. Ishizu T, Hamaguchi H, Nitta N, Seo Y, Matsuo H and Shiina T: Intervendor variability of carotid intima–media thickness measurement: validation study using newly developed ultrasound phantom. J. Med. Ultrason. 2020; **47**: 155–165.

276. Cafarelli A, Verbeni A, Poliziani A, Dario P, Menciassi A and Ricotti L: Tuning acoustic and mechanical properties of materials for ultrasound phantoms and smart substrates for cell cultures. Acta Biomater. 2017; **49**: 368–378. Available at: https://www.sciencedirect.com/science/article/pii/S1742706116306468?via%3Dihub, accessed June 17, 2019.

277. Moshayedi P, da F Costa L, Christ A, Lacour SP, Fawcett J, Guck J and Franze K: Mechanosensitivity of astrocytes on optimized polyacrylamide gels analyzed by quantitative morphometry. J. Phys. Condens. Matter 2010; **22**: 194114.

278. Koh E, Freedman BR, Ramazani F, Gross J, Graham A, Kuttler A, Weber E and Mooney DJ: Controlled Delivery of Corticosteroids Using Tunable Tough Adhesives. Adv. Healthc. Mater. 2023; **12**.

279. Hu Y, Weng W, Zhang Y, Zhu Y and Zhang X: Enhanced transscleral delivery using superficial ultrasound exposure and drug-loaded hydrogel. Int. J. Pharm. 2023; **645**:

123359.

280. Sun D, Liu J, Xue L, Li L, Xie D, … Chen C: A solid ultrasonic coupling membrane for superficial vascular ultrasonography. Nanoscale 2022; **14**: 3545–3553.

281. Sun D, Liu J, Xue L, Li L, Xie D, … Chen C: Retraction: A solid ultrasonic coupling membrane for superficial vascular ultrasonography. Nanoscale 2022; **14**: 17803–17803.

282. Narayanan KB, Choi SM and Han SS: Biofabrication of Lysinibacillus sphaericus-reduced graphene oxide in three-dimensional polyacrylamide/carbon nanocomposite hydrogels for skin tissue engineering. Colloids Surfaces B Biointerfaces 2019; **181**: 539–548.

283. Wu DT, Freedman BR, Vining KH, Cuylear DL, Guastaldi FPS, Levin Y and Mooney DJ: Tough Adhesive Hydrogel for Intraoral Adhesion and Drug Delivery. J. Dent. Res. 2023; **102**: 497–504.

284. Morris VB, Nimbalkar S, Younesi M, McClellan P and Akkus O: Mechanical Properties, Cytocompatibility and Manufacturability of Chitosan:PEGDA Hybrid-Gel Scaffolds by Stereolithography. Ann. Biomed. Eng. 2017; **45**: 286–296.

285. Aliabouzar M, Zhang GL and Sarkar K: Acoustic and mechanical characterization of 3D-printed scaffolds for tissue engineering applications. Biomed. Mater. 2018; **13**: 055013.

286. Paulsen SJ, Mitcham TM, Pan CS, Long J, Grigoryan B, Sazer DW, Harlan CJ, Janson KD, Pagel MD, Miller JS and Bouchard RR: Projection-based stereolithography for direct 3D printing of heterogeneous ultrasound phantoms. Edited by W-N Lee. PLoS One 2021; **16**: e0260737. Available at: https://dx.plos.org/10.1371/journal.pone.0260737.

287. Wang P, Berry DB, Song Z, Kiratitanaporn W, Schimelman J, Moran A, He F, Xi B, Cai S and Chen S: 3D Printing of a Biocompatible Double Network Elastomer with Digital

Control of Mechanical Properties. Adv. Funct. Mater. 2020; **30**.

288. Xu J, Cai H, Wu Z, Li X, Tian C, … Guo F: Acoustic metamaterials-driven transdermal drug delivery for rapid and on-demand management of acute disease. Nat. Commun. 2023; **14**: 869.

289. Demitri C, Sannino A, Conversano F, Casciaro S, Distante A and Maffezzoli A: Hydrogel based tissue mimicking phantom for *in-vitro* ultrasound contrast agents studies. J. Biomed. Mater. Res. Part B Appl. Biomater. 2008; **87B**: 338–345.

290. Casciaro S, Conversano F, Musio S, Casciaro E, Demitri C and Sannino A: Full experimental modelling of a liver tissue mimicking phantom for medical ultrasound studies employing different hydrogels. J. Mater. Sci. Mater. Med. 2009; **20**: 983–989. Available at: http://link.springer.com/10.1007/s10856-008-3644-6.

291. Ommen ML, Schou M, Beers C, Jensen JA, Larsen NB and Thomsen EV: 3D printed calibration micro-phantoms for super-resolution ultrasound imaging validation. Ultrasonics 2021; **114**: 106353. Available at: https://linkinghub.elsevier.com/retrieve/pii/S0041624X21000019.

292. Rikli RE and Jones CJ: Functional Fitness Normative Scores for Community-Residing Older Adults, Ages 60-94. J. Aging Phys. Act. 1999; **7**: 162–181. Available at: https://journals.humankinetics.com/view/journals/japa/7/2/article-p162.xml.

293. Coppens AB: Simple equations for the speed of sound in Neptunian waters. J. Acoust. Soc. Am. 1981; **69**: 862–863.

294. Mackenzie K V.: Nine-term equation for sound speed in the oceans. J. Acoust. Soc. Am. 1981; **70**: 807–812.

295. Wong GSK and Zhu S: Speed of sound in seawater as a function of salinity, temperature,

and pressure. J. Acoust. Soc. Am. 1995; **97**: 1732–1736.

296. Leroy CC, Robinson SP and Goldsmith MJ: A new equation for the accurate calculation of sound speed in all oceans. J. Acoust. Soc. Am. 2008; **124**: 2774–2782.

297. Denisin AK and Pruitt BL: Tuning the Range of Polyacrylamide Gel Stiffness for Mechanobiology Applications. ACS Appl. Mater. Interfaces 2016; **8**: 21893–21902. Available at: https://pubs.acs.org/doi/10.1021/acsami.5b09344.

298. Li C, Allen J, Alliston T and Pruitt LA: The use of polyacrylamide gels for mechanical calibration of cartilage — A combined nanoindentation and unconfined compression study. J. Mech. Behav. Biomed. Mater. 2011; **4**: 1540–1547.

299. Engler A, Bacakova L, Newman C, Hategan A, Griffin M and Discher D: Substrate Compliance versus Ligand Density in Cell on Gel Responses. Biophys. J. 2004; **86**: 617–628.

300. Hazeltine LB, Simmons CS, Salick MR, Lian X, Badur MG, Han W, Delgado SM, Wakatsuki T, Crone WC, Pruitt BL and Palecek SP: Effects of Substrate Mechanics on Contractility of Cardiomyocytes Generated from Human Pluripotent Stem Cells. Int. J. Cell Biol. 2012; **2012**: 1–13.

301. Kamanyi AE, Ahmed Mohamed ET, Ngwa W and Grill W: Determination of sound velocity and acoustic impedance of thin chitosan films by phase-sensitive acoustic microscopy. In: Health Monitoring of Structural and Biological Systems 2010. Edited by T Kundu. Vol 7650. SPIE 2010; pp 76502A. Available at: http://proceedings.spiedigitallibrary.org/proceeding.aspx?doi=10.1117/12.847745.

302. Hansen C, Hüttebräuker N, Wilkening W and Ermert H: Three-dimensional Reconstruction of Fine Vascularity in Ultrasound Breast Imaging Using Contrast-

enhanced Spatial Compounding. Acad. Radiol. 2008; **15**: 1155–1164. Available at: https://linkinghub.elsevier.com/retrieve/pii/S1076633208002201.

303. Koch A, Stiller F, Lerch R and Ermert H: 3D-pulse-echo-tomography for breast cancer and rheumatoid arthritis diagnosis — add-on-system and latest in-vivo-results. In: 2016 IEEE International Ultrasonics Symposium (IUS). IEEE 2016; pp 1–4.

304. Liu Z, Maemichi T, Matsumoto M, Okunuki T, Tanaka H, Katsutani H, Li Y and Kumai T: Change in the sub-sesamoid soft tissue thickness under different loading conditions. J. Phys. Ther. Sci. 2023; **35**: 2023–042.

305. Huynh TC and Ledoux WR: Instrumented Footwear to Measure Plantar Tissue Properties. ProQuest Diss. Theses 2020. Available at: https://www.proquest.com/dissertations-theses/instrumented-footwear-measure-plantar-tissue/docview/2456773650/se-2?accountid=14784.

306. Telfer S, Woodburn J and Turner DE: Measurement of functional heel pad behaviour in-shoe during gait using orthotic embedded ultrasonography. Gait Posture 2014; **39**: 328–332. Available at: https://linkinghub.elsevier.com/retrieve/pii/S0966636213004426.

307. Chang R-F, Chen C-J, Takada E, Chou Y-H and Chen D-R: Image stitching for three-pass whole breast ultrasound. In: Medical Imaging 2006: Ultrasonic Imaging and Signal Processing.Vol 6147. SPIE 2006; pp 61470L.

308. Wang C, Yan X, Smith M, Kochhar K, Rubin M, Warren SM, Wrobel J and Lee H: A unified framework for automatic wound segmentation and analysis with deep convolutional neural networks. Annu. Int. Conf. IEEE Eng. Med. Biol. Soc. IEEE Eng. Med. Biol. Soc. Annu. Int. Conf. 2015; **2015**: 2415–2418.

309. Fernando M, Crowther R, Lazzarini P, Sangla K, Cunningham M, Buttner P and Golledge

J: Biomechanical characteristics of peripheral diabetic neuropathy: A systematic review and meta-analysis of findings from the gait cycle, muscle activity and dynamic barefoot plantar pressure. Clin. Biomech. 2013; **28**: 831–845. Available at: https://linkinghub.elsevier.com/retrieve/pii/S0268003313001897.

310. Frykberg RG, Lavery LA, Pham H, Harvey C, Harkless L and Veves A: Role of Neuropathy and High Foot Pressures in Diabetic Foot Ulceration. Diabetes Care 1998; **21**: 1714–1719. Available at: https://diabetesjournals.org/care/article/21/10/1714/21795/Role-of-Neuropathy-and-High-Foot-Pressures-in.

311. Patry J, Belley R, Côté M and Chateau-Degat M-L: Plantar Pressures, Plantar Forces, and Their Influence on the Pathogenesis of Diabetic Foot Ulcers. J. Am. Podiatr. Med. Assoc. 2013; **103**: 322–332. Available at: http://www.japmaonline.org/doi/abs/10.7547/1030322, accessed October 8, 2018.

312. Tang UH, Zügner R, Lisovskaja V, Karlsson J, Hagberg K and Tranberg R: Foot deformities, function in the lower extremities, and plantar pressure in patients with diabetes at high risk to develop foot ulcers. Diabet. Foot Ankle 2015; **6**: 27593. Available at: https://www.tandfonline.com/doi/full/10.3402/dfa.v6.27593.

313. Melai T, IJzerman TH, Schaper NC, de Lange TLH, Willems PJB, Meijer K, Lieverse AG and Savelberg HHCM: Calculation of plantar pressure time integral, an alternative approach. Gait Posture 2011; **34**: 379–383. Available at: https://linkinghub.elsevier.com/retrieve/pii/S0966636211001858.

314. Mueller MJ, Zou D and Lott DJ: “Pressure Gradient” as an Indicator of Plantar Skin Injury. Diabetes Care 2005; **28**: 2908–2912. Available at: https://diabetesjournals.org/care/article/28/12/2908/22775/Pressure-Gradient-as-an-

Indicator-of-Plantar-Skin.

315. Lung C-W, Hsiao-Wecksler ET, Burns S, Lin F and Jan Y-K: Quantifying Dynamic Changes in Plantar Pressure Gradient in Diabetics with Peripheral Neuropathy. Front. Bioeng. Biotechnol. 2016; **4**. Available at: http://journal.frontiersin.org/Article/10.3389/fbioe.2016.00054/abstract.

316. Melai T, IJzerman TH, Schaper NC, de Lange TLH, Willems PJB, Meijer K, Lieverse AG and Savelberg HHCM: Calculation of plantar pressure time integral, an alternative approach. Gait Posture 2011; **34**: 379–383.

317. Otsu N: A Threshold Selection Method from Gray-Level Histograms. IEEE Trans. Syst. Man. Cybern. 1979; **9**: 62–66. Available at: http://ieeexplore.ieee.org/document/4310076/.

318. Zou D, Mueller MJ and Lott DJ: Effect of peak pressure and pressure gradient on subsurface shear stresses in the neuropathic foot. J. Biomech. 2007; **40**: 883–890.

319. Lung C-W, Mo P-C, Cao C, Zhang K, Wu F-L, Liau B-Y and Jan Y-K: Effects of walking speeds and durations on the plantar pressure gradient and pressure gradient angle. BMC Musculoskelet. Disord. 2022; **23**: 823. Available at: https://bmcmusculoskeletdisord.biomedcentral.com/articles/10.1186/s12891-022-05771-2.

320. Ledoux WR, Shofer JB, Cowley MS, Ahroni JH, Cohen V and Boyko EJ: Diabetic foot ulcer incidence in relation to plantar pressure magnitude and measurement location. J. Diabetes Complications 2013; **27**: 621—626. Available at: https://europepmc.org/articles/PMC4227535.

321. Crawford F, Cezard G and Chappell FM: The development and validation of a multivariable prognostic model to predict foot ulceration in diabetes using a systematic review and individual patient data meta-analyses. Diabet. Med. 2018; **35**: 1480–1493.

Available at: https://onlinelibrary.wiley.com/doi/10.1111/dme.13797.

322. Brady LM, Rombokas E, Wang Y-N, Shofer JB and Ledoux WR: The effect of diabetes and tissue depth on adipose chamber size and plantar soft tissue features. Foot 2023; **56**: 101989.

323. Treece GM, Gee AH, Prager RW, Cash CJC and Berman LH: High-definition freehand 3-D ultrasound. Ultrasound Med. Biol. 2003; **29**: 529–546. Available at: https://linkinghub.elsevier.com/retrieve/pii/S0301562902007354.

324. Weide G, Van Der Zwaard S, Huijing PA, Jaspers RT and Harlaar J: 3D ultrasound imaging: Fast and cost-effective morphometry of musculoskeletal tissue. J. Vis. Exp. 2017; **2017**.

325. Cash CJC, Treece GM, Berman LH, Gee AH and Prager RW: 3D reconstruction of the skeletal anatomy of the normal neonatal foot using 3D ultrasound. Br. J. Radiol. 2005; **78**: 587–595. Available at: http://dx.doi.org/10.1259/bjr/29830482.

326. Behforootan S, Chatzistergos PE, Chockalingam N and Naemi R: A clinically applicable non-invasive method to quantitatively assess the visco-hyperelastic properties of human heel pad, implications for assessing the risk of mechanical trauma. J. Mech. Behav. Biomed. Mater. 2017; **68**: 287–295. Available at: https://www.sciencedirect.com/science/article/pii/S175161611730067X?via%3Dihub, accessed May 21, 2018.

327. Naemi R, Chatzistergos P, Sundar L, Chockalingam N and Ramachandran A: Differences in the mechanical characteristics of plantar soft tissue between ulcerated and non-ulcerated foot. J. Diabetes Complications 2016; **30**: 1293–1299. Available at: https://www.sciencedirect.com/science/article/pii/S1056872716301830, accessed October

8, 2018.

328. Chen WM, Lee PVS, Lee SJ and Lee T: Investigation of plantar barefoot pressure and soft-tissue internal stress: A three-dimensional finite element analysis. IFMBE Proc. 2009; **23**: 1817–1820.

329. Chen W-M, Lee S-J and Lee PVS: Plantar pressure relief under the metatarsal heads – Therapeutic insole design using three-dimensional finite element model of the foot. J. Biomech. 2015; **48**: 659–665. Available at: https://www.sciencedirect.com/science/article/pii/S002192901400709X, accessed October 8, 2018.

330. Taş S, Onur MR, Yılmaz S, Soylu AR and Korkusuz F: Shear Wave Elastography Is a Reliable and Repeatable Method for Measuring the Elastic Modulus of the Rectus Femoris Muscle and Patellar Tendon. J. Ultrasound Med. 2017; **36**: 565–570. Available at: http://doi.wiley.com/10.7863/ultra.16.03032, accessed December 18, 2018.

331. MCINTOSH RL and ANDERSON V: A COMPREHENSIVE TISSUE PROPERTIES DATABASE PROVIDED FOR THE THERMAL ASSESSMENT OF A HUMAN AT REST. Biophys. Rev. Lett. 2010; **05**: 129–151. Available at: https://www.worldscientific.com/doi/abs/10.1142/S1793048010001184.

332. Duck FA: Mechanical Properties of Tissue. In: Physical Properties of Tissues. Elsevier 1990; pp 137–165. Available at: https://linkinghub.elsevier.com/retrieve/pii/B9780122228001500097.

333. Ledoux WR: Plantar Soft Tissue. In: Foot and Ankle Biomechanics. Elsevier 2023; pp 135–147.

334. Stess RM, Jensen SR and Mirmiran R: The role of dynamic plantar pressures in diabetic

foot ulcers. Diabetes Care 1997; **20**: 855–8. Available at: http://www.ncbi.nlm.nih.gov/pubmed/9135955.

335. Fernando ME, Crowther RG, Lazzarini PA, Yogakanthi S, Sangla KS, Buttner P, Jones R and Golledge J: Plantar pressures are elevated in people with longstanding diabetes-related foot ulcers during follow-up. Edited by Y-K Jan. PLoS One 2017; **12**: e0181916. Available at: https://dx.plos.org/10.1371/journal.pone.0181916.

336. Falzon B, Formosa C, Camilleri L and Gatt A: Duration of Type 2 Diabetes is a Predictor of Elevated Plantar Foot Pressure. Rev. Diabet. Stud. 2017; **14**: 372–380. Available at: http://www.soc-bdr.org/content/e4/e887/volRdsVolumes19576/issRdsIssues20715/chpRdsChapters20727/strRdsArticles20753/?preview=preview.

337. Fawzy OA, Arafa AI, Wakeel MA El and Kareem SHA: Plantar Pressure as a Risk Assessment Tool for Diabetic Foot Ulceration in Egyptian Patients with Diabetes. Clin. Med. Insights Endocrinol. Diabetes 2014; **7**: CMED.S17088. Available at: http://journals.sagepub.com/doi/10.4137/CMED.S17088.

338. Mueller MJ, Zou D, Bohnert KL, Tuttle LJ and Sinacore DR: Plantar Stresses on the Neuropathic Foot During Barefoot Walking. Phys. Ther. 2008; **88**: 1375–1384. Available at: https://academic.oup.com/ptj/article/88/11/1375/2858158.

339. Caselli A, Pham H, Giurini JM, Armstrong DG and Veves A: The Forefoot-to-Rearfoot Plantar Pressure Ratio Is Increased in Severe Diabetic Neuropathy and Can Predict Foot Ulceration. Diabetes Care 2002; **25**: 1066–1071. Available at: https://diabetesjournals.org/care/article/25/6/1066/21266/The-Forefoot-to-Rearfoot-Plantar-Pressure-Ratio-Is.

340. Fang F, Wang Y-F, Gu M-Y, Chen H, Wang D-M, Xiao K, Yan S, Yao L-L, Li N, Zhen Q and Peng Y-D: Pedobarography - a novel screening tool for diabetic peripheral neuropathy? Eur. Rev. Med. Pharmacol. Sci. 2013; **17**: 3206–12. Available at: http://www.ncbi.nlm.nih.gov/pubmed/24338463.

341. Sinacore DR, Bohnert KL, Hastings MK and Johnson JE: Mid foot kinetics characterize structural polymorphism in diabetic foot disease. Clin. Biomech. 2008; **23**: 653–661. Available at: https://linkinghub.elsevier.com/retrieve/pii/S0268003307000915.

342. Bus SA, Maas M, de Lange A, Michels RPJ and Levi M: Elevated plantar pressures in neuropathic diabetic patients with claw/hammer toe deformity. J. Biomech. 2005; **38**: 1918–1925. Available at: https://linkinghub.elsevier.com/retrieve/pii/S0021929004004026.

343. Waldecker U: Pedographic classification and ulcer detection in the diabetic foot. Foot Ankle Surg. 2012; **18**: 42–49. Available at: http://dx.doi.org/10.1016/j.fas.2011.03.004.

344. Sinacore DR, Bohnert KL, Hastings MK and Johnson JE: Mid foot kinetics characterize structural polymorphism in diabetic foot disease. Clin. Biomech. 2008; **23**: 653–661.

345. Alviti F, D'Ercole C, Schillizzi G, Mangone M, Bernetti A, … Cantisani V: Elastosonographic evaluation after extracorporeal shockwave treatment in plantar fasciopathy. Med. Ultrason. 2019; **21**: 399. Available at: https://medultrason.ro/medultrason/index.php/medultrason/article/view/1976.

346. Beydoğan E and Yalçın A: Is 2D SWE sufficient as clinical diagnosis in patients with plantar fasciitis? Acta radiol. 2023; **64**: 147–152. Available at: http://journals.sagepub.com/doi/10.1177/02841851211058928.

347. Gatz M, Bejder L, Quack V, Schrading S, Dirrichs T, Tingart M, Kuhl C and Betsch M:

Shear Wave Elastography (SWE) for the Evaluation of Patients with Plantar Fasciitis. Acad. Radiol. 2020; **27**: 363–370. Available at: https://linkinghub.elsevier.com/retrieve/pii/S1076633219302260.

348. Schillizzi G, Alviti F, D'Ercole C, Elia D, Agostini F, … Cantisani V: Evaluation of plantar fasciopathy shear wave elastography: a comparison between patients and healthy subjects. J. Ultrasound 2021; **24**: 417–422. Available at: https://link.springer.com/10.1007/s40477-020-00474-7.

349. Baur D, Schwabl C, Kremser C, Taljanovic MS, Widmann G, Sconfienza LM, Sztankay J, Feuchtner G and Klauser AS: Shear Wave Elastography of the Plantar Fascia: Comparison between Patients with Plantar Fasciitis and Healthy Control Subjects. J. Clin. Med. 2021; **10**: 2351. Available at: https://www.mdpi.com/2077-0383/10/11/2351.

350. Chino K, Lacourpaille L, Sasahara J, Suzuki Y and Hug F: Effect of toe dorsiflexion on the regional distribution of plantar fascia shear wave velocity. Clin. Biomech. 2019; **61**: 11–15. Available at: https://linkinghub.elsevier.com/retrieve/pii/S0268003318306338.

351. Jiang Z-Z, Shen H-L, Zhang Q, Ye G, Li X-C and Liu X-T: Elasticity evaluation of the plantar fascia: A shear wave elastography study involving 33 early-stage plantar fasciopathy subjects. Front. Physiol. 2022; **13**. Available at: https://www.frontiersin.org/articles/10.3389/fphys.2022.1060728/full.

352. Chen TL-W, Agresta CE, Lipps DB, Provenzano SG, Hafer JF, Wong DW-C, Zhang M and Zernicke RF: Ultrasound elastographic assessment of plantar fascia in runners using rearfoot strike and forefoot strike. J. Biomech. 2019; **89**: 65–71. Available at: https://linkinghub.elsevier.com/retrieve/pii/S0021929019302775.

353. Yang Y, Qiu L, Wang L, Xiang X, Tang Y, Li H and Yan F: Quantitative Assessment of

Skin Stiffness Using Ultrasound Shear Wave Elastography in Systemic Sclerosis. Ultrasound Med. Biol. 2019; **45**: 902–912. Available at: https://linkinghub.elsevier.com/retrieve/pii/S0301562918305271.

354. Yang Y, Wang L, Yan F, Xiang X, Tang Y, Zhang L, Liu J and Qiu L: Determination of Normal Skin Elasticity by Using Real-time Shear Wave Elastography. J. Ultrasound Med. 2018; **37**: 2507–2516. Available at: https://onlinelibrary.wiley.com/doi/10.1002/jum.14608.

355. Xiang X, Yan F, Yang Y, Tang Y, Wang L, Zeng J and Qiu L: Quantitative Assessment of Healthy Skin Elasticity: Reliability and Feasibility of Shear Wave Elastography. Ultrasound Med. Biol. 2017; **43**: 445–452. Available at: https://linkinghub.elsevier.com/retrieve/pii/S030156291630326X.

356. Sobolewski P, Maślińska M, Zakrzewski J, Paluch Ł, Szymańska E and Walecka I: Applicability of shear wave elastography for the evaluation of skin strain in systemic sclerosis. Rheumatol. Int. 2020; **40**: 737–745. Available at: http://link.springer.com/10.1007/s00296-020-04539-y.

357. Zheng YP, Chen JG and Ling HY: DEVELOPMENT OF AN ULTRASOUND PLATFORM FOR THE EVALUATION OF PLANTAR SOFT TISSUE PROPERTIES: A FEASIBILITY STUDY ON SILICONE PHANTOM FEET. Instrum. Sci. Technol. 2011; **39**: 248–260. Available at: http://www.tandfonline.com/doi/abs/10.1080/10739149.2011.564703, accessed October 8, 2018.

358. Lei B, Huang S, Li H, Li R, Bian C, Chou Y-H, Qin J, Zhou P, Gong X and Cheng J-Z: Self-co-attention neural network for anatomy segmentation in whole breast ultrasound.

Med. Image Anal. 2020; **64**: 101753. Available at: https://www.sciencedirect.com/science/article/pii/S1361841520301171.

359. Lei B, Huang S, Li R, Bian C, Li H, Chou Y-H and Cheng J-Z: Segmentation of breast anatomy for automated whole breast ultrasound images with boundary regularized convolutional encoder–decoder network. Neurocomputing 2018; **321**: 178–186. Available at: https://www.sciencedirect.com/science/article/pii/S092523121831107X, accessed January 8, 2019.

360. Li H, Cheng J-Z, Chou Y-H, Qin J, Huang S and Lei B: AttentionNet: Learning Where to Focus via Attention Mechanism for Anatomical Segmentation of Whole Breast Ultrasound Images. In: 2019 IEEE 16th International Symposium on Biomedical Imaging (ISBI 2019). IEEE 2019; pp 1078–1081. Available at: https://ieeexplore.ieee.org/document/8759241/.

361. Wang F, Liu X, Qian B, Ruan L, Zhao R, Yin C, Yuan N, Wei R, Ma X and Wei J: Spatial Attention Lesion Detection on Automated Breast Ultrasound BT - Bioinformatics and Biomedical Engineering. In: Edited by I Rojas, O Valenzuela, F Rojas and F Ortuño. Cham: Springer International Publishing 2019; pp 216–227.

362. Abe T, Tayashiki K, Nakatani M and Watanabe H: Relationships of ultrasound measures of intrinsic foot muscle cross-sectional area and muscle volume with maximum toe flexor muscle strength and physical performance in young adults. J. Phys. Ther. Sci. 2016; **28**: 14–19.

363. Chang R, Kent-Braun JA and Hamill J: Use of MRI for volume estimation of tibialis posterior and plantar intrinsic foot muscles in healthy and chronic plantar fasciitis limbs. Clin. Biomech. 2012; **27**: 500–505.

364. Kimura T, Thorhauer ED, Kindig MW, Shofer JB, Sangeorzan BJ and Ledoux WR: Neuropathy, claw toes, intrinsic muscle volume, and plantar aponeurosis thickness in diabetic feet. BMC Musculoskelet. Disord. 2020; **21**: 485. Available at: http://europepmc.org/abstract/MED/32703177.

365. Kura H, Luo Z-P, Kitaoka HB and An K-N: Quantitative analysis of the intrinsic muscles of the foot. Anat. Rec. 1997; **249**: 143–151.

366. Kusagawa Y, Kurihara T, Maeo S, Sugiyama T, Kanehisa H and Isaka T: Associations of muscle volume of individual human plantar intrinsic foot muscles with morphological profiles of the foot. J. Anat. 2022; **241**: 1336–1343. Available at: https://onlinelibrary.wiley.com/doi/10.1111/joa.13753.

367. Kura H, Luo Z-P, Kitaoka HB and An K-N: Quantitative analysis of the intrinsic muscles of the foot. Anat. Rec. 1997; **249**: 143–151. Available at: https://onlinelibrary.wiley.com/doi/10.1002/(SICI)1097-0185(199709)249:1%3C143::AID-AR17%3E3.0.CO;2-P.

368. Abe T, Tayashiki K, Nakatani M and Watanabe H: Relationships of ultrasound measures of intrinsic foot muscle cross-sectional area and muscle volume with maximum toe flexor muscle strength and physical performance in young adults. J. Phys. Ther. Sci. 2016; **28**: 14–19. Available at: https://www.jstage.jst.go.jp/article/jpts/28/1/28_jpts-2015-655/_article.

369. Chang R, Kent-Braun JA and Hamill J: Use of MRI for volume estimation of tibialis posterior and plantar intrinsic foot muscles in healthy and chronic plantar fasciitis limbs. Clin. Biomech. 2012; **27**: 500–505. Available at: https://linkinghub.elsevier.com/retrieve/pii/S0268003311002956.

370. Ling H, Choi P, Zheng Y and Lau K: Extraction of mechanical properties of foot plantar tissues using ultrasound indentation associated with genetic algorithm. J. Mater. Sci. Mater. Med. 2007; **18**: 1579–1586. Available at: http://link.springer.com/10.1007/s10856-007-3025-6.

371. Teoh JC, Shim VPW and Lee T: Quantification of plantar soft tissue changes due to aging in various metatarsophalangeal joint angles with realistic tissue deformation. J. Biomech. 2014; **47**: 3043–3049. Available at: http://linkinghub.elsevier.com/retrieve/pii/S0021929014003728, accessed March 9, 2017.

372. Klaesner JW, Hastings MK, Zou D, Lewis C and Mueller MJ: Plantar tissue stiffness in patients with diabetes mellitus and peripheral neuropathy. Arch. Phys. Med. Rehabil. 2002; **83**: 1796–1801. Available at: https://linkinghub.elsevier.com/retrieve/pii/S0003999302006068.

373. Chao CYL, Zheng Y-P, Huang Y-P and Cheing GLY: Biomechanical properties of the forefoot plantar soft tissue as measured by an optical coherence tomography-based air-jet indentation system and tissue ultrasound palpation system. Clin. Biomech. 2010; **25**: 594–600. Available at: https://linkinghub.elsevier.com/retrieve/pii/S0268003310000938.

374. Hudak YF, Li J-S, Cullum S, Strzelecki BM, Richburg C, … Aubin PM: A novel workflow to fabricate a patient-specific 3D printed accommodative foot orthosis with personalized latticed metamaterial. Med. Eng. Phys. 2022; **104**: 103802. Available at: https://linkinghub.elsevier.com/retrieve/pii/S1350453322000510.

375. Song Y, Treanor D, Bulpitt AJ and Magee DR: 3D reconstruction of multiple stained histology images. J. Pathol. Inform. 2013; **4**: 7. Available at: https://linkinghub.elsevier.com/retrieve/pii/S2153353922006678.

376. Pichat J, Iglesias JE, Yousry T, Ourselin S and Modat M: A Survey of Methods for 3D Histology Reconstruction. Med. Image Anal. 2018; **46**: 73–105. Available at: https://linkinghub.elsevier.com/retrieve/pii/S1361841518300264.

377. Rivenson Y, Liu T, Wei Z, Zhang Y and Ozcan A: PhaseStain: Digital staining of label-free quantitative phase microscopy images using deep learning. 2018. Available at: http://arxiv.org/abs/1807.07701, accessed January 8, 2019.

378. Rivenson Y, de Haan K, Wallace WD and Ozcan A: Emerging Advances to Transform Histopathology Using Virtual Staining. BME Front. 2020; **2020**. Available at: https://spj.science.org/doi/10.34133/2020/9647163.

379. Rivenson Y, Wang H, Wei Z, de Haan K, Zhang Y, … Ozcan A: Virtual histological staining of unlabelled tissue-autofluorescence images via deep learning. Nat. Biomed. Eng. 2019; **3**: 466–477. Available at: https://www.nature.com/articles/s41551-019-0362-y.

380. Gupta L, Klinkhammer BM, Boor P, Merhof D and Gadermayr M: Stain independent segmentation of whole slide images: A case study in renal histology. In: 2018 IEEE 15th International Symposium on Biomedical Imaging (ISBI 2018). IEEE 2018; pp 1360–1364. Available at: https://ieeexplore.ieee.org/document/8363824/, accessed January 8, 2019.

381. Gadermayr M, Gupta L, Appel V, Boor P, Klinkhammer BM and Merhof D: Generative Adversarial Networks for Facilitating Stain-Independent Supervised and Unsupervised Segmentation: A Study on Kidney Histology. IEEE Trans. Med. Imaging 2019; **38**: 2293–2302.

382. Jurca A, Žabkar J and Džeroski S: Analysis of 1.2 million foot scans from North America, Europe and Asia. Sci. Rep. 2019; **9**.

383. Xu X, Lu Q, Yang L, Hu S, Chen D, Hu Y and Shi Y: Quantization of Fully

Convolutional Networks for Accurate Biomedical Image Segmentation. Available at: http://openaccess.thecvf.com/content_cvpr_2018/CameraReady/1173.pdf, accessed January 8, 2019.

384. Yin S, Peng Q, Li H, Zhang Z, You X, Furth SL, Tasian GE and Fan Y: Subsequent Boundary Distance Regression and Pixelwise Classification Networks for Automatic Kidney Segmentation in Ultrasound Images. 2018. Available at: http://arxiv.org/abs/1811.04815, accessed January 8, 2019.

385. Wang Y, Ni D, Dou H, Hu X, Zhu L, Yang X, Xu M, Qin J, Heng P-A and Wang T: Deep Attentive Features for Prostate Segmentation in 3D Transrectal Ultrasound. IEEE Trans. Med. Imaging 2019; **38**: 2768–2778. Available at: https://ieeexplore.ieee.org/document/8698868/.

386. Chen E, Mathai TS, Sarode V, Choset H and Galeotti J: A study of domain generalization on ultrasound-based multi-class segmentation of arteries, veins, ligaments, and nerves using transfer learning. arXiv 2020: 1–9.

387. Solberg OV, Lindseth F, Torp H, Blake RE and Nagelhus Hernes TA: Freehand 3D Ultrasound Reconstruction Algorithms-A Review. Ultrasound Med. Biol. 2007; **33**: 991–1009.

388. Freesmeyer M, Knichel L, Kühnel C and Winkens T: Stitching of sensor-navigated 3D ultrasound datasets for the determination of large thyroid volumes - a phantom study. Med. Ultrason. 2018; **20**: 480–486.

389. Harris A, Kishimoto J, Fenster A, de Ribaupierre S and Gardi L: Automated registration and stitching of multiple 3D ultrasound images for monitoring neonatal intraventricular hemorrhage. In: SPIE-Intl Soc Optical Eng 2018; pp 42.

390. Sun H, Yang J, Fan R, Xie K, Wang C and Ni X: Stepwise local stitching ultrasound image algorithms based on adaptive iterative threshold Harris corner features. Medicine (Baltimore). 2020; **99**: e22189.

391. Fan Z, Wang Z, Xin J, Wang Z, Liu L, Zhang X and Liu J: Dual-Enhanced Registration for Field of View Ultrasound Sonography. IEEE Access 2020; **8**: 128602–128612.

392. Cheung W, Stevenson GN, de Melo Tavares Ferreira AEG, Alphonse J and Welsh AW: Feasibility of image registration and fusion for evaluation of structure and perfusion of the entire second trimester placenta by three-dimensional power Doppler ultrasound. Placenta 2020; **94**: 13–19. Available at: https://www.sciencedirect.com/science/article/pii/S0143400420300850.

A Appendix A: Development of tissue-mimicking phantoms, evaluation of shear wave elastography at high strain, and comparison to mechanical testing

This work was performed in collaboration with Austin Ellis, a UWSOM student as part of the independent investigative inquiry program. A portion of A.2 was accepted to the Orthopaedic Research Society annual meeting, and A.2 and portions of A.1 are in preparation for submission to the journal *Physics in Medicine and Biology.*

A.1 Development of the phantoms

A.1.1 Introduction

Medical imaging phantoms are used to test medical imaging methods without risk to human subjects or patients. Phantoms can be used to test new protocols or for quality assurance to ensure that equipment is functioning as intended and expected. Phantoms should closely match the relevant physical properties of the biological tissue of interest. Gelatin is a common material in ultrasound phantoms, and prior work has detailed many ways to modulate its color, speed of sound, mechanical properties, backscatter, and attenuation to more closely match biological tissues. One property of particular importance for testing shear wave elastography (SWE) protocols is the speckle pattern texture as the speckles are used to track the propagation of the shear wave. Two common additives to create a textured speckle pattern include graphite and glass microspheres. However, these materials are not always easy or cost effective to obtain. The purpose of this work is to assess the effectiveness of commonly available items for use as speckle additives in gelatin ultrasound phantoms used for comparing SWE values to those obtained using mechanical testing. One challenge associated with creating gelatin phantoms capable of both SWE and mechanical testing is the requirement for the mechanical test specimen to be regularly shaped and flat on both the top and bottom to prevent irregular loading and slipping from between the clamps during dynamic loading. In order to accomplish several hundred regular specimens meeting these requirements, they were molded. However, this molding and demolding process required that the test specimens not be flipped, severely shaken, or otherwise disturbed during curing so as to preserve the smooth and flat quasi-frictionless compression platen contact surfaces.

A.1.2 Materials

A.1.2.1 Craft materials

Glitter is typically made from layered plastic polymers and reflective material such as aluminum. Some less reflective glitters may also be made from plastic polymers alone. Many plastic polymers have acoustic properties that are much closer to those of soft tissue than most metals. Glitter is often sold by size, making it easy to identify the average diameter of glitter particles. However, glitter often is not spherical, potentially disrupting its usefulness as a scattering material.

A.1.2.2 Kitchen materials

Some prior work has used cellulose as a scattering material (Franceschini 2010). Cellulose is the primary saccharide in the cell wall of most plants, making it a significant component of plant-derived spices. Spices are typically ground into relatively fine powders, which could be used as scattering materials. However, the resulting particles are not regulated by size.

A.1.2.3 Hobby materials

Aluminum oxide (Al2O3) and silicon carbide (SiC) are commonly used at various grit levels for polishing rocks. Grit levels generally correspond to specific particle diameters, making them easier to match to prior work using regulated particle sizes. (Graham) (Table A.1).

Table A.1-1 Example of conversion between grit and microns, reproduced from Graham (3).

Grit	µm
100,00	0.25
14,000	1
8000	3
3000	6.8
600	30
225	90

A.1.2.4 Scientific materials

Prior work has used graphite as a scattering material (Anderson 2011). Scientific quality graphite of <20um was purchased from Sigma Aldrich (St. Louis, MO, USA). The <20um was chosen based on the work of Dunmire using aluminum oxide as well as Anderson 2011 using graphite. Anderson et. al measure changes in acoustic properties with addition of graphite in a dose-response fashion. They found that addition of graphite increased shear wave speed as well as attenuation, but did not affect longitudinal sound speed. Graphite was purchased in the form of graphite lubricant used for locks.

A.1.2.5 Filters

Some materials are tightly controlled with a reliable particle size, while others can have large variability in the particle size represented in a given volume of material. One hypothesis was that large particles, having more mass, might sink to the bottom of the phantom, causing the increased settling, and therefore, filtering out the larger particles and using only the smaller particles may achieve the even distribution of scattering particles desired. IN an effort to control particle sizes of les regulated materials like spices, filter paper was acquired in 5-10µm, 10-15µm and 20-25µm pore diameters.

A.1.2.6 pH

Gelatin can solidify either by hydrogen bonding, a weaker bond formed by attraction between unevenly charged bonded atoms on of molecules, or by crosslinking covalent bonds, which are stronger bonds formed when molecules share electrons. The pH of the gelatin solution, a measure of the number of free electrons available in a solution, can affect the charge distribution and density of solidified gelatin. Higher pH may lead to more covalent crosslinking bonds, creating a stronger gelatin (Farris 2010). Additional studies have also correlated higher pH with higher melting temperature, further supporting the theory of increased crosslinking compared to hydrogen bond gelation. (Osorio 2007). Due to the potential effect of pH and water contaminants on gelatin bond formation, the pH of water used was measured, and gelatin phantoms were made from both tap and distilled water.

A.1.2.7 Pouring temperature

There are various methods reported in the literature for manufacturing gelatin phantoms, which include various temperatures at which the gelatin is poured into a mold and allowed to set. Some prior work has poured and degassed gelatin mixtures at high temperatures. Some prior work uses continuous mixing methods to maintain even particulate distribution throughout molten mixtures during cooling. Due to the need for plat molded surfaces, stirring was not an option, so lower pouring temperatures were investigated so that the gelatin mixture would be more viscous and set more quickly, leaving less time for scatterers to settle out of solution.

A.1.3 Methods

Phantoms were manufactured from 10% w/w gelatin, as scatterer settling was observed to increase with lower gelatin concentration. 580 mg gelatin was mixed with 5mL water until thoroughly saturated and then heated to 90C. The mixture was allowed to clarify and then the heat was reduced to 45^{o}C. At this temperature, scattering components were added and vigorously mixed before pouring into 1” diameter x 0.5” tall molds. Phantoms were allowed to cure at room temperature overnight.

In order to test the hypothesis that shorter cooling time would alleviate scatterer settling, a second set of phantoms were mixed and poured into molds at temperatures: 38, 33, and 29 deg. C. This second set of phantoms used a subset of scattering materials chosen from the initial round of testing.

A.1.3.1 Microscopy

In order to investigate the hypothesis that larger particles settled to the bottom of the phantoms and to identify the ideal particle size for the scatterers, phantoms were thinly sliced with a razor blade at the center of the sample and placed on a glass slide. The phantoms were then imaged at 10x magnification on a Nikon Eclipse i80 and images were captured using an attached digital camera in the Nikon NIS elements software. Images were acquired across the height of the sample, and a random sample of particles within the field of view were manually measured using the measurement tools in the NIS-Elements software.

A.1.3.2 Mechanical testing

In order to assess this, whether addition of scattering materials substantially affect the mechanics of the phantoms, samples were mechanically tested according to the intended protocol and compared to gelatin samples with no inclusions.

A.1.3.3 Ultrasound

In order to assess the visibility of the phantoms on ultrasound as well as the ability to measure shear wave elastography, phantoms were scanned in SWE mode using an Aixplorer and an SL18-5 probe. Phantoms were imaged in resolution mode with standard SWE optimization using the foot & ankle preset. The focus was set at the middle of the phantom, the sound speed was set to 1540m/s, the dynamic range was set to 62db and the gain was adjusted for each image. The quality and consistency of SWE signal was assessed as well as the clarity of the phantom texture and the attenuation through the sample.

A.1.4 Results

A.1.4.1 Scatterer size and distribution

Representative images from each of 4 scattering materials can be seen in Figure A.1.1.

Over the depth of the Al2O3 phantom, the suspended particles increased from 5um on average at the top to 10 um on average in the middle of the sample to around 20 um on average at the bottom of the sample. These phantoms also had a gradient of particles that caused a visible color gradient throughout the sample. Particles were irregularly shaped, but discrete, distinct, and rock-like in appearance.

Over the depth of the embossing powder phantom, particles were apparent at the top and bottoms surfaces, and though dense and occluding, making them difficult to measure, the average size of these particles was between 80 and 200 um. Very few particles were present at the midsection of the phantom, however, in this middle section heterogeneous orange-red sections, that had a smeared fluid like appearance were abundant. On the macroscale, again, a gradient of particles through the sample was apparent, however, the larger particles gathered at both the top and the bottom of the sample while few particles were suspended in the middle.

Over the depth of the Silicon carbide phantom, particles ranged somewhat in size, with the average particle size being around5 um at the top of the phantom, giving way to an average particle size around 15 um through the middle and bottom of the phantom. Particles were irregularly shaped and rock-like in appearance but were discrete and distinct.

The paprika phantom contained particles of widely varying sizes, from around 15 um to over 200 um. Particles were few in number, widely spaced, and irregularly shaped, with many particles having long cylindrical shapes while others were more circular. In addition to these particles, highly regular, circular blobs with the appearance of oil immersion were also present. These blobs had a typical size of around 10-20 um.

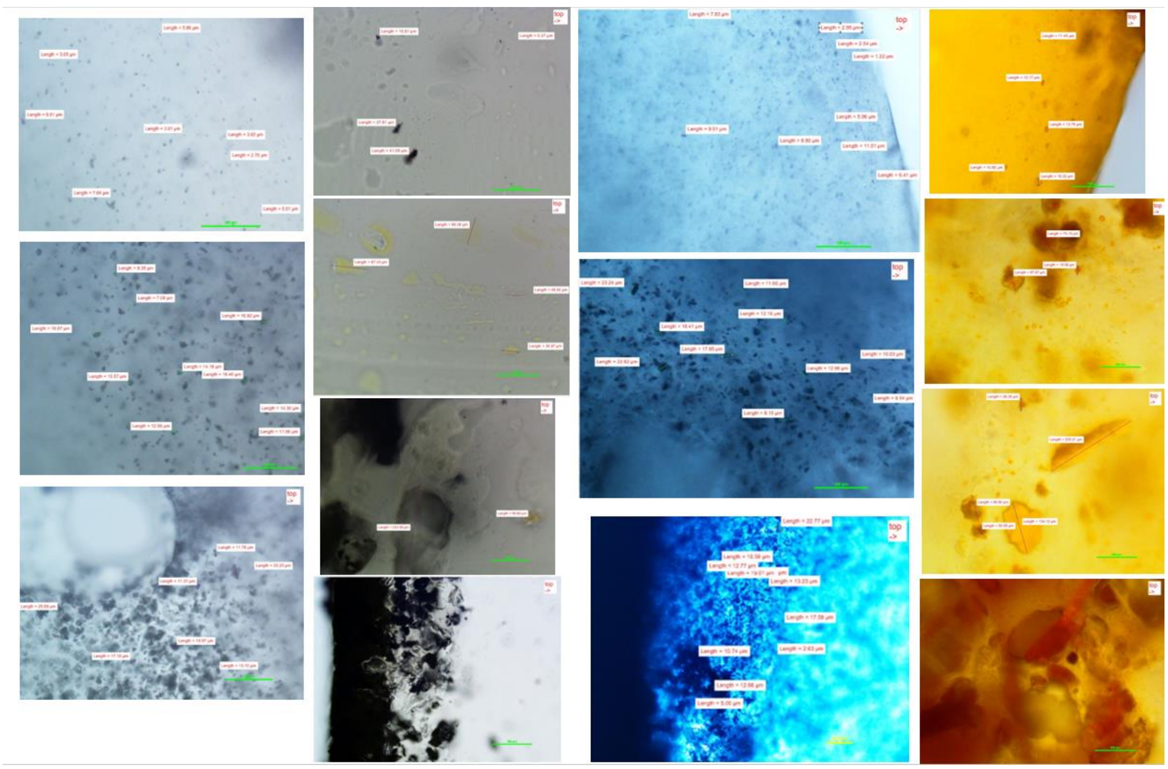

Figure A-1 Microscopy of phantom slice from the top of the sample (exposed to air) to the bottom of the sample (touching the inferior surface of the mold). From left to right: Al2O3, Embossing powder, Silicon Carbide, Paprika.

A.1.4.2 Mechanical properties

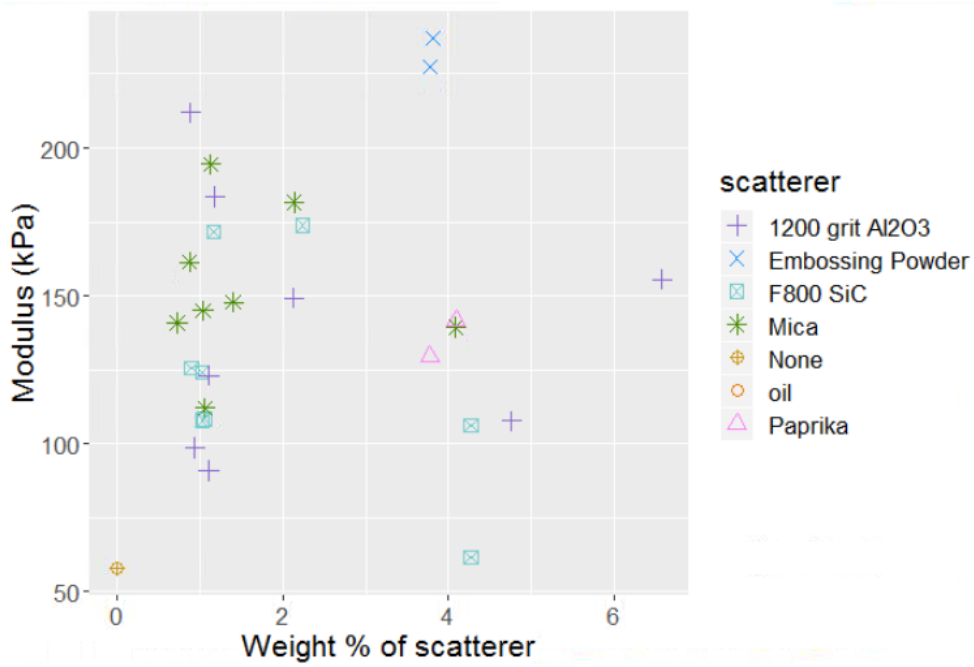

Figure A-2. Effect of scatterers on modulus measured using compression testing.

The final modulus for the tested samples can be seen in Figure A.1.2. All scatterers increased the modulus of the tested phantoms. However, the increase in modulus appeared to be more related to the specific material added rather than total the volume or mass of scatterers added. Silicon carbide, Mica, and aluminum oxide, all inert powdered particles, all behaved similarly, increasing the measured modulus by 30-130kPa but showing no differences with higher concentrations of scattering materials. Embossing powder had a more noticeable effect, increasing the measured modulus by 200 kPa.

In order to confirm that changes to gelatin or agar concentration were not confounding the scatterer observations, agar, gelatin, and scatterer concentrations were plotted with each other and/or

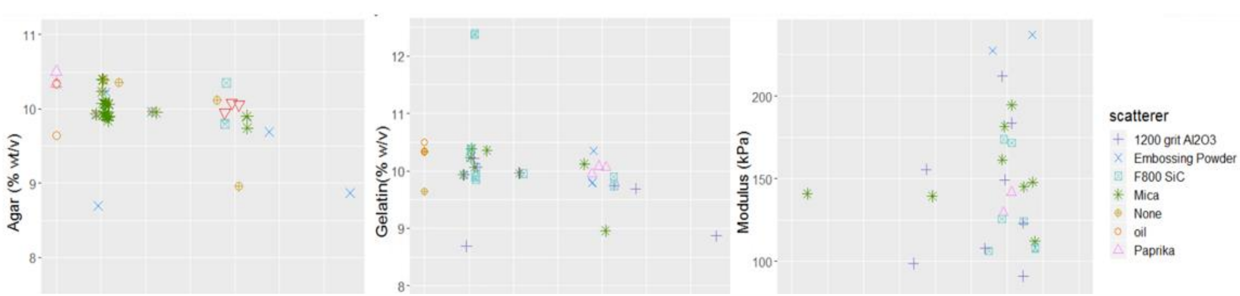

Figure A-3 Relationship between agar and gelatin, gelatin and scatterers, and gelatin and modulus.

modulus values (Figure A-3). Agar concentrations (Figure A-3.a) are clustered fairly closely for all samples except one mica sample, which also has a low gelatin concentration and a low scatterer concentration (Figure A-3.b). However, the corresponding modulus for the sample with that gelatin concentration is similar to three other samples with mica scatterers which have varying scatterer, agar, and gelatin concentrations. These results lend relative confidence to the effect of scattering materials increasing the measured modulus of the materials. This effect is expected to be more severe the farther the scattering material modulus is from the expected gelatin modulus. Moduli for scattering materials can be found in Table A.1.2. While data for paprika specifically could not be found, cellulose is one of the main components of plant matter and was used as an estimate of the dried paprika modulus. Similarly, young's modulus is not readily available for embossing powder. However, embossing powders are made of thermoplastic polyamide resins. While polyamides are a family of polymers with a wide range of mechanical properties, nylon was chosen as a stand-in for this calculation.

Table A.1-2 Young's modulus values for scatterer materials

Material	Young's modulus
Silicon Carbide	450 GPa
Aluminum Oxide	350 GPa
Mica	0.2 – 18 GPa
Cellulose	130 GPa
Nylon (a polyamide)	2.7 GPa

A.1.4.3 Ultrasound

All tested scatterers improved the SWE signal relative to no added scatterers. However, the embossing powder and paprika did not improve SWE signal as much as the other tested scatterers (Figure A-4). In the ultrasound images of AL2O3, there is a clear scatterer gradient, with substantial scattering material settling to the bottom of the phantom. Additionally, while the SWE signal is excellent when the top of the sample is in contact with the ultrasound transducer, the signal is less consistent, with more breaks in the color map when imaged with the bottom of the sample in contact with the transducer. The Mica and SiC both give reasonably good signal, however, the SWE signal in the Mica samples is not as consistent across the entire thickness of the sample as the signal in the SiC. Of these five conditions, the SiC appears to give the best SWE signal with the least texture differential.

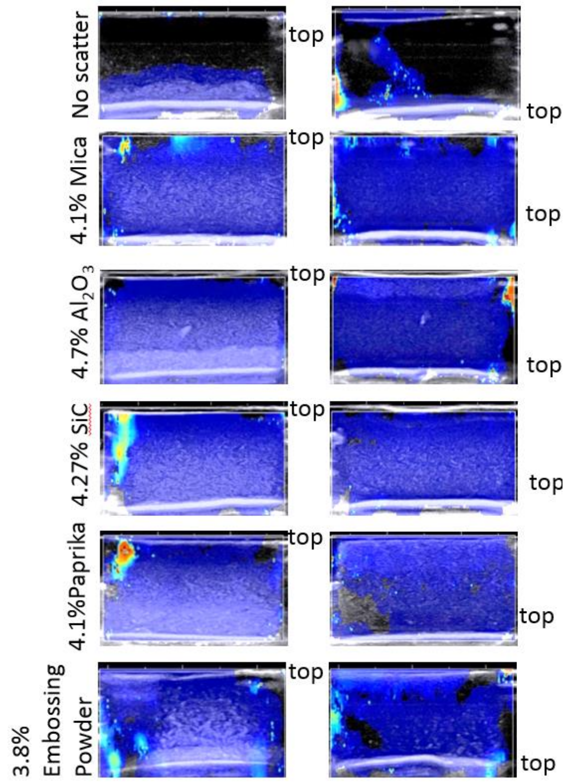

Figure A-4 SWE quality for phantoms made with similar concentrations of different scattering materials.

In comparing quantity of scatterers added, quantities under 1% by weight did not produce enough scatter to create consistent and comprehensive shear wave elastography maps.

A.1.4.4 Pouring Temperature

There was no strong relationship between modulus and pouring temperature (Figure A-5, left). Reported moduli were higher at 45°C pouring temperature and lower at 28°C pouring temperature, but similar among 33,38, and 47°C pouring temperatures. Similarly, reduced pouring temperature did not appear improve scatterer distribution or SWE signal quality (Figure A-5, right). Scatterers settled and obstructed ultrasound signal when mixed gelatin phantoms were poured at all tested temperatures.

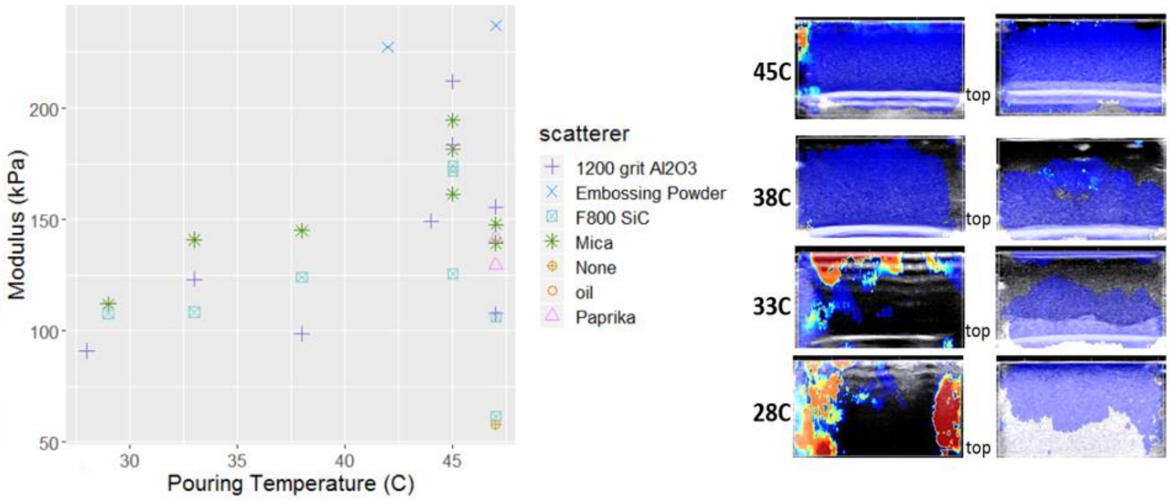

Figure A-5 Effect of pouring temperature on modulus, scatterer distribution, and SWE signal quality.

A.1.5 Conclusion

The temperature of the solution at the time of molding and the pH of the water were not observed to affect the distribution of scatterers in the phantom samples. However, the average diameter of the scattering material did have an effect on the scatterer distribution, with scattering materials in the range 5um-10um consistently suspended in the top portion of the phantoms while scattering materials with dimensions in the range 15um to 20 um were more likely to settle to the bottom regardless of material.

Scattering materials were shown to increase the measured modulus of the resulting phantoms relative to the samples made without any scattering materials. However, the quantity of scatterers added did not seem to affect the amount the modulus increased. It is possible that the differences in amounts of scattering material were not sufficiently varied to measure concentration dependence. Additionally, larger quantities of scattering material tended to settle more, creating layers of scattering material that interrupt the bonding and gelation of the gelatin, increasing likelihood of premature failure of the phantom materials.

Given the similarity in moduli between SiC, AlO2, Mica, and cellulose, it may not be surprising that adding similarly small quantities of the materials increase the modulus in the gelatin by a similarly small amount. However, the modulus of polyamides like those in embossing powder are several orders of magnitude smaller than those in SiC and Alo2, yet the phantoms using embossing power as scatterers had higher moduli than those with any other scattering material. Combined with the cross section of the embossing powder phantoms showing large heterogenous sections rather than discrete micron width scatterers, we hypothesize that the reactive thermoplastic polymers or other additives interact with the polymerizing gelatin to create an overall stiffer material in some sections of the phantom.

In the SiC and Al2O3 phantoms, the best diameter for suspension through most of the phantom was around 10um, with most particles over 15um sinking to the bottom of the phantom. Additionally, the hypothesized oil immersion bubbles in the paprika sample were also between 10u-20um. These areas of the phantoms also corresponded to the areas of best ultrasound signal. From these observations, we conclude that 10um is the ideal size for scattering particles and that 5-15um is likely an appropriate range of particles. The suspension of particles at this size is likely related to the density of the scattering material. SiC and Al2O3 have similar densities, 3.25 g/cm3 and 3 g/cm3, respectively. If future studies endeavor to use different materials for scattering, the densities of these materials should be taken into account when considering suspension in the gelatin medium.

A.1.6 References

1. Dunmire B, Kucewicz JC, Mitchell SB, Crum LA, Sekins KM. Characterizing an Agar/Gelatin phantom for image guided dosing and feedback control of high-intensity focused ultrasound. Ultrasound Med Biol. 2013;39(2):300–11.

2. Franceschini E, Yu FTH, Destrempes F, Cloutier G. Ultrasound characterization of red blood cell aggregation with intervening attenuating tissue-mimicking phantoms. J Acoust Soc Am [Internet]. 2010 Feb 1;127(2):1104–15. Available from: https://pubs.aip.org/jasa/article/127/2/1104/917885/Ultrasound-characterization-of-red-blood-cell
3. Graham JR. Gem Cutting Abrasives in Grit, Mesh, and Microns [Internet]. International Gem Society. Available from: https://www.gemsociety.org/article/gem-cutting-abrasives-grit-mesh-microns/
4. Anderson PG, Rouze NC, Palmeri ML. Effect of Graphite Concentration on Shear-Wave Speed in Gelatin-Based Tissue-Mimicking Phantoms. Ultrason Imaging [Internet]. 2011 Apr 1;33(2):134–42. Available from: http://journals.sagepub.com/doi/10.1177/016173461103300204
5. Farris S, Song J, Huang Q. Alternative Reaction Mechanism for the Cross-Linking of Gelatin with Glutaraldehyde. J Agric Food Chem [Internet]. 2010 Jan 27 [cited 2018 Mar 21];58(2):998–1003. Available from: http://pubs.acs.org/doi/abs/10.1021/jf9031603
6. Osorio FA, Bilbao E, Bustos R, Alvarez F. Effects of concentration, bloom degree, and pH on gelatin melting and gelling temperatures using small amplitude oscillatory rheology. Int J Food Prop. 2007;10(4):841–51.

A.2 Evaluation of SWE and comparison to mechanical testing

A.2.1 Abstract

Shear wave elastography, a technique for measuring the elastic modulus of a material through measurement of shear wave propagation, continues to gain interest as a noninvasive clinical measurement in biomechanics. Many pathological processes are tied to material mechanics, including diabetes. The plantar soft tissue has a unique viscoelastic stress response that may disrupt assumptions used to perform shear wave elastography, especially at higher stresses. Acoustoelastic theory may help improve the translation of shear wave elastography to clinical outcomes and prior work. This work develops a plantar soft tissue-mimicking phantom and evaluates the stress-strain response in comparison to the shear wave elastography measurements. Shear wave elastography underestimates young's modulus relative to classic mechanical testing by a factor of 6 when accounting for acoustoelastic effects, suggesting either a necessary experimental constant or an erroneous assumption in the derivation.

A.2.2 Introduction

In 2018 10.5% of Americans had been diagnosed with diabetes[1], and its prevalence is expected to grow to 33% of the population by 2050[2]. Of the individuals with diabetes, 2-3% will develop a foot ulcer annually[3], and diabetes-related ulceration often precedes lower extremity amputation4. Ulcer prevention therefore is an important component of diabetes management as preventative measures can be taken for diabetic patients at risk for ulceration, such as using site-specific load-reducing footwear. While these preventative measures may help, it is still currently difficult to predict ulcer formation in diabetic individuals. Changes in the mechanical properties of diabetic plantar soft tissue has been suggested to correlate with the development of ulcers and therefore may be useful in prevention strategies for patients with diabetes.

Prior work using ex vivo compression tests as well as ultrasound indentation tests investigated the differences in the mechanical properties of diabetic and non-diabetic plantar soft tissue. The differences in diabetic plantar tissue identified in various studies include increased stiffness[5,6], thickness[7,8], energy loss[5,9], hardness[10], and relaxation modulus[11,12] compared to non-diabetic plantar soft tissue. These properties have also been demonstrated to vary by plantar location[5,6,11,13], making quantification and comparison particularly difficult. These mechanical changes have been hypothesized to contribute to abnormal distribution and dissipation of stress applied to plantar soft tissue and subsequent development of ulcers, but difficulty in measurement of in vivo internal mechanical properties has prohibited translation of these findings to clinical predictive and preventative measures.

Shear wave elastography (SWE) is a non-invasive technique used to quantify the mechanical properties of soft tissues. SWE measures the speed of propagating shear waves in tissue, which is directly related to tissue stiffness or elasticity[14]. However, there is a lack of validation and standardization in SWE measurements for plantar tissue applications that has limited its use in clinical practice as it is difficult to compare SWE results to other mechanical testing methods. Additionally, SWE may be sensitive to compression applied to the tissue while imaging[15], adding additional hurdles to comparison of published works.

The use of phantoms can provide a standardized environment to assess the accuracy and reliability of SWE in acquiring mechanical properties. Phantoms have previously been used in conjunction with SWE to mimic and evaluate the mechanical properties of a variety of low stiffness tissues including breast[16], liver[16], and vasculature[17]. Prior testing of plantar soft tissue using traditional methods at physiological loads yielded 600-1000kPa modulus at 50% strain[5], both of which are higher than previously reported mechanical properties of phantoms. Mechanical testing studies have also shown that plantar soft tissue demonstrates a nonlinear stress/strain relationship with an elongated toe region[5]. This necessitates the development of phantoms that mimic the higher strain range of plantar soft tissue properties and its nonlinear stress/strain relationship.

Tissue mimicking phantoms are commonly composed of varying concentrations of agar and gelatin and The use of phantoms can provide a standardized environment to assess the accuracy and reliability of SWE in acquiring mechanical properties. Phantoms have previously been used in conjunction with SWE to mimic and evaluate the mechanical properties of a variety of low stiffness tissues including breast[16], liver[16], and vasculature[17]. Prior testing of plantar soft tissue using traditional methods at physiological loads yielded 600-1000kPa modulus at 50% strain[5], both of which are higher than previously reported mechanical properties of phantoms. Mechanical testing studies have also shown that plantar soft tissue demonstrates a nonlinear stress/strain relationship with an elongated toe region[5]. This necessitates the development of phantoms that mimic the higher strain range of plantar soft tissue properties and its nonlinear stress/strain relationship.

Tissue-mimicking phantoms are commonly composed of varying concentrations of agar and gelatin and additional studies have evaluated the effects of various additives including oil dispersion and formaldehyde[18]–[23]. Agar has been shown to increase the nonlinearity of the stress/strain relationship in phantoms while gelatin demonstrates a somewhat linear stress/strain relationship[18]. Safflower oil dispersions have been shown to decrease the elastic modulus and increase nonlinearity of gelatin-agar mixtures[18], while aldehydes have been used to increase cross-linking and, as a result, stiffness in gelatins[24]. Glyoxal, a dialdehyde often substituted for formaldehyde in tissue fixation due to higher stability[25], was investigated as a crosslinking agent to increase the stiffness and temperature stability of the phantoms.

In this study, we aim to investigate the use of shear wave elastography to measure the mechanical characteristics of phantoms that mimic the properties of plantar soft tissue. We will create phantoms with different compositions of gelatin, agar, and various additives to mimic the range of stiffness found in human tissue. We will then simultaneously obtain the modulus of the phantoms by classic mechanical testing and SWE. We have hypothesized that the SWE modulus of plantar soft tissue mimicking phantoms will agree with the modulus obtained from mechanical testing.The findings of this study will provide insight into the validity of SWE for measurement of mechanical characteristics of high stiffness tissues. The use of phantom materials will also provide a standardized validation method for SWE measurements, which can be applied to other soft tissue imaging techniques.Materials and Methods

A.2.2.1 Phantom Manufacturing

Phantoms were made from concentrations of 10-25% Gelatin and 0.5-2% agar (Table A.2-1). The lower range of gelatin content was chosen based on prior work and concentrations of 2.5% increments were tested up to 25% to attempt to match the high compression stiffness seen in prior testing of plantar soft tissue. Agar ranges (1-3%) were chosen from prior work to introduce nonlinearity, and two concentrations of safflower oil were investigated based on prior work to increase nonlinearity and modulate higher-stiffness gelatin concentrations via-oil-in-water dispersions (Table A.2-1).

Gelatin (225g bloom, Type B, Sigma-Aldrich, St. Louis, MO, USA) and agar (A7002, Sigma-Aldrich, St. Louis, MO, USA) were dissolved in distilled water, heated to 85°C, and held there until the solution clarified. The solution was then cooled at room temperature. To prevent microbial growth, 0.11%wt. Germall plus was added when the solution reached 50°C and 12.5mg/ml F800 grit silicon carbide, used for ultrasound scattering, was added at 45°C. For solutions containing either glyoxal or safflower oil, additives were stirred into solution at 42°C. The solution was then poured into a cylindrical mold with a 2.5cm diameter and allowed to polymerize overnight at room temperature. After polymerization, the phantoms were removed from their molds, weighed, coated in safflower oil to prevent desiccation, and stored in individual containers. Six phantoms were made for each condition in Table A.2-1 so that two compression tests could be done in triplicate.

Table A.2-1 Tested concentrations of phantom components agar, gelatin, oil, and crosslinker glyoxal.

Agar % wt	Gelatin %wt	Oil %vol	Glyoxal %vol
0.5	10		0.15,0.32
1	10		
2	10		
0.5	12.5		
1	12.5		
2	12.5		
0.5	15		0.15,0.32
1	15		
2	15		
.5	15		
1	15	20,30	
2	15		
0.5	17.5		
1	17.5	20,30	
2	17.5		
0.5	20		
1	20	20,30	
2	20		
0.5	25		
1	25	20,30	
2	25		

A.2.2.2 Mechanical Testing

The ultrasound transducer (SLH 20-6, Supersonic Imagine, Aix en Provence, France) was connected in series with the 250N load cell of an ElectroPuls E3000 (Instron, Norwood, MA), using a custom compression platen designed in Solidworks and printed in acrylonitrile styrene acrylate on an F370 (Stratasys, Prairie, MN). The platen consisted of two halves that enclosed the transducer so that element surface was flush with the compression surface to allow simultaneous mechanical testing and ultrasound imaging. The bottom compression platen was replaced with a block of high-density polyethylene (HDPE) to reduce reflection artifacts from the interface between the phantoms and the platen relative to typical metal platens (Figure A-6).

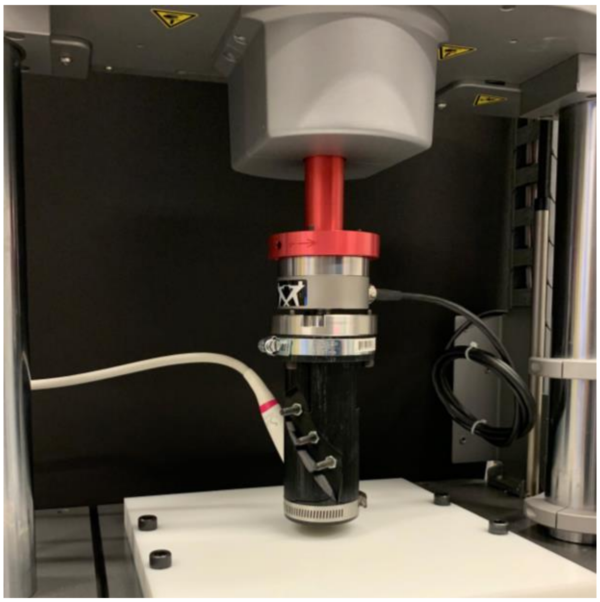

Figure A-6 Mechanical test set up featuring Instron with 250N load cell sandwiched between the crosshead and the custom printed ultrasound interface platen. The bottom platten is 25.4mm thick high density polyethylene

To begin testing, the phantoms were removed from storage, and the diameter and height of each phantom was measured 4 times using digital calipers (Mitutoyo Corp., Kawasaki, Japan; accuracy ±10 μm). Subsequently, two mechanical testing protocols were performed. The first dynamic test consisted of 3 sets of 20 triangle waves to 40% compressive strain at frequencies of 1 Hz and 3Hz in displacement control. Physiologic compression of plantar fat has been measured at 50%, however, 40% was chosen to reduce risk of phantom damage prior to completion of testing at multiple frequencies. B-mode images were acquired during this dynamic compression test using the MATLAB (Natick, MA) research interface. The second test consisted of 14 sequential ramp-hold sets where the ramp applied compression of 3.5-4.5% strain at a rate of 2.5mm/s in displacement control and the hold consisted of 3 seconds to allow 4 SWE acquisitions using the MATLAB research interface.

Stress (σ) and strain (ε) were calculated as applied force divided by the initial cross-sectional area, and axial displacement divided by the initial height, respectively. The elastic modulus (E) for each phantom was calculated from the last three waves of each set of triangle waves as the slope of a linear fit of the loading stress-strain curve after the inflection point [5]. Moduli were averaged across the three tests at each frequency and then compared to the moduli and curves of plantar soft tissue from [5] to determine which concentrations best mimicked plantar soft tissue. The mechanical elastic modulus from the ramp-hold test (E_m) was calculated as the slope of a linear fit to the stress-strain curve for each ramp step. Start points for the data used in the calculation of the mechanical elastic modulus was standardized to begin at the displacement when the applied load was equal to -0.4N.

A.2.2.3 Image Analysis

To measure the elastic modulus from SWE (E_s), the shear wave images taken during each ramp step were cropped to remove SWE artifacts related to reflection at the transducer face and the phantom-HDPE interface. The shear wave speed (c_{sw}) was averaged over the phantom area and across the three images taken at each step using custom MATLAB code and the averaged shear wave speed was used to calculate an elastic modulus according to the equation:

$$E_s=3*\rho*c_{sw}^2$$

Equation A.2-1

where ρ is the density calculated per sample using the pre-storage weight and post-storage dimensions [14].

A.2.2.4 Moduli comparison

A relationship between the moduli derived from SWE and mechanical testing can be derived from Hooke's law ($E_m=\sigma/\varepsilon$), equation (A.2-1), and the acoustoelastic equation $\rho c_{sw}^2 = \mu - \sigma(A/12\mu)$ [14,26], where μ is the shear modulus, and A is a Landau second order elastic coefficient. Rearranging the acoustoelastic elastic equation in terms of σ yields

$$\sigma = (\mu - \rho c_{sw}^2)\ (12\mu/A)$$

Equation A.2-2

Then, substituting the shear wave modulus for ρc_{sw}^2 and σ for $E_m\varepsilon$ yields

$$E_m = (\mu - E_s/3)\ (12\mu/A\varepsilon)$$

Equation A.2-3

Finally, solving for E_s gives the modulus calculated from shear waves in terms of the modulus calculated by elastic mechanics.

$$E_s = 3\mu - (A\varepsilon/4\mu)E_m$$

Equation A.2-4

A and μ were calculated from the slope of the shear wave speed plotted against axial stress using the acoustoelastic equation and the theoretical slope ($A/4\mu$) and intercept (3μ) were calculated for each sample. A linear regression of E_s vs E_m, where corresponding values were taken at the same strain level, was performed using the MATLAB function polyfit, and the experimental slope and intercept were compared to the theoretical values.

A.2.3 Results

Moduli increased with both increasing gelatin and agar content (Figure A-7). The phantom moduli at higher gelatin concentrations were consistent with moduli of plantar soft tissue at the same strain (620kPa vs 600 kPa (nondiabetic)). The lower agar and gelatin concentrations demonstrated moduli consistent with prior work using similar concentration gelatin-agar phantoms.

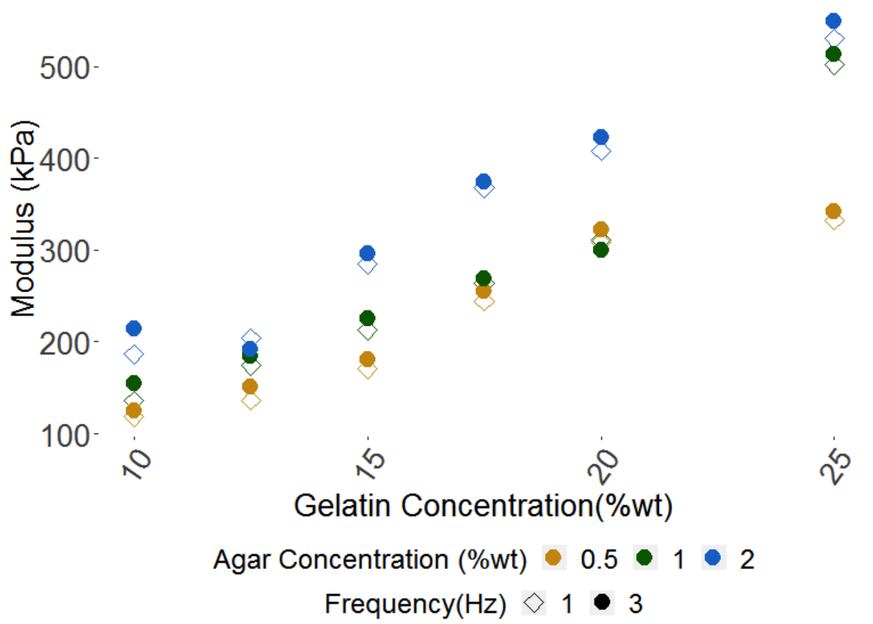

Figure A-7 Mechanical moduli from triangle wave testing for each agar-gelatin concentration.

The final strain of the SWE test varied between 45-65% depending on the initial height of the phantom (Figure A-8). The SWE modulus increased as the strain increased. Noise near the ultrasound transducer (top of image) and the HDPE platen (bottom of image) prevented meaningful measurements near the phantom boundaries.

With increasing gelatin content, the stress-strain curves demonstrated more rapid stress increases and less nonlinearity (Figure A-9a). With increasing agar content, the stress-strain curves again demonstrated more rapid stress increases but did not demonstrate the same reduced nonlinearity (Figure A-9b). Both increasing gelatin and agar content resulted in increased calculated final moduli. Addition of glyoxal demonstrated a mild increase in moduli with what appears to be no effect on the nonlinearity of the stress strain curve (Figure A-9c). Oil-containing phantoms have an elongated region of low stress (Figure A-9d) but a similar final slope to samples of the same gelatin-agar content without oil. The 25% gelatin, 1% agar, and 30% oil phantom most closely resembled the stress/strain curve seen in mechanical testing of plantar soft tissue.

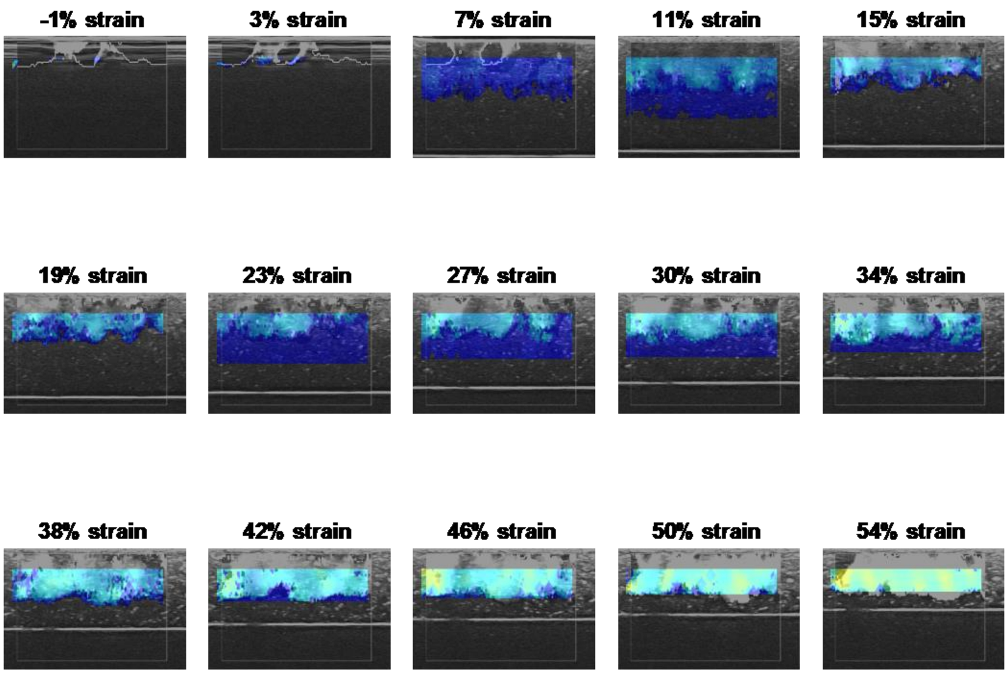

Figure A-8 SWE images for each step-down compression of the 25% gelatin, 1% agar, and 30% oil phantom, which most closely resembles plantar soft tissue mechanics. The portion of each image in color was used for calculation of the SWE moduli. Dark blue is low strain, red is high strain. Noisy signal (grayscale) was excluded from calculations.

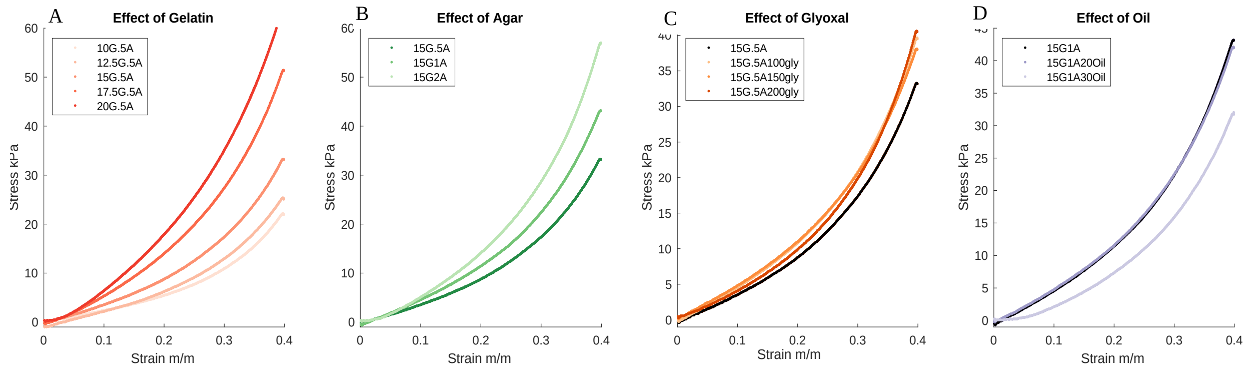

Figure A-9 Representative loading curves for, A. Varying concentrations of Gelatin with 0.5% agar. B. 15% Gelatin with varying concentrations of agar. C. 15% Gelatin 0.5% agar with varying concentrations of glyoxal. D. 25% Gelatin 1% agar with varying oil dispersion concentrations

The SWE modulus (Es) increased linearly with the Classic modulus (Em) (R^2=0.98, Figure A-10). The slope of the linear fit averaged across all the experimental data is lower than that from the theoretical equation by a factor of 6.6 ±1.16. The theoretical slope, A/4μ, is 1.69±0.50 while the slope obtained experimentally averaged across all samples was 0.16±0.04. The averaged experimental intercept ((2.73±0.39)*μ) generally agrees with the theoretical intercept of 3μ.

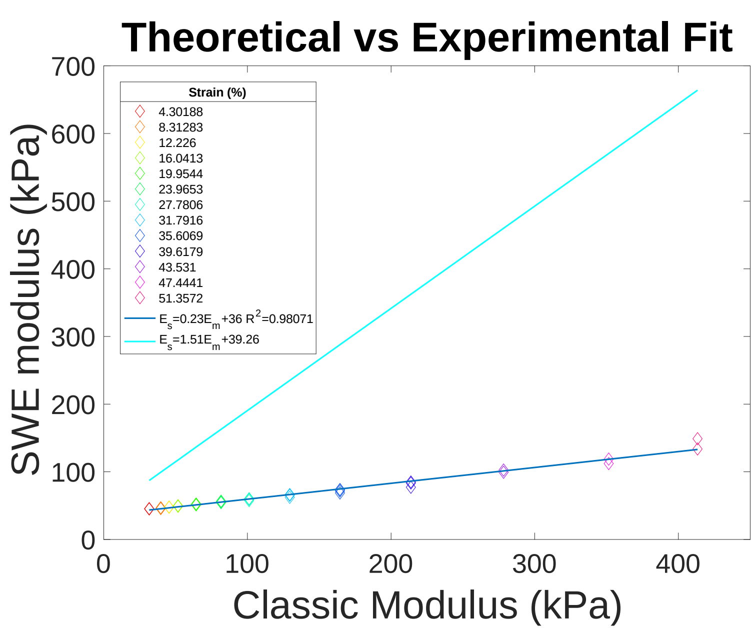

Figure A-10 The experimentally obtained classical and SWE moduli were plotted with a linear fit (dark blue) to compare to the expected theoretical equation (light blue).

A.2.4 Discussion

Ultrasound and (SWE) continue to gain popularity across biomechanical study as techniques for measuring soft tissue structure and material properties *in vivo*. However, there remain questions about how well phantom materials mimic soft tissues under high loads and strains and how well the SWE technique behaves in high-strain, highly loaded musculoskeletal tissues such as the plantar soft tissue.

Phantoms with gelatin-agar concentrations above 27% combined had moduli in the range of plantar soft tissue moduli. However, the initial toe region of the stress/strain curve of the phantoms was shorter than what has previously been reported for plantar soft tissue[5]. With the addition of oil, the stress-strain curve exhibited a longer toe region, but not to the extent of the initial region of the plantar soft tissue. While a higher oil content may be able to increase the toe region further, the image quality begins to degrade at higher oil content, and the phantoms tested may have already been close to the maximum dispersion possible while maintaining structural integrity. As a result of this lesser viscosity, the phantoms with similar high-strain properties to plantar soft tissue had higher moduli at low strain. Despite prior reporting that formaldehyde can effectively crosslink gelatin and increase the modulus of phantoms made with formaldehyde [27], the larger aldehyde glyoxal did not appear to have this effect.

SWE values and mechanical testing are not typically reported together in the literature, making comparisons between results derived from the two methods difficult. Theoretically, these two measurements should be linked through acoustoelasticity. However, while the experimental intercepts of SWE moduli regressed on classic moduli values deviated minimally from the expected intercept of 3μ, the experimental slope was over 6 times lower than the expected value of $A/4\mu$ across all phantoms, suggesting either a necessary experimental constant or an erroneous assumption in the derivation. The derivations assume linear elastic behavior and do not account for nonlinear viscoelastic effects demonstrated in both the plantar soft tissue and the phantoms. While assuming linear elastic behavior in tissue is often justified by linear-approximate behavior at low strain, plantar soft tissue undergoes strain up to 50% physiologically, which results in substantial viscoelastic nonlinearity as previously reported [5]. Both increased strain and strain rate result in increased load resistance in a viscoelastic material. However, SWE induces small compressions in the shear wave which may not induce an increase of the same magnitude seen in the mechanical testing due to the nonlinearity of these stress-strain responses. Additionally, while there is expected to be more tension in the material as a result of the compression, these test were performed in unconfined uniaxial compression, and there could be induced anisotropy in the molecular distribution that affect the sound speed in the shear direction differently than in the axial direction. A more confined experiment may yield lower deviations in theoretical and expected values. Finally, some relaxation occurred during the hold required for SWE acquisition (Figure A-11). This reduction in applied stress could also contribute to the underestimation of SWE relative to the theoretical calculated using the applied load.

The viscoelastic effect is unlikely to be the only contributing factor for the difference between the expected and measured results as we would expect to less of the viscoelastic effects at higher strain and lower strain with the greatest effect in the middle of the curve, however the difference between expected and measured moduli is consistent across all strains. However, these findings suggest that the use of SWE at high strain in soft tissues should be considered carefully, as quantitative values are lower than those obtained from classic mechanical approaches.

Prior research has led to some development of guidelines for the clinical use of SWE. These guidelines advise that minimum compression should be applied to the tissue during imaging. Our study evaluated the use of SWE at strains up to 50%, as this is the physiologic strain that plantar soft tissue undergoes. Imaging the tissue in an unloaded state provides an assessment of stiffness at very low strains only and cannot provide any information on its nonlinear response to loading. Being able to assess the nonlinear mechanical behavior of soft tissues would significantly enhance the diagnostic potential of shear wave elastography.

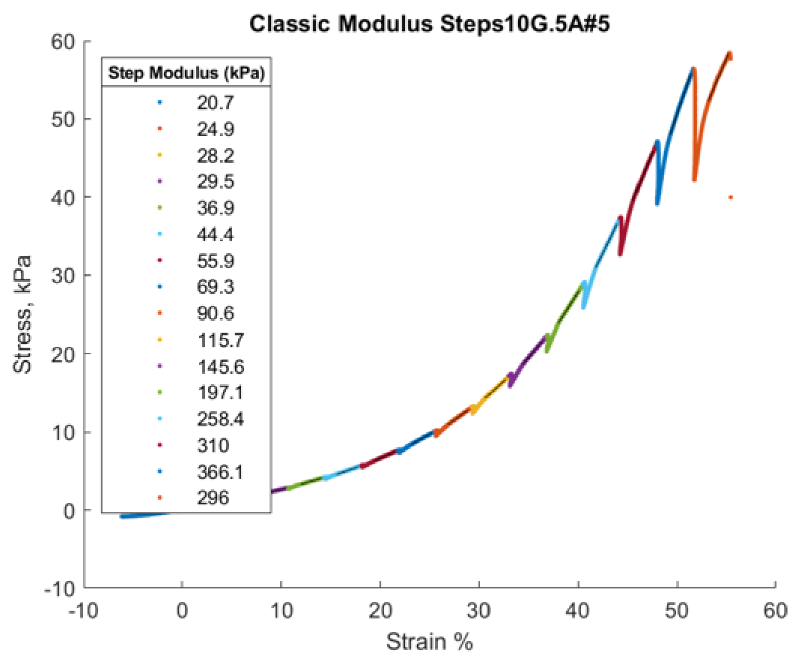

Figure A-11 Stress-strain curve recorded during a sample ramp-hold SWE test. Each color is a different step. Relaxation can be seen in during the hold phase between ramps.

There are several limitations to this work. First, our mechanical chain includes several components made of more flexible materials than those typically used for mechanical testing. This limitation is mitigated by the testing of relatively soft materials with moduli order of magnitude lower than the paten components. Phantoms with previously reported gelatin-agar concentrations did demonstrate low-strain moduli comparable to those previously reported [18,19,20,21], supporting the validity of our methods. Second, as mentioned, there was some relaxation in the hold phase where the SWE images were acquired. While this relaxation could result in reduced tension and reduced shear wave speed, relaxation stress did not dip below the stress applied at the previous step, and a stress in the middle of the ramp curve was used for the theoretical calculation, mitigating this effect. Another limitation is repeated testing of the phantoms. The six sets of triangle waves were performed sequentially, and the order of frequencies was not varied. It is possible that some microcracking occurred during the initial testing that could affect subsequent measurements. However, a lower strain was chosen to mitigate this risk, and there were no obvious failures or visible damage to the specimens during testing. Similarly, the SWE phantoms were not the same phantoms used for the triangle testing. It is possible that insufficient mixing or some other manufacturing defects caused the mechanical properties to differ between the SWE and mechanical testing discs. However, phantoms were made from the same stock solution, mitigating this risk. Finally, phantoms were not tested dynamically to 50% strain, and they did not perfectly match the plantar soft tissue. These results may not be applicable directly to soft tissue and should be replicated in a cadaveric study.

A.2.5 Conclusion

The ability to modify the phantoms to mimic plantar soft tissue properties over large strain may improve testing and validation of SWE methods in high-strain musculoskeletal applications. This method demonstrated the feasibility of simultaneously using mechanical testing and SWE to measure mechanical properties. Our study utilized plantar tissue mimicking phantoms to assess the ability of SWE to determine mechanical properties. Future studies will be needed to take the next steps of simultaneously using mechanical testing and SWE to acquire the mechanical properties of actual plantar soft tissue. Prior studies have examined the mechanical properties of plantar soft tissue using classical mechanical testing, as well as compared shear wave elastography to computational modeling methods of obtaining mechanical properties such as finite element modeling, however these computational modeling is not the ideal standard for determining mechanical properties and has many limitations.

A.2.6 References

[1] CDC, “National Diabetes Statistics Report 2020. Estimates of diabetes and its burden in the United States.,” Atlanta, GA, 2020.

[2] J. P. Boyle, T. J. Thompson, E. W. Gregg, L. E. Barker, and D. F. Williamson, “Projection of the year 2050 burden of diabetes in the US adult population: dynamic modeling of incidence, mortality, and prediabetes prevalence,” Popul. Health Metr., vol. 8, no. 1, p. 29, Dec. 2010.

[3] R. E. Pecoraro, G. E. Reiber, and E. M. Burgess, “Pathways to diabetic limb amputation. Basis for prevention.,” Diabetes Care, vol. 13, no. 5, pp. 513–21, May 1990.

[4] G. E. Reiber, R. E. Pecoraro, and T. D. Koepsell, “Risk factors for amputation in patients with diabetes mellitus. A case-control study.,” Ann. Intern. Med., vol. 117, no. 2, pp. 97–105, Jul. 1992.

[5] S. Pai and W. R. Ledoux, “The compressive mechanical properties of diabetic and non-diabetic plantar soft tissue,” J. Biomech., vol. 43, no. 9, pp. 1754–1760, Jun. 2010.

[6] L. Brady, S. Pai, J. M. Iaquinto, Y.-N. Wang, and W. R. Ledoux, “The compressive, shear, biochemical, and histological characteristics of diabetic and non-diabetic plantar skin are minimally different,” J. Biomech., vol. 129, p. 110797, Dec. 2021.

[7] W. R. Ledoux, S. Pai, J. B. Shofer, and Y. N. Wang, “The association between mechanical and biochemical/histological characteristics in diabetic and non-diabetic plantar soft tissue,” J. Biomech., vol. 49, no. 14, pp. 3328–3333, 2016.

[8] C. Y. L. Chao, Y.-P. Zheng, and G. L. Y. Cheing, “Epidermal Thickness and Biomechanical Properties of Plantar Tissues in Diabetic Foot,” Ultrasound Med. Biol., vol. 37, no. 7, pp. 1029–1038, Jul. 2011.

[9] Y.-K. Jan, C.-W. Lung, E. Cuaderes, D. Rong, and K. Boyce, “Effect of viscoelastic properties of plantar soft tissues on plantar pressures at the first metatarsal head in diabetics with peripheral neuropathy,” Physiol. Meas., vol. 34, no. 1, pp. 53–66, Jan. 2013.

[10] A. Piaggesi et al., “Hardness of plantar skin in diabetic neuropathic feet,” J. Diabetes Complications, vol. 13, no. 3, pp. 129–134, 1999.

[11] S. Pai and W. R. Ledoux, “The shear mechanical properties of diabetic and non-diabetic plantar soft tissue,” J. Biomech., vol. 45, no. 2, pp. 364–370, 2012.

[12] S. Pai and W. R. Ledoux, “The quasi-linear viscoelastic properties of diabetic and non-diabetic plantar soft tissue,” Ann. Biomed. Eng., vol. 39, no. 5, pp. 1517–1527, May 2011.

[13] L. M. Brady, E. Rombokas, Y.-N. Wang, J. B. Shofer, and W. R. Ledoux, “The effect of diabetes and tissue depth on adipose chamber size and plantar soft tissue features,” Foot, vol. 56, p. 101989, Sep. 2023.

[14] J. Bercoff, M. Tanter, and M. Fink, “Supersonic shear imaging: a new technique for soft tissue elasticity mapping,” IEEE Trans. Ultrason. Ferroelectr. Freq. Control, vol. 51, no. 4, pp. 396–409, Apr. 2004.

[15] J.-L. Gennisson et al., “Acoustoelasticity in soft solids: Assessment of the nonlinear shear modulus with the acoustic radiation force,” J. Acoust. Soc. Am., vol. 122, no. 6, pp. 3211–3219, Dec. 2007.

[16] Y. Jiang et al., “Characterization of the nonlinear elastic properties of soft tissues using the supersonic shear imaging (SSI) technique: Inverse method, ex vivo and in vivo experiments,” Med. Image Anal., vol. 20, no. 1, pp. 97–111, Feb. 2015.

[17] E. Maksuti, E. Widman, D. Larsson, M. W. Urban, M. Larsson, and A. Bjällmark, “Arterial Stiffness Estimation by Shear Wave Elastography: Validation in Phantoms with Mechanical Testing,” Ultrasound Med. Biol., 2016.

[18] T. Z. Pavan, E. L. Madsen, G. R. Frank, A. Adilton O Carneiro, and T. J. Hall, “Nonlinear elastic behavior of phantom materials for elastography,” Phys. Med. Biol., vol. 55, no. 9, pp. 2679–2692, 2010.

[19] E. L. Madsen, M. A. Hobson, H. Shi, T. Varghese, and G. R. Frank, “Tissue-mimicking agar/gelatin materials for use in heterogeneous elastography phantoms,” Phys. Med. Biol., vol. 50, no. 23, pp. 5597–5618, Dec. 2005.

[20] T. Z. Pavan, E. L. Madsen, G. R. Frank, J. Jiang, A. A. O. Carneiro, and T. J. Hall, “A nonlinear elasticity phantom containing spherical inclusions,” Phys. Med. Biol., vol. 57, no. 15, pp. 4787–4804, Aug. 2012.

[21] E. L. Madsen, J. A. Zagzebski, R. A. Banjavie, and R. E. Jutila, “Tissue mimicking materials for ultrasound phantoms,” Med. Phys., vol. 5, no. 5, pp. 391–394, Sep. 1978.

[22] A. Cafarelli, A. Verbeni, A. Poliziani, P. Dario, A. Menciassi, and L. Ricotti, “Tuning acoustic and mechanical properties of materials for ultrasound phantoms and smart substrates for cell cultures,” Acta Biomater., vol. 49, pp. 368–378, Feb. 2017.

[23] P. Movahed, W. Kreider, A. D. Maxwell, B. Dunmire, and J. B. Freund, “Ultrasound-Induced Bubble Clusters in Tissue-Mimicking Agar Phantoms,” Ultrasound Med. Biol., vol. 43, no. 10, pp. 2318–2328, Oct. 2017.

[24] T. J. Hall, M. Bilgen, M. F. Insana, and T. A. Krouskop, “Phantom materials for elastography,” IEEE Trans. Ultrason. Ferroelectr. Freq. Control, vol. 44, no. 6, pp. 1355–1365, 1997.

[25] Y. Wang, K. Lee, S. Pai, and W. Ledoux, “Histomorphometric comparison after fixation with formaldehyde or glyoxal,” Biotech. Histochem., vol. 86, no. 5, pp. 359–365, Oct. 2011.

[26] M. F. Hamilton, Y. A. Ilinskii, and E. A. Zabolotskaya, “Separation of compressibility and shear deformation in the elastic energy density (L),” J. Acoust. Soc. Am., vol. 116, no. 1, pp. 41–44, Jul. 2004.

[27] C. Tengroth, U. Gasslander, F. O. Andersson, and S. P. Jacobsson, “Cross-Linking of Gelatin Capsules with Formaldehyde and Other Aldehydes: An FTIR Spectroscopy Study,” Pharm. Dev. Technol., vol. 10, no. 3, pp. 405–412, Jan. 2005.

B Appendix B: Code for Scanner Motion Control

The volumetric ultrasound scanner is controlled using MATLAB to control communication between the ultrasound and the Arduino the controls the motors. Both the MATLAB and Arduino code are provided here to better illustrate how the devices communicated to perform the scan.

B.1 Arduino Code

```
#include <digitalWriteFast.h>

const int numChar = 5;
unsigned long ttime = 0; // time in milliseconds
char receivedChar[numChar]; // the array for received data
char endMarker = '>';        // the end marker character
boolean newData = false;

volatile long _EncoderTicks = 0;

// set motor & encoder channels
#define driverPUL  7   // PUL- pin
#define driverDIR  6    // DIR- pin
boolean setdir = HIGH;
#define driverPULT  9   // PUL- pin
#define driverDIRT  10    // DIR- pin

#define encoderLchA  2 //interrupt 0
#define encoderLchB  8
#define encoderLindex  11

#define encoderTchA 3 //interrupt 1
#define encoderTchB 5
#define encoderTindex  12
//set initial vals
int encoder_countT = 0;
volatile bool _EncoderTBSet;
int encoderupdates = 0;
int val_LchA = 0 ;
int val_LchB = 0;
int val_TchA = 0;
int val_TchB = 0;
int val_Lindex = 0;
int val_Tindex = 0;

void setup()
{
  Serial.begin(960000);     // we need this for serial communication
  pinMode (driverPUL, OUTPUT);
  pinMode (driverDIR, OUTPUT);
  pinMode (driverPULT, OUTPUT);
  pinMode (driverDIRT, OUTPUT);
```

```
  pinMode(encoderLchA, INPUT);
  pinMode(encoderLchB, INPUT);
  pinMode(encoderTchA, INPUT);
  pinMode(encoderTchB, INPUT);
  attachInterrupt(1, countEncoderT, RISING);
}

void countEncoderT() {
  // for AMT20-V, A leads B for CCW rotation(CW = toward motor = negative motion)
  // AMT 20-V has 96-1024 pulses per revolution. PPR = number of high pulses an
encoder will have on either of its square wave outputs A or B over a single
revolution.
  // counts per revolution = ppr*4 for incremental quadrature encoders b/c/ have 2
offest square waves, so 4 states per pulse
  // what we are measuring is a count.
  // for 96 PPR = 384CPR, each count = 0.9375 degress & 0.0026 mm for a 1mm lead
  // interrupt will only fire on 'rising', don't need to read pin A
  _EncoderTBSet = digitalReadFast(encoderTchB);   // read the input pin
  // and adjust counter + if A leads B
#ifdef EncoderIsReversed
  encoder_countT -= _EncoderTBSet ? -1 : +1;
#else
  encoder_countT += _EncoderTBSet ? -1 : +1;
#endif
  encoderupdates++;
}

void record()
{
  char rChar;
  static int index = 0;
  while (Serial.available() > 0 && newData == false) // If something appears on
the serial port, run this
  {
    rChar = Serial.read();
    delayMicroseconds(50);
    if (rChar != endMarker && index <= 4)
    {
      receivedChar[index] = rChar;
      index++;
    }
    else
    {
      receivedChar[index] = '\0'; // terminate the string
      index = 0;                  // reset the counter
      newData = true;             // set the "newData" indicator to true, meaning
that the new data has arrived, and we can proceed further
   }}}

void sendParams()
{
  ttime = millis();
  Serial.print(ttime);
  Serial.print('_');
  Serial.print(receivedChar);
  Serial.println("LF,");
}

void printDataStream()
{
  ttime = millis();
  Serial.print("t");
```

```
  Serial.print(ttime);
  val_LchA = digitalReadFast(encoderLchA);
  val_LchB = digitalReadFast(encoderLchB);
  val_Lindex = digitalReadFast(encoderLindex);
  Serial.print("L");
  Serial.print(val_Lindex);
  Serial.print(val_LchB);
  Serial.print(val_LchA);
}

void printDataStream_LessL()
{
  val_LchA = digitalReadFast(encoderLchA);
  val_LchB = digitalReadFast(encoderLchB);
  val_Lindex = digitalReadFast(encoderLindex);
  Serial.print("L");
  Serial.print(val_Lindex);
  Serial.print(val_LchB);
  Serial.print(val_LchA);
}
void fullLOutputStepL(long cycles, int delayTime) {
  digitalWrite(driverDIR, setdir);
  int counts = 1;
  unsigned long t2 = 0;
  int PULhigh = 0;
  unsigned long t1 = 0;
  //int timewaster = 0; //unused
  printDataStream();
  Serial.print('i');
  Serial.print(cycles);
  Serial.print('T');
  Serial.print(delayTime);
  Serial.print("C");
  Serial.print(counts);
  t1 = micros();
  for (int i = 0; i < cycles; i++) {
    if (cycles < 4000) {
      printDataStream_LessL();
    }
    else {
      Serial.print("L");
      Serial.print(val_Lindex);
      delayMicroseconds(100); // delay to reduce serial output between motor pulses
     }
    t2 = micros();
    if (t2 - t1 > delayTime ) {
      if (PULhigh < 1) {
        digitalWriteFast(driverPUL, HIGH);
        Serial.print("M");
        PULhigh = 1;
        t1 = micros();
      }

     else if (PULhigh > 0) {
        digitalWriteFast(driverPUL, LOW);
        ttime = millis();
        Serial.print("t");
        Serial.print(ttime);
        PULhigh = 0;
        counts++;
```

```
        Serial.print("C");
         Serial.print(counts);
         t1 = micros();
        }
      }
    }
    newData = false;
    Serial.print('T');
    Serial.print(encoder_countT);
    Serial.print("__\0");
  }

  void fullLOutputStepT(long cycles, int delayTime) {
    digitalWrite(driverDIRT, setdir);
    int counts = 1;
    unsigned long t2 = 0;
    int PULhigh = 0;
    unsigned long t1 = 0;
    printDataStream();
    Serial.print("C");
    Serial.print(counts);
    t1 = micros();
    for (; counts < cycles;) {
      //printDataStream_LessL();
      t2 = micros();
      if (t2 - t1 > delayTime ) {
        if (PULhigh < 1) {
          digitalWriteFast(driverPULT, HIGH);
          Serial.print("M");
          //if (counts % 10 < 1) {
            Serial.print('E');
            Serial.print(encoder_countT);
          //}
          printDataStream_LessL();
          PULhigh = 1;
          t1 = micros();
        }
        else if (PULhigh > 0) {
          digitalWriteFast(driverPULT, LOW);
          printDataStream();
          PULhigh = 0;
          counts++;
          Serial.print("C");
          Serial.print(counts);
          t1 = micros();
        }
      }
    }
    newData = false;
    Serial.print('T');
    Serial.print(encoder_countT);
  Serial.print("__\0");
  }
  //move the motor
  void execute()
  { int counts = 1;
    unsigned long t2 = 0;
    int PULhigh = 0;
    unsigned long t1 = 0;
    int delayTime = 400; // 2500 steps/s -> could maybe go down to 350 (per motor
  torque), but might lose some encoder resolution
```

```
  //int cycles = 600; // 0.5 mm = 600 cycles 550 = ~.45
  //int cycles = 550; // 0.4565 mm
  int cycles = 500; // 0.415 mm
  //int cycles = 450; // 0.3735 mm

  if (receivedChar[0] == '3') {
    //cycles = 2880; // if SWE, change to 2.4 -> ftL <250
    //cycles = 2940; // if SWE, change to 2.45 -> ftL <260
    cycles = 3060; // if SWE, change to 2.55 -> ftL <270
    //cycles = 3120; // if SWE, change to 2.65 -> ftL <280
    //cycles = 3240; // if SWE, change to 2.7 -> ftL <280
  }
  //else if (recievedChar [0] == '3') {
  if (newData == true)
  { //set motor direction
    if (receivedChar[1] == '1') {
      digitalWrite(driverDIR, HIGH);
    }
    else if (receivedChar[1] == '2') {
      digitalWrite(driverDIR, LOW);
    }
    //perform motor motion and encoder readout to serial
    printDataStream();
    Serial.print("C");
    Serial.print(counts);
    t1 = micros();
    for (int i = 0; i < cycles; i++) {
      printDataStream_LessL();
      t2 = micros();
      if (t2 - t1 > delayTime ) {
        if (PULhigh < 1) {
          digitalWriteFast(driverPUL, HIGH);
          Serial.print("M");
          //printDataStream_LessL();
          PULhigh = 1;
          t1 = micros();
        }
        else if (PULhigh > 0) {
          digitalWriteFast(driverPUL, LOW);
          ttime = millis();
          Serial.print("t");
          Serial.print(ttime);
          PULhigh = 0;
          counts++;
          Serial.print("C");
          Serial.print(counts);
          t1 = micros();
        }
      }

    }
  }
  newData = false;
Serial.print('T');
  Serial.print(encoder_countT);
  Serial.print("__\0");
}
void execute_transverse()  //move the motor
{ int counts = 1;
  unsigned long t2 = 0;
  int PULhigh = 0;
  unsigned long t1 = 0;
```

```
  int delayTime = 500; // don't go below 500 ms for 0.8 A motors delay=500 => 2000
pps => 10mm/s
  int motorhighs = 0;

  if (newData == true)
  { if (receivedChar[1] == '1') {
      digitalWrite(driverDIRT, HIGH);
    }
    else if (receivedChar[1] == '2') {
      digitalWrite(driverDIRT, LOW);
    }
    //    if (ebrake > 0 ) { // check variable & break if switched to 1? - add to
each loop?
    //      break
    //    }
    Serial.print("C");
    Serial.print(counts);
    printDataStream();
    t1 = micros();
    for (; counts < 1000;) { // change to 6000 -7000 AND change matlab to one call
for runtime; 1000 counts = approx 5mm
      t2 = micros();
      if (t2 - t1 > delayTime ) {
        if (PULhigh < 1) {
          digitalWriteFast(driverPULT, HIGH);
          motorhighs++;
          PULhigh = 1;
          t1 = micros();
        }
        else if (PULhigh > 0) {
          digitalWriteFast(driverPULT, LOW);
          PULhigh = 0;
          counts++;
          if (counts % 40 < 1) {

            Serial.print('E');
            Serial.print(encoder_countT);
          }
          if (counts % 100 < 1) {
            Serial.print('M');
            Serial.print(motorhighs);
            Serial.print('u');
            Serial.print(encoderupdates);
            Serial.print("C");
            Serial.print(counts);
            printDataStream();
          }
          t1 = micros();
        }}}}
  newData = false;
  printDataStream_LessL();
  Serial.print("__\0");
}
void execute_jog()  //move the motor
{ int counts = 1;
  unsigned long t2 = 0;
  int PULhigh = 0;
  unsigned long t1 = 0;
  int cycles = 360; //initialize array of cycles to perform for 0.3 mm movements
  int delayTime = 2500;
  if (receivedChar[2] == '1') {
    delayTime = 2500;
```

```
    cycles = 1700;
  }
  else if (receivedChar[2] == '2') {
    delayTime = 1000;
    cycles = 720;
  }
  else if (receivedChar[2] == '3') {
    delayTime = 500;
    cycles = 360;
  }
  if (newData == true){
    if (receivedChar[1] == '1') {
      setdir = HIGH;
      fullLOutputStepL(cycles, delayTime);
    }
    else if (receivedChar[1] == '2') {
      setdir = LOW;
      fullLOutputStepL(cycles, delayTime);
    }
    else if (receivedChar[1] == '3') {
      setdir = HIGH;
      fullLOutputStepT(cycles, delayTime);
    }
    else if (receivedChar[1] == '4') {
      setdir = LOW;
      fullLOutputStepT(360, delayTime);
    }
  }
  newData = false;
  printDataStream_LessL();
  Serial.print("__\0");
}

void execute_move()  //move the motor
{ int counts = 1;
  unsigned long t2 = 0;
  int PULhigh = 0;
  unsigned long t1 = 0;
  long cycles[7] = {360, 1200, 2400, 6000, 12000, 24000, 60000}; //initialize array
of cycles to perform for 0.3, 1, 2, 5, 10, 20, 50 mm movements
  int delayTime = 2500;
  int multiplier = 1;

  if (receivedChar[2] == '1') {
    delayTime = 2500;
    multiplier = 5;
  }
  else if (receivedChar[2] == '2') {
    delayTime = 1000;
    multiplier = 2;
  }
  else if (receivedChar[2] == '3') {
    delayTime = 500;  }
if (newData == true)
  { int numcycles = receivedChar[3] - '0';

    if (receivedChar[1] == '1') {
      setdir = HIGH;
      fullLOutputStepL(cycles[numcycles]*multiplier, delayTime);
    }
    else if (receivedChar[1] == '2') {
      setdir = LOW;
```

```
      fullLOutputStepL(cycles[numcycles]*multiplier, delayTime); // alt option to
convert to int?
    }
    else if (receivedChar[1] == '3') {
      setdir = HIGH;
      fullLOutputStepT(cycles[numcycles]/6, delayTime); //not sure if this will
work
    }
    else if (receivedChar[1] == '4') {
      setdir = LOW;
      fullLOutputStepT(cycles[numcycles]/6, delayTime); //not sure if this will
work
    }
  }
  newData = false;
  printDataStream_LessL();
  Serial.print("__\0");
}


void loop()
{ //printDataStream_LessL();
  if (Serial.available() > 0)
  {
    record();
    sendParams();
    if (receivedChar[0] == '1') {
      execute();
    }
    else if (receivedChar[0] == '2') {
      execute_transverse();
      delay(.2) ;
    }
    if (receivedChar[0] == '3') {
      execute(); //execute longitudinal SWE
    }
    else if (receivedChar[0] == '4') {
      execute_jog();
      delayMicroseconds(1) ;
    }
    else if (receivedChar[0] == '5') {
      execute_move();
      delayMicroseconds(1) ;
    }
  }
```

B.2 MATLAB Code (main functions, excluding GUI set up)

```
function executeScan(btn, ControlFig, teststruct)
%{
executeScan(btn, ControlFig, teststruct) performs the ultrasound scan on
the press of the 'Collect' button
inputs:
    btn - 'collect' button push
    ControlFig - the parent figure that contains the GUI
    teststruct - the structure containing all the button states and GUI
    feature values
outputs: saves the scan image structures and teststruct to file. (dialog box comes
up after scan to allow you to save to desired location)
%}

selection=uiconfirm(ControlFig, 'Collect Data?','Confirm Collect', 'Options',
{'Yes', 'No'}, 'DefaultOption', 1, 'CancelOption', 2);
if strcmp(selection,'No')
    return
end
% check that sanity checks are true

if sum([teststruct.Calibrate.Value teststruct.AixRemote.Value teststruct.Img.Value
teststruct.ImgParams.Value teststruct.PowerOn.Value teststruct.Motorhome.Value
teststruct.Serial.Value teststruct.qest.Value])<8
    errordlg('One or more checkboxes missing')
    return
end
if contains(teststruct.subjID.Value, 'Anon')
    warndlg('Subject ID not changed')
end
if teststruct.ftL.Value==100
    warndlg('Foot length not changed')
end
if teststruct.ftW.Value==50
    warndlg('Foot width not changed')
end
if strcmp(teststruct.ScanType.Value,'Select Scan')
    errordlg('You did not select a scan type')
    return
end
if ~contains(teststruct.arduinoPort.Value,'COM')
    errordlg('Serial port is not valid. Please select the COM port connected to
arduino. ')
    return
end

%% set up aixplorer control
if ~exist('srv')
    addpath('bin', 'commands', 'sequence_libs', 'xmltree-2.0');
    startSonicLab
    srv=remoteDefineServer(teststruct.AIP.Value); % change this to IP addresws from
gui inputs
end
```

```
%% Number of scans, longitudinal direction
switch teststruct.ScanType.Value
    case 'Bmode unweighted'
        remoteToggleMode(srv,'B')
        res= 0.415; %mm
        numScansLong = floor(teststruct.ftL.Value/(res));
    case 'Bmode weighted'
        remoteToggleMode(srv,'B')
        res= 0.415; %mm
        numScansLong = floor(teststruct.ftL.Value/res);
    case 'SWE unweighted'
        res= 2.51; %mm
        numScansLong = floor(teststruct.ftL.Value/res);
end

%% TAKE SCANS
%Longitudinal scan 1 %%%%%%%%%%%%%%
Tmoves = ceil(teststruct.ftW.Value/(51-10))-1; % calc # transverse moves needed
if contains(teststruct.ScanType.Value, 'Bmode')
    switch Tmoves
        case 1
            disp('Two longitudinal scans')
            Long1 = LongScan(numScansLong, teststruct.arduinoPort.Value, srv, 'toe',
             teststruct); % first scan posterior-anterior
            Tread1=moveTverse( teststruct.arduinoPort.Value , 'scan');
            Long2 = LongScan(numScansLong, teststruct.arduinoPort.Value,
srv,'motor',
             teststruct); % second scan anterior-posterior
            Treturn=moveTverse( teststruct.arduinoPort.Value , 'return'); % sends
motor back home
            uisave({'teststruct', 'Long1', 'Long2','Tread1', 'Tmoves'},
['UltrasoundScannerData_' char(datetime('now','Format','yyyyMMdd_HHmmssSSS'))])

        case 2
            tic
            disp('Three longitudinal scans')
            Long1 = LongScan(numScansLong, teststruct.arduinoPort.Value, srv, 'toe',
             teststruct);
            Tread1=moveTverse( teststruct.arduinoPort.Value , 'scan');
            Long2 = LongScan(numScansLong, teststruct.arduinoPort.Value, srv,
'motor',
             teststruct);
            Tread2=moveTverse( teststruct.arduinoPort.Value , 'scan');
            Long3 = LongScan(numScansLong, teststruct.arduinoPort.Value, srv, 'toe',
             teststruct);
            % send motor back home
            ReturnLong = LongReturn(teststruct.ftL.Value,
teststruct.arduinoPort.Value,
             'motor', teststruct);
            Treturn=moveTverse( teststruct.arduinoPort.Value , 'return');
            Treturn2=moveTverse( teststruct.arduinoPort.Value , 'return');
            uisave({'teststruct', 'Long1', 'Long2', 'Long3','Tread1', 'Tread2',
             'Tmoves'}, ['UltrasoundScannerData_'
             char(datetime('now','Format','yyyyMMdd_HHmmssSSS'))])
    end
elseif contains(teststruct.ScanType.Value, 'SWE')
    switch Tmoves
        case 1
            disp('Two longitudinal scans')
            Long1 = LongScan_SWE(numScansLong, teststruct.arduinoPort.Value, srv,
'toe', teststruct);
```

```
            Tread1=moveTverse( teststruct.arduinoPort.Value , 'scan');
            Long2 = LongScan_SWE(numScansLong, teststruct.arduinoPort.Value, srv,
             'motor', teststruct);
       % return motor to home
            Treturn=moveTverse( teststruct.arduinoPort.Value , 'return');
            uisave({'teststruct', 'Long1', 'Long2', 'Tread1', 'Treturn',
'Tmoves'}, ['UltrasoundScannerData_'
char(datetime('now','Format','yyyyMMdd_HHmmssSSS'))])

        case 2
            disp('Three longitudinal scans')
            Long1 = LongScan_SWE(numScansLong, teststruct.arduinoPort.Value, srv,
             'toe', teststruct);
            Tread1=moveTverse( teststruct.arduinoPort.Value , 'scan');
            Long2 = LongScan_SWE(numScansLong, teststruct.arduinoPort.Value,
             srv,'motor', teststruct);
            Tread2=moveTverse( teststruct.arduinoPort.Value , 'scan');
            Long3 = LongScan_SWE(numScansLong, teststruct.arduinoPort.Value, srv,
             'toe', teststruct);% send motor back home
            ReturnLong = LongReturn(teststruct.ftL.Value,
             teststruct.arduinoPort.Value, 'motor', teststruct);
            Treturn=moveTverse( teststruct.arduinoPort.Value , 'return');
            Treturn2=moveTverse( teststruct.arduinoPort.Value , 'return');
            uisave({'teststruct', 'Long1', 'Long2', 'Long3', 'Tread1', 'Tread2',
             'Treturn','Treturn2','Tmoves','ReturnLong'},
       ['UltrasoundScannerData_'
             char(datetime('now','Format','yyyyMMdd_HHmmssSSS'))])
    end
else
    warndlg('Unrecognized scan type - scan not taken')
end
disp('done scan')
end

%---------------------------------------------------------------------------------
function scanIms=LongScan(numScans, arduinoPort, srv, direction, teststruct)
% take the scan in the longitudinal direction - takes images
% inputs:
%     numScans = number of scans
%     arduinoHandle = object containing arduino information
%     srv = object containing Aixplorer information
%     out1 = either 0 or 1, variable controlling direction of the motor
%     (high first or low first)default is high first
%     pd = motor rate for scan; default is 100us -> speed is hardcoded into
%     arduino code for now

warning('off', 'serialport:serialport:ReadWarning');
% define direction of linear motion
remoteFreeze(srv, 1)
remoteFreeze(srv, 0) % force unfreeze
scanIms(numScans,1).img=[]; % num imgs
% start uno
uno=serialport(arduinoPort,  960000, 'DataBits', 8, 'Timeout', 0.07); % 2^14 %
warning('off', 'serialport:serialport:ReadWarning');
if strcmp(direction, 'toe')
    for k=1:numScans
        tic
        if teststruct.stopbtn.Value
            disp('stopped')
            teststruct.stopbtn.Value=0;
            break
        end
```

```
        write(uno, '11>', 'char') %write to uno (longitudinal and direction CCW)
        timetest2(k,1)=toc;
        scanIms(k,1).printout1=read(uno, 5885, "char"); %
        timetest2(k,2)=toc;
        [scanIms(k,1).img, infostruct(k,1).info]=getLiveScreen(srv);
        scanIms(k,1).timestamp=datetime;
        timetest2(k,3)=toc;
        if rem(k,400)==0
            remoteFreeze(srv, 1)
            remoteFreeze(srv, 0) % force unfreeze every~25s - Aixplorer loop is
30s
        end
        pause(.055)
    end
elseif strcmp(direction, 'motor')
    for k=1:numScans
        tic
        if teststruct.stopbtn.Value
            disp('stopped')
            teststruct.stopbtn.Value=0;
            break
        end
        write(uno, '12>', 'char') %write to uno (longitudinal and direction CW)
        timetest2(k,1)=toc;
        scanIms(k,1).printout1=read(uno, 5885, "char");
        timetest2(k,2)=toc;
        [scanIms(k,1).img, infostruct(k,1).info]=getLiveScreen(srv);
        scanIms(k,1).timestamp=datetime;
        timetest2(k,3)=toc;
        if rem(k,400)==0
            remoteFreeze(srv, 1)
            remoteFreeze(srv, 0) % force unfreeze every~25s - Aixplorer loop is
30s
        end
        pause(.055)
    end
end
clear uno
  scanIms(1,1).info=infostruct(1,1).info;
scanIms(1,1).timetest=timetest2;
remoteFreeze(srv, 1) % freeze after end of scan to reduce energy transferred into
plantar tissue
end
%--------------------------------------------------------------------------------
function scanIms=LongScan_SWE(numScans, arduinoPort, srv, direction, teststruct)
% take the scan in the longitudinal direction - takes images
% inputs:
%     numScans = number of scans
%     arduinoHandle = object containing arduino information
%     srv = object containing Aixplorer information
%     out1 = either 0 or 1, variable controlling direction of the motor
%     (high first or low first)default is high first
%     pd = motor rate for scan; default is 100us

remoteFreeze(srv, 1)
remoteFreeze(srv, 0) % force unfreeze
scanIms(numScans,1).img=[]; % num imgs
% start uno
uno=serialport(arduinoPort,  960000, 'DataBits', 8, 'Timeout', 0.07); % 2^14 %
if strcmp(direction, 'toe')
    for k=1:numScans
```

```
tic
        if teststruct.stopbtn.Value
            disp('stopped')
            teststruct.stopbtn.Value=0;
            break
        end
        write(uno, '31>', 'char');
        pause(0.1) % pause so that there is info to collect from arduio
        timetest2(k,1)=toc;
        scanIms(k,1).
       printout1=read(uno, 17620, "char");
        timetest2(k,2)=toc;
        pause(0.2) % pause to avoid motion in the SWE image
        [scanIms(k,1).img, scanIms(k,1).info1]=getLiveScreen(srv);
        [scanIms(k,1).SWEMap, scanIms(k,1).info2]=getSWE(srv, 'last');
        scanIms(k,1).timestamp=datetime;
        timetest2(k,3)=toc;
        pause(0.65)
        scanIms(k,1).img2=getLiveScreen(srv);
        [scanIms(k,1).SWEMap2]=getSWE(srv, 'last');
        scanIms(k,1).time2=datetime;
        pause(0.65)
         scanIms(k,1).img3=getLiveScreen(srv);
        [scanIms(k,1).SWEMap3]=getSWE(srv, 'last');
        scanIms(k,1).time3=datetime;
        pause(.65)
        scanIms(k,1).img4=getLiveScreen(srv);
        [scanIms(k,1).SWEMap4]=getSWE(srv, 'last');
        scanIms(k,1).time4=datetime;
        if rem(k,32)==0
            [scanIms(k,1).Maps2]=getSWE(srv, 'all'); % can pull 326 maps
            remoteFreeze(srv, 1)
            remoteFreeze(srv, 0) % force unfreeze every~25s - Aixplorer loop is
30s
        end
        timetest2(k,4)=toc;
    end
elseif strcmp(direction, 'motor')
    for k=1:numScans
        tic
        if teststruct.stopbtn.Value
            disp('stopped')
            teststruct.stopbtn.Value=0;
            break
        end
        write(uno, '32>', 'char')
        pause(0.1)
        timetest2(k,1)=toc;
        scanIms(k,1).printout1=read(uno, 17620, "char"); % 685 should b
        timetest2(k,2)=toc;
        pause(0.2)
        [scanIms(k,1).img, scanIms(k,1).info1]=getLiveScreen(srv);
        [scanIms(k,1).SWEMap, scanIms(k,1).info]=getSWE(srv, 'last');
        scanIms(k,1).timestamp=datetime;
        pause(0.65)
        scanIms(k,1).img2=getLiveScreen(srv);
        [scanIms(k,1).SWEMap2, scanIms(k,1).info2]=getSWE(srv, 'last');
        scanIms(k,1).time2=datetime;
        pause(0.65)
        scanIms(k,1).img3=getLiveScreen(srv);
        [scanIms(k,1).SWEMap3, scanIms(k,1).info3]=getSWE(srv, 'last');
        scanIms(k,1).time3=datetime;
```

```
pause(.65)
        scanIms(k,1).img4=getLiveScreen(srv);
        [scanIms(k,1).SWEMap4]=getSWE(srv, 'last');
        scanIms(k,1).time4=datetime;
%          pause(0.1)
        if rem(k,32)==0
            [scanIms(k,1).Maps2]=getSWE(srv, 'all'); % can pull 326 maps
            remoteFreeze(srv, 1)
            remoteFreeze(srv, 0) % force unfreeze every~25s - Aixplorer loop is 30s
        end
         timetest2(k,3)=toc;
    end
end
[scanIms(k,1).Maps2]=getSWE(srv, 'all'); % full last batch of SWE maps not captured
after last freeeze/unfreeze
remoteFreeze(srv, 1) % freeze after end of scan to reduce energy trasnferred into
plantar tissue
scanIms(1).readTime = timetest2;
end
%--------------------------------------------------------------------------------
function TverseScans=moveTverse(arduinoPort,direction)
% take the scan in the longitudinal direction - takes images
% inputs:
%     dist = distance to move (tducer width - desired overlap)
%     lead = lead of lead screw
%     microstep = steps per revolution (via motor controller)
%     arduinoHandle = object containing arduino information
%     out1 = either 0 or 1, variable controlling direction of the motor
%     (high first or low first)default is high first
%     pd = motor rate for scan; default is 100us
uno=serialport(arduinoPort,  960000, 'DataBits', 8, 'Timeout', 0.15); % 2^14 %
pause(1.5)

if strcmp(direction, 'scan')
    for q=1:7
       write(uno, '22>', 'char')
    end
    TverseScans.time1=toc;
    TverseScans(1).printout1=read(uno, 8585, "char"); % 685 should b
    TverseScans.time2=toc;
    pause(0.8)
elseif strcmp(direction, 'return')
    for q=1:7
       write(uno, '22>', 'char')
    end
    TverseScans.time1=toc;
    TverseScans(1).printout1=read(uno, 8585, "char"); % 685 should b
    TverseScans.time2=toc;
    pause(0.8)
end
end
%--------------------------------------------------------------------------------
function scanIms=LongReturn(footL, arduinoPort, direction, teststruct)
% take the scan in the longitudinal direction - takes images
% inputs:
%     numScans = number of scans
%     arduinoHandle = object containing arduino information
%     srv = object containing Aixplorer information
%     out1 = either 0 or 1, variable controlling direction of the motor
%     (high first or low first)default is high first
%     pd = motor rate for scan; default is 100us -> speed is hardcoded into
%     arduino code for now
```

```
% define direction of linear motion
% start uno
uno=serialport(arduinoPort,  960000, 'DataBits', 8, 'Timeout', 0.05); % 2^14 %
clear movmnts nummvmnts
pause(3)
distmm=footL-10;
possibledists=[50,20,10,5,2,1,0.3];
indx=2;
pause(5-0.5*movmnts(1)) % for some reason, if don't have this pause, first step
won't execute?
movmnts(1)=min(find(floor(distmm./possibledists)));
nummvmnts(1)=floor(distmm./possibledists(movmnts(1)));
remainder=rem(distmm, possibledists(movmnts(1)));
while remainder>0.20001
    movmnts(indx)=min(find(floor((remainder+.00001)./possibledists)));
    nummvmnts(indx)=floor(remainder./possibledists(movmnts(indx)));
    remainder=rem(remainder, possibledists(movmnts(indx)))
    indx=indx+1;
end
% assign arduino code for speed
    s='3';
% assign arduino code for direction and axis
    d='2';
for k=1:length(movmnts)
    for n=1:nummvmnts(k)
        if teststruct.stopbtn.Value
            disp('stopped')
            teststruct.stopbtn.Value=0;
            break
        end
        tic
        t=num2str(7-movmnts(k));
        write(uno, ['5' d s t '>'], 'char') %write to uno 1 (longitudinal) and 2
(direction CW)
        disp(['5' d s t '>'])
        scanIms(k,1).movetime2(k,1)=toc;
        scanIms(k,1).printout1=read(uno, 5585*(8-(7-movmnts(k)))^2, "char"); % 685
should b
        scanIms(k,1).movetime2(k,2)=toc;
        pause(17/movmnts(k)-0.8)
        disp(num2str(5585*(8-(7-movmnts(k)))^2))
    end
end
clear uno
end

%-----------------------------------------------------------------------------------
function Joginfo=Jog_motor(btn, teststruct, direction, speed)
% take the scan in the longitudinal direction - takes images
% inputs:
%     numScans = number of scans
%     arduinoHandle = object containing arduino information
%     srv = object containing Aixplorer information
%     out1 = either 0 or 1, variable controlling direction of the motor
%     (high first or low first)default is high first
%     pd = motor rate for scan; default is 100us -> speed is hardcoded into
%     arduino code for now
```

```
% define direction of linear motion
uno=serialport(teststruct.arduinoPort.Value,  960000, 'DataBits', 8, 'Timeout',
0.05); % 2^14 %
pause(1.5)
% assign arduino code for speed
if contains(speed.SelectedObject.Text, '2')
    s='1';
elseif contains(speed.SelectedObject.Text, '5')
    s='2';
elseif contains(speed.SelectedObject.Text, '10')
    s='3';
end
% assign arduino code for direction and axis
if strcmp(direction, 'motor')
    d='1';
elseif strcmp(direction, 'toe') % direction of motor
    d='2';
elseif strcmp(direction, 'arch') % direction of motor
   d='3';
elseif strcmp(direction, 'ankle') % direction of motor
    d='4';
end
if teststruct.stopbtn.Value
    disp('stopped')
    teststruct.stopbtn.Value=0;
else
    write(uno, ['4' d s '>'], 'char') %write to uno 1 (longitudinal) and 2
(direction CW)
    Joginfo.jogtime(1,1)=toc;
    Joginfo.jogOut(1,1).printout1=read(uno, 5585, "char"); % 685 should b
    Joginfo.jogtime(1,2)=toc;
    pause(.04)
end
end

%----------------------------------------------------------------------------
function Moveinfo=moveMotorDistance(btn, teststruct,  speed, distance)
uno=serialport(teststruct.arduinoPort.Value,  960000, 'DataBits', 8, 'Timeout',
0.05); % 2^14 %
distmm=distance.Value;
mms=speed.Value;
possibledists=[50,20,10,5,2,1,0.3];
indx=2;
movmnts(1)=min(find(floor(distmm./possibledists)));
nummvmnts(1)=floor(distmm./possibledists(movmnts(1)));
remainder=rem(distmm, possibledists(movmnts(1)));
while remainder>0.20001 % (0.3mm is smallest move)
    movmnts(indx)=min(find(floor((remainder+.00001)./possibledists)));
    nummvmnts(indx)=floor(remainder./possibledists(movmnts(indx)));
    remainder=rem(remainder, possibledists(movmnts(indx)));
    indx=indx+1;
end
% assign arduino code for speed
if contains(speed.Value, '10') % make condition for 10 first, otherwise
    s='3';
elseif contains(speed.Value, '5')
    s='2';
elseif contains(speed.Value, '1')
    s='1';
end
```

```
% assign arduino code for direction and axis
disp(teststruct.axisbg.SelectedObject.Text)
if strcmp(teststruct.axisbg.SelectedObject.Text, 'A')
    d='1';
elseif strcmp(teststruct.axisbg.SelectedObject.Text, 'P') % direction of motor
    d='2';
elseif strcmp(teststruct.axisbg.SelectedObject.Text, 'M') % direction of motor
   d='3';
elseif strcmp(teststruct.axisbg.SelectedObject.Text, 'L') % direction of motor
    d='4';
end
pause(5-0.5*movmnts(1))
for k=1:length(movmnts)
    for n=1:nummvmnts(k)
        if teststruct.stopbtn.Value
            disp('stopped')
            teststruct.stopbtn.Value=0;
            break
        end
        tic
        t=num2str(7-movmnts(k));
        write(uno, ['5' d s t '>'], 'char')
        disp(['5' d s t '>'])
        Moveinfo.movetime2(k,1)=toc;
        Moveinfo.moveOut(k,1).printout1=read(uno, 5585*(8-(7-movmnts(k)))^2,
             "char");
        Moveinfo.movetime2(k,2)=toc;
        pause(.04)
        disp(num2str(5585*(8-(7-movmnts(k)))^2))
    end
end
end
```

C Appendix C: DVC sensitivity analysis

In order to choose the DVC run with optimized parameters for obtaining the metrics of interest, a variety of DVC parameters were tested, and several metrics were chosen to assess the quality of the results using each set of parameters: vertical displacement (C1), quality of the moving image remapped to the reference image using the calculated displacement (C2, C3), the total average vertical strain (C3, C4), and the correlation value (C3, C4). From prior work, the total average vertical strain is expected to be around 50% underneath the load bearing bones. Using initial thicknesses (e.g. around 2cm at the heel) expected averaged displacements (e.g. 10cm) can be estimated. The displacement is expected to be highest toward the bone with a gradient of lower displacements moving toward the skin using an oversimplified assumption of linear elasticity and modeling different materials as springs in series. The correlation value is an internal metric of how well 'matching' subvolumes correlate. Higher values indicate a better match. Finally, the remapped images should closely resembled the reference images.

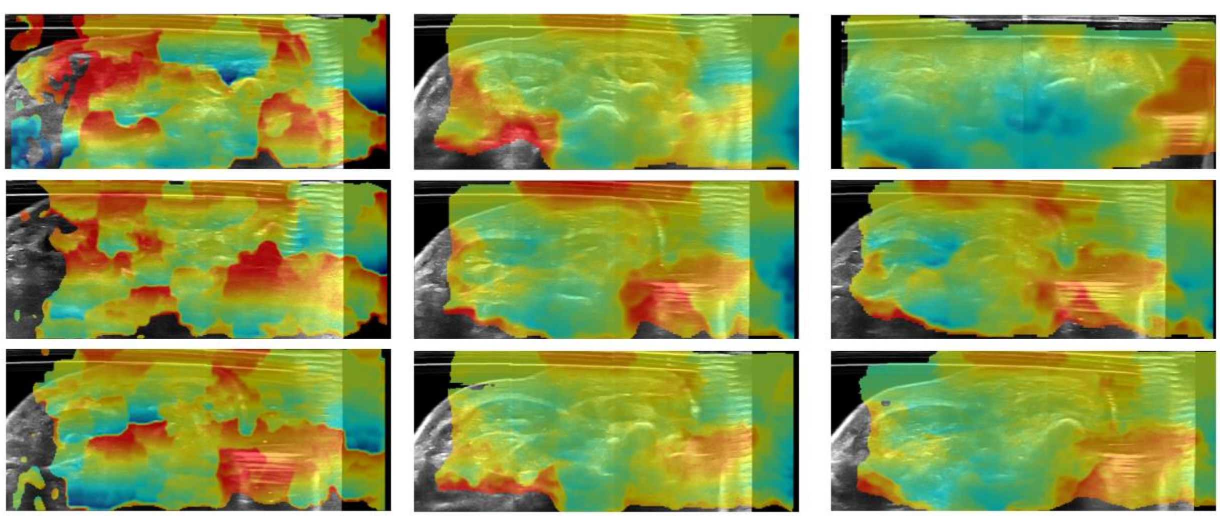

'poor' fit. Displacement is noisy, lots of red (displacement in opposite direction of expected)

'OK' fit. Displacement relatively smooth, mostly yellow (zero) or cool (displacement in expected direction)

'good' fit. Displacement largely cool (In expected direction) and gradient is more cool toward bones (more displacement in deeper tissue)

Figure C-1 Representative Coronal slices used to assess feasibility of the vertical displacement result. Examples pulled from both C1 and C2.

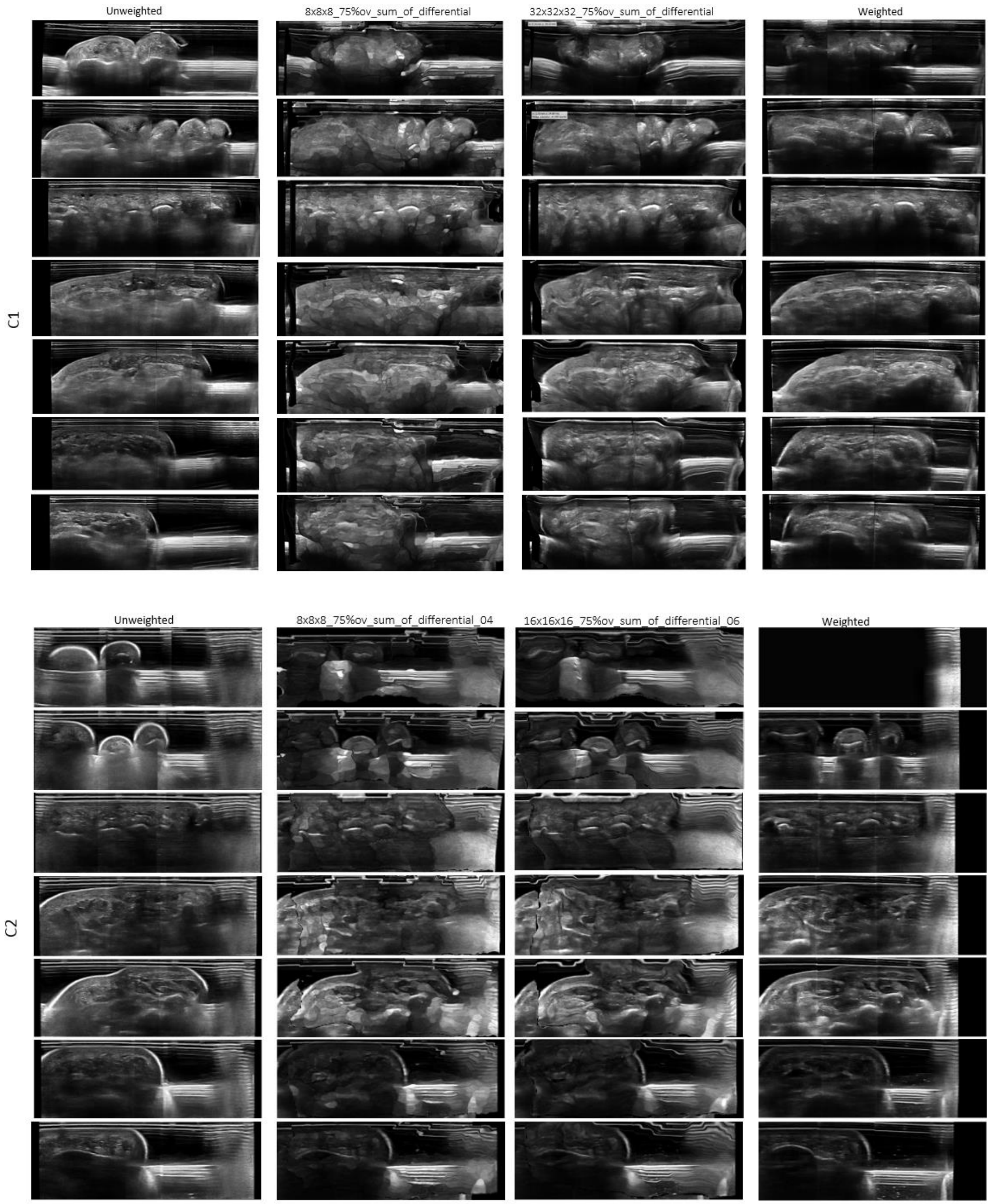

Figure C-2 Left**.** Unweighted reference image. Middle. Representative coronal slices of weighted volume remapped to the unweighted volume to assess the quality of the total displacement result. Examples rated ‘good’. Bone and skin margins, bright lines, and general shapes match well between the reference and remapped images. Right. Weighted ‘deformed’ volume to which displacement is applied to obtain the remapped volumes.

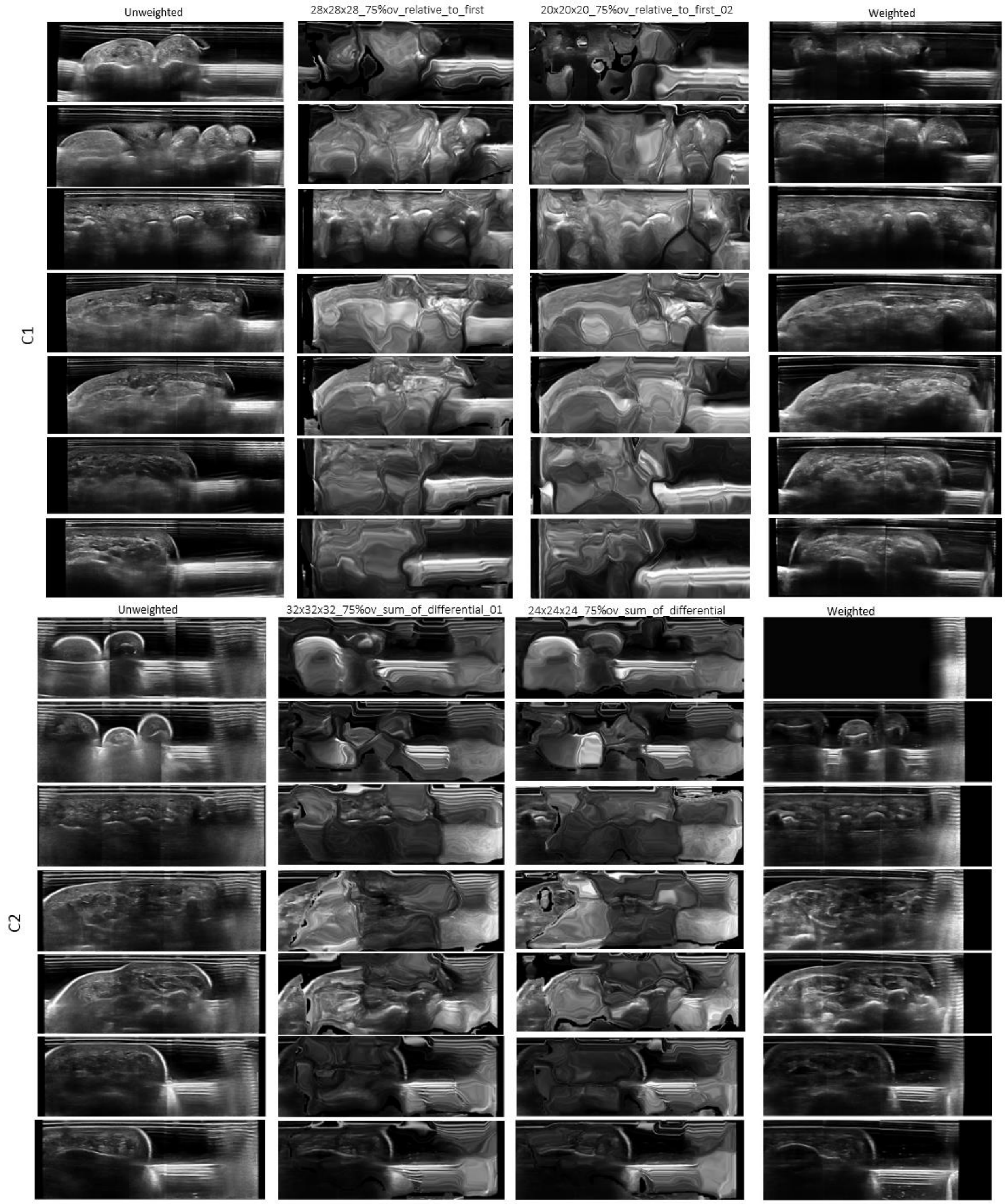

Figure C-3 Left. Unweighted reference image. Middle. Representative coronal slices of weighted volume remapped to the unweighted volume to assess the quality of the total displacement result. Examples not rated ‘good’. Large whorls obscure fine detail, the skin-plate margin is distorted, and bones are unclear. Right. Weighted ‘deformed’ volume to which displacement is applied to obtain the remapped volumes.

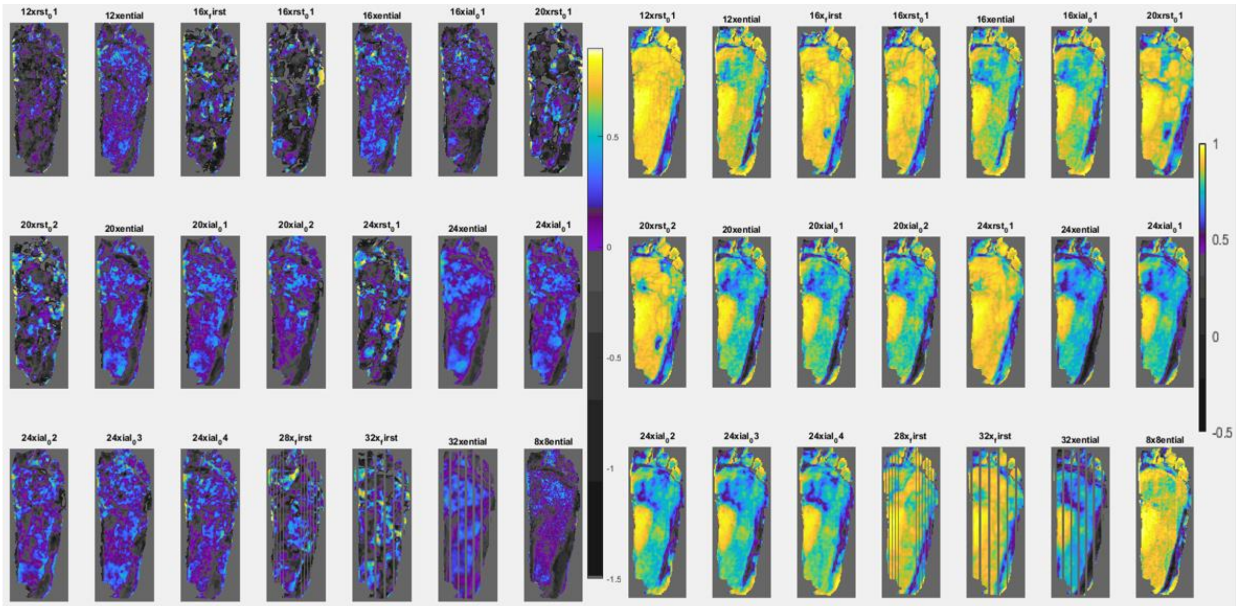

Figure C-4 Spatial maps of average vertical strain and correlation value used to assess the accuracy, feasibility, and confidence of the result for subject C1. Vertical strain is expected to be between 0-50% for load bearing regions, the ideal correlation value is 1.

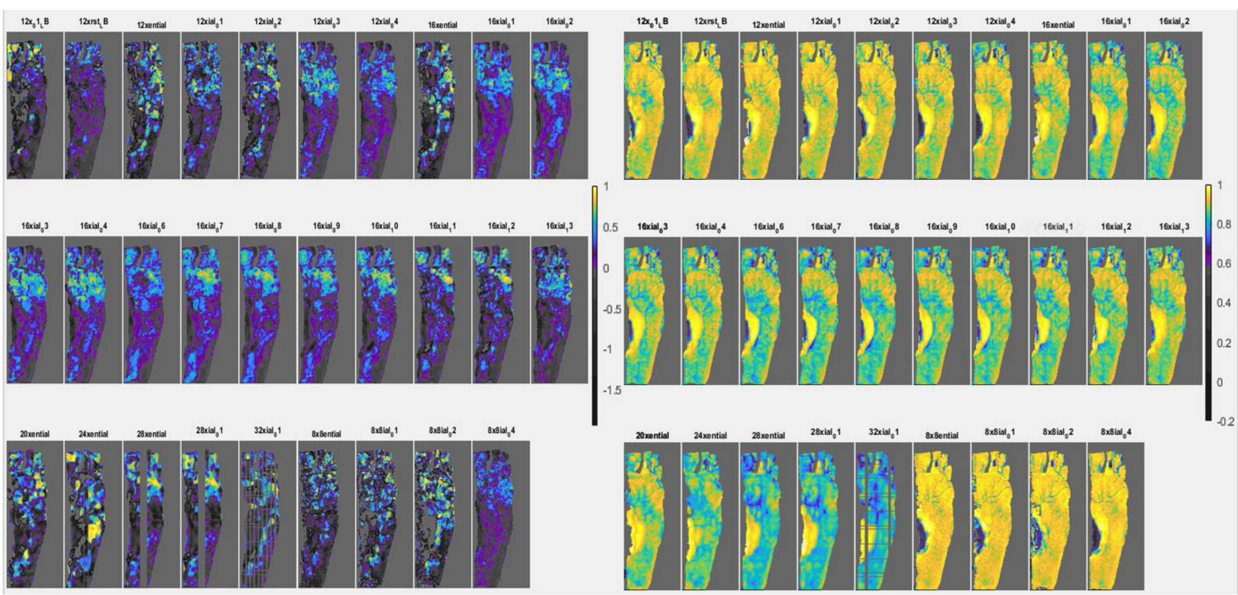

Figure C-5 Spatial maps of average vertical strain and correlation value used to assess the accuracy, feasibility, and confidence of the result for subject C2. Vertical strain is expected to be between 0-50% for load bearing regions, the ideal correlation value is 1.